Growth and Characterisation of Terrace Graded Virtual Substrates with $Si_{1-x}Ge_x$ $0.15 \leq x \leq 1$.

By

Lee John Nash

This thesis is submitted in partial fulfilment of the requirements towards the degree of Doctor of Philosophy for work carried out in the Department of Physics of the University of Warwick.

September 2005

Abstract

Growth of *terrace graded* virtual substrates, pioneered by Capewell (2002), has been conducted utilising *solid-source molecular beam epitaxy* (SS-MBE) to produce structures of higher composition (up to pure germanium) and greater thickness (up to 20 μm) than previously investigated. Terrace grading offers a number of advantages over more conventional grading techniques which include the reduction of surface threading dislocation density, reduction of surface roughness and the possibility of the complete elimination of threading dislocation *pile-up*. The closely spaced pile-up of threading dislocations is believed to have a significant impact on the electrical properties of processed devices, and its elimination is a key goal in this work.

Numerous terrace graded virtual substrate compositions have been grown and characterised during the course of this work and, were appropriate, comparison made with more conventional structures. The complete elimination of threading dislocation pile-up has been demonstrated at compositions of 30% and 40%, with a reduced threading dislocation density in comparison to equivalent linear graded structures. A major reduction in threading dislocation density has been accomplished though post growth *ex-situ* annealing at 900ºC for an extend period of time, though the exact mechanism remains uncertain. The possible role of surface precipitates enabling reduction of dislocation pile-up and/or density is considered along with the effects of unwanted particulate contamination during growth.

Table of Contents

List of Figures

List of Tables

Acknowledgements

I would like take this opportunity to thank my supervisors Prof. E.H.C. Parker and especially Dr. T.J. Grasby for their support and advice.

I would like to thank all of the members of the Nano Silicon group both new and old for their friendship and advice and above all for making the last four years enjoyable and most entertaining. I would also like to give special thanks to Adam Capewell who has always found time to answer any questions I have posed and Dominic Fulgoni for his light-hearted and always colourful name calling.

For experimental work carried out on my behalf I would like to thank Dr. T.J. Grasby for selected MBE material growths (75043, 75044, 76007 and 76009) and Neil Wilson (University of Warwick) for all AFM imaging.

Finally, I would like to thank my Mom and family for their support when I was growing up (and not out) without which I am sure I would not have reached such lofty heights and I dedicate this work in the memory of my late Father, John Nash.

Declaration

This thesis is submitted to the University of Warwick in support of my application for degree of Doctor of Philosophy. Except where specifically stated all of the work described in this thesis was carried out by the author or under his direction

Chapter 1

1 Introduction

1.1 Semiconductor Technology

The semiconductor industry is one of the largest in the world with sales totalling more than $200 billion in 2004 (SIA-Online 2005). Silicon based technologies constitute 97% of the industry (Paul 2004) and growth in the semiconductor industry has been driven by the every increasing performance and complexity of silicon based integrated circuits (IC) and micro-processors in particular. The low cost and abundance of raw silicon material, combined with the excellent oxide, SiO_2, formed on its surface has historically allowed the density of transistor devices to double every eighteen months since the prediction was first made by Moore (1965). The unprecedented pace of development in the semiconductor sector has primarily been achieved through scaling of the *metal-oxide-semiconductor field effect transistor* (MOSFET) feature size that form the basis of microprocessor technology. The current generation of AMD (Advanced Micro Devices) consumer microprocessors contain up to 233 million transistors in an area of less than 200 mm^2 and are fabricated at the 90 nm technology node with transistor channel lengths around 65 nm (AMD 2005).

1.2 MOSFET Scaling

The scaling of MOSFET device dimensions has allowed an increase in transistor packing density (Figure 1.1) and speed whilst moderating power consumption. A basic guideline for device scaling is to retain a constant electric field within the device whilst reducing device dimensions (gate length, gate oxide thickness

etc) and applied voltages (supply voltage) and also increasing the substrate doping concentration by a common factor. In principle, this yields a speed increase in the circuit whilst the power dissipated per chip area remains unchanged (Taur 1998). A schematic of an n-MOSFET transistor is shown in Figure 1.2.

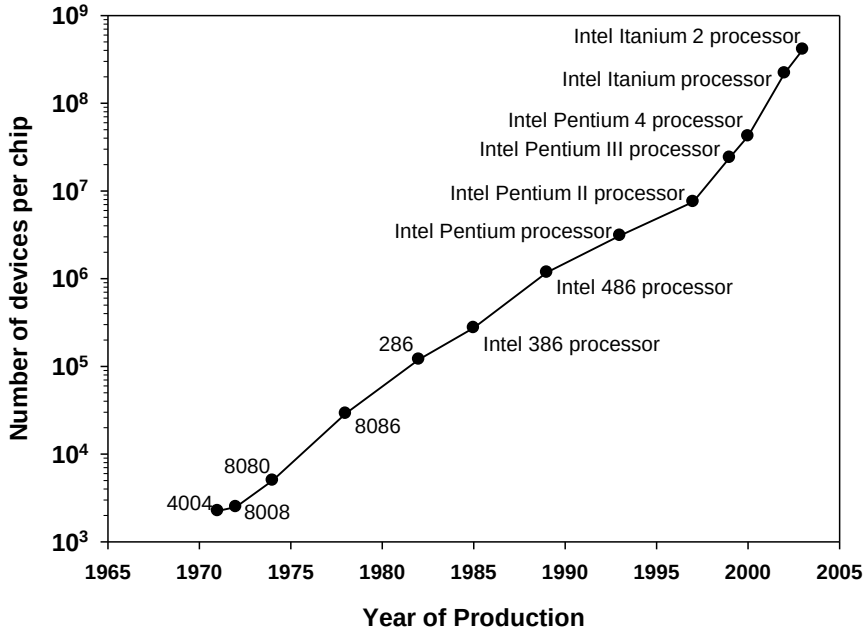

Figure 1.1 – Showing the rising number of transistors contained within Intel® processors (Intel 2005).

Unfortunately performance enhancement by scaling alone has a limited future as we rapidly approach a number of important obstacles. Of primary concern is the spiralling cost of new fabrication plants required to manufacture each successive generation of scaled devices, predicted to exceed $10 billion by 2010 (Paul 1999). The reduction in oxide thickness, required with each new generation, is also resulting in an increasing current leakage due to quantum mechanical tunnelling, leading to higher power dissipation and reduced device reliability. The oxide thickness in production by Intel® at the 90 nm technology node is only 1.2 nm (Ghani *et al.* 2003).

At present a great deal of research interest is focused toward development of *high-k* dielectrics to alleviate this problem.

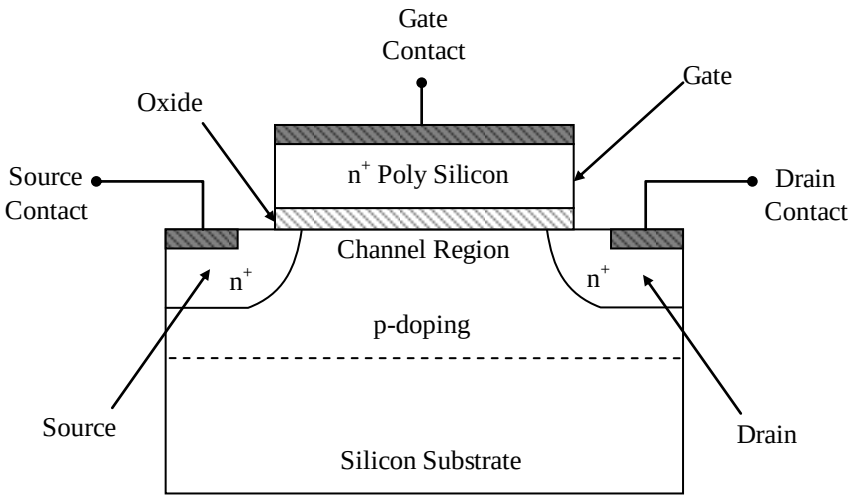

Figure 1.2 – Schematic representation of an n-MOSFET transistor.

1.3 Introduction of Strain Engineering

The introduction of strain to the MOS transistor channel provides the opportunity to obtain enhanced drive (on) currents and thereby device performance at existing technology nodes and a great deal of interest is currently focused on so-called *strained silicon* technologies. Carrier mobility, μ, is an important parameter for device performance that determines the carrier drift velocity, v, in an applied electric field, E (at low electric fields), see equation (1.1).

$$v = \mu E \tag{1.1}$$

Strain-induced enhancements in carrier mobility will result in increased MOSFET drain current, allowing faster transistor operation (Nicholas 2004).

The application of biaxial tensile strain to silicon has a significant effect on the electronic band structure of the semiconductor, affecting both the conduction and

valence bands. The conduction band minima of unstrained silicon occur along the six <001> crystal directions (Δ minima) and are six-fold degenerate. The application of biaxial tensile strain lifts this degeneracy forming a two-fold and four-fold degenerate set (Figure 1.3). The energy of the two-fold degenerate valleys are lowered, becoming preferentially occupied by electrons, reducing intervalley scattering and lowering the in-plane conduction mass (related to the curvature of the surface). This yields a higher electron mobility (Rim *et al.* 2003) as can be seen from examination of equation (1.2).

$$\mu = \frac{q\tau}{m^*} \tag{1.2}$$

where q is electronic charge, τ is the mean free relaxation time of the carrier and m^* is the carrier effective mass.

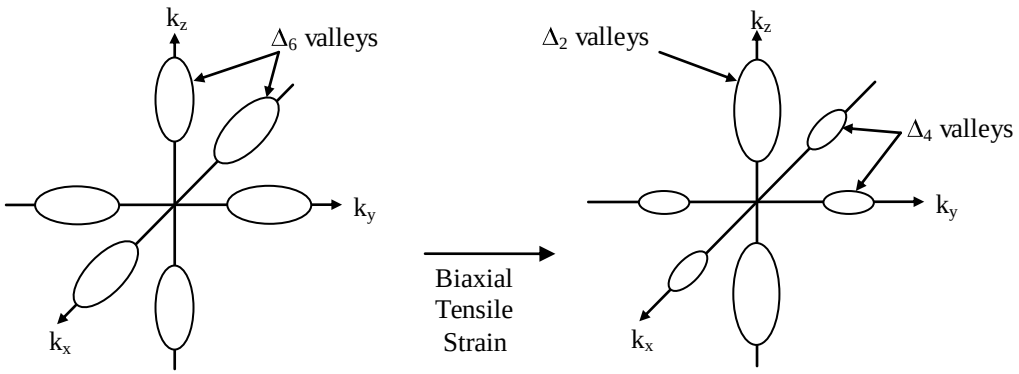

Figure 1.3 – Schematic representation of the constant-energy ellipses for unstrained and strained silicon showing the lifting of degeneracy by the application of tensile strain Takagi *et al.* (1996).

Similarly the valence band has degeneracy of the light and heavy hole bands (so named because of the effective masses of carriers in these bands) lifted at the zone centre (Figure 1.4). Greater strain is required to reduce inter-valley scattering in the

valence band. For a recent review of the electrical properties of strained silicon the reader is referred to Nicholas (2004).

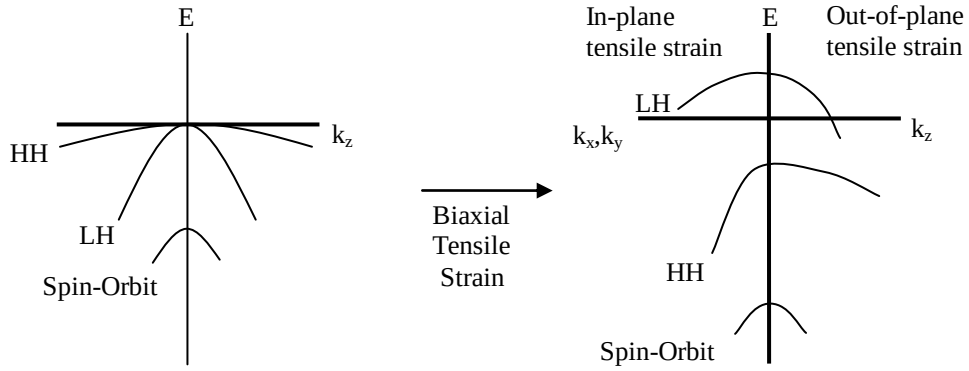

Figure 1.4 – Biaxial tensile induced changes in the valence band of silicon Rim *et al.* (2003).

The application of strain to silicon material within the channel region of an FET (Field Effect Transistor) has been approached from two distinct directions. Intel® has pioneered *process-induced strain*, where uniaxial strain (tensile or compressive) is applied directly to the channel region of a device structure through novel processing steps (Ghani *et al.* 2003). A second approach involves biaxial global straining of the whole silicon layer. This is achieved through the epitaxial deposition of a relaxed silicon-germanium layer possessing a greater lattice constant than bulk silicon onto which a thin strained silicon channel may be deposited yielding a biaxial tensile strained silicon layer. This global strain tuning layer is called a *virtual substrate*, and the work in this thesis is concerned with investigations that could lead to significant improvement in the quality of such structures.

1.4 Silicon-Germanium Technology

Incorporation of germanium into a silicon lattice can be achieved over the entire compositional range of $Si_{1-x}Ge_x$ for $0 < x < 1$ to form a random alloy with the lattice parameter varying almost linearly with composition, in close accordance with Vegard's Law (chapter 2 section 2.2.1). Interest in low composition relaxed virtual substrates is mainly based on the benefits of increased carrier mobility provided, whilst retaining compatibility with existing fabrication technology. Oberhüber *et al*. (1998) have theoretically predicted enhancements for electron mobility in silicon, when deposited on a fully relaxed $Si_{1-x}Ge_x$ alloy with x = 15-25% to form a biaxial tensile strained layer. An enhancement is also predicted for hole mobility but requires a greater strain, equivalent of deposition on a fully relaxed silicon germanium alloy with x = 30%. These predictions are shown graphically in Figure 1.5.

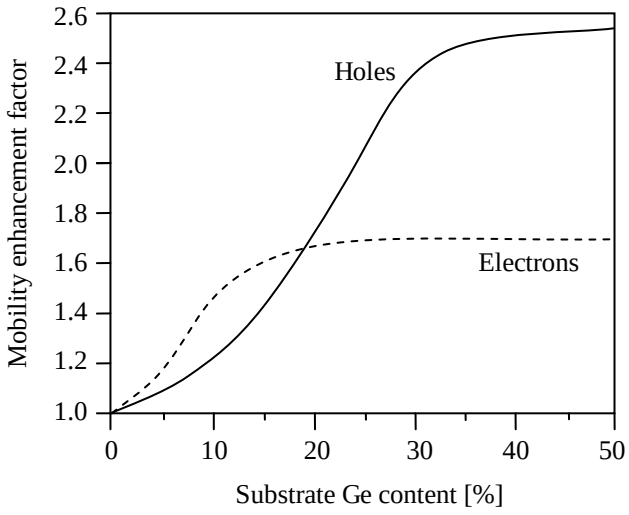

Figure 1.5 – Theoretical prediction of electron (dotted line) and hole (solid line) mobility enhancement in a strained silicon MOS device structure under low field conditions Oberhüber *et al.* (1998).

A major problem with this technology is that the quality of the virtual substrate is compromised by defects generated by the strain relaxation process, leading to

degradation of device performance, reliability and yield issues and manufacturing problems.

Germanium possess the highest bulk electron and hole mobilities of any bulk elemental semiconductor (comparison with silicon given in Table 1.1) but the low natural abundance of germanium makes bulk wafers uneconomic for mass production.

	Bulk Electron Mobility ($cm^2V^{-1}s^{-1}$)	Bulk Hole Mobility ($cm^2V^{-1}s^{-1}$)
Silicon	**1450**	**505**
Germanium	**3900**	**1800**

Table 1.1 – Room temperature bulk lattice mobilities of electrons and holes in unstrained, undoped Si and Ge. Reproduced from a paper by Schäffler (1997).

The utilisation of silicon as a cheap platform on which a virtual substrate based relaxed pure germanium structure is formed could allow the integration of III-V optoelectronic devices, that share lattice parameters close to that of germanium (e.g. GaAs), to be incorporated into a highly integrated circuit, Figure 1.6.

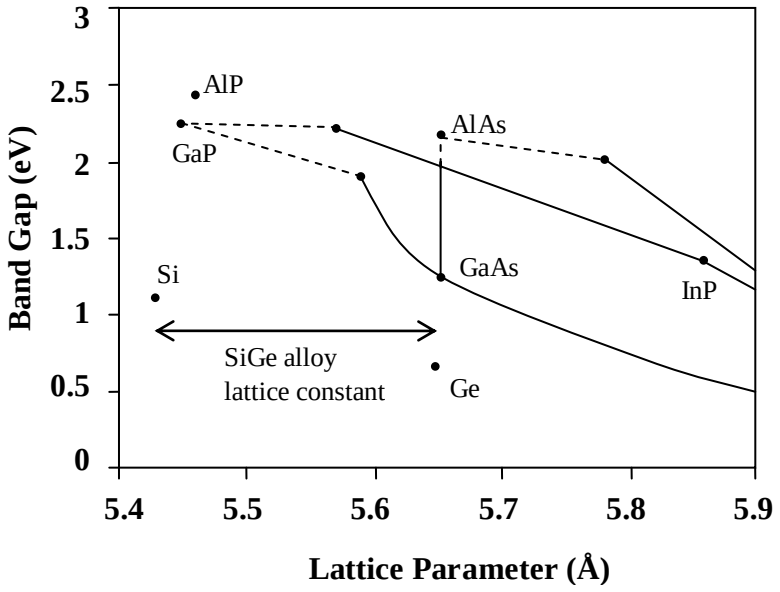

Figure 1.6 – A map of band gap versus lattice constant for the III-V alloys and Si and Ge Fitzgerald *et al.* (1999).

This would allow the development of optical interconnect technologies and allow further assimilation of high frequency device architectures into highly integrated circuits. Also the possibility of virtual substrate based germanium channel (relaxed or strained) MOSFET devices is now of extreme interest with many investigations into high-k dielectrics for germanium underway. This would allow very high channel carrier mobilities to be harnessed and would provide a valuable performance boost to the mainstream microelectronics industry.

1.5 Layer Transfer Technology

The reduction of transistor feature size has given rise to numerous so called *short channel effects* (SCE) that become an increasing problem for smaller devices (Nicholas 2004). To combat some of these effects AMD have introduced a layer transfer technology into their mainstream device processing in the form of silicon-on-insulator (SOI), demonstrating it to be a mature process (Soitec 2003). The SOI is provided by bonding a thin (minimum 50 nm) silicon layer to the surface of an oxidised silicon wafer forming an SOI structure, illustrated in Figure 1.7.

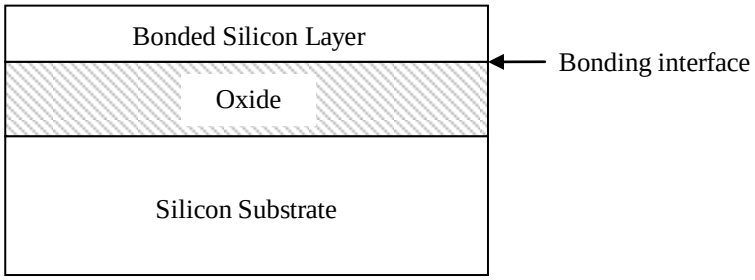

Figure 1.7 – Schematic illustration of the layered structure of an SOI (silicon-on-insulator) wafer.

The relevance of this technology in the current study is that the *Smart Cut*™ technology (Soitec 2003) used in the layer transfer process, can be equally applied to

the transfer of other materials, including a strained-silicon layer produced on a virtual substrate. Critically this process removes the virtual substrate from the active layer. In this situation the quality of the transferred layer reflects the quality of the virtual substrate and is paramount, almost certainly impacting on the behaviour of the strained layer during device processing. The possibility of re-growing and reusing the base structure with this technology could further reduce cost.

1.6 Thesis Aims and Structure

The main drive of this thesis is to investigate and control the silicon-germanium relaxation process to enable further improvement in the quality of relaxed virtual structures. The virtual substrate structures were grown epitaxially using solid-source MBE (molecular beam epitaxy) at the University of Warwick on commercial silicon (001) orientated wafers. Specifically this work aims to extend that of Capewell (2002) on a novel germanium grading technique, known as *terrace grading*, to far greater thickness and composition ranges than hitherto, making comparison with more conventional structures. Ultimately the work should enable progress toward the production of planar, defect free platforms, terminating at an arbitrary composition between silicon and pure germanium, thereby facilitating further improvements in CMOS device performance and integration of III-V optical devices.

In the following chapters 2 and 3, the principles of silicon-germanium epitaxial growth and strain relief along with a description of the experimental techniques used in growth and characterisation are presented. In chapters 4, 5 and 6 experimental results and discussion for three compositional ranges are presented. Chapter 7 summaries the key points of the investigation and draws conclusions based on the combined evidence collected and proposes further avenues of work.

Chapter 2

2 Principles of Epitaxial Growth and Strain Relief

In this chapter issues concerning the epitaxial growth of silicon and silicon germanium alloys will be discussed and the process of strain relief through dislocation formation and propagation introduced.

2.1 Epitaxial Growth

Epitaxial growth is the extension of a crystalline substrate in a planer manner. A classical model of growth developed by Burton, Cabrera and Frank (BCF Model) remains a useful starting point for our understanding of epitaxial crystal growth (Burton *et al.* 1951). This classical work is not concerned with the reconstruction or bonding of a real crystal surface and as such applies equally to all crystal systems. Growth is described as a result of exchange of molecules between an adsorbed surface layer and vapour (source of molecules) and diffusion of mobile species along the surface until incorporated at a step edge or defect. Epitaxial growth can proceed with the nucleation and growth of two dimensional islands (*2-D island growth*) by the incorporation of mobile unbound surface atoms, now called *adatoms*, at the surface. On a stepped surface growth can proceed by incorporation at the existing step edges resulting in *step flow* growth. Recognition of the reality of imperfect surfaces is highlighted as important in understanding nucleation rates observed in practice.

Knowledge of the movement of an adatom across a real silicon surface is important in understanding epitaxial growth processes. The movement of an adatom across an oxide free and clean silicon surface is greatly influenced by the reconstruction (re-ordering) of the surface. Reconstruction of the silicon surface

allows a reduction in the number of dangling bonds providing a lower surface energy that is energetically favoured (Chadi 1983). A high temperature cleaned silicon (001) surface has been found to display a (2x1) dimer construction lying along <110> directions. A dimer is the rebonding of two neighbouring surface atoms due to the re-hybridisation of the surface dangling bonds (Gawlinski and Gunton 1987).

The silicon substrates used for s*olid-source molecular beam epitaxy* (SS-MBE) in this work have vicinal surfaces (stepped) based on (001) with a surface misorientation of around 0.1º toward <110>. Vicinal surfaces are preferred for epitaxial growth because their stepped surface promotes layer-by-layer growth through terrace extension (step flow) rather than 2-D islanding that can lead to less perfect growth. Growth that proceeds primarily by 2-D island nucleation can lead to the formation of anti-phase boundaries between separately nucleated islands, Figure 2.1.

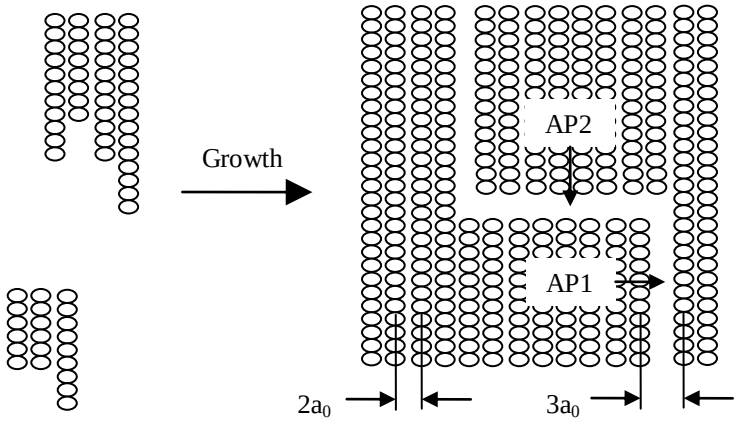

Figure 2.1 – Schematic illustration of silicon islands on the Si (001) – (2x1) surface and the formation of antiphase domain boundaries when these islands intersect. Antiphase boundaries running parallel and perpendicular to the dimer rows are denoted AP1 and AP2 respectively. a_0 is 3.85Å, the lattice (001) constant of the silicon (001) surface Bronikowski *et al.* (1993).

Anti-phase boundaries form because there are two possible sites at which islands can nucleate; when islands initially formed from different sites meet they may be out of

phase and unable coalesce, resulting in a row of surface vacancies and eventually grown-in defects that may result in the loss of epitaxy (Bronikowski *et al.* 1993).

As growth proceeds the orientation of each subsequent layer is perpendicular to the one before and a nomenclature related to the orientation of the dimerisation on the top terrace to the step edge was proposed by Chadi (1987) (although the opposite to that first proposed is now used!). A single step having an upper terrace with dimerisation parallel to its edge is referred to as type A, S_A, with the terrace above it labelled T_A, and a single step with upper terrace of dimerisation perpendicular to its edge as a type B step, S_B, terrace T_B.

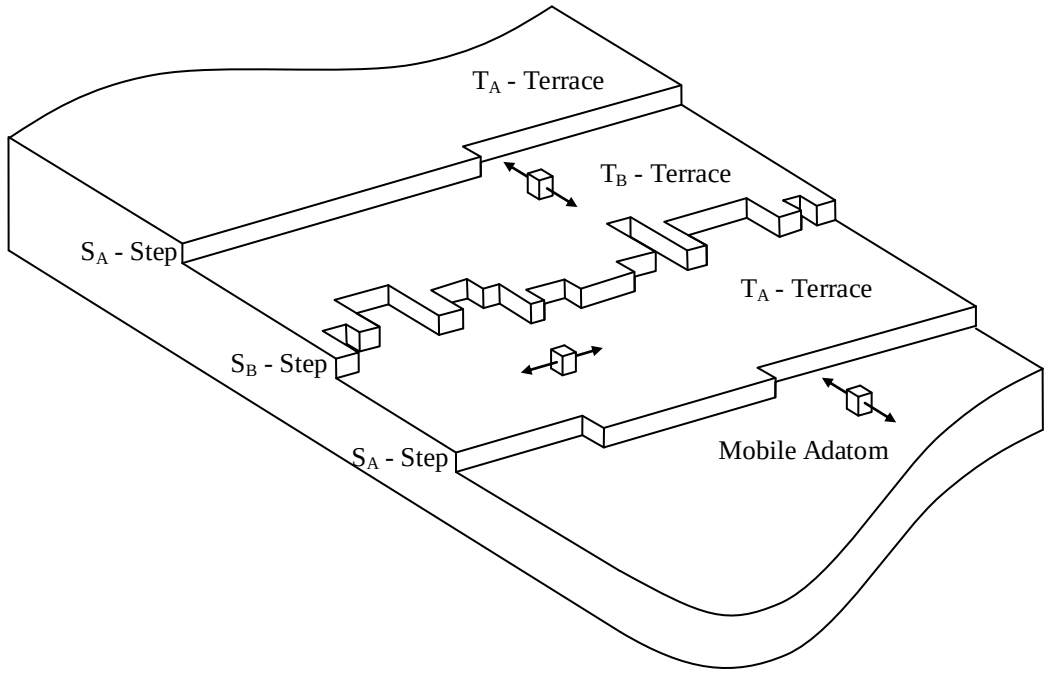

Figure 2.2 – Schematic representation of a vicinal silicon wafer surface. The mobile adatoms most easily move along dimer rows and this direction is indicated with arrows.

Figure 2.2 is a schematic representation of a vicinal silicon wafer surface. Double height steps can also exist and are labelled D_A and D_B respectively as before and are bounded by terraces of the same type. The reconstructed silicon surface greatly influences adatom transport and it has experimentally been found that

transport along dimer rows occurs more rapidly than across them and was determined by examination of *denuded zone* size (Mo and Lagally 1991). Due to the presence of dangling bonds, attachment at the end of a dimer row is far more likely than at the sides, for this reason T_B terraces will generally advance more quickly than T_A terraces.

Jernigan and Thompson (2001) have investigated the evolution of a silicon (001) substrate under normal growth temperatures (350 to 800ºC) and rates (1Å/s) using Scanning Tunnelling Microscopy (STM) to directly image the surface. They have shown that a transition from step flow to 2-D island growth occurred as the temperature was reduced to around 500ºC and that the transition did not occur abruptly, but for a limited temperature window showed characteristics of both growth modes simultaneously. This transition marks a shift from growth dominated by equilibrium processes to one more governed by kinetic processes. This transition will be greatly dependent upon growth rate, surface orientation and the surface species present.

2.2 Heteroepitaxial Growth

The growth of an atomic species upon a substrate of differing composition is referred to as heteroepitaxy and is probably the most important application of epitaxy. There are three recognised growth modes that can be adopted by heteroepitaxial layers; the following inequality determines the mode of growth adopted:

$$\gamma_{12} + \sigma_2 < \sigma_1 \tag{2.1}$$

where γ_{12} - sum of the interface energy between the film and substrate, σ_1 - bare substrate surface energy, σ_2 - epilayer surface energy.

For lattice matched systems two dimensional Frank-van der Merwe (FvM) growth will occur if equation (2.1) is satisfied (Frank and van der Merwe 1949). The epilayer will otherwise be unable to *wet* the substrate surface and growth will result in the formation of isolated three dimensional islands, Volmer-Weber growth (VW) (Volmer and Weber 1926). For non-lattice matched systems strain plays an important role in the evolution of film morphology. A strained epitaxial layer may initially satisfy the above condition for Frank-van der Merwe growth, however at greater thicknesses the strain energy of the film may be sufficient to negate this situation. If such a situation occurs then growth will evolve from van der Merwe to the Volmer Weber growth mode and as such is described separately as the Stranski-Krastanov (SK) mode of growth (Stranski and Krastanov 1938). All 3 growth modes are depicted in Figure 2.3. If the strained layer does not initially satisfy the condition in equation (2.1) then growth is in the Volmer-Weber mode.

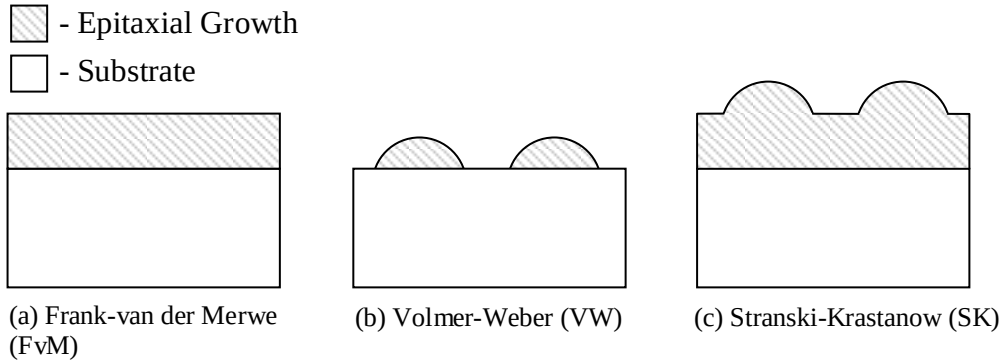

Figure 2.3 – Schematic representation of the growth modes (a) Frank-van der Merwe (FvM) (b) Volmer-Weber (VW) (c) Stranski-Krastanov (SK).

2.2.1 Germanium Incorporation

Silicon heteroepitaxy most commonly involves the addition of germanium and is the main focus of the work presented herein. Germanium shares the same diamond lattice structure as silicon having a bulk lattice constant (length of unit cell) ~4.2% larger. The diamond lattice structure (Figure 2.4) consists of a face centred cubic lattice (fcc) with a basis of atoms situated at (0, 0, 0) and (¼, ¼, ¼) relative to the sides of the unit cell. Germanium forms a random alloy when introduced into a silicon lattice (silicon and germanium atoms randomly occupy lattice sites) over the entire compositional range, with the lattice parameter of the $Si_{1-x}Ge_x$ mixture varying almost linearly. This is in accordance with Vegard's Law, an empirical rule that predicts a linear relationship (at constant temperature) for the variation of lattice constant for an alloy between that of the constituent elements. The epitaxial growth of germanium and silicon-germanium alloy upon silicon has been found to follow a Stranski-Krastanov growth mode where both growth rate and temperature are important parameters.

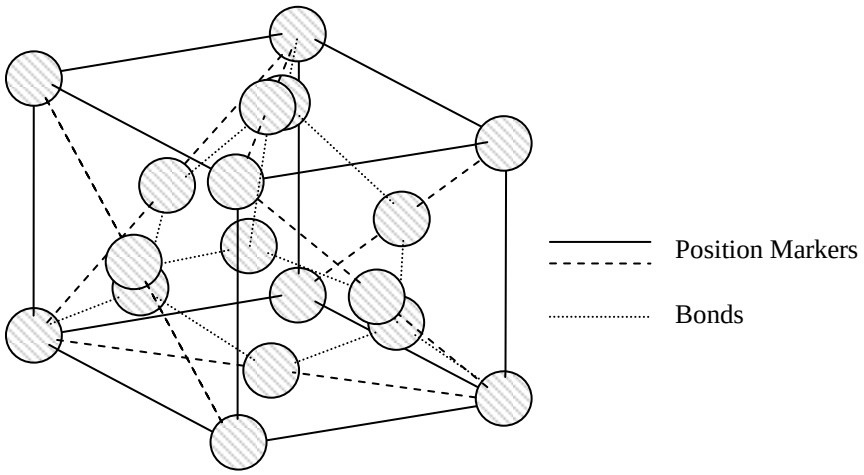

Figure 2.4 – Schematic diagram of the silicon or germanium diamond crystal lattice. Lattice is fcc with a basis of atoms at (0, 0, 0) and (¼, ¼, ¼).

2.2.2 Critical Thickness

An important parameter for Stranski-Krastanov growth is the *critical thickness, h_c,* the thickness at which misfit strain starts to be relieved by dislocation introduction in a strained layer. It is important to bear in mind that it is possible to have a strained layer which although below the critical thickness has already deviated from 2-D growth, undergoing elastic deformation of the surface. Matthews and Blakeslee (1974) first described the critical thickness of an epitaxial layer to be determined by the mechanical equilibrium (force balance) of tension of a grown-in threading dislocation (dislocation that extends from the bulk to a free surface) and the force exerted by the misfit strain (see Figure 2.9 and Section 2.3). For thicker layers it will become energetically favourable for the layer strain to be partially relieved by the propagation of a dislocation through the layer leaving a misfit dislocation at the substrate layer interface.

The Matthews and Blakeslee approach assumes that a number of threading dislocations already exist in the underlying substrate and that growth is being conducted at an equilibrium temperature. The assumption of growth at an equilibrium temperature led to an under estimation of the critical thickness experimentally observed in $Si/Si_{1-x}Ge_x$ layers grown at temperatures lower than the 900ºC required for equilibrium. People and Bean (1985) reviewed this work and produced an improved description of the problem suitable for application to growth at lower temperatures. In this treatment the critical thickness is determined by energy balance, relaxation will only occur when a reduction of the strain energy by formation of a misfit dislocation is energetically favourable. Their treatment provided a thermodynamically metastable upper limit for critical layer thickness and did not assume the pre-existence of threading dislocations. The concept of a *metastable* film

with an *effective critical thickness* is introduced, where although reaching the *equilibrium critical thickness* is necessary to allow dislocation propagation, this will not occur unless sufficient thermal activation energy is present. The effect of film roughening upon critical thickness is not considered.

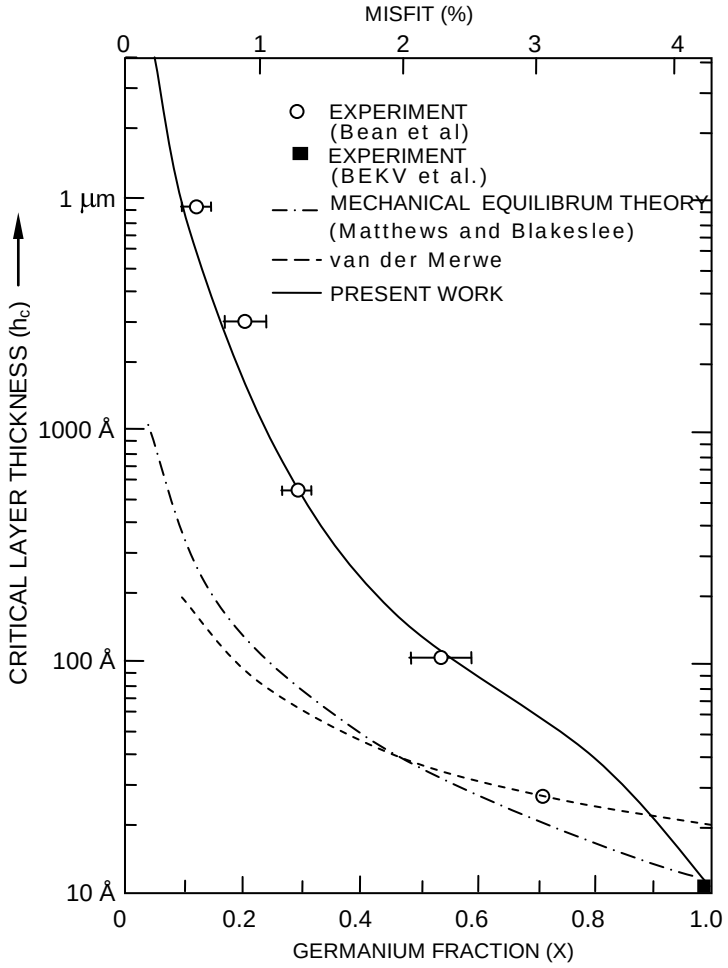

Figure 2.5 – Open circles show experimental data for critical layer thickness of Ge_xSi_{1-x} alloys vs Ge content *x*. The misfit varies from 0 to 4.2% at x=1.0. The solid curve gives the present results, as obtained by energy balance arguments People and Bean (1985).

Houghton *et al.* (1995) demonstrated that at higher temperatures (comparable to those used for device processing) the *effective* h_c approaches the *equilibrium* h_c, and speculated on the role of surface morphology as an alternative means of strain relaxation. It has been found experimentally that partial elastic relaxation of an island

permits a reduction in elastic free energy outweighing the increase in surface energy, due to the increased surface area, even though the strain energy at intervening cusps is locally higher (Cullis 1996). A migration of germanium atoms occurs toward the tops of islands where the local lattice parameter is greater. When the built-up strain can no longer be accommodated solely by elastic relaxation, plastic deformation inevitably occurs with dislocation formation preferentially occurring at the highly strained cusps.

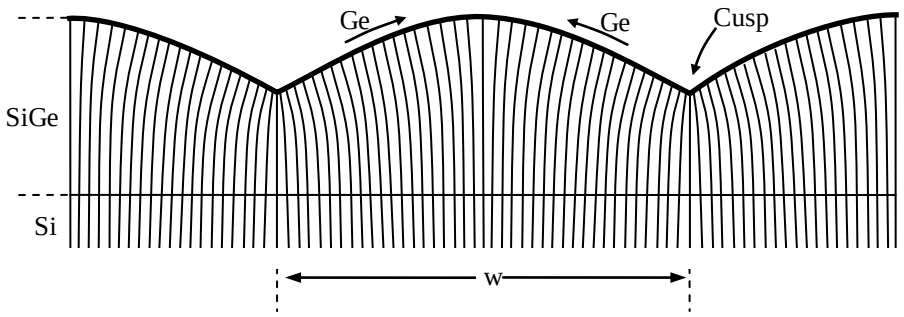

Figure 2.6 – Diagram showing elastic distortion of vertical lattice planes in a morphologically undulating heteroepitaxial layer (w is the wavelength of undulation) under compressive stress upon its substrate Cullis (1996).

The sign of the strain is of additional importance, it has been demonstrated that layers under compressive strain (e.g. SiGe grown on Si) show far greater roughening than layers under tensile strain (e.g. Strained Si on SiGe) even for the same layer composition (Roland 1996). Step density and in particular the step free energy have been suggested as a mechanism. The step free energy is approximated to the step energy, defined as the energy difference between a surface with and without a step. Theoretical investigation of this issue employing a molecular dynamics simulation has found that overall the effect of tensile strain is to lower step energies whilst compressive strain results in higher step energies, consistent with experiment (Xie *et al.* 1994; Roland 1996).

2.3 Exceeding the Critical Thickness and Virtual Substrates

Pseudomorphic (fully strained) silicon-germanium layers become limited in their application at higher germanium concentration, where the critical thickness of such layers decrease to such an extent that they are no longer viable for applications such as carrier confinement. To illustrate this point, a pure germanium layer grown directly onto a silicon substrate has a critical thickness of around 3 monolayers (Mo *et al.* 1990). The fabrication of an intermediate layer with terminating lattice spacing between that of the silicon substrate and germanium has a number of important benefits. Such intermediate layers could allow compressive, tensile or strain relaxed silicon-germanium layers with compositions reaching pure germanium. For example allowing the production of tensile strained silicon on a silicon based substrate and a platform on which III-V technologies could be integrated, all of which could help further extend the life of this cheap, current and mature technology. Such relaxed intermediate layers have become known as *virtual substrates*.

The formation of a virtual substrate requires the strain relaxation of an intermediate layer, through the introduction of dislocations, assuming a lattice parameter equal to that of bulk material at the same composition (plastic deformation). The strain within a pseudomorphic epitaxial layer can be expressed in terms of the misfit resulting from the differing lattice parameters, being equal in magnitude but opposite in sign to that of the misfit:

$$Misfit = -\varepsilon = \frac{a_{layer} - a_{substrate}}{a_{substrate}} \tag{2.2}$$

where a_{layer} is the bulk lattice parameter of the epitaxial layer, $a_{substrate}$ is the bulk lattice parameter of the substrate and ε is the pseudomorphic layer strain.

A dislocation is the boundary between regions within a crystal that are discontinuous, with the accommodation of lattice mismatch between the layer and substrate being achieved through the generation and extension of *misfit dislocations*.

2.3.1 Burgers Vector Analysis

The magnitude and direction of a Burgers vector characterises the crystal displacement due to a dislocation. Burgers vector analysis can be used to characterise a dislocation, its motion and interactions with other dislocations (Cottrell 1964). The Burgers vector of a perfect dislocation can be determined by following the Burgers-Frank method (Cottrell 1964), illustrated in Figure 2.7.

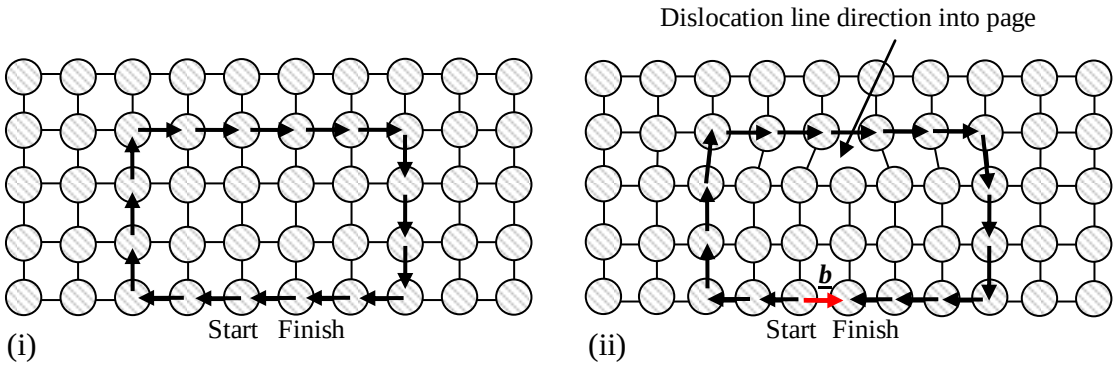

Figure 2.7 – The Burgers vector of a dislocation can be determined by completing a right-handed circuit in a perfect region of crystal (i) and then making a comparative circuit around the dislocation (ii). The Burgers vector, $\underline{b}$, is defined as the vector needed to close the circuit from start to finish (RH/SF convention).

A unit vector along the dislocation line is chosen at an arbitrary point and defined as its *line direction*. In a clockwise direction, with respect to the line direction, complete a circuit around a region of perfect crystal lattice, stepping between atomic lattice positions. The same circuit completed around a part of the lattice containing the dislocation will be incomplete, corresponding to the displacement in the lattice due to the dislocation. The vector required for completion of the circuit directed from start

to finish corresponds to the dislocations *Burgers vector*, $\underline{b}$. Importantly, a Burgers vector is a conserved quantity being the same along the entire length of a dislocation.

2.3.2 Dislocation Motion

The expansion of a misfit dislocation occurs preferentially by *glide* of the threading dislocation through the epilayer, Figure 2.8. Glide is the movement of a dislocation within a plane purely by the local rearrangement of atomic bonds. Glide of a dislocation can occur in any plane that contains both the *line direction* and the *Burgers vector* (Hull and Bacon 2002). The *glide velocity* of a dislocation is an important quantity as will be discussed below, the thermally activated glide velocity is given by:

$$v_g = B\varepsilon \exp\left(-E_g / kT\right) \tag{2.3}$$

where v_g is the glide velocity, ε is the mismatch strain, E_g is the thermal activation barrier for glide, k is Boltzmann's constant, T is temperature in Kelvin and B is a constant (Mooney 1996).

The activation barrier for glide has been measured for the silicon-germanium system and is given by:

$$E_g = \left(2.16 - 0.7x\right) \text{eV} \tag{2.4}$$

where x is germanium content (Tuppen and Gibbings 1990).

Equations (2.3) and (2.4) indicate that the glide velocity of a dislocation is highly sensitive to both temperature and composition and that the activation energy

barrier for glide is relatively low at around 2 eV - this is low compared with the activation energies for homogeneous nucleation at 40 eV (Hull and Bean 1989) and modified Frank-Read multiplication nucleation at 4 eV (Mooney *et al*. 1994).

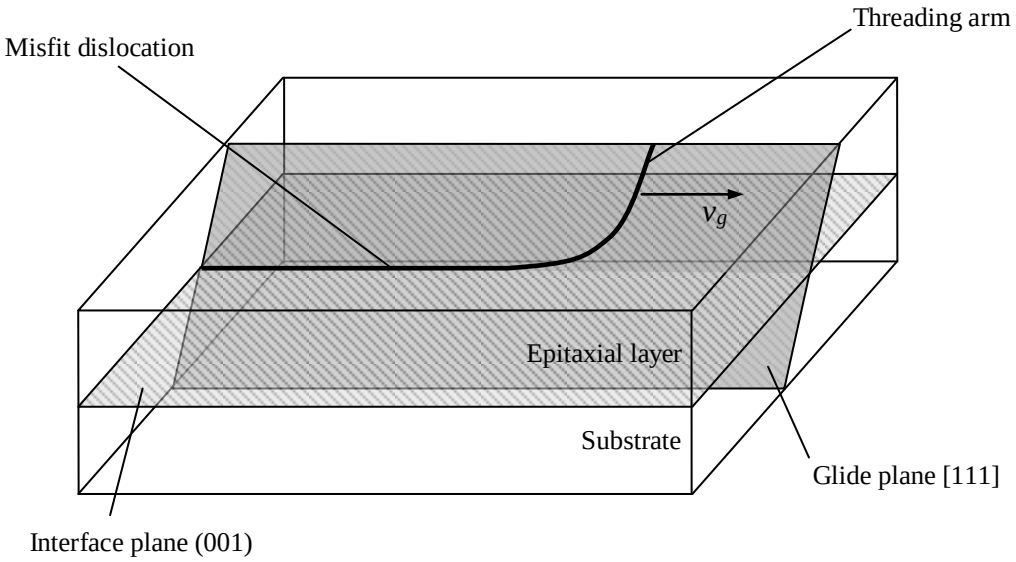

Figure 2.8 – Schematic diagram of a threading dislocation propagating through an epitaxial layer leaving an interface misfit dislocation behind.

Threading dislocations have been found to glide a factor of 5000 times more quickly in bulk germanium than bulk silicon (Kasper 1995). Glide velocity can also be strongly influenced by presence of dopants and impurities, the presence of n-type doping $>10^{17}$ cm^{-3} having been shown to enhance dislocation motion in silicon (Kasper 1995).

Movement of a dislocation can occur in a manner that is none conservative, rather than by simple bond rearrangement, requiring mass transport and leading to the production of either voids or interstitials. Such movement is called *climb*, as to perform such motion requires the dislocation to have climbed out of its glide plane. Climb only becomes an important factor in dislocation motion at higher temperatures or where there is an abundant supply of vacancies or interstitials.

The propagation of a dislocation occurs in order to relieve strain within the epitaxial layer. The amount of strain relieved is related to the Burgers vector of the dislocation and in particular to the component of the Burgers vector resolved perpendicular to the line direction in the layer interface plane in which the strain is present. This is known as the *effective Burgers vector*, $\underline{b}_{eff}$.

$$\underline{b}_{eff} = \underline{b}\cos\lambda \tag{2.5}$$

where $\underline{b}$ is the Burgers vector of the dislocation and λ is the angle between the Burgers vector and the direction within the interfacial plane which is perpendicular to the line direction (Bolkhovityanov *et al.* 2001).

The strain energy relieved, E_r, by a misfit dislocation of length, l, at an epitaxial layer depth below a free surface, d, is given by (illustrated in Figure 2.9):

$$E_r = 2G\varepsilon\frac{(1+\nu)}{(1-\nu)}\underline{b}_{eff}ld \tag{2.6}$$

where G is the shear modulus and ν is Poisson's ratio. For derivation see example in Capewell (2002).

The elastic strain energy associated with screw, edge and mixed dislocations differs (section 2.3.3), however a further approximation of the *strain energy per unit length* is valid for all:

$$E_{elastic\ strain} = \alpha G\underline{b}^2 \tag{2.7}$$

where $\alpha \approx 0.5\text{-}1.0$, G is shear modulus, $\underline{b}$ is Burgers vector.

Importantly, the elastic strain energy is proportional to the square of the dislocations Burgers vector and as a result smaller Burgers vectors are favoured, the energy of a dislocation clearly also increases linearly with misfit length (Hull *et al.* 2002).

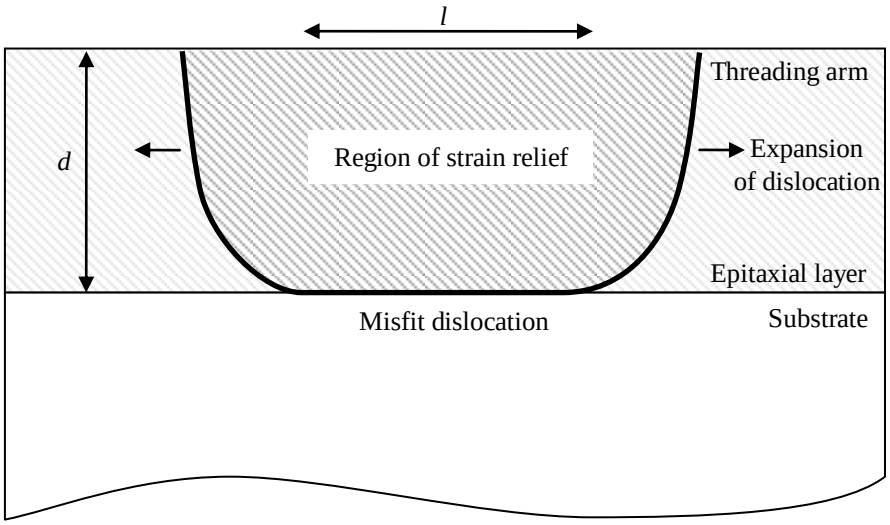

Figure 2.9 – Diagram illustrating the strain relief provided by an expanding misfit dislocation as the threading arms glide apart.

A dislocation cannot terminate within the crystal bulk, it must either terminate upon itself, at a node with another defect or at a free surface (Kasper 1995). Dislocations are usually connected at either end to the growth surface (closest free surface) by a *threading dislocation*. Propagation of a dislocation will occur until (a) it reaches a wafer edge, where the misfit will terminate directly; (b) sufficient strain has been relieved by the misfit that further expansion is energetically unfavourable; (c) it meets another threading dislocation mutually annihilating; or (d) it is unable to pass another orthogonally placed dislocation becoming *pinned* (trapped). The annihilation of two threading dislocations requires them to share equal Burgers vectors, forming a continuous misfit dislocation.

Ideally all threading dislocations will either mutually annihilate or reach the edge of the wafer reducing the number of threading dislocations remaining at the surface to zero. Surface threading dislocations are unwelcome in virtual substrates (*buffers*) used for device processing, with a clear link between current leakage and threading density, that leads to degraded performance (Giovane *et al.* 2001). Surface undulations have also been found to be increased when large numbers of threading dislocations *pile-up* along orthogonal misfit dislocations (Fitzgerald *et al.* 1999). The annihilation of threading dislocations is statistically unlikely, although LeGoues (1994) has found that the modified Frank-Read multiplication mechanism can lead to self-aligned dislocations where the likelihood of annihilation is greatly increased (discussed in section 2.3.7.3).

2.3.3 Nature of Dislocations

The nature of a dislocation is commonly described in terms of the relationship between the Burgers vector and line direction. When a dislocation Burgers vector and line dislocation are perpendicular it is referred to as an *edge dislocation*, and when parallel to one another as a *screw dislocation*. In instances where a dislocations Burgers vector and line direction are at some other arbitrary angle then it is described as a *mixed dislocation*.

The nature of a dislocation has important consequences in relation to propagation through a crystal. As stated in Section 2.3.2, glide of a dislocation can only occur along planes that contain *both the line direction* and the *Burgers vector*. In the case of pure screw dislocations where the Burgers vector and line direction are parallel glide is possible on *any plane*. However for edge dislocations where the

Burgers vector and line direction are orthogonal, glide is possible in only *one plane*. Mixed dislocations will similarly be limited to glide on only *one plane*.

2.3.4 Silicon and Germanium Crystal System

In every crystal system a preferred glide plane exists, were dislocation propagation is most easily accomplished, having the lowest Peierls stress (Peierls 1940). The Peierls stress is the applied stress required to overcome the lattice resistance to the movement of a dislocation in an otherwise perfect lattice. For the diamond lattice these are the (111) planes, being the most closely packed (Cottrell 1964), with the intersection of these planes with the (001) occurring along [110], hence it is in these directions that misfit dislocations propagate. In a face centred cubic structure such as the silicon and germanium crystal lattice the shortest translation vector is ½[110].

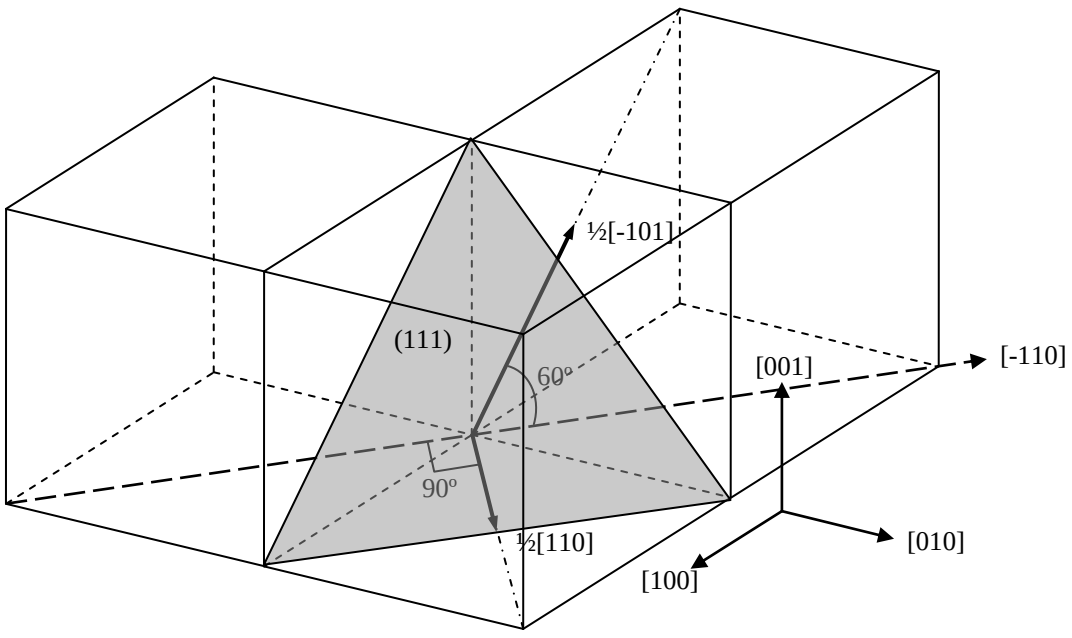

Figure 2.10 – Diagram illustrating the relationship between dislocation Burgers vectors of the form ½[110], with specific reference to the (111) glide plane and its intersection with the (001) along the [-110] line direction.

As the energy of a dislocation is proportional to the square of its Burgers vector (section 2.3.2), the most energetically favourable Burgers vectors are of this form. Such Burgers vectors are situated at angles of either 60º or 90º to the line direction of the dislocation and in this system are commonly referred to as 60º and 90º dislocations, see Figure 2.10.

Although a 90º dislocation more efficiently relieves strain in the (001) plane, as the Burgers vector is the same as the effective Burgers vector in this case, it is unable to glide in the preferred (111) plane (this contrasts with the 60º dislocation) and so extension of the misfit can only occur through climb. It is therefore most common under normal conditions that 60º dislocations are favoured even though they are less efficient at relieving strain, with misfit extension through glide along the (111) plane.

It is important to note that a 60º dislocation (perfect) is unstable against dissociation into closely spaced 30º and 90º dislocations (partial) separated by a stacking fault (Hull and Bean 1993). This is a demonstration of *Frank's Rule* that if a dislocation with Burgers vector $\underline{b}_1^2 > (\underline{b}_2^2 + \underline{b}_3^2)$ then it is unstable and favourable to dissociate into two dislocations $\underline{b}_2$ and $\underline{b}_3$ (Hull *et al.* 2002). The opposite case follows similarly.

2.3.5 Dislocation Nucleation

A modern silicon wafer can be expected to be essentially dislocation free (density < $10/cm^2$) (Goorsky 2000); however, the complete relaxation of a strained silicon-germanium epitaxial layer requires the presence of a large number of dislocations. It is clearly important to identify and understand the manner in which new dislocations are *nucleated* (created) to be able to improve and optimise the

structure and growth parameters used in the creation of virtual substrates. The mechanisms for dislocation nucleation can be placed into three broad categorises, *homogeneous*, *heterogeneous* and *multiplication* (Kasper 1995).

Homogeneous nucleation is the spontaneous creation of dislocations at a free surface due to intrinsic epilayer strain. An activation energy of 40 eV (Hull *et al.* 1989) is calculated for dislocation formation of this type, and is only likely to occur under conditions of significant epilayer strain and high material quality were no other mechanisms are available or at very high temperature.

Heterogeneous nucleation can occur through the inclusion of particulates or impurity precipitates that result in a local lattice strain that is significantly higher than in the bulk. As such the rate of heterogeneous nucleation is likely to be very dependent on the cleanliness of the epitaxial growth chamber, and could contribute significantly to dislocation nucleation in an epilayer of low strain.

Multiplication mechanisms allow for a rapid increase in dislocation nucleation, whereby a small number of initial dislocations can repeatedly act to generate many additional dislocations. The rate at which multiplication sources can be generated is entirely governed by the presence of dislocations formed by other means. There is strong evidence to suggest that the dominant mechanism for dislocation generation in a thick, low strained epilayer is multiplication (LeGoues *et al.* 1992). The modified Frank-Read multiplication mechanism has been specifically proposed and will be discussed in detail later.

2.3.6 Orthogonal Misfit Dislocation Interactions

The *driving force* for dislocation motion in a strained epilayer is the net excess stress, σ_{ex}, due to lattice mismatch and can be expressed as follows:

$$\sigma_{ex} = \sigma_a - \sigma_T \tag{2.8}$$

where σ_a is the applied stress from lattice mismatch, σ_T is the self energy of the misfit dislocation line per unit length (line tension) (Dodson and Tsao 1987).

A common and important interaction between misfit dislocations occurs at the intersection of a moving threading segment with an existing orthogonally located dislocation, see Figure 2.11. The proximity of an orthogonally located misfit dislocation results in additional traction on the glide plane of the threading dislocation, termed the *interaction force (G_I)* by Freund (1990) and described as:

$$G_I = -\int_{B_g} \sigma_{ij}^I n_j \underline{b}_i dx_3' \tag{2.9}$$

where σ_{ij}^I is the additional contribution to the applied stress field due to dislocation interaction, n_j is the number of intersected orthogonal dislocations, $\underline{b}_i$ is the Burgers vector of the intersecting dislocation, and B_g is the boundary defined by the intersecting dislocation threading arm, integrated in a direction orthogonal to the intersecting misfit within the glide plane.

In layers with low amounts of strain *all* such interactions lead to blocking of the moving dislocation (Stach *et al*. 2000). In this *blocking regime*, insufficient stress remains from lattice mismatch to overcome the local stress present due to the existing misfit dislocation, such that the excess stress experienced by the threading arm is reduced to zero and its progress is blocked.

In general, for layers with greater excess stress the outcome of this type of interaction is dependent on the relationship between the dislocation Burgers vectors, the depth at which the encounter occurs, the material composition of the layer and the unrelieved misfit strain present. Stach *et al.* (2000) observed that intersections

between dislocations with parallel Burgers vectors undergo a splitting reaction, forming into two separate dislocations each with a 90º bend, Figure 2.11.

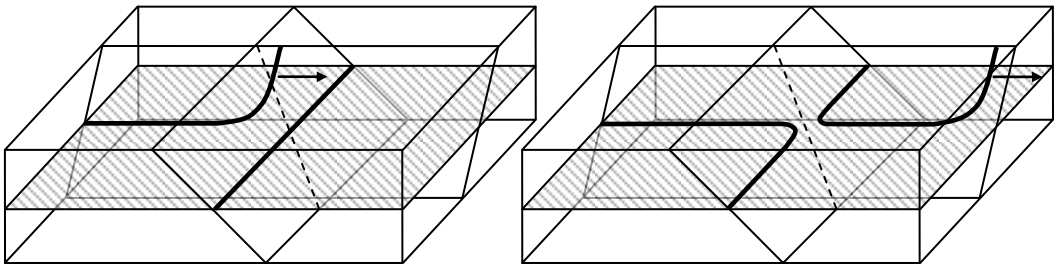

Figure 2.11 – Diagrams illustrating how (a) the intersection of an orthogonally placed misfit dislocation by a moving threading segment can (b) result in a splitting reaction, if the dislocations share parallel Burgers vectors. Misfit segments both lie in the shaded plane with the glide planes for each represented.

In all but the lowest composition and thinnest samples (the *blocking regime*) dislocation splitting was required (but not alone sufficient) for blocking to occur between two dislocations. Importantly it was discovered that dislocations pinned after a splitting reaction required the application of far more stress to free than would have been required to initially avoid pinning. It is suggested that dislocation motion can be stopped at thicknesses and compositions far in excess of that predicted theoretically, and that the reality of a 60º dislocation actually moving as a closely spaced 30º and 90º partial dislocation may provide an explanation (Stach *et al*. 2000).

A similarly important interaction occurs when a propagating misfit dislocation encounters multiple (more than one) closely spaced orthogonal misfit dislocations. Freund (1990) notes that if n closely spaced dislocations with identical Burgers vectors are encountered the magnitude of the interaction force is magnified a factor of approximately n, see equation (2.9). This increase in interaction stress has the effect

of extending the blocking regime to regions of higher stress. This type of interaction is extremely important when considering dislocation nucleation by multiplication, discussed in section 2.3.7.2.

2.3.7 Multiplication Mechanisms

2.3.7.1 Frank-Read Mechanism

Frank-Read multiplication sources can result when a section of dislocation becomes pinned at either end by the climb or jog (step moving dislocation from one atomic slip plane to another) of the dislocation between different glide planes, represented schematically in Figure 2.12 (a).

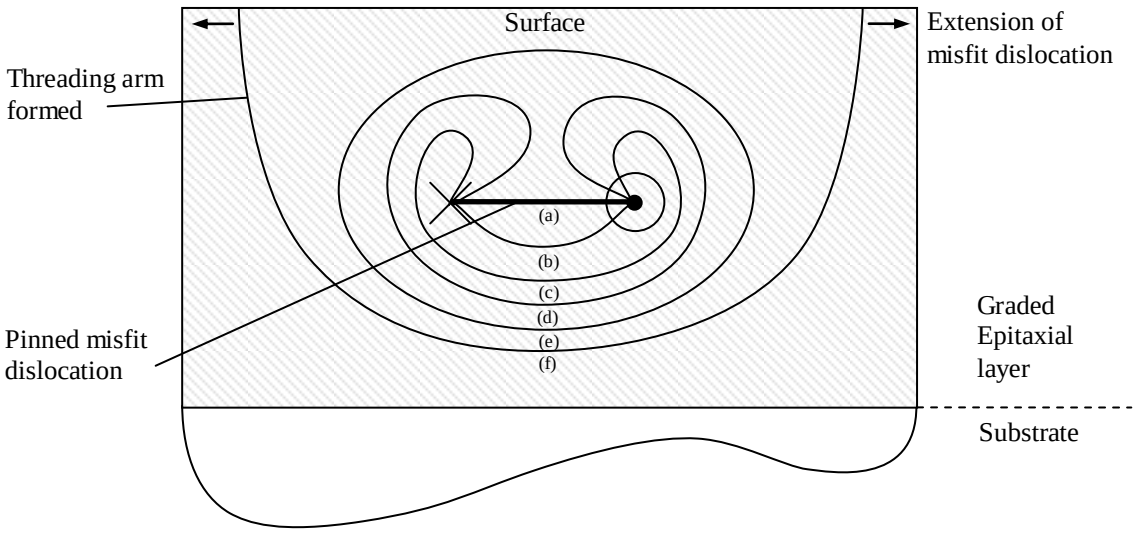

Figure 2.12 – Schematic cross-sectional representation of a Frank-Read dislocation source. The central dislocation line marked (a) is pinned at either end by jog of the dislocation on to different glide planes marked by the cross and point. Expansion of the dislocation is shown (b)-(d) until it eventually closes upon itself (e). The complete loop continues to grow, intersecting the growth surface forming two threading arms which glide apart (indicated with arrows), whilst the original dislocation returns to its original state (a).

The influence of a shear stress on the pinned segment can cause it to bow out (LeGoues *et al.* 1992) toward the substrate along a single glide plane, Figure 2.12 (b-d), eventually closing upon itself to form a complete dislocation loop as well as reforming the initial dislocation. The loop then continues to expand until it intersects the surface at which point the formed threading arms glide away from one another, Figure 2.12 (f). This process can be repeated as long as sufficient stress remains available to drive bowing of the initial dislocation.

2.3.7.2 Modified Frank-Read Mechanism (MFR)

A multiplication mechanism similar in nature to that of a Frank-Read source was first analysed by LeGoues (1992) in the silicon germanium crystal system in linearly graded layers with a shallow rate of grading, and has since become referred to as the *modified* Frank-Read mechanism (MFR).

The intersections of orthogonal misfit dislocations having parallel Burgers vectors undergo a splitting reaction forming two corner dislocations (Lefebvre *et al.* 1991). MFR sources are formed at such intersections providing that one corner is able to initially reduce its length by bowing down into the substrate; configurations for the four slip systems of the MFR mechanism are detailed by Mooney *et al.* (1994). In a similar manner to Frank-Read sources the dislocations begin to bow, however in this case the two orthogonal dislocations bow on separate glide planes connected along a line common to both. The bowing continues until the two segments unite to form a dislocation loop connected between glide planes along the common line. The loop continues to grow in size until the top intersects the sample surface whereby two threading dislocation arms form, gliding away and forming two new misfit dislocations on the same glide plane as the parent dislocations but spatially separated

in the layer. Figure 2.13 (a) and (b) show schematically the initial situation with one corner starting to bow, as well as the situation a short time later once the loop has been formed intersecting the surface resulting in two new threading arms. The MFR source is able to nucleate many additional dislocations provided sufficient misfit stress remains unrelieved, the resulting dislocation network is shown schematically in Figure 2.13 (c) and (d).

A characteristic trait of dislocation multiplication is illustrated in Figure 2.13 (d), where dislocations are pushed deep into the underlying substrate by the repeated generation of dislocations on the same two glide planes. Each misfit dislocation has the effect of producing a small step upon the surface of the sample around 2.8 Å high (Lutz *et al.* 1995), further dislocations nucleated upon the same glide plane (the case for MFR) result in a linear increase in step size. The commonly observed consequence of a *pile-up* of misfit dislocations is to produce a *cross-hatch* on the sample surface that is visible using optical methods.

Cross-hatch is an undesirable quality on a relaxed buffer layer, a non-planar surface is detrimental to the electrical performance of devices processed on top and could prove a problem for lithography in more extreme cases. Fitzgerald *et al.* (1992) proposed an alternate view that the amplitude of cross-hatching observed in graded buffer layers could not be explained as solely due to the steps produced by underlying dislocations. It was proposed instead that the inhomogeneous strain fields emanating from dislocations were responsible for roughening of the surface during growth.

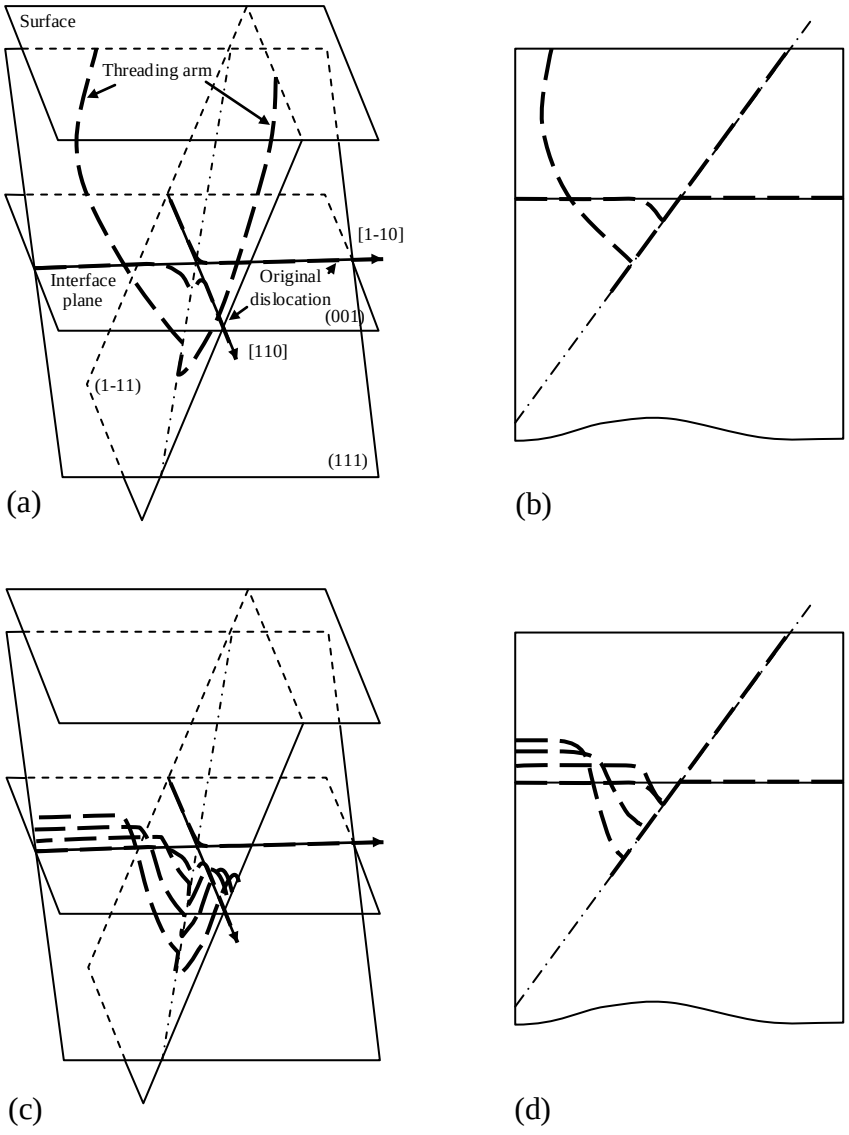

Figure 2.13 – Schematic representation of the formation and operation of a modified Frank-Read multiplication source. Pictures (a) and (c) show a three dimensional representation whilst (b) and (d) show a corresponding [1-10] projection. (a) and (b) Two dislocations with the same 1/2[10-1] Burgers vector cross with a 90° angle in the plane of the interface. All of the planes and directions are indicated. The typical annihilation of the intersection is represented, as well as the bending of one of the corners toward the substrate resulting from the interaction between the two corners. In addition a fully formed loop that has intersected the surface is shown. (c) and (d) Repeated operation of the source results in a double pile-up of misfit dislocations along the two glide planes involved in the mechanism LeGoues *et al.* (1992).

The presence of large misfit pile-ups within a sample has further consequences to the quality of the resulting buffer layer. As mentioned previously in section 2.3.6 the presence of n closely spaced misfits sharing identical Burgers vectors result in the interaction stress for an orthogonally incepting dislocation being magnified n times

and can have the effect of arresting a mobile threading dislocation. Many mobile threading dislocations will become trapped at the same misfit pile-up resulting in *threading dislocation pile-up* (section 2.4.3). The work of Fitzgerald *et al.* (1999) indicates that the surface undulation resulting from misfit pile-ups is itself responsible for dislocation pinning by reducing the thickness of overlying material to less than the critical thickness required to drive dislocation motion. Once pinned the strain field at the sample surface due to threading dislocations causes adatom incorporation to be reduced locally, further exacerbating the cross hatch amplitude, resulting in positive feedback (Fitzgerald and Samavedam 1997).

The operation of MFR sources require that intersecting dislocations are pinned at a great enough distance apart so that sufficient stress is present to bow the dislocations. For this reason the rate at which a layer is graded in composition plays an important role, a lower grading rate ensures a larger separation between pinning events.

2.3.7.3 Self Annihilation of Threading Dislocations in MFR

MFR sources are formed when a mobile threading dislocation intercepts a pre-existing orthogonal misfit dislocation forming a corner dislocation. It is highly likely that other corner dislocations will be formed by intersection of the same pre-existing dislocations. The result of this is that newly formed dislocations (MFR) will be self-aligned by virtue that they originate along the same original dislocation network and may annihilate one another. The idea of self aligned sources as an explanation for the low threading dislocation densities, rather than extremely high glide velocities, found for samples having relaxed by MFR mechanism was first proposed by LeGoues (1994). It is noted that this mechanism will only occur in isolated areas bounded by

the extent of the original dislocations that were present to form the MFR sources. Pinning is to be expected at intersection of regions originating from different misfit dislocations.

2.4 Virtual Substrate Structures

There have been many approaches explored in the production of high quality virtual substrates involving compositional variation, temperature variation and even the intentional introduction of defects (Kasper and Lyutovich 2004). The following is a brief summary of the evolution of virtual substrate design (from the early 1980's) leading to the idea of *terrace grading* that forms the main focus of this work.

2.4.1 Constant Composition

The most basic form of virtual substrate consists of a layer with uniform composition that greatly exceeds the critical thickness value for relaxation. Such structures undergo sudden relaxation with a network of misfit dislocations forming at the epilayer growth interface. The sudden onset of strain relief leads to large numbers of dislocations being formed and as the misfit dislocation network is confined to a single plane a significant number of interactions occur. Numerous dislocations become pinned and are unable to further contribute to the relaxation process, resulting in the need to introduce even greater numbers of dislocations. As a consequence virtual substrates of this variety contain extremely high numbers of surface threading dislocations, even a $Si_{0.7}Ge_{0.3}$ layer results in a threading dislocation density in the range $10^{10} – 10^{11}$ cm^{-2} (Larsen 2000).

2.4.2 Step Grading

A much improved virtual substrate can be formed using a series of compositionally stepped layers. Such a structure requires fewer dislocations to relax each layer, and with fewer dislocations at each interface less interaction occurs, less pinning events result in threading dislocation densities being reduced. Subsequent layers also inherit existing dislocations that allows more gradual strain relief, forming longer misfits, again reducing the surface threading dislocation density. It has been shown that reductions in dislocation numbers are obtainable in this way with dislocation densities $<10^7/cm^2$ for a $Si_{0.7}Ge_{0.3}$ virtual substrate (Mooney 1996) although this still remains high compared to that achievable through linear grading.

2.4.3 Linear Grading

The successive integration toward smaller more numerous steps in the extreme limit results in a layer of continual compositional grading, having in effect an infinite number of stepped interfaces. The misfit dislocation network is no longer confined to either a single or small number of layers but can instead form anywhere throughout the layer. Such a layer allows strain to build slowly with dislocations introduced a few at a time, promoting the expansion of existing dislocations with a reduced likelihood of interaction. Once initial misfit dislocations have formed either homogeneously or heterogeneously the gradual application of strain is conducive to further nucleation by means of dislocation multiplication (MFR) as a consequence of the low nucleation energy barrier.

Fitzgerald *et al.* (1992) and Dutartre *et al.* (1994) have demonstrated that the surface threading density is linked to the compositional grading rate and that a grading

rate of 10%/μm provides a good compromise between layer thickness and surface threading density, see Figure 2.14.

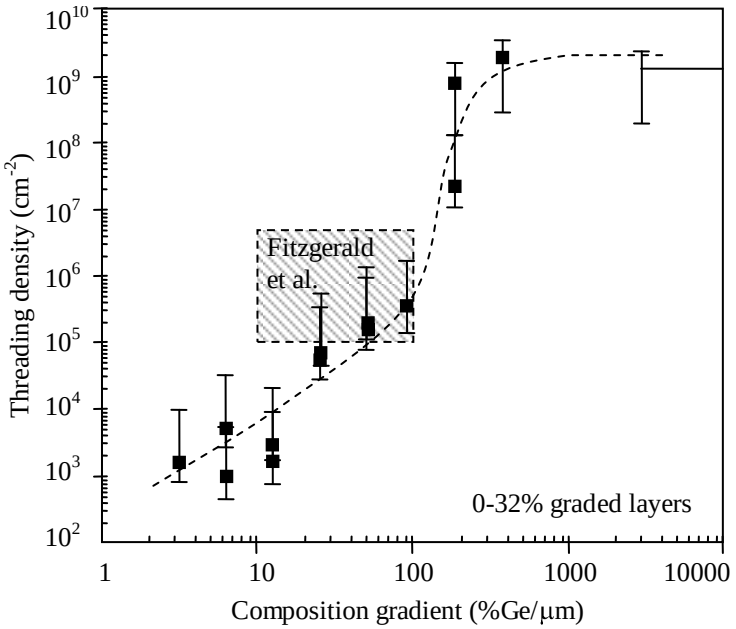

Figure 2.14 – A graph showing threading dislocation density vs. grading rate for graded buffers. The cap layers are 1.1 μm thick and 32% Ge rich. The straight line corresponds to a 1.1 μm thick uniform (32%) layer. For comparison the results of Fitzgerald *et al.* (1992) are also shown contained within the broken rectangle. Reproduced from a paper by Dutartre *et al*. (1994).

Numerous authors have shown how linear compositional grading can allow the reduction of threading dislocation densities, for example $Si_{0.7}Ge_{0.3}$ layers have been fabricated with densities between 10^3 – $8x10^5/cm^2$ (Dutartre *et al.* 1994; Hartmann *et al.* 2004) and even 100% germanium structures with densities as low as $10^6/cm^2$ (LeGoues *et al.* 1992; Currie *et al.* 1998) although additional processing steps were required to achieve some of these densities.

The operation of the MFR mechanism as discussed earlier results in the formation of regular surface undulations (cross-hatch) and is the key limitation of this approach with such surfaces not well suited to device fabrication or lithographic definition of structures. In addition the dislocations formed in this manner all share

the same Burgers vector lying on the same glide plane and can result in the *pile-up* of many mobile threading dislocations that are unable to contribute to further relaxation.

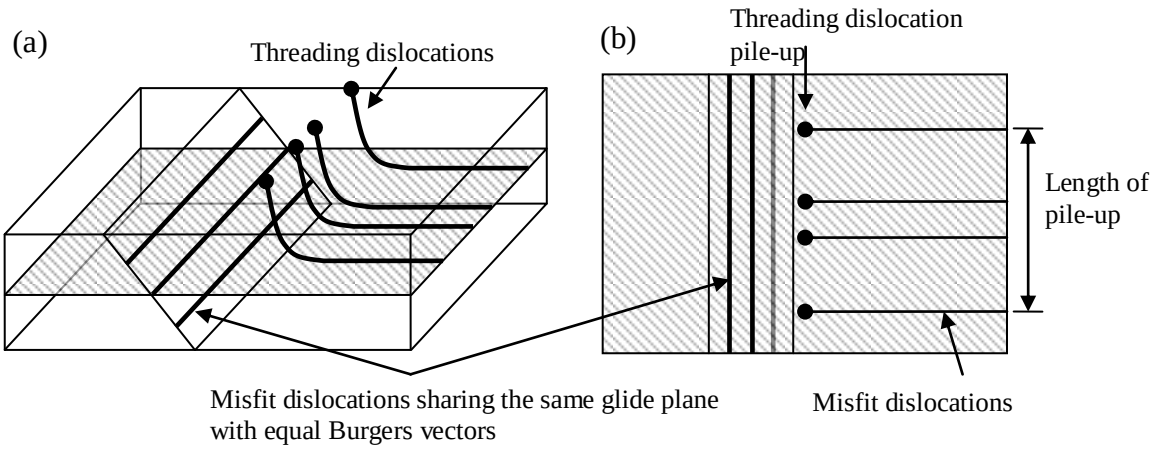

Figure 2.15 – Schematic diagram showing the pinning of threading dislocations against a network of misfit dislocations generated by the modified Frank-Read multiplication mechanism. (a) in 3-D view (b) plan view looking along the [001] direction.

Dislocation pile-up is believed to be of far greater detriment to the performance of a processed device than individual isolated threading dislocations. Individual dislocations are detrimental to device performance giving rise to an increased leakage current for devices containing threading dislocations (Giovane *et al.* 2001) but at low threading dislocation levels < $10^4/cm^2$ are at an acceptable level for operation of majority carrier devices (Tezuka *et al.* 2002). However when large numbers of surface threading dislocations lie in close proximity in the form of pile-up, the current leakage could logically be imagined to increase by a factor of *n* (where n is the number of dislocations) and may result in complete device failure rendering an integrated circuit inoperable (*device killer*).

The density of dislocation pile-up is often quoted as a length density (cm/cm^2) and as a more conventional area density ($dislocations/cm^2$) for lower levels, though whether such instances should be referred to as pile-up is debatable.

2.4.4 Terrace Grading

The concept of terrace grading is a recent development in virtual substrate design (Capewell 2002; Capewell *et al.* 2002), in principle retaining the advantages of grading (dislocation separation) whilst offering reduced surface cross-hatch, fewer threading dislocations, the possibility of thinner structures and the elimination of pile-up. Terrace graded virtual substrates combine graded compositional layers with uniform compositional stages. The introduction of the uniform composition regions allows for the separation of multiplication dislocation sources between graded regions, such that the formation of new multiplication sources is unlikely to occur in registry with those present in preceding graded layers as each layer will form a new network. As a consequence of the limited amount of misfit dislocation pile-up that can occur at any one source, the amplitude of the resulting surface cross-hatch is limited, Figure 2.16.

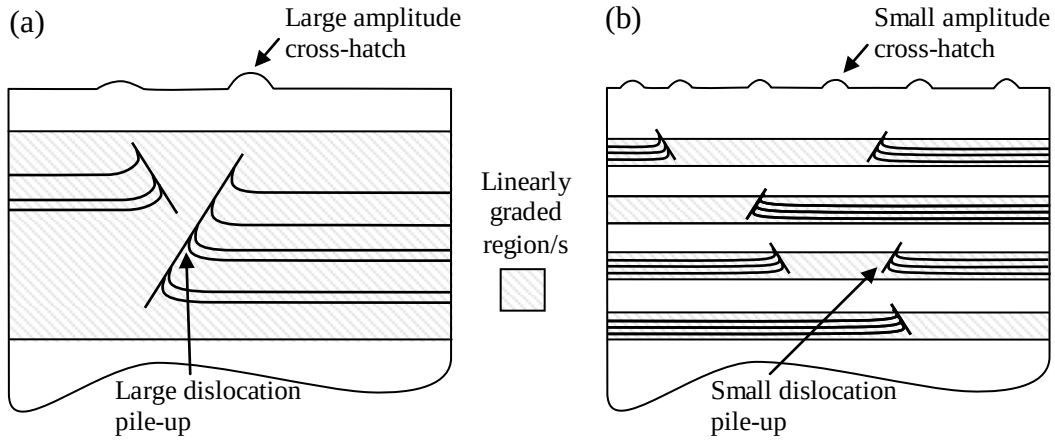

Figure 2.16 – Schematic cross-sectional diagram viewed along a [110] direction. In a linearly graded layer (a) the dislocations form large pile-ups that traverse the layer. In the terrace graded layers (b) pile-ups are confined in the graded layers and since these layers are isolated pile-ups do not build throughout the structure. Reproduced with permission (Capewell 2002).

An additional benefit of the uniform regions arise from the release of pinned threading dislocations, caught at the web like dislocation networks extending out from multiplication sources. In extreme cases many dislocations can become trapped along a single plane leading to threading dislocation pile-up.

The presence of an increased number of mobile threading dislocations at the start of a graded layer leads to a reduction in the required nucleation rate of multiplication sources in that region. A terrace graded virtual substrate will therefore benefit from the more efficient utilisation of existing misfit dislocations in relaxation, containing fewer but longer misfit dislocations, as well as displaying a reduction of surface cross-hatch and reduced threading dislocation pile-up. A threading dislocation density of $1x10^6/cm^2$ has been demonstrated with this technique at a germanium composition of 50% in a thickness of only 2 μm, with far greater improvement expected for layers of more conventional thickness (Capewell *et al.* 2002).

Chapter 3

3 Experimental Methods

This chapter describes the equipment used to grow and characterise the silicon-germanium virtual substrate structures investigated within this thesis. The basic operating principles of each technique are discussed and where appropriate any modifications made during the course of this work are presented.

3.1 Solid Source Molecular Beam Epitaxy (SS-MBE)

The majority of the samples investigated during the course of this thesis have been grown by the author using solid-source molecular beam epitaxy (SS-MBE) within a Vacuum Generators V90S growth system. Unlike many forms of chemical vapour deposition (CVD) and similar competing technologies, SS-MBE enables independent alteration of certain growth parameters without any interdependence. Most importantly this allows modification of growth temperature independently of the epitaxial growth rate and layer composition is determined directly by the ratio of incident silicon to germanium flux. Both of these advantages have been used to best effect in the creation of silicon-germanium virtual substrates with simultaneous variation of both composition and temperature.

3.1.1 V90S Growth System and Vacuum Pumping

The Vacuum Generators V90S growth system provides deposition of silicon, germanium and silicon-germanium alloys along with boron and antimony dopants within an ultra high vacuum (UHV) environment, essential for high quality epitaxial layer growth. UHV describes pressures below ~10^{-9} mbar and are necessary to

maintain a low level of impurity influx (Farrow 1995). The growth system consists of three main chambers conventionally referred to as the *fast entry lock* (FEL), *preparation chamber* (PREP) and *growth chamber* (GROWTH) each maintained at a successively higher vacuum, shown schematically in Figure 3.1.

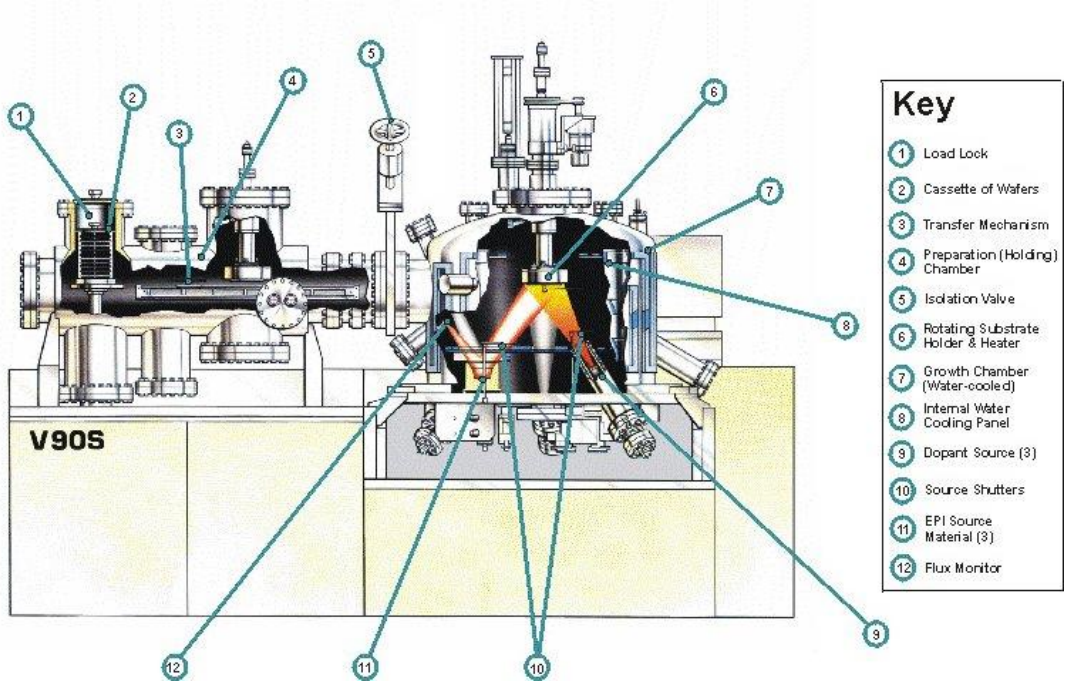

Figure 3.1 – Schematic of the Vacuum Generators V90S SS-MBE growth system. Reproduced with kind permission (Grasby 2000).

The sequence of chambers is necessary to maintain UHV conditions within the GROWTH chamber by minimising exposure to atmospheric water vapour. *Wafers*, thin crystalline discs of silicon (~1 mm thick, 4 inch diameter), are admitted into the vacuum system through the FEL which is vented and evacuated regularly to *dry nitrogen* to permit the loading and retrieval of wafers. The vacuum is maintained independently within each chamber through a combination of vacuum pumps. Pumping in FEL and GROWTH is provided by a Pfeiffer *turbo molecular pump*, backed by an oil free Leybold Ecodry *rotary* to achieve an ultimate vacuum of

$\sim 10^{-8}$ mbar and 10^{-11} mbar respectively. The oil free nature of all the pumps used is critical throughout but especially within GROWTH and precludes the possibility of *oil back-streaming* into the chamber introducing contamination (Grasby 2000).

A turbo molecular pump consists of a series of high velocity spinning blades (rotors) separated by stationary blades (stators) with pumping achieved by a net momentum transfer from the rotor to an incident molecule directing it through the pump (Roth 1996). Correct operation requires the particles mean free path to be large enough that is more likely to interact with the vessel containing it than another molecule and is known as *molecular flow*, occurring for pressures $\leq 1 \times 10^{-10}$mbar. For this reason it necessary to back (pump upon) a turbo molecular pump with a secondary pump to maintain a low back pressure for continued operation.

Around an hour of pumping is necessary from atmospheric pressure to achieve an acceptable vacuum in FEL, allowing wafer admission into PREP, after which loading from PREP to GROWTH occurs automatically in quick succession. During normal operation PREP is only ever open to one chamber at the same time. The chamber is pumped by a Varian Star Cell ion getter pump operating at 2 kV and does not require secondary pumping; though a starting pressure less than $\sim 10^{-3}$ mbar is needed for initial operation.

During the course of this work the number of wafers that could be simultaneously admitted into the vacuum system was limited to less than the maximum 6 which the loading carriage is designed to handle. Wafers held near the top of the carriage were shaken out of position by the sudden motion in opening FEL to PREP; following this work the problem has been rectified by softening the viton seal between FEL and PREP with *in-situ* heating.

3.1.2 Chamber Outgassing

The necessity to achieve and maintain a UHV environment for epitaxial growth requires not only a specialised pumping system but also the *baking* or *outgassing* of the entire vacuum system each time either GROWTH or PREP is vented to atmosphere. The large volume of gas initially contained within the vacuum system can be quickly pumped away achieving a vacuum around ~10^{-7} mbar. Further reductions in pressure continue with an approximate t^{-1} (where t is time) dependence due to the slow release of physisorbed gases from chamber walls, with H_2O becoming the dominant gas load at lower pressures. Baking at high temperatures greatly accelerates this process with physisorbed gases, only weakly held onto surfaces by weak van der Waals forces, quickly removed by heating above 120ºC and chemisorbed layers, chemically bonded to the chamber surface, removed by surface heating in excess of 200ºC (Farrow 1995). It is standard procedure after each *growth series* to bake the system for around seven days at approximately 200ºC to achieve UHV conditions.

3.1.3 Substrate Heater and Control

Substrate temperature is a critical growth parameter for SS-MBE, as for all epitaxial growth processes and is of importance to the work presented in this thesis. The V90S is equipped with a resistively heated graphite meander located a couple of millimetres behind the rear of the substrate and is capable of achieving sustained temperatures in the range ~20-1000ºC. Substrate temperature was calibrated using both high and low temperature optical pyrometers situated outside of the vacuum system and a calibration curve created from these measurements was stored in the EpiCAD control software. The EpiCAD (v2005.125) control software is provided by

EpiMax Computer Aided Design © 2003 and when utilising full growth automation, is responsible for control of all matrix and effusion sources as well as heater temperature, wafer rotation and shutter actions. No real-time feedback was utilised for heater control, although the substrate temperature was continuously monitored by a high temperature pyrometer over the range 600-1000ºC. Dependent upon a substrate's bulk resistivity a small surface temperature difference can occur for a given power setting (Lambert 2000), though this effect can be neglected in the current work. Improved uniformity in both heating and flux distribution was achieved by rotating the substrate at a constant velocity of approximately 5 rpm and has been shown to yield a uniformity of ± 3-5% across a 4 inch substrate (Grasby 2000).

3.1.4 Electron Beam Evaporators

Evaporation by radiative heating of silicon is not practical for matrix level epitaxial layer growth because of its high melting point (~1400º C) and chamber dimension. It is far simpler to evaporate silicon and germanium sources by direct electron bombardment using an electron beam evaporator. The V90S utilises three AP&T electron evaporators, two silicon and one germanium, to provide matrix level growth at a rate of between 0.01 As^{-1} and 1 As^{-1} (from each evaporator). Improved flux uniformity is provided by the off-centre situation of each electron evaporator.

The main body of the electron evaporator consists of an oxygen-free high-purity copper hearth (see Figure 3.2) that has a number of channels machined through to permit water cooling. A tungsten filament is held at a DC potential of -9 kV relative to the grounded hearth, and the filament heated by a superimposed AC current to provide electron emission. The emitted electron beam is deflected by a permanent magnet through 270° along an arced path so that it is normally incident upon the

charge, shielding the substrate and charge from the filament (reducing the likelihood of contamination). Fine adjustments of the beam position on the charge are possible using electromagnets situated near the filament and in the body of the evaporator. The AP&T position coils are additionally designed to allow defocusing of the electron beam, achieved by increasing the field in both lateral electromagnets equally.

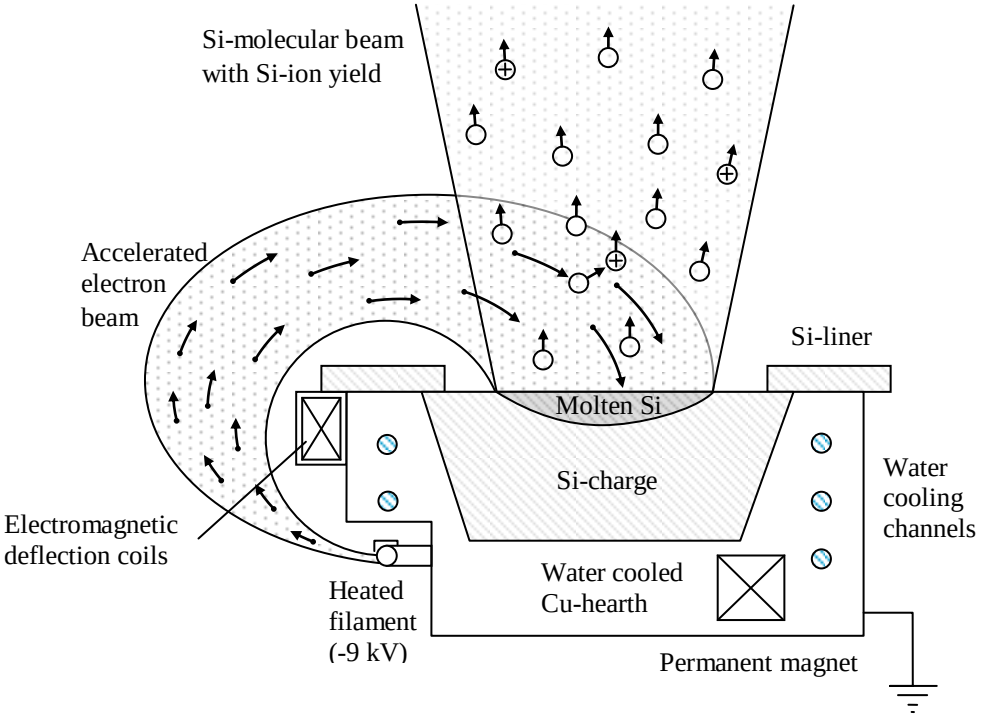

Figure 3.2 – Schematic of electron beam evaporator situated within the V90S growth chamber. Adapted from an image published by Kasper *et al.* (1998).

A defocused beam is used to form a surface melt of around 5 cm diameter with a shallow depth, as this has been found to result in a lower ion yield believed to provide higher quality growth (Eifler *et al.* 2002). To further prolong the life of each charge a *melt-back* is periodically conducted, where the energy input is increased over that in normal operation and the beam carefully moved to melt-back a significant

proportion of the charges surface, eliminating any crater that had been formed, returning a flat surface.

Flux control of the electron evaporators is maintained by an adapted INFICON Sentinel III EIES (electron induced emission spectroscopy) close loop feedback system that eliminates any long term drift in the flux. The Sentinel system only provides a relative correction with the absolute growth rate determined through separate calibration and stored as a *lookup curve* within the control software. Each evaporator has a Sentinel flux monitoring head, placed at an angle protruding out from the chamber side wall, positioned so as to not intercept flux emitted from the other two evaporators; this is discussed in greater detail in section 3.2.1.

Rapid interruption to the flux is achieved using shutter blades that physically shadow the substrate from the source of flux. This highlights the fundamentally important operational principle of solid-source MBE, *direct line of sight*, without which growth on the wafer surface does not occur. This simplistic approach of source shuttering means that rapid flux interruption is available (< 1 second) and largely determines the growth rate chosen to retain accurate control. As previously stated, growth is typically conducted at a rate in the region of 1 $Å s^{-1}$ providing in principle lateral thickness control in the order of Angstroms.

The extended length of time required here to grow higher percentage virtual substrates meant that the longevity of the electron evaporator power supplies became an important issue. During growth excess material can begin to flake from the chamber walls and may be electrostatically attracted to the electron evaporator filaments, sometimes forming a short circuit to ground. Such events are often resolved immediately with the material vaporised by the arcing current but can

occasionally cause a drop in evaporator potential sufficient to trip safely interlocks on the power supply.

For further information regarding silicon-germanium SS-MBE the reader is referred to *Molecular Beam Epitaxy – Applications to Key Materials (Chapter 1)* (Farrow 1995).

3.1.5 Substrate Cleaning *In-Situ* and *Ex-Situ*

Numerous approaches to substrate preparation were available during this work, the route chosen dependent upon the application of the substrate. Chemical cleaning methods are typically utilised only for cases of fully strained structures or layer re-growth on relaxed buffers and such procedures are presented in Appendix I. Chemical cleaning was not available during the course of this work and so high temperature *in-situ* cleaning had to be adopted.

3.1.6 *In-Situ* High Temperature Oxide Desorption

The native oxide present on the surface of silicon substrates was desorbed under UHV conditions (Kasper *et al.* 1998) at the beginning of each growth sequence, ramping the wafer temperature up to 890ºC over a period of 15 minutes and holding it there for a further 20 minutes. It was found that ramping over a period less than 15 minutes resulted in the occurrence of slip lines at the wafer edge due to temperature non-uniformity across the wafer surface. A 50 nm silicon buffer layer was grown immediately following this procedure whilst the temperature was simultaneously reduced to that required at the start of the virtual substrate growth sequence.

3.2 System Developments

During the course of this work the V90S was retrofitted with an automated wafer transfer system utilising laser pickups to determine the position of the wafer platen. Once a wafer cassette has been loaded and FEL has attained a high vacuum, further wafer manipulation is carried out automatically, transferring between FEL and GROWTH and visa-versa. Ultimately the EpiCAD growth control software will be integrated with the automated wafer transfer software enabling unattended operation for extended periods of time, though this was not in place during the current work.

3.2.1 Electron Induced Emission Spectroscopy (EIES)

The INFICON Sentinel III flux monitoring system (EIES) utilised on the V90S SS-MBE growth system monitors the requested flux rate from the electron beam evaporators, providing a signal that is used in a control loop to compensate for changes in the flux with time. The basic principle of operation involves the excitation of incident evaporant species, within a sensor head situated in the vacuum system, by direct electron bombardment from a heated tungsten filament. Subsequent light emission is channelled along a light pipe through a thin film filter into a photomultiplier tube (PMT) located outside of the vacuum system. The signal is used for feedback control to maintain the evaporant flux at the desired level. Two distances play critical roles in determining signal strength, the source-to-sensor head and the sensor-head-to-photomultiplier tube distance. The flux density of atomic species arriving at the sensor head falls off as $1/d^2$ (d is distance) as does the light intensity transmitted along the light pipe.

The initial arrangement had the sensor head placed at an inclined angle to the source at a distance of 240 mm with a sensor head PMT separation of 360 mm

(Kubiak *et al.* 1991), shown schematically in Figure 3.3. As a consequence of this geometric arrangement part of the molten area of a depleted charge may lose line of sight to the sensor aperture and not be detected. Ideally the sensor should be situated above the molten charge with a relationship similar to that of the wafer. To achieve this, a unique sensor head assembly was constructed in which the light pipe length was substantially reduced to a distance of only 80 mm to allow its situation at the top of the growth chamber. An opening made though the top internal water cooling panel allowed line of sight down onto the charge with a sensor to charge distance of 650 mm, shown schematically in Figure 3.3. This provided an overall source-to-PMT distance for the old and new sensor head positions of 600 mm and 730 mm respectively.

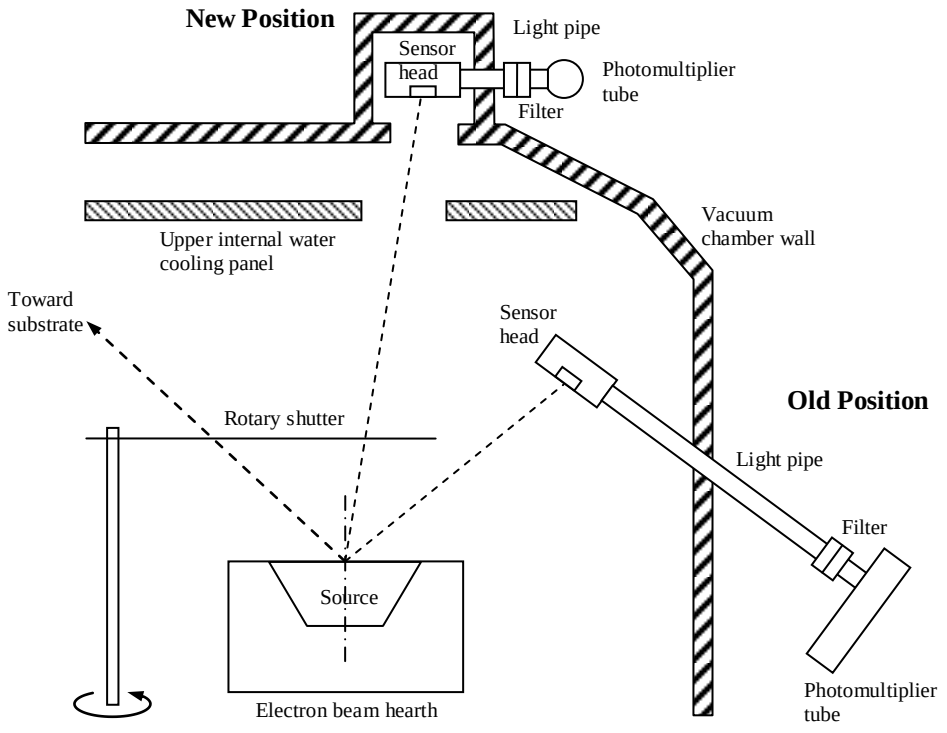

Figure 3.3 – Schematic representation (not to scale) of a silicon electron evaporator and shutter situated inside the V90S UHV growth system with two sets of Sentinel heads, positioned at the side and top of the chamber. Also shown is the modified internal upper water cooling panel allowing line of sight down to the evaporant source.

To assess the performance of the new head assembly measurements were made simultaneously with both the original and new heads. The electron evaporator power level was incrementally increased under computer control, using first the original sensor head for feedback control, followed by the new sensor head, the resulting traces are given in Figure 3.4. The PMT range (7) was set equal for both channels but different correction factors were applied to each trace so that the flux rate indicated between them was in close agreement at medium flux rates.

It is immediately obvious from Figure 3.4 that the signal to noise ratio of the new upper sensor head position is greater than sensor head in the original side position. This situation was expected given the greater overall path from source to PMT of the new upper sensor position. The increased noise level can be seen to have only a small effect on the stability of the power control graph due to the purposely damped response of the feedback system.

To allow usage of the upper sensor heads during a growth sequence will require further work, modification of the shutter blades is needed to allow continuous flux monitoring whilst retaining the ability to shutter a wafer from matrix species (see Figure 3.3). In addition only silicon charges have so far been monitored in this new configuration and it remains to be seen whether the germanium melt can be controlled in the same manner given a noticeably higher initial noise level. If this system were implemented it would have the further advantage of freeing three side ports that could be used to accommodate more effusion sources.

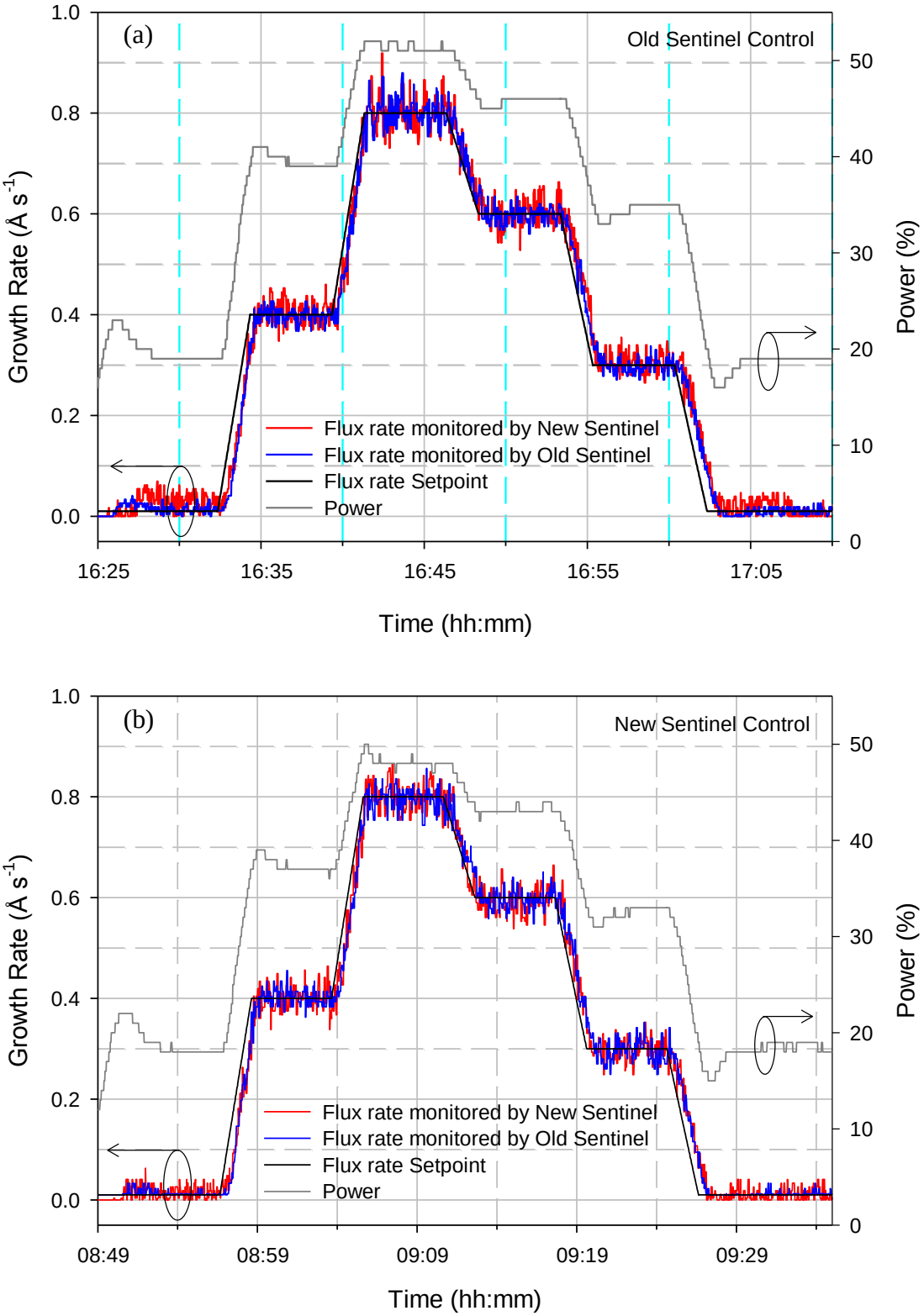

Figure 3.4 – Montage of graphs showing flux rate monitored from the silicon charge by Sentinel heads in the upper (new) and side (old) locations, as well as the actual set point and power usage. (a) Flux feedback control provided from the old Sentinel head position (b) Flux feedback control provided from the new Sentinel head position.

3.3 Nomarski Optical Interference Microscopy

Optical observation of an epitaxially grown structure provides a direct means with which to quickly examine surface morphology. A standard optical microscope does not possess the ability to resolve the small features present on a typical epitaxial layer, as stipulated by the Raleigh criterion. Far smaller features can however be visualised by utilising optical interference contrast available in a Nomarski interference microscope. A Reichart-Jung Nomarski inference microscope equipped with a Nikon DN100 digital camera was used to obtain interference contrast images of epitaxial wafer surfaces. Interchangeable lenses allowed an image to be formed at a magnification of x10, x50 or x100 which was effectively increased in the digital image due to the size of the cameras CCD (charge coupled device) and by x10 at the eye piece.

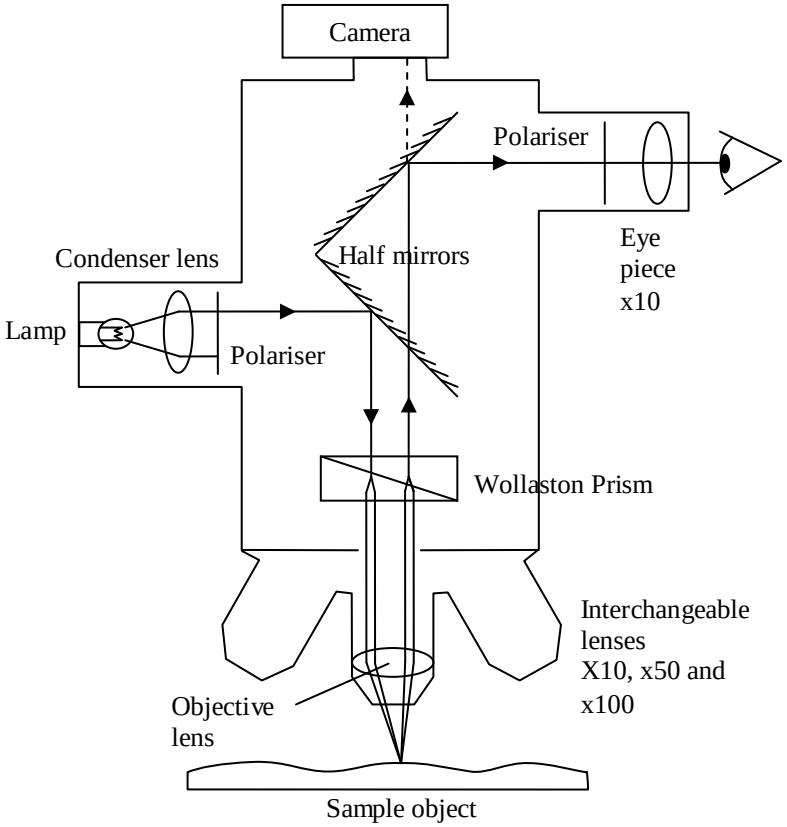

Figure 3.5 – Schematic representation of a Nomarski optical interference microscope.

In a Nomarski microscope the light source illuminating the object of interest is plane polarised before being split into two orthogonally polarised beams. A phase shift between the beams will arise due to any slopes on the objects surface. The beams are then reflect back from the objects surface through an objective lens and are subsequently recombined by the prism with which they had originally been split (Wollaston Prism). Finally the light is reflected either toward an eye piece or camera through a second polariser that is crossed with respect to the first, recombining the two beams and giving rise to interference contrast. Sensitivity to height change allows this technique to image tiny features, in the order of nanometres but provides no quantitative height information. It is difficult to ascertain whether surface features protrude out from or into the surface of a substrate or to have much sense of depth and are the greatest shortcomings of this technique. For further information the reader is directed to *Optics 3rd Edition* (Hecht 1997).

3.4 Defect Etching

The presence of threading dislocations at the surface of a relaxed virtual substrate structure is undesirable due to the detrimental effect upon electronic devices (Giovane *et al*. 2001) and structures subsequently processed. It is important therefore that the density and arrangement of any surface threading dislocations can be determined. Schimmel etchants were employed in this study to reveal the presence of surface threading dislocations (Schimmel 1979; Archer 1982; Werner *et al.* 2004).

The standard Schimmel etch utilised in the majority of this work comprised of a mixture of CrO_3 (0.75M) : HF (50%) : H_2O in the ratio 2 : 4 : 3. This etchant removes surface silicon (or silicon-germanium) material through a continual process of oxidation (with CrO_3) and oxide removal (with HF), diluted with H_2O allowing

material removal at a controlled rate (Kulkarni 2003). The etch rate is known to be highly sensitive to doping concentration and type (Archer 1982), surface strain, as well as having a strong dependency upon germanium concentration (Werner *et al.* 2004). The local strain associated with the emergence of a threading dislocation at the surface causes the local etch rate to be enhanced forming a visible etch pit and forms the basis of this technique. It should be noted that temperature can also have a significant effect, and in extreme cases hillocks can from rather than pits over a 10º temperature range (Föll 2005). A modified Schimmel etch comprising CrO_3 (0.4M) : HF (50%) in the ratio 55 Vol% : 45 Vol% was used to allow defect revealing in samples where the uniform top layer was < 1 μm for which this modified etchant was specifically developed.

It should be made clear that this technique, though routinely utilised throughout the industry, should be treated with caution as not all of the conditions affecting the formation of etch pits are well understood. Though the absence of countable etch pits may well indicate an extremely low defect density (here $< 1x10^3/cm^2$) the possibility that threading dislocations have not been revealed should also be considered.

Etch pit counting was accomplished using an optical microscope equipped with Nomarski interference and digital images taken with a Nikon DN100 CCD camera. The free image processing and analysis software *Image Tool v3.00* developed by the University of Texas Health Science Centre was used to count large numbers of etch pits where manual hand counting was impractical. By selecting a narrow grey scale band containing the etch pits, an algorithm is able to identify *objects* marking them on screen. Computerised etch pit identification was only possible for normal optical images where etch pits appear as dark diagonal dots.

These objects are then classified in terms of their pixel area to eliminate noise and large particulate contaminants, with selected area ranges tabulated and displayed as a colour coded map for clarity. Any objects missed or misidentified can then by manually taken into account and the process repeated on further images.

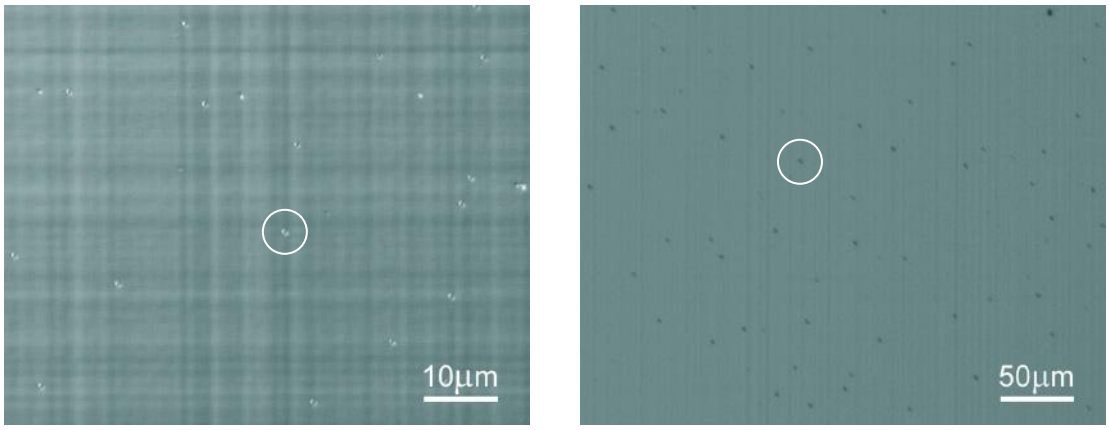

Figure 3.6 – Example images of etch pit formation after Schimmel etching around surface threading dislocations (a) at x50 magnification with interference contrast (b) at x10 magnification without interference contrast. A threading dislocation is highlighted in each image by a white circle.

3.5 Transmission Electron Microscopy (TEM)

A transmission electron microscope operates in a way analogous to an optical microscope expect that an image, rather than being formed using electromagnetic radiation at an optical wavelength (600-900 nm) and focused with traditional lenses, is formed using highly accelerated electrons with far a shorter wavelength (~0.003 nm) and manipulated using electromagnetic lenses. This characterisation technique allows the study of crystalline materials (amongst others) to determine such parameters as layer thickness, strain variation and the presence of defects and dislocations, all of which are important in obtaining an understanding of an epitaxially grown semiconductor layer. The micrographs presented in this thesis were obtained by the author using a JEOL JEM-2000FX TEM. Specimen preparation is of great

importance to this technique as transmission of electrons through a specimen necessarily requires electron transparency, in relation to this material system this equates to a thickness of ~500 nm.

3.5.1 Sample Preparation

Preparation of an epitaxially grown structure for analysis in a transmission electron microscope requires sample thinning in a selected orientation. In general, a cross-sectional analysis of a layer structure provides the most useful information and requires numerous stages of preparation to meet the strict requirement of electron transparency. These stages are shown schematically in Figure 3.7.

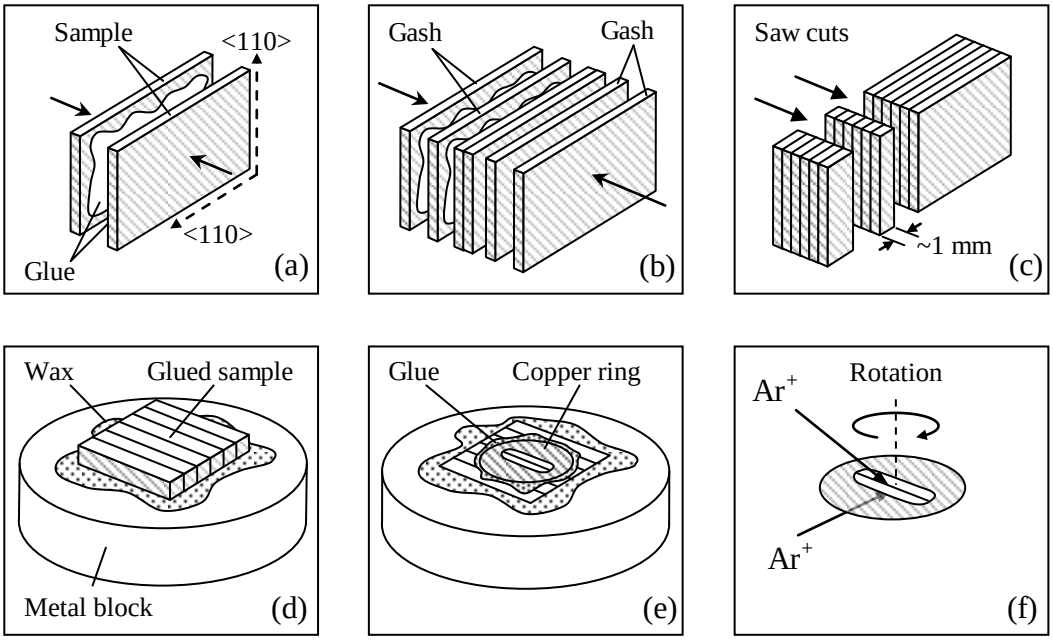

Figure 3.7 – A series of schematics showing important stages in TEM sample preparation. (a) initial bonding of epitaxial surfaces together (b) bonding of additional gash material (c) diamond sawn section for grinding (d) sample section waxed ready to grind (e) ground and polished sample with copper support ring attached (f) final sample structure ready to be ion beamed until electron transparent.

Small sections of the sample (approximately 10 mm x 5 mm) are prepared by *cleaving* along [110]. Two such pieces are glued face together with M-bond 610 adhesive, with further sacrificial pieces added either side building out the cross-sectional diameter so than it can be easily handled, Figure 3.7 (a, b). Curing of the adhesive is accelerated by heating in an oven at 180ºC for 2 hours and to reduce the amount of material that must be ground away, a small segment of this layer sandwich is prepared using a Southbay Technology diamond saw, Figure 3.7 (c).

An ultimate sample thickness of less than 10 μm is required through the process of mechanical polishing. Silicon carbide grinding paper (from P120 grit to P1200 grit) is used on a Buehler Metaserv Motopol 12 (at 150 rpm) grinding wheel to achieve an overall sample thickness of approximately 400 μm and the surface polished using 6 μm and 1 μm diamond suspension and cloth pads to remove surface scratches that could weaken the thinned sample or lead to uneven thinning during ion beaming. Further thinning and polishing down to less than 10 μm is conducted on the opposite side of the sample, exposed by turning over and re-fixing. The preparation of a sample in this manner is extremely time consuming and difficult, with a high rate of sample loss at this stage.

To enable handling of the thinned section a copper supporting ring from Agar Scientific (G2500C slit) is glued to the sample surface using Araldite Rapid; the slot (1 mm x 2 mm) is directed along the central glue line revealing the region of interest, Figure 3.7 (e). After 24 hours of curing the sample protruding past the copper ring perimeter is carefully removed with a scalpel blade and the sample released from its support and cleaned of residual wax in isopropanol [$(CH_3)_2CHOH$].

An electron transparent sample is produced by ion milling in a Gatan 691 Precision Ion Polisher (PIPS) using an ionised beam of argon atoms accelerated at

4.5 kV to erode the sample surface whilst it is being continually rotated. An incident gun angle setting of 3 units from below and 5 units from above has been found to provide optimum thinning, with beaming stopped once the thin film has perforated at its centre, Figure 3.7 (f).

For further detailed information on specimen preparation techniques the reader is referred to *Specimen Preparation in Materials Science* (Goodhew 1972)**.**

3.5.2 Transmission Electron Microscope Construction

The JEOL JEM-2000FX TEM consists of an evacuated column containing from top to bottom, an electron source, a condenser aperture, two electromagnetic (EM) condenser lenses, a sample holder, EM objective lens, objective aperture, a series of EM projector lenses and a phosphor imaging screen with camera below, see Figure 3.8.

The electron beam emitted at the top of the column (200 kV) is collimated and passes through the first condenser lenses forming a well defined virtual electron source of variable size, whilst a second condenser lenses allows the illuminated beam area to be controlled. After passing through the sample the objective lens forms a magnified intermediate image, which in normal imaging mode is in the object plane of the first projector lens, being further magnified and projected on to the phosphor screen. Varying the strength of the objective lens provides adjustment of the image focus. A diffraction mode (discussed later) is also available where an image of the samples reciprocal lattice can be observed. This is achieved by adjusting the strength of the first projector lens so that its object plane coincides with the back focal plane of the objective lens. At the back focal plane all parallel rays cross at the same point producing a spot with a position related to the incident beam angle.

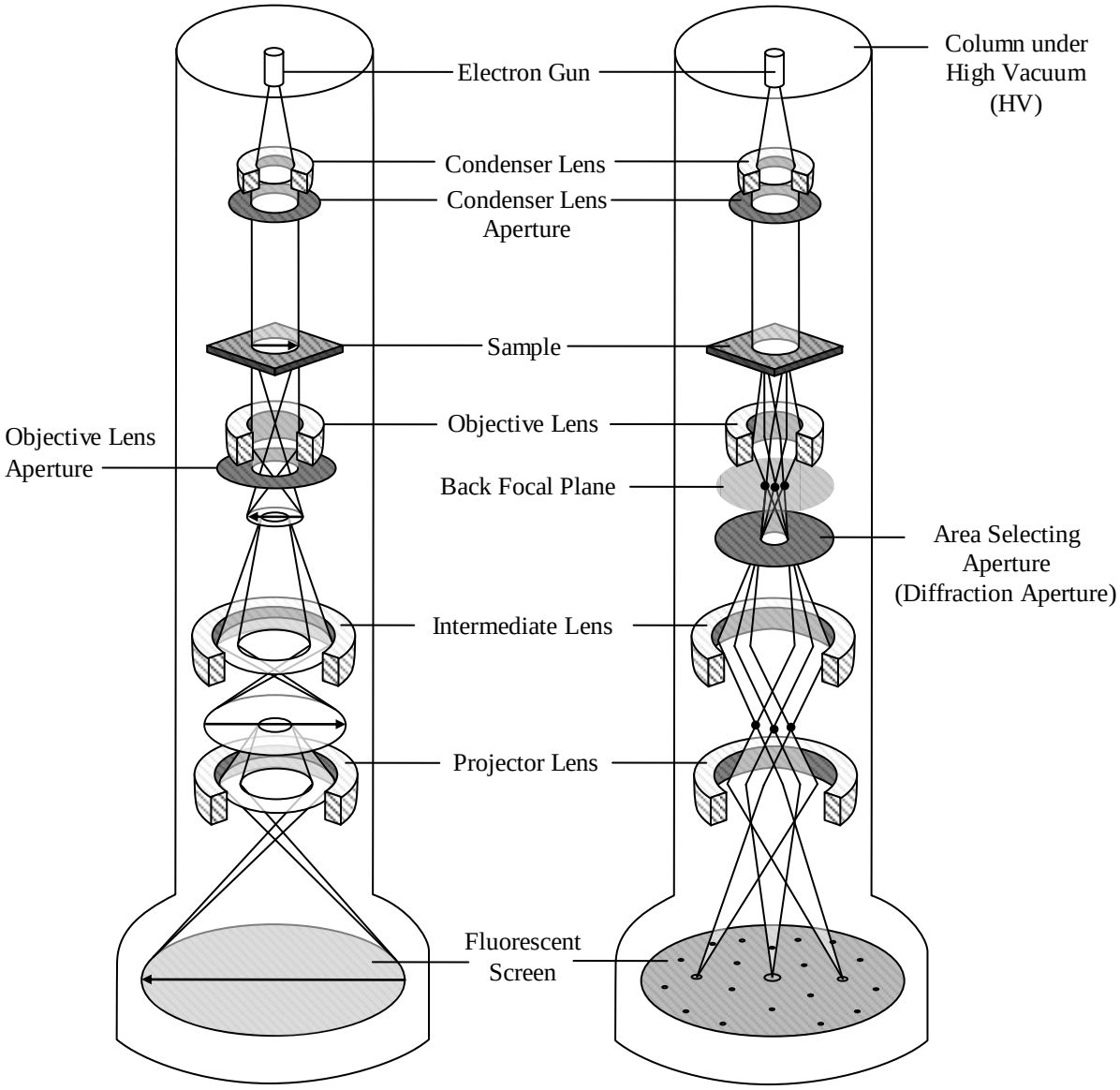

Figure 3.8 – Schematic of a Transmission Electron Microscope (TEM) in (a) bright field imaging mode (b) diffraction imaging mode.

3.5.3 Operation of the Transmission Electron Microscope

A thinned specimen is secured into a double tilt holder capable of sample reorientation in two independent directions and admitted into the electron microscope through a vacuum load lock. The electron beam current is raised to its operation level (119 μA) and the perforated hole in the specimen is located. Column lenses and apertures are setup in sequence, moving from top to bottom along the column. The

top condenser aperture is checked to ensure alignment along the central axis of the column by variation of the beams illuminated area from a condition of under to over focused, the beam remaining centralised when set correctly. Correction is also made to ensure the beam remains central when the spot size is varied. Any astigmatism (different focal planes in orthogonal directions) introduced by the condenser lenses should be corrected and the region of interest in the sample located and focused. With no condenser aperture engaged a focused image should contain virtually no contrast (assuming little compositional variation). It is extremely important that the specimen is held in the eucentric position, located along the central axis of the tilt holder. Positioning above or below the eucentric position will result in the region viewed changing upon tilting and can make it impossible to attain a sharp focus, see Figure 3.9. The eucentric sample position is found by rocking the sample back and forth through ~60º whilst altering its height; the sample remains almost still when set correctly.

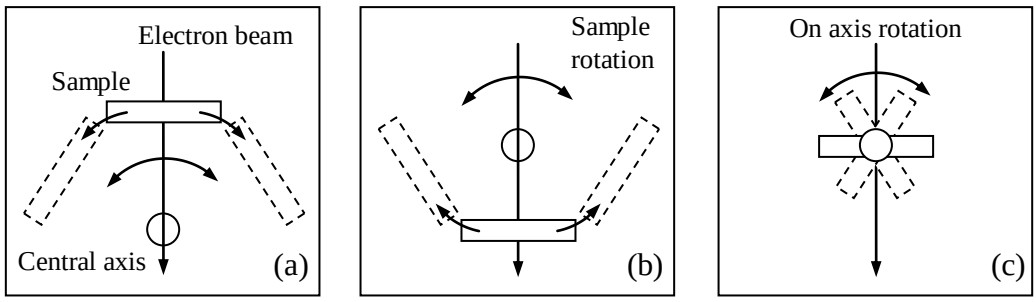

Figure 3.9 – Schematic diagrams showing (exaggerated) effect of sample tilt in various situations (a) sample above eucentric position (b) sample below eucentric position (c) sample at eucentric position.

The micrographs presented throughout this thesis utilise diffraction contrast, set in the diffraction mode by sample tilting, discussed in section 3.5.4.

Further refinements often necessary when working at higher magnifications (> x50,000) include correction for non-parallel illumination falling on the objective lens that can degrade image quality, corrected by using the *HT wobbler*. The potential on the electron gun anode is varied, periodically altering the electrons energy (velocity) hence their trajectories after passing through each of the lenses, when correctly compensated the image at the screen centre should not move. Finally astigmatism of the objective lens can be correct to obtain an extremely sharp focus and is best altered whilst viewing an irregular material such as the glue join between sample pieces where a mottled pattern becomes evident.

3.5.4 Two Beam Diffraction Condition

Image contrast in transmission electron microscopy can arise for a number of reasons including: atomic density and sample thickness variations; selective diffraction from sample bending; and variation in atomic plane spacing caused by strain or crystal imperfections. Selective use of diffraction provides the best contrast in TEM micrographs.

The phenomenon of electron diffraction arises from the elastic scattering of electrons (in this case considered to be waves) by atoms within a crystal lattice such that in particular directions coherent scattering occurs resulting in a strong reflection. Although such scattering occurs due to the interaction with individual atoms, Bragg (1913) gave a simple geometric analysis based on coherent reflections from planes of atoms that has become known as Bragg's Law.

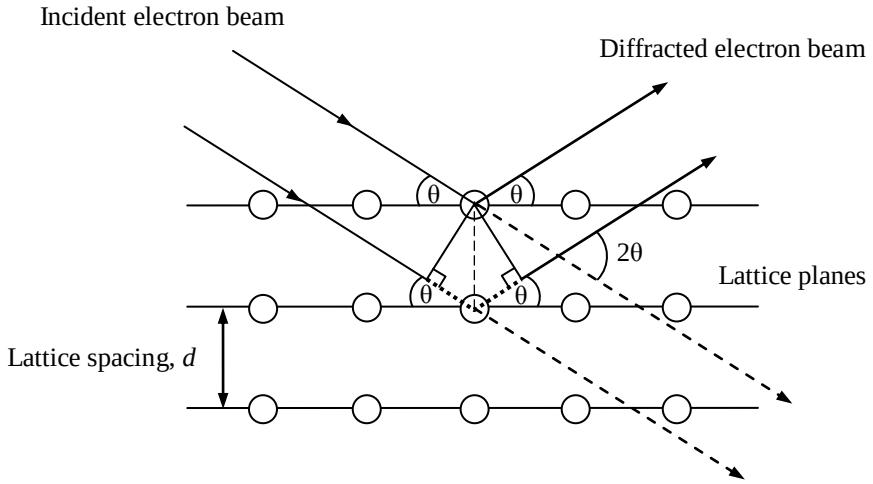

Figure 3.10 – Schematic diagram illustrating the geometric relationship between the incident electron radiation, atomic lattice planes and the diffracted beam.

$$n\lambda = 2d_{hkl}\sin\theta \tag{3.1}$$

where n is an integer, λ is wavelength, d_{hkl} is atomic plane spacing and θ is the angle between the lattice planes and the incident beam.

Within the electron microscope, diffraction contrast is achieved by selective removal of diffracted beams using the objective aperture. When an electron beam passes through a crystalline sample orientated along its *major pole axis* many planes give rise to diffracted beams resulting in a complex image, often with dim contrast. To achieve strong contrast the sample is tilted into the so called *two beam condition*.

In the diffraction imaging mode the sample tilt controls are used to orientate the sample such that diffraction occurs from a single set of planes, leaving only two visible reciprocal lattice points corresponding to the straight through and diffracted beams. A representation of the reciprocal lattice visible when imaging along the [110] direction is given in Figure 3.11, where the separation distance corresponds to the inverse of real plane separations and the direction relative to the centre position

corresponds to the direction of the surface normal of the planes in question, further detail in section 3.6.1.

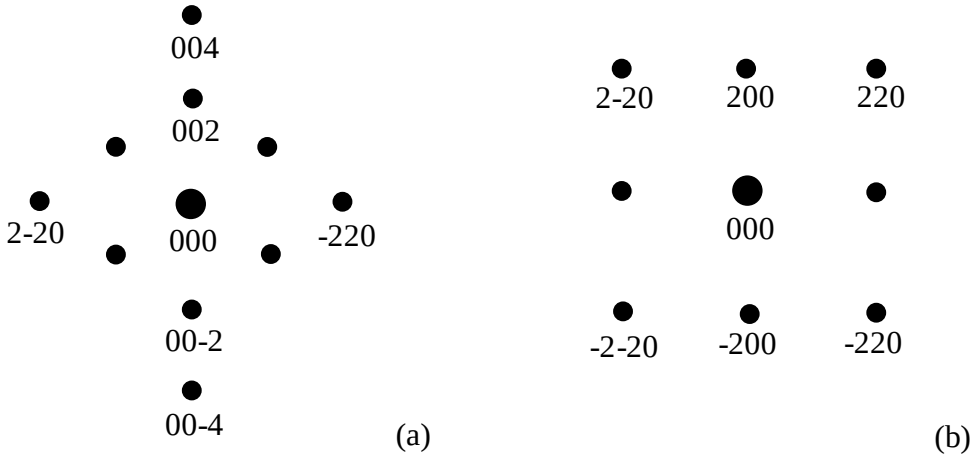

Figure 3.11 – Reciprocal lattice sections visible in the TEM diffraction mode when an fcc crystal is viewed along (a) [110] direction (cross-sectional) (b) [001] direction (plan view). Only selected lattice points are shown.

In practice the desired plane is selected by following and positioning of the lattice points along *Kikuchi lines* visible in thicker sample regions, providing a convenient reference frame for navigation and orientation when in the diffraction imaging mode.

Kikuchi lines are phenomena visible in the diffraction mode arising from inelastic scattering of electrons within the sample. Inelastically scattered electrons give rise to a general background intensity of the diffraction pattern; however a number of electrons from these secondary sources will be incident at the Bragg angle of specific planes and undergo diffraction. As most electrons are only scattered through small angles a net gain and associated net loss will occur in two directions as illustrated in Figure 3.12. The angular separation 2θ results in the intersection of the Kikuchi lines with the beam centre and corresponding reciprocal lattice point.

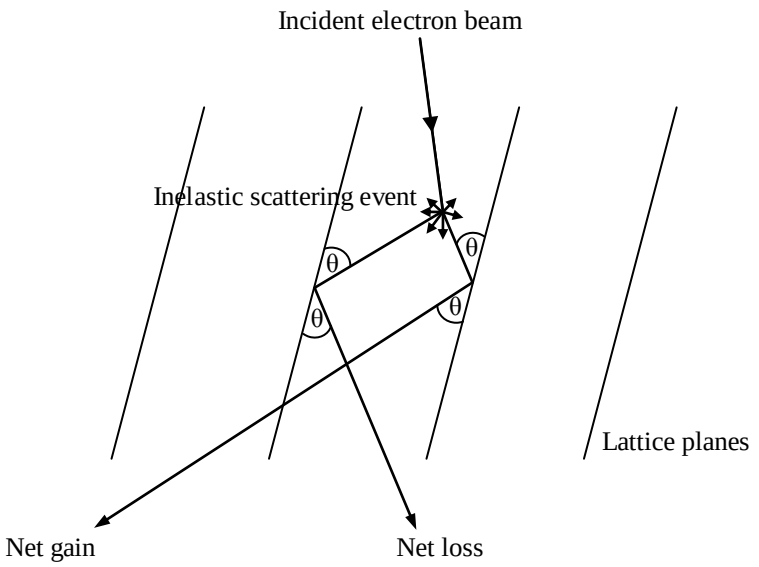

Figure 3.12 – Schematic representation of the origin of Kikuchi lines from inelastic scattering events. Paired light and dark bands originate due to net gain and loss in directions that satisfy the Bragg condition for diffraction. Reproduced from *Specimen Preparation in Materials Science* (Goodhew 1972).

Selection of the appropriate two beam condition is in general made by choosing a set of planes that have had their spacing disturbed by the feature of interest. In the case of a fully strained pseudomorphic layer the biaxial tetragonal distortion results in alteration of the spacing between (001) planes. Due to symmetry considerations the (001), (002) and (003) diffraction spots are forbidden, hence the (000) and (004) diffraction spots are chosen for *strain contrast*. The other major features of interest are dislocations within relaxed (fully or partially) silicon-germanium layers where the diffraction condition is chosen dependant upon the dislocations Burgers vector (lattice displacement). Clearly the spacing of atomic planes orthogonal to this direction will be altered, shown schematically in Figure 3.13, with dislocation Burgers vector of the form ½[110] in this crystal system the spacing of (110) planes and those parallel will be effected. For this reason *dislocation contrast* is achieved by selection of the (000) and (220) diffraction spots.

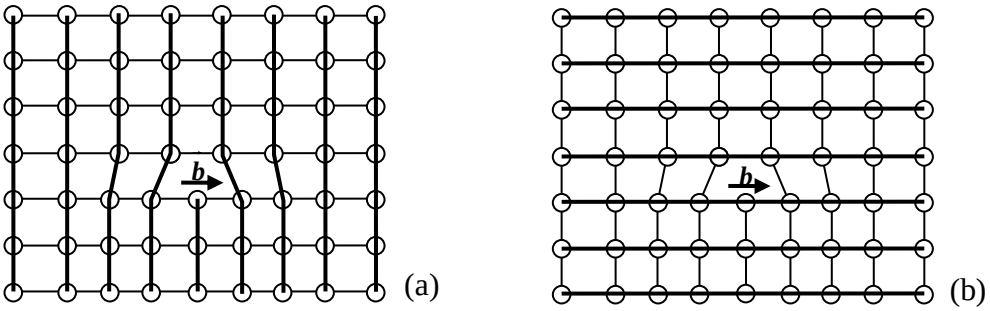

Figure 3.13 – Schematic diagram showing the effect of an edge dislocation on lattice planes in orthogonal directions. Clearly the planes highlighted in (a) are more distorted by the dislocation than in (b) and are perpendicular to the dislocations Burgers vector. Reproduced with kind permission (Capewell 2002).

It is important to note that length distortion will occur upon movement away from the major pole axis in the diffraction mode as in real space the sample is being viewed at an increasing angle. When imaging with (000) and (004) (strain contrast mode) deviation in length *along* a grown layer will occur whilst when imaging (000) and (220) (dislocation contrast) layer thickness will be distorted, this is simply understood with aid of the pictorial representation in Figure 3.14.

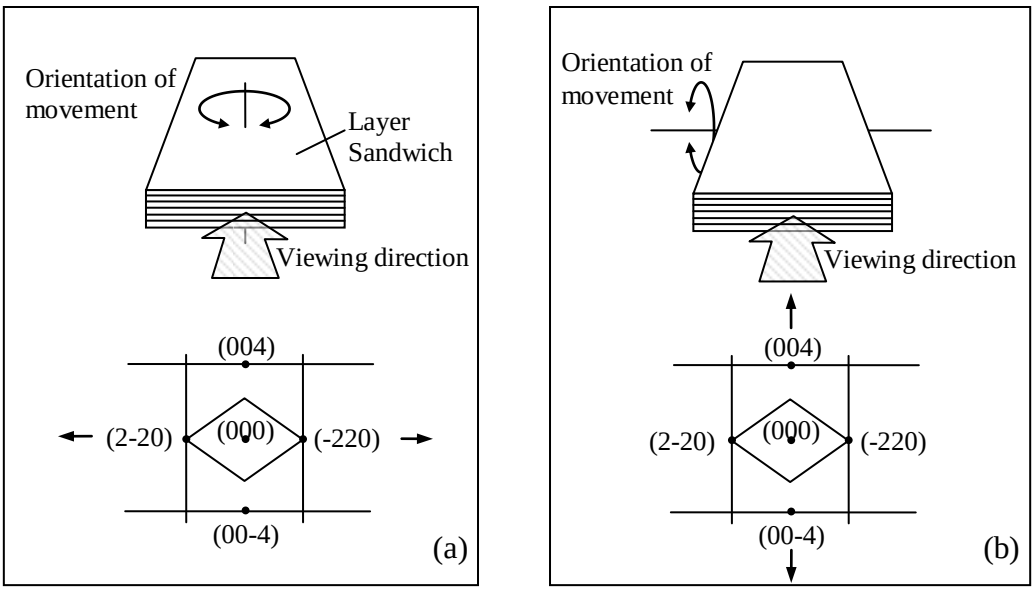

Figure 3.14 – Schematic of real space sample tipping with respect to reciprocal space observed in diffraction mode. Arrows indicate the respective motions.

Enough emphasise cannot be placed on the importance of good specimen preparation as no amount of setup can compensate for a poorly prepared sample. Warped or rippled films can also prove difficult to clearly image as segments will undoubtedly meet the Bragg condition yielding dark bands across the image, though minimisation of such effects can be achieved with experience.

For a comprehensive consideration of the principles and practice of electron microscope operation the reader is referred to *Principles and Practice of Electron Microscope Operation* (Agar 1974).

3.5.5 Energy Dispersive X-ray Spectroscopy (EDS)

Energy dispersive X-ray spectroscopy provides valuable quantitative compositional analysis to the TEM. EDS is the measurement of characteristic X-rays emitted from a selected area of a specimen during high energy electron bombardment within the TEM. A qualitative analysis of elements present within the sample can be obtained from the characteristic X-ray spectrum resulting from this interaction, with a quantitative analysis obtained through the rate detection of these characteristic X-rays.

EDS was provided in the JEOL JEM-2000FX by an EDAX instrument operating at normal incidence, requiring the removal of the objective aperture from the electron beam and insertion of the detector head into the main column. Spot size was reduced until the received counts dropped to around 2500 cps providing optimal counting conditions with minimal detector dead time. The typical collection time used in this work was 50 seconds and quantification of the spectrum made automatically by the *Genesis* collection software. Care should be taken when performing analysis to ensure a *sufficiently thin region* is imaged to avoid the matrix effects of absorption and fluorescence (GENSIS Spectrum User's manual). In

practice a region is *thin* when a count rate of ~2500 cps can be obtained at a spot size of 4L and a beam current of 119 μA. It is also important to understand that the finite spot size can make accurate compositional determination of very thin (< 50 nm) epitaxial layers impossible due to beam overlap with adjacent layers.

3.6 High Resolution X-ray Diffraction

High resolution X-ray diffraction allows the determination of both the composition and strain state of an epitaxial layer; during this work it was used to determine these parameters only for epitaxial layers of uniform composition. In simple terms the principle of high resolution X-ray diffraction is a practical application of Bragg's Law combined with highly precise angular positioning.

The high resolution diffractometer used in this work was a Philips PW1835 with a high power copper X-ray source ($CuK\alpha_1$ λ= 1.540597Å) operating at 40 kV / 40 mA, and fitted with a germanium 4 crystal monochromator to provide a well collimated parallel beam.

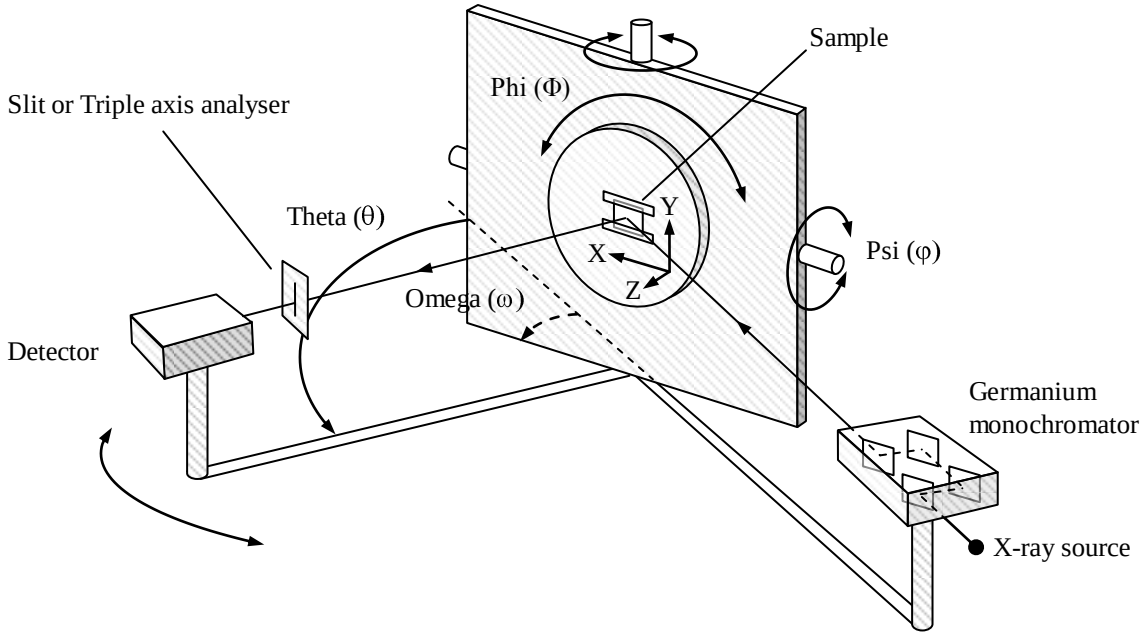

Figure 3.15 – Schematic diagram of a high resolution X-ray spectrometer.

The sample was fixed using 3M Scotch tape (for stress free mounting) to a stage providing linear motion in 3-dimensions as well as rotation in three separate directions. The angular resolution of the detector is determined either by a copper slit (1 mm wide) or a triple axis germanium crystal analyser, permitting resolution at ~12 arc seconds (with slight loss of beam intensity). A schematic diagram is shown in Figure 3.15.

The characterisation of the epitaxial layers grown during this work required collection of symmetric [004] and asymmetric [224] *omega (ω)- omega-2theta (ω–2θ) scans* more commonly referred to as *reciprocal lattice maps*. Two scans are required to enable the calculation of the in-plane and out-of-plane lattice constant. The [004] scan allows direct determination of the out-of-plane lattice spacing whilst the [224] scan consists of components from both, allowing the extraction of the in-plane lattice parameter when combined with the [004] scan.

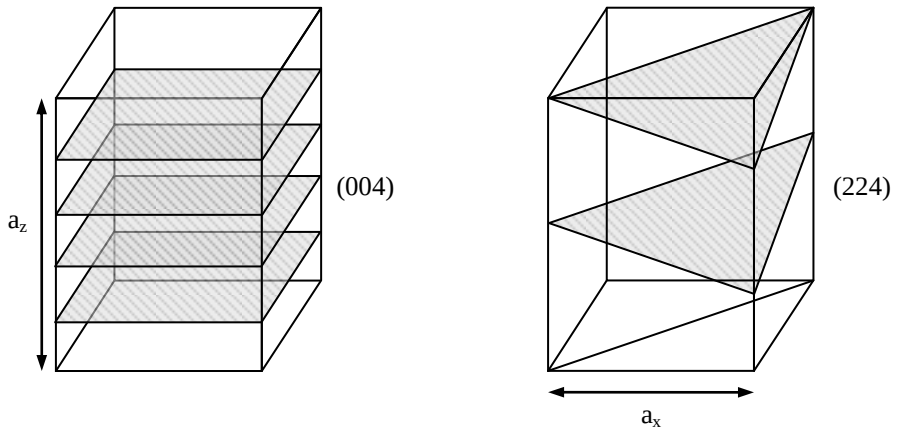

Figure 3.16 – Schematic representations of a tetragonally distorted cubic unit cell showing that the (004) spacing is entirely out of plane whilst the (224) contain components both in plane, a_x, and out of plane, a_z.

3.6.1 The Reciprocal Lattice and Ewald Sphere Construction

The planes of a crystal lattice in real space can be represented by a series of points in *reciprocal lattice space*. A reciprocal lattice can be constructed from a real space lattice by combining a series a *reciprocal lattice vectors* with lengths inversely proportional to lattice spacing and orientation defined by the surface normal of the corresponding planes.

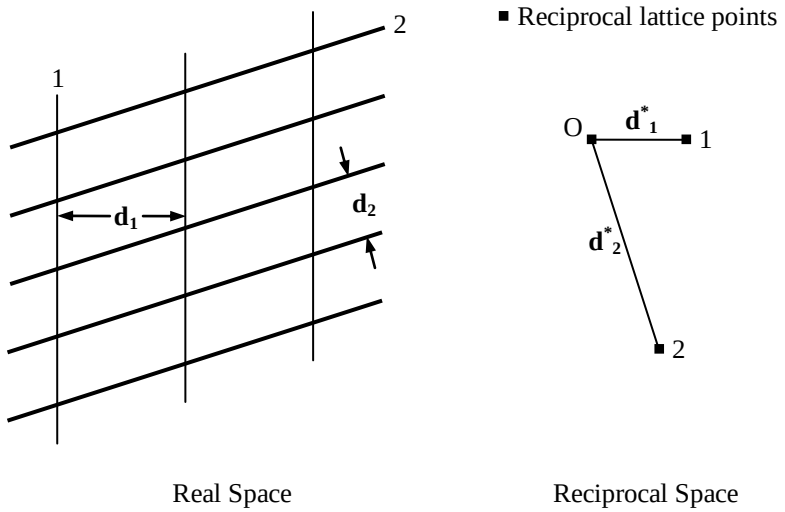

Figure 3.17 – Diagrams illustrating how a reciprocal lattice is derived from the real space lattice and how they are related. d_1 and d_2 are the spacing between sets of planes 1 and 2 respectively whilst d^* are the corresponding reciprocal lattice vectors. Reproduced from *The Basics of Crystallography and Diffraction* (Hammond 2001).

The end points of the reciprocal lattice vectors are known as *reciprocal lattice points* and are labelled with plane indices with which they correspond. All lattice vectors originate at the centre of reciprocal lattice space and an entire reciprocal lattice is constructed by combination of points corresponding to all of the real space lattice planes.

The Ewald reflecting sphere construction makes use of reciprocal lattice space to provide a geometrical expression of Bragg's Law. The construction consists of a sphere in reciprocal lattice space with a diameter equal to $1/\lambda$ (λ is the X-ray

wavelength) with the reflecting crystal located at its centre and the origin of reciprocal space located at the intercept between the transmitted beam and the sphere. When the crystal is orientated such that the Bragg condition is satisfied then the intersection of the diffracted beam with the sphere will coincide with the position of the corresponding reciprocal lattice point. Hence satisfaction of Bragg's Law is equivalent to the intersection of a reciprocal lattice point by the sphere in this arrangement.

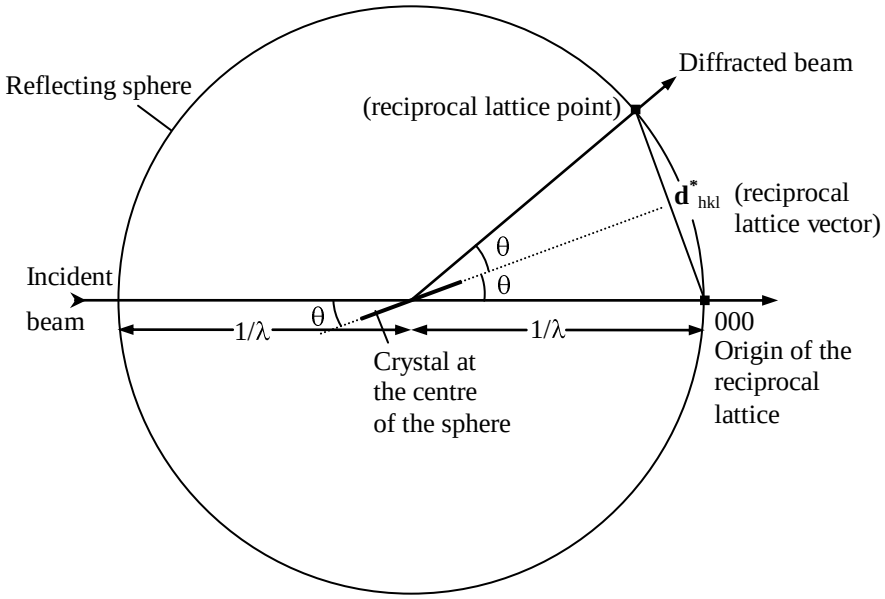

Figure 3.18 – Ewald reflecting sphere construction for a set of planes at the correct Bragg angle. Reproduced from *The basics of crystallography and diffraction* (Hammond 2001).

A more complex geometrical construction based upon the Ewald reflecting sphere construction which is related to the experimental setup of the high resolution diffractometer, illustrates the purpose of conducting an omega (ω) - omega-2theta (ω–2θ) scan in mapping a selected region of reciprocal lattice space, Figure 3.19

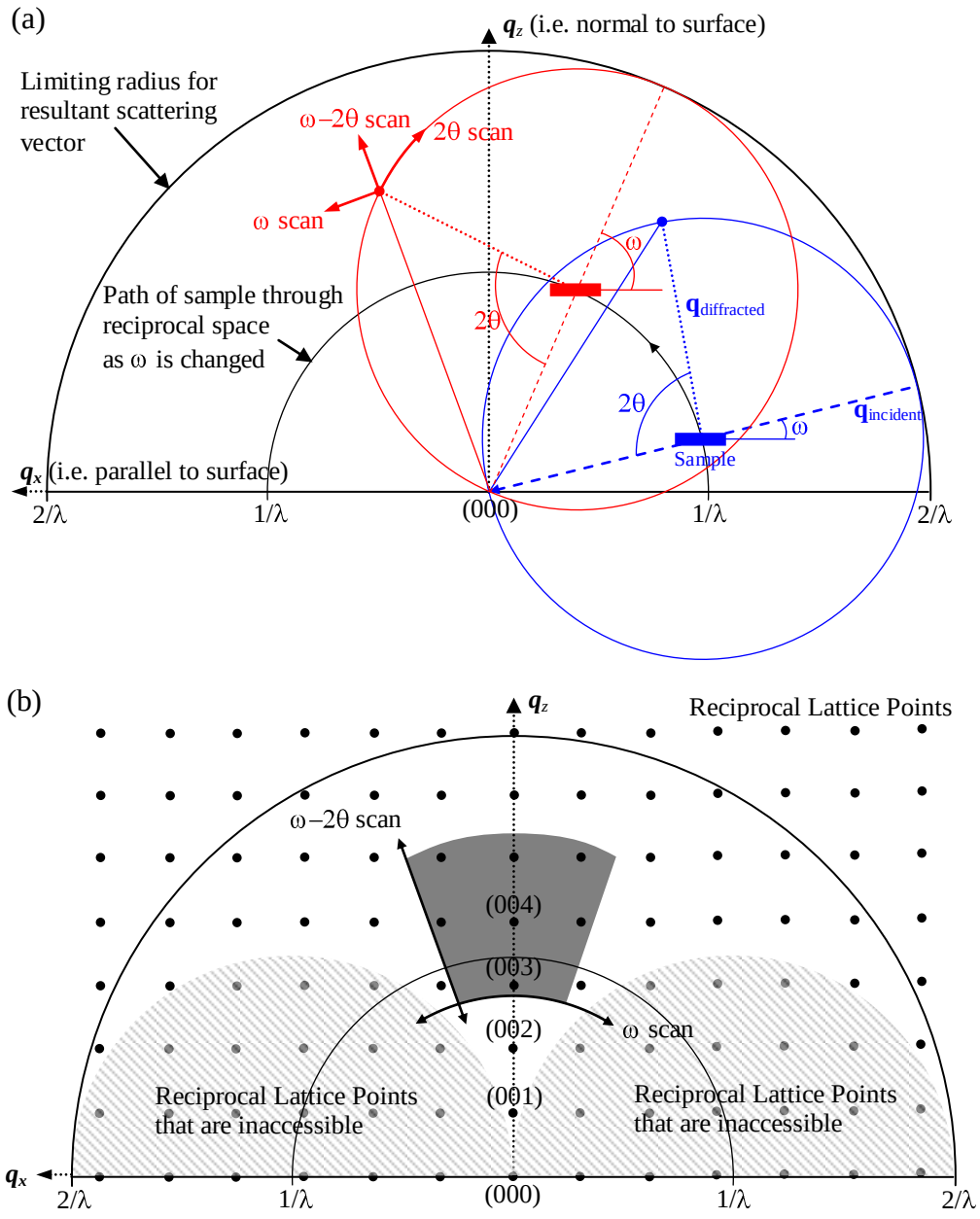

Figure 3.19 – Schematic diagrams showing how the Ewald sphere construction relates to the experimental parameters of the apparatus. Diagrams are reproduced with kind permission of Stuart Jollands (University of Warwick, unpublished).

For further information regarding general crystallographic and diffraction theory the reader is referred to *The Basics of Crystallography and Diffraction* (Hammond 2001).

3.6.2 Setup for an Omega - Omega-2Theta Scan

Initial setup requires the 2theta (2θ) position to be calibrated, as this will serve as a reference for all subsequent positioning; with the sample out of the X-ray beam and the triple axis analyser in place, 2theta (2θ) is scanned and the peak maxima zeroed. The sample is located at the centre of stage rotation and the Z position (Figure 3.15) adjusted to achieve a *half-cut beam*, where half the maximum straight through intensity reaches the detector. An omega (ω) scan is conducted with the peak position chosen and zeroed, the half-cut beam is then reset and omega (ω) rescanned. The stage is now moved using the data collector software to the reflection of interest, usually the asymmetric [224] scan is conducted first enabling phi (Φ) and psi (φ) to be adjusted accurately.

An initial omega (ω) scan is followed by a 2theta (2θ) scan with each peak maxima set in the software centring the scan. A phi (Φ) scan is made over the large angular range of 10º and once set (at peak maxima) is only altered in an increment of 90º for the second set of orthogonal scans. To maximise the diffracted beam intensity a series of psi (φ) scans are conducted each made with a small change in the value of omega (ω) until a single peak (often starts as a double) with a maximum intensity is observed. Psi (φ) is then set and a final omega (ω) scan conducted to ensure the scan has remained centralised in omega (ω).

An omega-2theta (ω–2θ) scan involves scanning the detector arm at twice the rate of the sample stage to maintain the Bragg angle relationship for parallel planes with varying lattice spacing. That is to say those reflections from parallel planes with different lattice spacing will occur at different Bragg angles but have an equal incident and reflected angle, thus as the angle between source and stage increases as omega (ω), the relative difference between the stage and detector must also increase as

omega (ω) and so as 2theta (2θ) relative to the source. To enable an omega (ω) - omega-2theta (ω–2θ) scan to be performed the diffractometer must be programmed to scan over an appropriate angular range in both omega (ω) and omega-2theta (ω–2θ). An omega-2theta (ω–2θ) line scan is made to identify the appropriate range and centre, whilst the omega (ω) range is estimated from experience or prior knowledge. This procedure is then repeated for the [004] symmetric scan and again for both [224] and [004] scans with phi (Φ) +90º to determine if any asymmetry in the relaxation exists between orthogonal directions.

Once the values of omega (ω), 2theta (2θ), phi (Φ) and psi (φ) have been identified for each scan, an automated batch scan file is created that performs a sequence of omega-2theta (ω–2θ) scans stepping omega (ω) between each, saving the results to hard disk for later analysis.

3.6.3 Analysis of an Omega - Omega-2Theta Scan

The collected scans are analysed using the specialised X-ray software *X'Pert Epitaxy v4* provided by Pan Analytical. The four scans are loaded together and peaks corresponding to the substrate and epitaxial layers are marked and the reflections from which the scan originated entered. The software is then able to directly calculate the lattice parameter in the growth direction (inversely proportional to the distance in reciprocal space) from the [004] reciprocal space map. The deviation of the layers reciprocal lattice point from a straight line passing through the silicon substrate reciprocal lattice point from the origin is due to layer tilt. With the layer tilt known the in-plane lattice parameter can be directly determined and the layer relaxation can be calculated from the position of the equivalent reciprocal lattice point in the [224] reciprocal space map (Bauer *et al.* 1995).

For more in-depth information concerning sample alignment and general X-ray diffraction from crystalline semiconductors the reader is referred to *X-ray Scattering from Semiconductors* (Fewster 2000).

3.7 Atomic Force Microscopy (AFM)

Atomic force microscopy (AFM) is a form of scanning probe microscopy (SPM) capable of high vertical resolution imaging of surface topographical features on a wide variety of surfaces (both conducting and insulating) relying upon the mutual repulsion of a sample surface and scanning tip due to interaction between all of their associated electrons. Features are imaged using piezoelectric scanners to raster a fine probe attached to the end of a cantilever across the surface of a sample over an area up to 100 μm x 100 μm. The AFM work presented herein was conducted on behalf of the author by Neil Wilson (University of Warwick) using a Digital Instruments Nanoscope III AFM in which the sample stage is scanned and the probe held still, Figure 3.20.

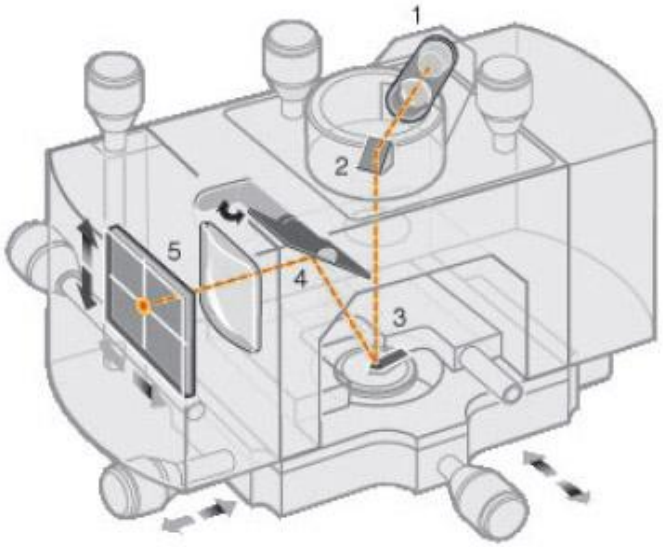

Labels:

1. Laser
2. Mirror
3. Cantilever
4. Tilt mirror
5. Photodetector

Figure 3.20 – Schematic diagram of a scanned sample AFM instrument with the main components indicated. Reproduced from Veeco training manual (Veeco 2000).

The extremely high vertical resolution of this technique is due to a highly accurate position sensitive detector allowing detection of movements < 1 Å, detailed in Figure 3.21. Two main imaging modes exist in AFM, contact mode and tapping mode.

3.7.1 Contact Mode

Contact mode is the most basic manner of operation in which the probe is held directly in contact with the sample surface whilst it is being scanned. A constant force is maintained between the sample and probe by monitoring and restoring the deflection of the cantilever at the end of which the probe is attached. The cantilever deflection is monitored by collecting laser light, emitted from a solid state diode that is reflected off the back of the cantilever, using a position sensitive detector consisting of a four part photodiode. The deflection is restored using a highly sensitive piezoelectric height controller in a feedback loop, with height information derived from this feedback signal.

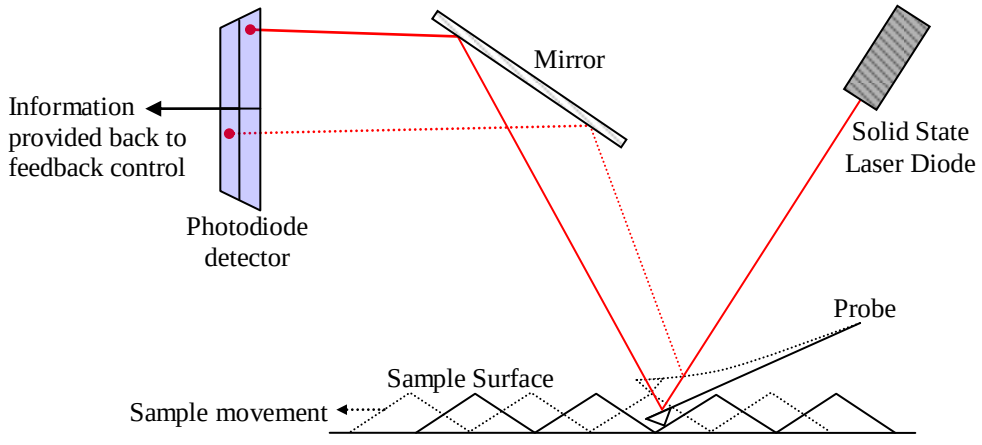

Figure 3.21 – Schematic diagram showing the basic principle of AFM operation. Movement of the sample beneath the probe causes it to rise and fall altering the path of the reflected laser light. Feedback control compensates lowering or raising the sample to maintain a constant applied force to the surface.

Contact mode uses a silicon nitride tip mounted on a short thin cantilever to provide a low contact force that can accurately follow surface morphology. The images in this thesis were obtained in contact mode over areas no larger than 10 μm x 10 μm at a scanning frequency of 1 Hz.

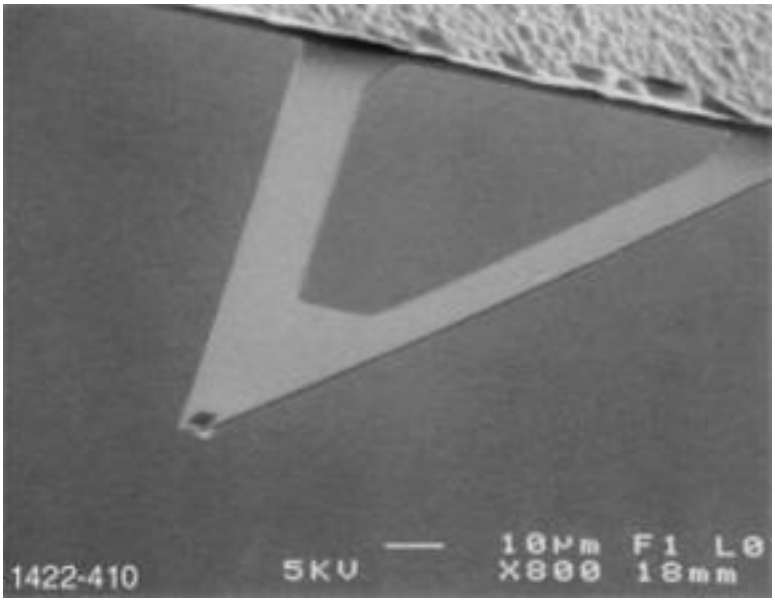

Figure 3.22 – Scanning electron microscope (SEM) image of a silicon carbide tipped cantilever AFM probe. Reproduced from Veeco training manual (Veeco 2000).

The scan rate is chosen to allow time for the feedback loop to respond to changes in sample morphology to provide close tracking of the surface. The lateral (X, Y) positioning of the tip is far less accurate than the vertical (Z) positioning and is not tracked in real-time. The resolution of lateral positioning is ultimately limited by the tip radius and side wall angle. A clean sample surface is essential as debris build up at the tip can result in a generally lower image resolution as well as image distortions, Figure 3.23. All samples investigated were ultrasonically cleaned in de-ionised water after cleaving.

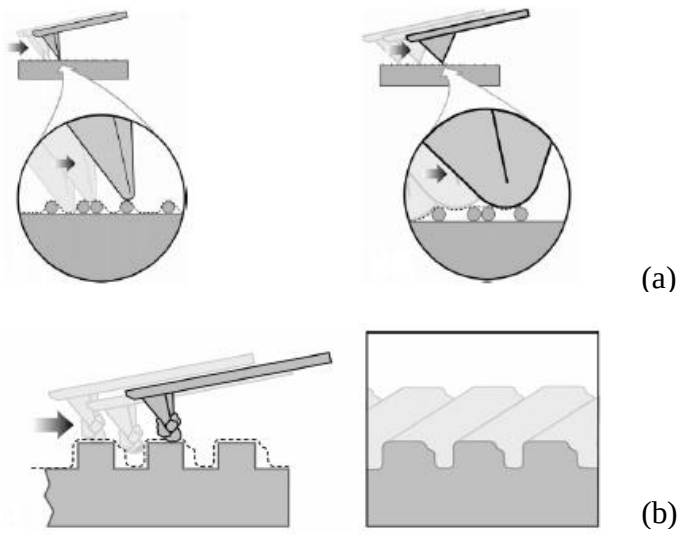

Figure 3.23 – Schematic diagrams showing (a) the image profiles of spheres scanned with a sharp (left) and dull (right) probe (b) Image profile of trenches scanned with a dirty tip. Reproduced from Veeco training manual (Veeco 2000).

3.7.2 Image Processing

It is necessary to perform a certain level of image processing before useful information can be extracted from scanned images. As the piezoelectric scanners are attached at one end and free at the sample, the motion obtained often deviates from that of an ideal plane, resulting in a bowed motion. The *planefit* filter allows the elimination of such anomalies by calculating a single polynomial fit for the entire image and then subtracting it. All images presented have undergone a 3rd order planefit removing both tilt and bow from the image.

Selected images have additionally undergone zero order *flattening* to remove vertical offsets between adjacent scan lines in the fast scanning direction. Zero order flattening subtracts an average Z value from each point in the scan line. Such offsets can arise from a number of sources, in this case the hard samples investigated resulted in tip damage causing sudden offsets in a number of images.

It is clearly important that any processing is applied equally to all images that are being compared to ensure a fair comparison is made.

Chapter 4

4 Low Composition Regime (0-25%)

The concept of *terrace grading* introduced by Capewell (2002) (Capewell *et al.* 2002) has been shown to offer clear improvements over more conventional stepped and linear graded structures. Capewell (2002) demonstrated that a good quality virtual substrate with a terminating germanium composition of 50% could be fabricated entirely within a thickness of only 2 μm with the following characteristics, ≥ 96 percent relaxation in the final layer, an RMS (root mean square) roughness of 3.1 nm and a surface threading density of $3x10^6/cm^2$ with only a small number of pile-ups visible. Due to the relatively thin layers used, annealing became essential to achieve high levels of relaxation. The persistence of multiplication sources between graded regions was substantially reduced, a central aim of terrace grading, though doubts remained as to whether relaxation of the lower layers had fully occurred before the addition of subsequent layers.

The application of low composition virtual substrates has primarily been for the production of strained silicon surface channel device structures. It is theoretically predicted that strain increases electron and hole mobility, but there is no additional *electron mobility enhancement* for strain resulting from a relaxed germanium concentration of more than 15% (Oberhüber *et al.* 1998), although experimental evidence appears contradictory (Takagi *et al.* 2005). The mobility enhancement for holes is predicted and experimentally found to continue to increase beyond 25%, see Figure 4.1. In this work these structures have the additional role of providing a basis for higher composition virtual substrates, discussed in chapters 5 and 6.

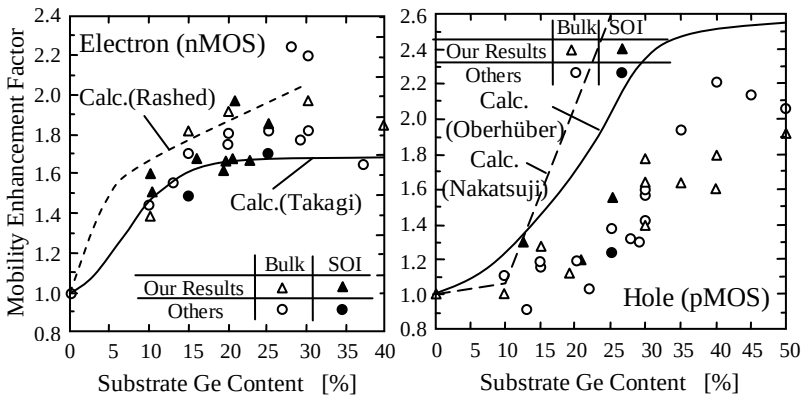

Figure 4.1 – Experimental and theoretical enhancement factors of electron and hole mobility, defined by the ratio of mobility in strained-Si to unstrained Si MOSFET's, as a function of composition. Since the enhancement factor of hole mobility is dependent on E_{eff}, the maximum values, typically seen in low E_{eff} region, are plotted in this figure. Reproduced from a paper by Takagi *et al.* (2005).

The current state of the art 15% conventionally graded virtual substrate structures for which data has been published contain a surface threading density of $2x10^4/cm^2$ (Olsen *et al.* 2003) and represent an order of magnitude improvement over the work a decade earlier of Fitzgerald *et al.* (1991). More exotic approaches also exist for low composition virtual substrates, including low temperature 15% buffers with a threading density $\leq 10^4/cm^2$ (Linder *et al.* 1997), 15% stepped layers with high and low temperature stages with a threading density of $10^3/cm^2$ (Gaiduk *et al.* 2000) and isolated 25% SiGe mesa structures on SOI with a threading density $\leq 10^3/cm^2$ (Tezuka *et al.* 2002).

Low composition silicon-germanium virtual substrates are currently available from numerous commercial sources such as IQE who provide highly relaxed 17% buffers with threading densities $< 3x10^5/cm^2$ and threading dislocation pile-up $< 3\ cm/cm^2$ and 20% buffers with threading densities $< 5x10^5/cm^2$ with threading dislocation pile-up $< 10\ cm/cm^2$ both with micro-roughness $R_a < 10Å$ (IQESiltronic 2005).

The focus of the current work is to further improve the *quality* of the virtual substrate, in terms of relaxation, surface roughness, surface threading density and threading dislocation pile-up. Whilst the work of Capewell (2002) considered layer structures with graded and terraced regions each of no more than 200 nm, the work presented herein investigates the advantages of terrace grading at thicknesses between 200 nm and 1 μm. The greater spatial separation of misfit dislocations and the lower rate of strain increase should result in fewer dislocation interactions, lower threading density and smoother surfaces.

Although the aim of optimised *thin* virtual substrate structures may still have important applications, improvements in layer transfer technology and its growing mainstream acceptance mean that total layer thickness is of lesser importance than the final layer quality, providing they can be economically produced with sufficient smoothness (< 1 nm RMS) and appropriate defect density. Ideally the defect level will be as close as possible to zero for highly reliable device structures (LeGoues 1996) though $< 10^4/cm^2$ is stated as an acceptable level for majority carrier devices (Tezuka *et al.* 2002).

4.1 Growth Parameters

4.1.1 15% Linear Graded Virtual Substrates

To investigate the effect of layer thickness and growth temperature on relaxation and surface morphology at low germanium concentration, a matrix of layer recipes was explored, Table 4.1. The lower limit for thickness investigated was chosen at 200 nm, as thinner layers are known to result in poor material quality (Capewell 2002) whilst the upper limit was chosen to be 1μm which results in a near

optimum grading rate (Dutartre *et al.* 1994). An initially high upper growth temperature (for SS-MBE) of 850ºC was selected to ensure a high level of relaxation for all layers under investigation. A lower temperature limit of 700ºC will provide some kinetic suppression of surface roughening (Kasper 1995). The relaxation of thinner layers is known to be incomplete when grown at lower temperature (700ºC) and so for consistency, anneal steps were provided to all layers irrespective of thickness.

	700ºC	775ºC	850ºC
1μm	75027	75034	75028
600nm	75032	75033	75031
200nm	75022	-	75030

Table 4.1 – A summary of parameter variations explored within the 15% virtual substrate structures, showing growth temperature and layer thickness, with the resulting sample labels shown for reference (grown in numerical order).

All substrates were given an *in-situ* high temperature anneal at 890ºC to desorb native oxide from the growth surface (Kasper *et al.* 1998). Growth of a 50 nm silicon layer followed, at a temperature ramping from 890ºC to that of the initial SiGe layer providing a clean high quality growth platform. A silicon-germanium layer linearly grading in composition from 0.1% to 15% germanium was deposited with a thickness of 200 nm, 600 nm or 1 μm. Virtual substrate growth was completed by a silicon-germanium layer of uniform germanium composition and of equal thickness to the preceding graded layer. Each virtual substrate was grown at a constant temperature of 700ºC, 775ºC or 850ºC throughout, at a total growth rate of 0.6 Å/s (Grasby 2002) and annealed at 890ºC for 25 minutes (ramped up over 20 minutes) after growth had been completed. A graphical representation of this structure is given

in Figure 4.2. Although it is recognised that a graded temperature profile would most likely yield further improvements, for clarity at this stage this was not utilised.

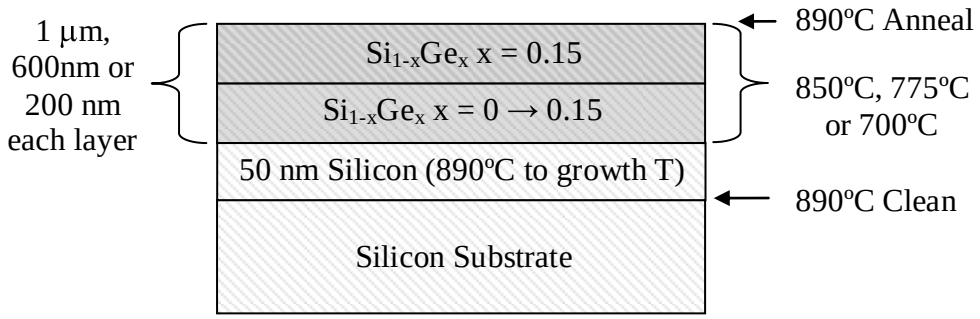

Figure 4.2 – Schematic representation of linear graded 15% virtual substrate specifications showing all possible growth parameter variations explored.

4.1.2 25% Terrace Graded Virtual Substrates

Two 25% terrace graded structures, 75037 (25%, 700-650ºC, 1 μm) and 75029 (25%, 850-800ºC, 1 μm), were grown as a continuation of the sample structures 75027 (15%, 700ºC, 1 μm) and 75028 (15%, 850ºC, 1 μm) described previously. After annealing of the first terrace grade the substrate was allowed to fall to a temperature 50ºC lower than that at which the preceding layer had been grown. Additional layers were grown with a graded germanium composition from 15% to 25% and capped with a layer of 25% constant composition. A final anneal was then given, 50ºC lower than that given to the first terrace. An additional structure 75036 (25%, 850-800ºC, 200 nm) with 200 nm thick layers was grown as a continuation of the sample structure 75030 (15%, 850ºC, 200 nm). A graphical representation of these structures is given in Figure 4.3.

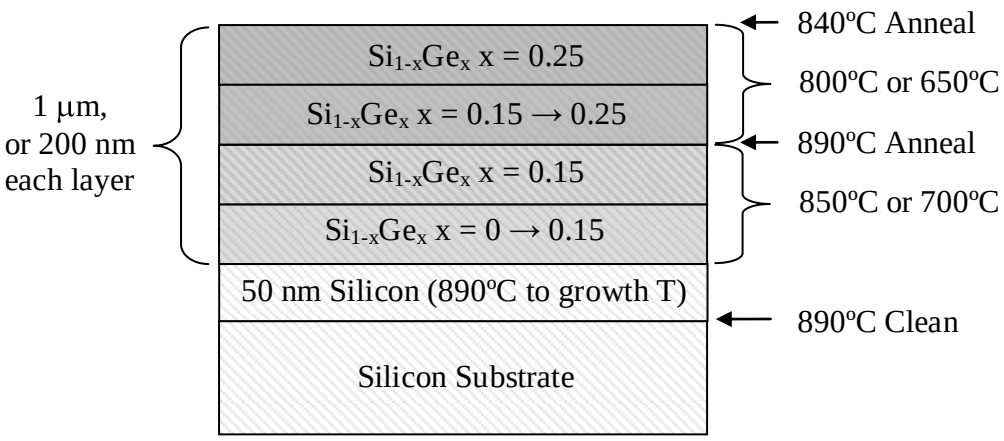

Figure 4.3 – Schematic representation of terrace graded 25% virtual substrate specifications showing the growth parameter variations explored.

The growth temperature is reduced with increasing composition in order to suppress surface roughening (Mooney *et al*. 1995) in line with the difference between the melting points of silicon and germanium. The difference in melting point is approximately 500ºC and so a reduction at around 50ºC per 10% is approximately equivalent. The wafer identification numbers for the 25% samples are given in Table 4.2.

	700-650ºC	850-800ºC
1μm	75037	75029
200nm	-	75036

Table 4.2 – A summary of parameter variations explored within the 25% virtual substrate structures, with the resulting sample labels shown for reference.

4.2 Nomarski Interference Imaging

Visual inspection provided a quick and simple analysis for the large number of grown layers and with the aid of a microscope equipped with interference capabilities tiny surface features have been imaged.

4.2.1 15% Virtual Substrate

A trend of increasing cross-hatch coarseness at greater thickness is apparent between the samples grown at 850ºC, but less distinct between the lower temperature samples where adatom mobility is kinetically suppressed to a greater degree. A selection of optical interference images taken at x100 magnification is presented in Figure 4.4.

The difference in cross-hatch spacing between samples of different thickness almost certainly results from the different grading rates. Similar qualitative trends have been observed both by Fitzgerald *et al.* (1992) and Dutartre *et al.* (1994) when investigating 30% virtual substrate structures by means of SEM and AFM respectively, grown with grading rates between 10-80%/μm comparable to the work herein. Both found the surface RMS roughness to increase with increased grading rate, with Dutartre *et al.* (1994) finding it to *rapidly* increase at grading rates in excess of those currently investigated. Fitzgerald *et al.* (1997) attributed the variation in cross-hatch spacing to unequal adatom incorporation across the surface, as a consequence of inhomogeneous strain fields emanating from dislocations below, with the roughness linked to the critical thickness at which dislocations were introduced. Although the effect of inhomogeneous strain fields may play a role in determining surface morphology, I believe that in this instance this effect may simply shape existing features generated from the underlying dislocation network.

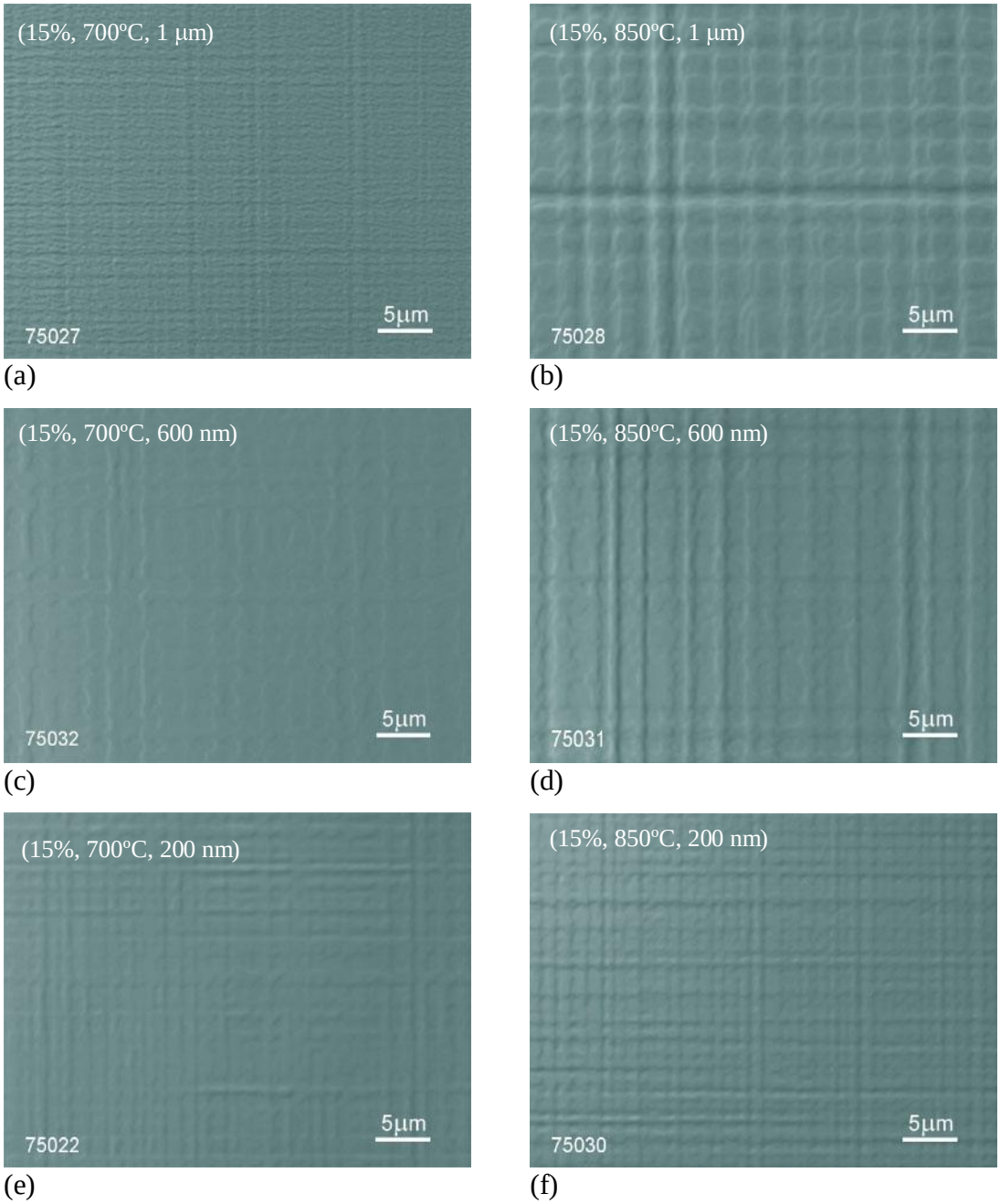

Figure 4.4 – Nomarski interference images taken at x100 magnification of the 15% linearly graded samples (a) 75027, (b) 75028, (c) 75032, (d) 75031, (e) 75022 and (f) 75030.

The work of Shiryaev *et al.* (1995) on *ex-situ relaxed* metastable linearly graded virtual substrate structures clearly shows a *"pronounced shear-band pattern"* composed of a collection of similarly sized rectangular blocks (<110> orientated) that are displaced in height relative to one another, though no indication is given to origin of the widely spaced arrangement. A structure with a grading rate of 15%/μm

(similar to 75027 (15%, 700ºC, 1 μm) and 75028 (15%, 850ºC, 1 μm)) and terminating composition of 22% is revealed by AFM to have surface features of a similar order in size to those seen on 75028 (15%, 850ºC, 1 μm) at around 2 μm x 2 μm, Figure 4.5.

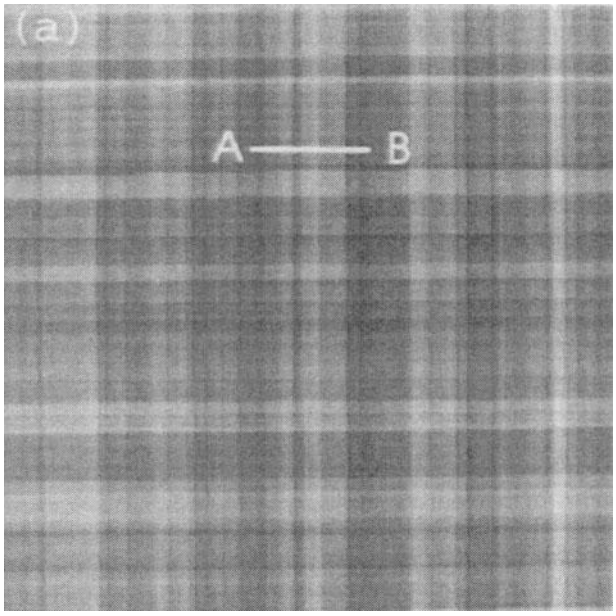

Figure 4.5 – An AFM (21x21 μm^2) image of the slip-band pattern on the surface of a graded layer with a thickness of 1.5 μm and a Germanium gradient of 15%/μm, grown at 530ºC, after annealing at 620ºC for 1 hour. Full height scale is 47 nm. Reproduced from a paper by Shiryaev *et al.* (1995).

Cross-sectional TEM and X-ray evidence (sections 4.3 and 4.4) would suggest that the grading achieved did not match that which had been intended, instead consisting of a sharp initial jump in concentration followed by a gentle increase composition. Features such as those observed by Shiryaev *et al.* (1995) may have formed abruptly during growth, subsequently forming the basis for evolution of the surfaces seen in Figure 4.4, resulting in their unusual appearance.

The areas immediately surrounding the hatching in Figure 4.4 (b) appear to have formed round edged hillocks with flat tops that often appear to blend into one

another. It should be noted that without knowledge of feature direction gained from AFM it would be difficult to discount interpretation of the inverse image where raised hatches enclose round edged trenches with flat bottoms, highlighting one of the limitations of this particular technique if used in isolation.

Instances of individual large hatches are likely to be the result of a large number of misfits locally piling up on the same or closely separated glide planes, probably as a result of a nucleation mechanism like the modified Frank-Read; the increased stress field associated with misfit pile-ups are believed to result in larger surface disturbances (Fitzgerald *et al*. 1992).

In the thinner layer structures stress will build more quickly and the closer spatial separation of the misfit dislocations will have led to a higher probability of interaction and blocking. The requirement for mobile threading dislocations able to continue relaxation of the layer results in further misfit introduction and a more closely spaced network of misfit dislocations hence a finer cross hatch pattern. Additionally strain fields emanating from underlying misfit dislocations as modelled by Fitzgerald (1992) are much closer to the growth surface and may play an increasingly important role.

The surface of 75027 (15%, 700ºC, 1 μm) Figure 4.4 (a) and 75028 (15%, 850ºC, 1 μm) Figure 4.4 (b) show the greatest difference in surface morphology between samples of equal thickness. The distinct cross-hatch pattern displayed by the high temperature sample is almost absent on the surface of 75027 (15%, 700ºC, 1 μm) in the image shown in Figure 4.4 (a) and closer examination reveals the presence of many smaller features. Jernigan and Thompson (2001) found at a temperature of around 650ºC that silicon growth moved from a clearly defined step flow regime, progressing toward growth by 2-D island formation found at 500ºC whilst still

exhibiting characteristics of step flow. This can be understood in terms of the reduction of adatom mobility with reducing temperature as adatoms are less likely to reach existing surface steps before island formation. The layers studied here are far thicker than any considered by Jernigan and Thompson (2001), with increasingly large numbers of surface terraces forming, growth may well shift further toward a 2-D island like mode of growth forming many new islands resulting in the observed surface.

The reduced visible contrast displayed by layers grown at lower temperature indicates for all thicknesses investigated, samples grown at higher temperatures have a greater surface undulation. This is supported by AFM measurements of surface RMS roughness presented in section 4.5 At higher temperatures adatom mobility will be greater than at lower temperatures and will enable to some extent the incorporation of adatom species so as to locally reduce stress at the surface elastically (Cullis 1996), possibly accompanied by a greater sensitivity to strain fields, exaggerating the cross-hatch features.

4.2.2 25% Virtual Substrates

A marked growth temperature dependence of surface morphology persists with the 25% terrace graded virtual substrates. The unusual surface features of 75029 (25%, 850-800ºC, 1 μm) observed at x100 optical magnification (compare Figure 4.6 (b) with Figure 4.4 (b)) endure and appear to show the development of an even more detailed surface structure, the origin of which is unclear.

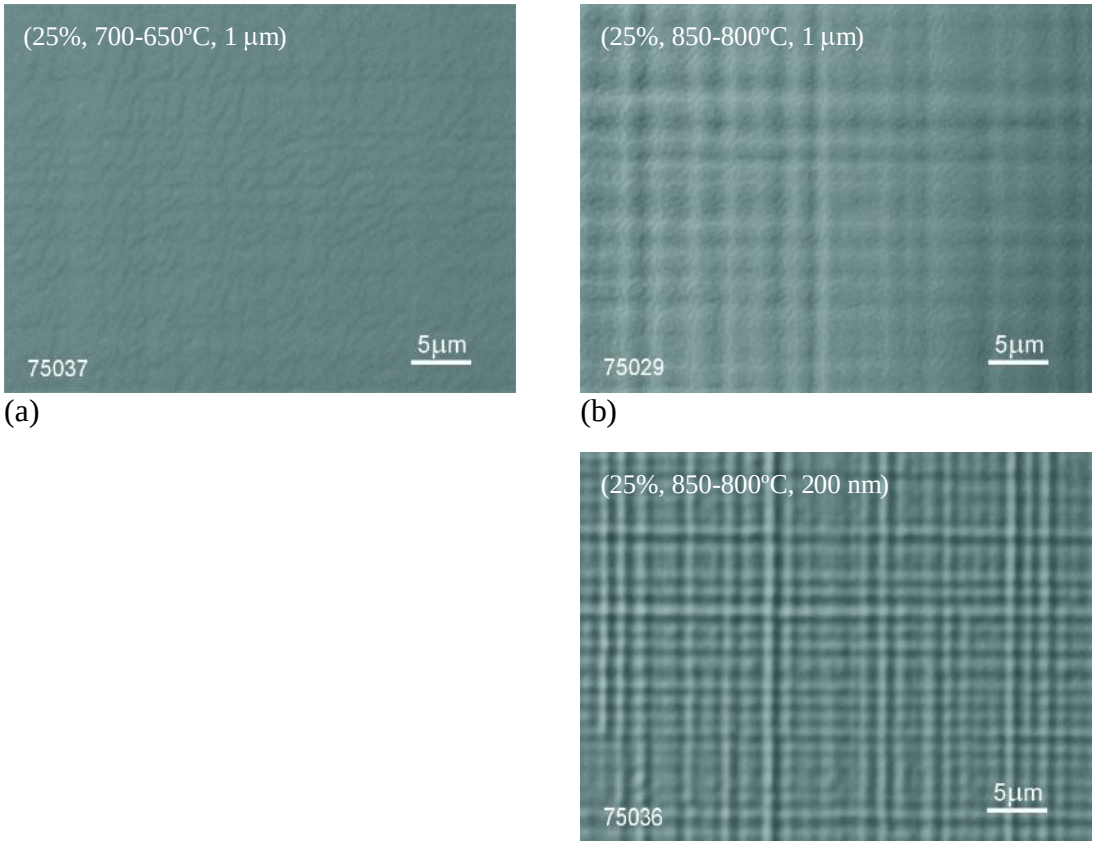

Figure 4.6 – Nomarski interference images taken at x100 magnification of the terrace graded 25% samples (a) 75037, (b) 75029, and (c) 75036.

Similarly the lower temperature sample 75037 (25%, 700-650ºC, 1 μm), whilst resembling the comparable lower composition layer 75027 (15%, 700ºC, 1 μm), appears to have evolved wider surface features. The evolution toward larger surface features is unexpected and would appear to indicate an increased adatom diffusion length despite the reduction in growth and anneal temperature. Compositional measurements performed using energy dispersive X-ray spectroscopy (EDS) show the upper terrace to contain only 20% germanium (section 4.3.3) rather than the intended 25%, with the deposition of 2 μm of material having occurred at a much reduced grading rate and misfit strain. The reduced strain in the over-layer may well explain the increased feature size, highlighting the important effect layer strain has on surface morphology.

The surface of the 200 nm terrace graded sample 75036 (25%, 850-800ºC, 200 nm) grown at high temperature appears significantly different to all of the previously grown layers. Most striking is the definition of cross-hatch suggesting the surface has undergone a transition to 3-D growth. Under conditions of great stress and high adatom mobility, limited strain relief can be achieved through elastic deformation of the surface (Cullis 1996) without requiring the introduction of dislocations, with preferential incorporation of germanium adatoms at the peak of surface disturbances. This demonstrates that the growth temperature had not been reduced sufficiently in line with composition, for such a high rate of grading, promoting strain relaxation by alternate means.

4.3 Cross-Sectional Transmission Electron Microscopy (XTEM)

This type of analysis provides a large amount of information about lattice mismatched materials and is an invaluable tool for these investigations. The additional quantitative analysis provided by EDS on material composition provides a helpful comparison with data determined from X-ray analysis.

4.3.1 15% Virtual Substrates

A collection of representative cross-sectional transmission electron micrographs are presented in Figure 4.7. Dislocation density and distribution appears similar between samples of equal thickness grown at the various temperatures, an indication that annealing has had the desired effect on the thinner samples. The lack of threading segments visibly intersecting the surface indicates a surface threading density of $\leq 10^8$-10^9 cm^{-2} (Fitzgerald *et al.* 1992), indicative of a good quality virtual substrate buffer layer. Evidence of the modified Frank-Read multiplication

mechanism can be seen in the 1 μm layered sample pictured in Figure 4.7 (c), characterised by a series of closely separated dislocations sharing a common origin at a dislocation line inclined at 55º to the growth plane, usually indicative of clean growth conditions, Figure 4.7 (c).

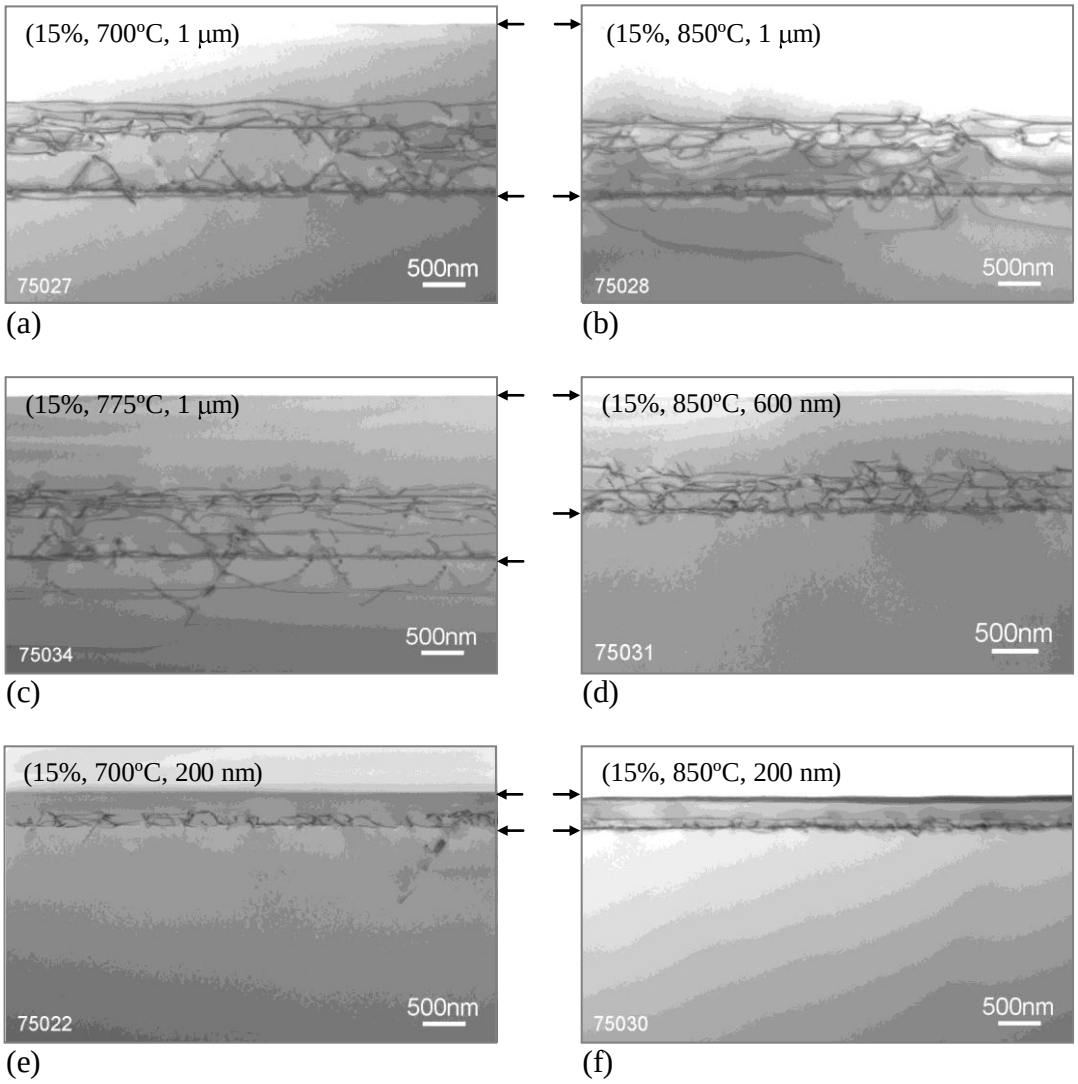

Figure 4.7 – Cross-sectional transmission electron micrographs (in the (220) two beam diffraction condition) of the linear graded 15% samples (a) 75027, (b) 75028, (c) 75034, (d) 75031, (e) 75022 and (f) 75030. The surface of the epitaxial layer is near the top of each image (marked with the upper arrow) and the initial growth interface below (marked by the lower arrow).

The greater separation of misfit dislocations in the 1 μm and 600 nm samples show that for all three temperatures investigated, the misfit dislocations present in the

graded region appear to share similar lengths. This is an indication that the rate of dislocation nucleation is similar, although cross-sectional images are far from ideal for this type of assessment. A distinct difference in misfit length is evident between the 200 nm layers were the dislocations will be more closely packed.

An increase in dislocation length may exist between 75027 (15%, 700ºC, 1 μm) and 75028 (15%, 850ºC, 1 μm) although this interpretation is subject to uncertainty given the unknown thickness of each prepared sample. An increase in dislocation length with temperature is not unexpected owing to the exponential dependence of glide velocity with temperature and a linear dependence on strain, equation (2.3). This allows existing misfit dislocations to more quickly relax the layer reducing the need for additional dislocation nucleation. Fitzgerald *et al.* (1999) highlight this in their analysis of the rate of change of strain relaxation,

$$\frac{\partial \delta}{\partial t} = C \left(\delta_{eq} - \delta \right) \tag{4.1}$$

where C is a constant, linearly dependent upon threading density and exponentially dependent upon temperature, δ is the amount strain relieved by threading dislocation motion and δ_{eq} is the strain relief desired for equilibrium.

At lower temperatures or higher grading rates equation (4.1) illustrates that the dislocation glide velocity may be insufficient to maintain the required strain relief allowing excess stress to build. Eventually this would result in the need for further dislocation nucleation, possibly elastic deformation of the surface and even progression toward a 3-D growth mode.

Such an effect could have been further exaggerated by the introduction of point defects from ion bombardment. It has been observed that significant electron

charging of the growth manipulator and wafer can result if they are not grounded adequately. The electron beam evaporators situated around the base flange of the V90S MBE growth chamber are the source of these stray electrons. At lower growth temperatures such defects may persist and could provide a lower energy barrier for dislocation nucleation.

The intended linear compositional grading would be expected to promote a uniform distribution of misfit dislocations throughout the graded region. The 1 μm thick samples however do not appear to show such a distribution with the cross-sectional TEM images showing regions devoid of dislocations, Figure 4.7 (a). Thin regions of 1 μm structured samples prepared for cross-sectional TEM show a dense collection of misfits near the initial growth interface separated from a region of closely spaced misfits. Thicker regions appear to contain a more uniform distribution throughout, no doubt as a result of dislocations being superimposed, although a dense network remains visible at the initial growth interface. Both these situations are shown together at the extremes of Figure 4.8. These images indicate that the actual graded region is more akin to a layer of near uniform composition, followed by a rapid linear grade. The misfit networks of the 200 nm layer structures are too tightly confined to make this observation. High resolution EDS (or secondary ion mass spectroscopy, SIMS) could allow a direct determination of the true grading profiles for these samples and provide definitive corroboration.

A final interesting feature observed in the cross-sectional TEM of sample 75034 (15%, 775ºC, 1 μm) are the extremely long misfit dislocations pushed deep within the substrate, Figure 4.7(c). The modified Frank-Read mechanism is known to produce such features but surprisingly, dislocations of similar character were not observed in samples grown at either higher or lower temperatures. Portions of the

cross-sectional TEM images of 75034 (15%, 775ºC, 1 μm) do not show these misfits and look similar to the high and low temperature samples. It may therefore be coincidental that these features were observed in this case alone and such regions clearly may exist in the other samples.

EDS measurements confirm the achieved composition for all of the samples grown to be 15% ± 2% as intended.

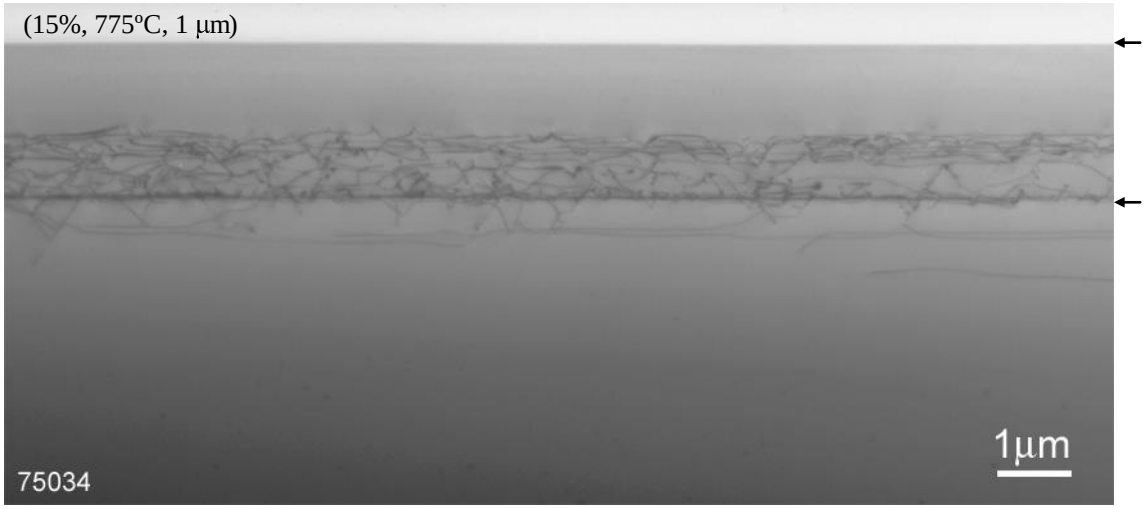

Figure 4.8 – Cross-sectional transmission electron micrographs (in the (220) two beam diffraction condition) of the 15% sample 75034. The surface of the epitaxial layer is near the top of the image (marked with the upper arrow) with the initial growth interface below (marked by the lower arrow).

4.3.2 25% Virtual Substrates

A collection of representative cross-sectional transmission electron micrographs are presented in Figure 4.9. The lower terrace of the 1 μm samples appear very similar to the 15% virtual substrates grown previously and the low levels of dislocation interaction visible between the two graded regions provides evidence that a high degree of relaxation has been maintained. Both the high and low temperature 1 μm samples appear to contain slightly longer misfits in the 15-25% graded region than in the 0-15% region, which is again expected for reasons given in

section 4.3.1. The pre-existing threading dislocations supplied by the lower layer seem to have enabled continuous strain relief with reduced misfit interaction.

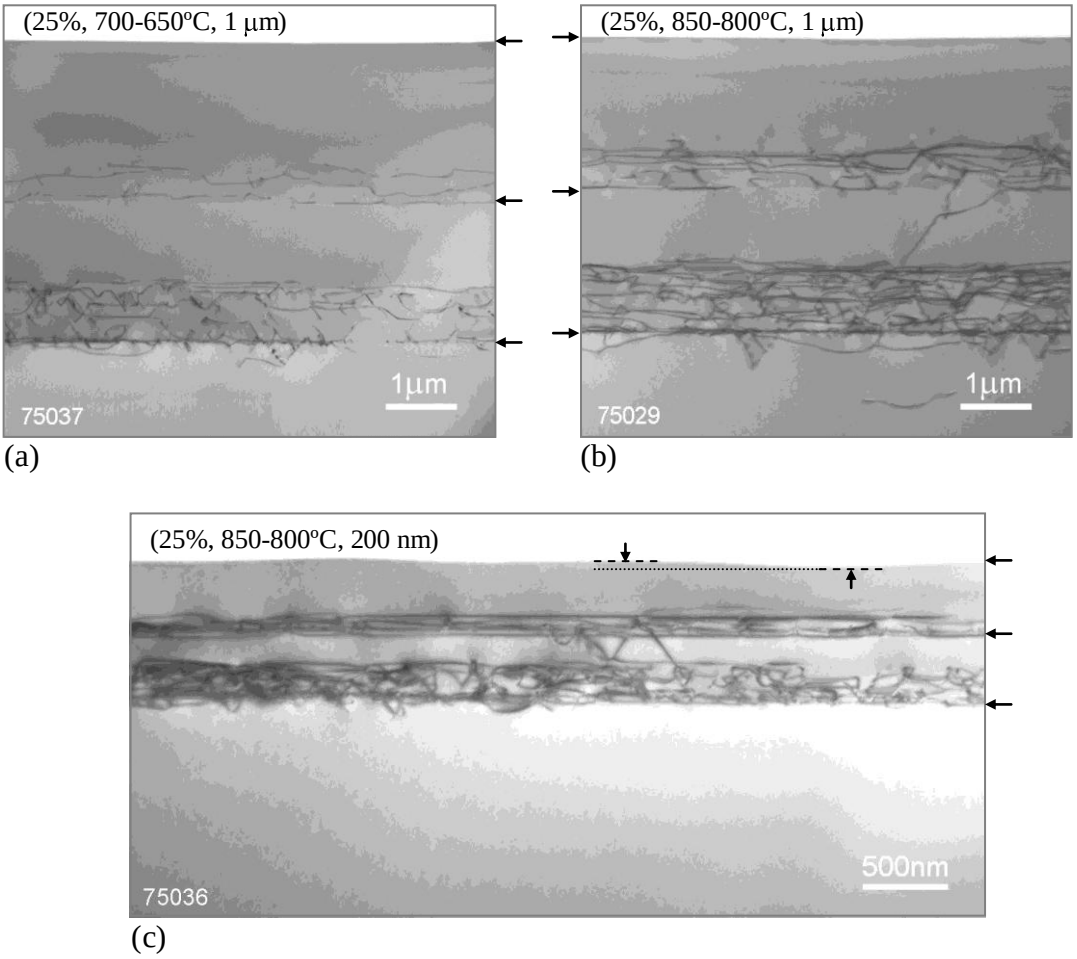

Figure 4.9 – Cross-sectional transmission electron micrographs (in the (220) two beam diffraction condition) of the 25% samples (a) 75037, (b) 75029 and (c) 75036. The surface of the epitaxial layer is near the top of the images (marked with the upper arrow) with the initial growth interface below (marked by the bottom arrow) and the top of the first constant composition layer in between (marked with the middle arrow).

The 200 nm terrace graded sample shows similar features in both dislocation network separation and increased misfit length in the top network to the 1 μm structured layers, Figure 4.9 (c). The length of misfits in the upper graded region in this sample are clearly far longer than in the underlying network, the difference likely

exaggerated as a result of the tighter lateral confinement of dislocations within the thinner graded regions.

Terrace grading allows most dislocations that had become blocked within a graded region to again glide, so that in the second graded region stress is relieved immediately and continuously with no urgent need for additional dislocation introduction. Fewer dislocations become blocked, and the misfits formed are far longer.

The surface of 75036 (25%, 850-800ºC, 200 nm) has visible surface undulations, Figure 4.9 (c), that have an amplitude of tens of nanometres (indicated in the image). This supports the observations made in section 4.2.2 (Nomarski interference images) of a transition toward 3-D growth, the result of elastic deformation of the surface to aid strain relief. The growth temperature of 800ºC is clearly too great for a terrace graded virtual substrate on this scale.

4.3.3 EDS Results for 25% Terrace Graded Structures

Compositional measurements made with EDS confirm that both high temperature terrace graded structures 75029 (25%, 850-800ºC, 1 μm) and 75036 (25%, 850-800ºC, 200 nm) have terrace compositions of 16% ± 2% and 26% ± 2%. The low temperature terrace graded sample 75037 (25%, 700-650ºC, 1 μm) has an initial terrace composition of 16% ± 2% but a final terrace composition of only 20% ± 2%. The data logged during growth indicates that additional power was supplied to maintain what the flux monitoring system recorded as a constant flux. It appears however that shadowing, as the silicon melt moved down into the charge, caused overcompensation in power and a dilution of the composition. It is important for this reason to maintain as flat a charge surface as possible.

4.4 High Resolution X-ray Diffraction

High resolution X-ray diffraction is a technique that allows a highly accurate determination of an epilayer composition as well as determination of the strain state. Both of these parameters are critically important in assessing layer quality and for comparison between similar structures. Two sets of omega (ω) - omega-2theta (ω–2θ) scans along a set of planes parallel to the (004) and (224) were obtained with 90º rotations in phi (Φ). Calculation of the terrace layer concentrations and relaxation for the 15% linear graded samples 75027 (700ºC), 75028 (850ºC) and the *25% terrace graded* sample 75029 (850ºC) with 1 μm layers are given in Table 4.3 and for the 15% samples 75022 (700ºC) and 75030 (850ºC) with 200 nm layers in Table 4.4.

	75027 15% (700°C, 1 μm)			75028 15% (850°C, 1 μm)			75029 25%, (850°C, 1 μm)		
	Comp. %	Relaxation %		Comp. %	Relaxation %		Comp. %	Relaxation %	
Terrace		Φ=0º	Φ=90º		Φ=0º	Φ=90º		Φ=0º	Φ=90º
0-15%	9	105	101	9	112	104	9	107	108
15%	16	93	89	16	94	90	16	100	98
25%	-	-	-	-	-	-	24	95	94

Table 4.3 – X-ray compositional and relaxation data for the 15% samples 75027, 75028 and 25% sample 75029. Compositional error ±0.5%, relaxation error ±5%. An inherently greater error exists for the Intermediate layer as no defined peak position exists.

The results in Table 4.3 and Table 4.4 are consistent with the compositional analysis provided using EDS and a trend of higher relaxation at greater thickness and higher growth temperature is evident. In addition to the substrate and layer peaks that were expected in the omega (ω) omega-2theta (ω–2θ) scans, an additional feature situated between the substrate and first layer peak was present for all of the low

composition samples investigated and is labelled *0-15% (Intermediate)* in Table 4.3 (and Table 4.4) as well as Figure 4.10. The presence of the broad peak corroborates the observations made using cross-sectional TEM that appeared to show that the initial graded region did not grade linearly as intended. The presence of a broad peak indicates that a region with a very shallow grading profile exists, such that it is almost of constant composition; the compositional value obtained is clearly an average.

	75022 15% (700ºC, 200 nm)			75030 15% (850ºC, 200 nm)		
	Comp. %	Relaxation %		Comp. %	Relaxation %	
Terrace		Φ=0º	Φ=90º		Φ=0º	Φ=90º
0-15% Intermediate	8	88	83	9	109	94
15%	16	58	53	16	69	62

Table 4.4 – X-ray compositional and relaxation data for the 15% samples 75022 and 75030. Compositional error ±0.5%, relaxation error ±5%. An inherently greater error exists for the Intermediate layer as no defined peak exists.

Comparison between 75027 (15%, 700ºC) and 75028 (15%, 850ºC), the 1 μm layer structures, show near equal relaxation despite a 150ºC difference in growth temperature. In this instance it would appear that the overlaying constant compositional layer is of sufficient thickness to have provided enough strain to relax the underlying material fully. This is not the case however for samples 75022 (15%, 700ºC) and 75030 (15%, 850ºC), the 200 nm layer structures, with a difference in relaxation of around 10% indicating that the growth temperature has had a greater impact. According to Matthews and Blakeslee (1974) the equilibrium critical thickness of material required for dislocation propagation at 15% is around

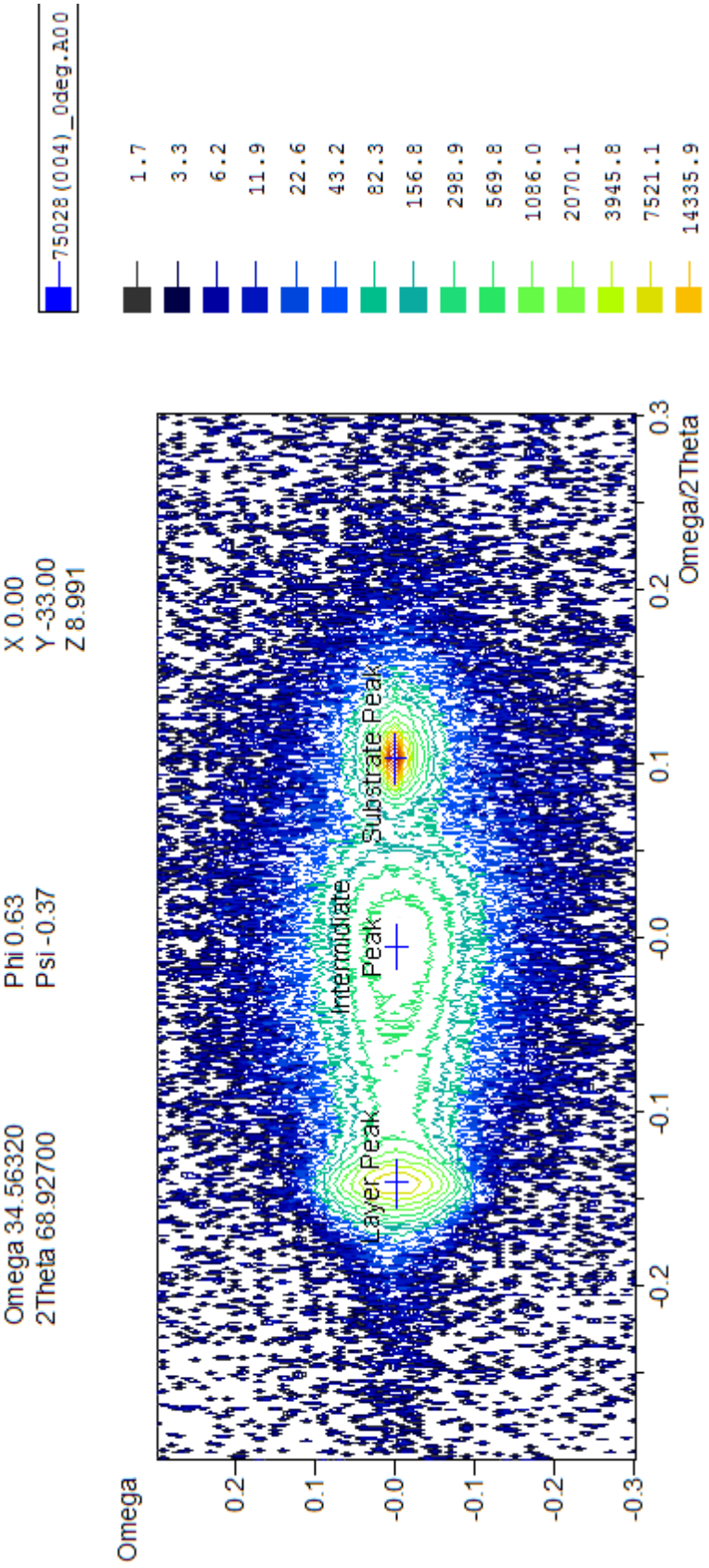

Figure 4.10 – Omega (ω) omega-2theta (ω–2θ) scan in the 004 direction from sample 75028

200 nm (at 10% this roughly doubles). As these layers would have only just exceeded this equilibrium critical thickness, dislocation propagation is only possible provided sufficient thermal energy is available (could be metastable). These results in particular strongly suggest that in the work of Capewell (2002) *even with in-situ annealing fuller relaxation of lower layers would have occurred only after additional layer growth*. The theoretical predictions of People and Bean (1985) (Figure 2.5) for lower temperature growth make this result even more surprising as the critical thickness for dislocation introduction for a 15% constant compositional layer is stated as around 400 nm! Clearly relaxation has occurred as a result of the growth temperatures utilised and perhaps has been enhanced by the presence of heterogeneous nucleation sources such as carbon precipitates at the initial growth surface. The presence of carbon precipitates on the surface of wafers that have not undergone *ex-situ* cleaning has been observed previously in pseudomorphic strained layers where it leads to so called *pagoda defects* (Dynna *et al.* 1992). Such contamination may also be visible in the cross-sectional analysis of medium compositional layers (discussed in length in Chapter 5).

Comparison between samples 75028 (15%, 850ºC, 1 μm) and 75029 (25%, 850-800ºC, 1 μm) that share an identical lower terrace highlights the effect of the continued compositional increase. The 15% terrace has been further relaxed by the addition of the overlying layers, whilst the new terminating layer is again 95% relaxed. Although further relaxation may be possible simply through raised growth temperature or prolonged annealing, the addition of an over-graded layer (higher composition than finally required) will ultimately be necessary to achieve 100% relaxation. Finally a point that will be properly discussed later with reference to the medium compositional regime is the noticeable difference in relaxation between

phi (Φ) orientations. Although the uncertainty in the determined relaxation is comparable to the differences observed, a small but systematic trend in relaxation appears present.

Table 4.5 and Table 4.6 show the angles determined between the (004) planes in the constant compositional layer and the (004) planes within the silicon substrate.

	75027 15% (700°C, 1 μm)		75028 15% (850°C, 1 μm)		75029 25% (850°C, 1 μm)	
	Angle between Substrate and layer		Angle between Substrate and layer		Angle between Substrate and layer	
Terrace	**[004] Φ=0°**	**[004] Φ=90°**	**[004] Φ=0°**	**[004] Φ=90°**	**[004] Φ=0°**	**[004] Φ=90°**
15%	**0.04**	**-0.10**	**0.00**	**0.00**	**-0.04**	**0.01**
25%	**-**	**-**	**-**	**-**	**-0.04**	**0.01**

Table 4.5 – Data collected of angular separation (in degrees) in omega between (004) planes in the silicon substrate and constant compositional layer for the 15% samples 75027, 75028 and 25% sample 75029. The error in determination of the angular separation ± 0.01°.

	75022 15% (700°C, 200 nm)		75030 15% (850°C, 200 nm)	
	Angle between Substrate and layer		Angle between Substrate and layer	
Terrace	**[004] Φ=0°**	**[004] Φ=90°**	**[004] Φ=0°**	**[004] Φ=90°**
15%	**0.00**	**0.01**	**0.06**	**-0.11**

Table 4.6 – Data collected of angular separation (in degrees) in omega between (004) planes in the silicon substrate and constant compositional layer for the 15% samples 75022 and 75030. The error in determination of the angular separation ± 0.01°.

A substantial deviation in omega between some epitaxial layers and the silicon substrate on which they were grown is evident. This is an indication that in some of these samples the growth front is re-orientating as observed by LeGoues *et al.* (1993). It must however be kept in mind that these angles have been calculated between the *marked layer peak positions* and the *marked silicon peak position*, which themselves contain uncertainties of the same order.

4.5 Atomic Force Microscopy (AFM)

A selection of six 15% and 25% samples have been investigated using atomic force microscopy to obtain quantitative surface roughness data and to further examine some of the unusual surface features seen in the optical Nomarski interference images. Contact mode atomic force measurements were conducted for the 15% samples 75022 (700ºC, 200 nm), 75030 (850ºC, 200 nm), 75027 (700ºC, 1 μm) and 75028 (850ºC, 1 μm) along with the 25% samples 75037 (700-650ºC, 1 μm) and 75029 (850-800ºC, 1 μm). A summary of surface roughness and height range measurements made from 40 μm^2 scans are given in Table 4.7 and Table 4.8.

	75022 15% (700ºC, 200 nm)	75030 15% (850ºC, 200 nm)	75027 15% (700ºC, 1 μm)	75028 15% (850ºC, 1 μm)
RMS Roughness	**2.1 nm ±0.4 nm**	**4.2 nm ±0.4 nm**	**1.6 nm ±0.1 nm**	**5.1 nm ±0.9 nm**
Height Range	**15 nm ±2 nm**	**31 nm ±2 nm**	**12 nm ±2 nm**	**32 nm ±4 nm**

Table 4.7 – RMS surface roughness and height range measurements determined from AFM images of the 15% samples 75022, 75030, 75027 and 75028.

	75037 25% (700-650ºC, 1 μm)	75029 25% (850-800ºC, 1 μm)	Silicon epitaxy control
RMS Roughness	**1.4 nm ±0.3 nm**	**7 nm ±1 nm**	**-**
Height Range	**14 nm ±1 nm**	**44 nm ±6 nm**	**-**

Table 4.8 – RMS surface roughness and height measurements determined from AFM images of the 25% samples 75037 and 75029.

Higher growth temperatures appear to result in increased surface roughness and overall height range and are most likely a result of the greater adatom mobility provided by the additional thermal energy (discussed in more detail in section 4.2.). It also appears however, that surface roughness does not dramatically increase with composition in this regime when growing with reducing temperatures and utilising

terrace grading, this is important (though for 75037 (25%, 700-650ºC, 1 μm) the composition is known from EDS to be only 20% in section 4.3.3). The RMS roughness of the 1 μm layer structures is far greater than was expected for such a grading rate, especially compared to an RMS roughness of only 1.7 nm for a comparable fully relaxed $Si_{0.65}Ge_{0.35}$ virtual substrate reported by Rosenblad *et al.* (2000).

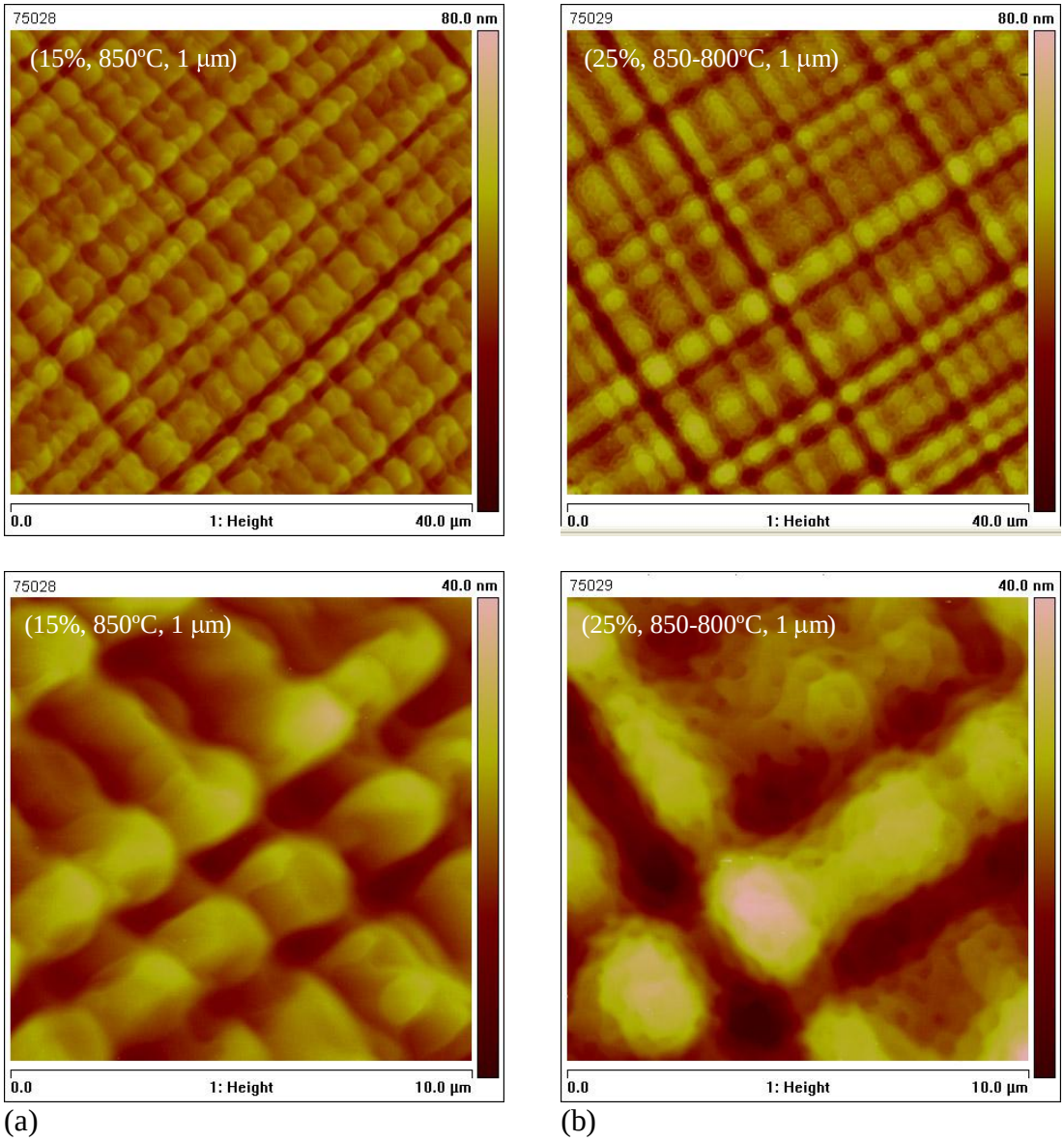

(a) (b)

Figure 4.11 – 40 μm x 40 μm and 10 μm x 10 μm area atomic force height profile scans for (a) 75028 and (b) 75029.

Atomic force micrographs of 75028 (15%, 850ºC, 1 μm) Figure 4.11 (a) and (c) reinforce the Nomarski interference images that appeared to show large, apparently flat topped, islands along the hatches with features around 2 μm x 2 μm in size. These features appear stepped (highlighted in Figure 4.12), overlaying one another but in only one direction, with step heights in the region of 5-10 nm over a length scale of ~2.5 μm, whilst the orthogonal direction appears to show no significant net rise.

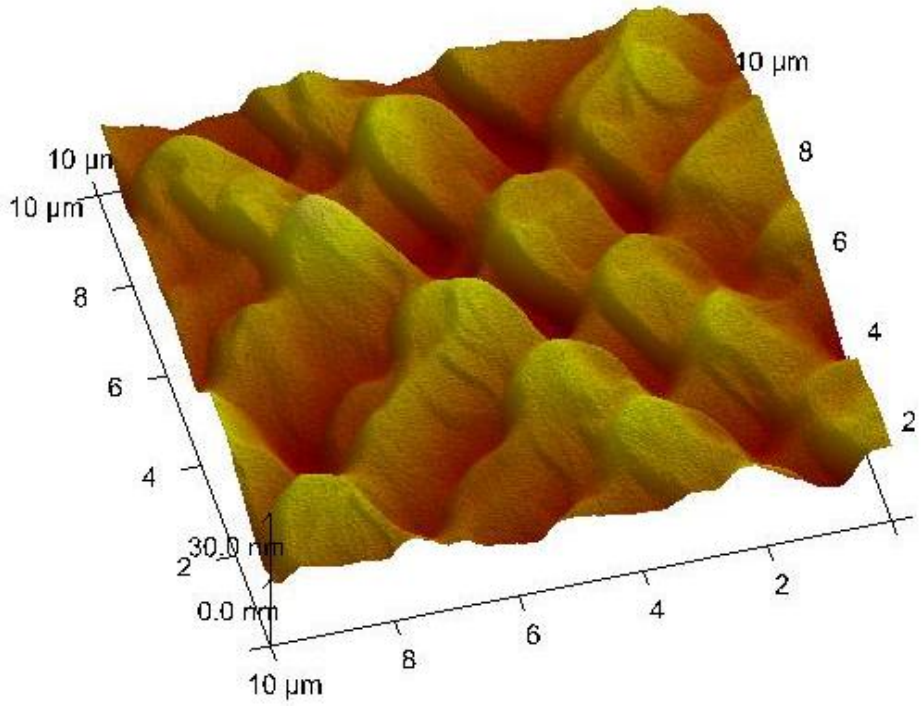

Figure 4.12 – A 3-dimensional presentation of a 10 μm x 10 μm area atomic force height profile scan for sample 75028 (15%, 850ºC, 1 μm) highlighting the apparent tilt in only one direction.

Individual atomic steps are far smaller than seen in Figure 4.12, only 2.715 Å (Kim *et al.* 1997), but if imagined bunched together then a 4 inch wafer with 5 nm steps, each consisting of around 9 atomic steps, every 2.5 μm would give rise to a macroscopic tilt of around 0.1º. The offcut measured from similar wafers detailed in later chapters is around this order suggesting this as a possible explanation for the apparent surface

asymmetry. Similar features can be seen on 75029 (25%, 850-800ºC, 1 μm) but all of the features appear rounded and now overlap, usually over far shorter distances, with the features being up to ~5 μm in length, Figure 4.11(b) and (d). The macroscopic cross-hatch density appears to have changed little between 75028 (15%, 850ºC, 1 μm) and 75029 (25%, 850-800ºC, 1 μm) (not shown).

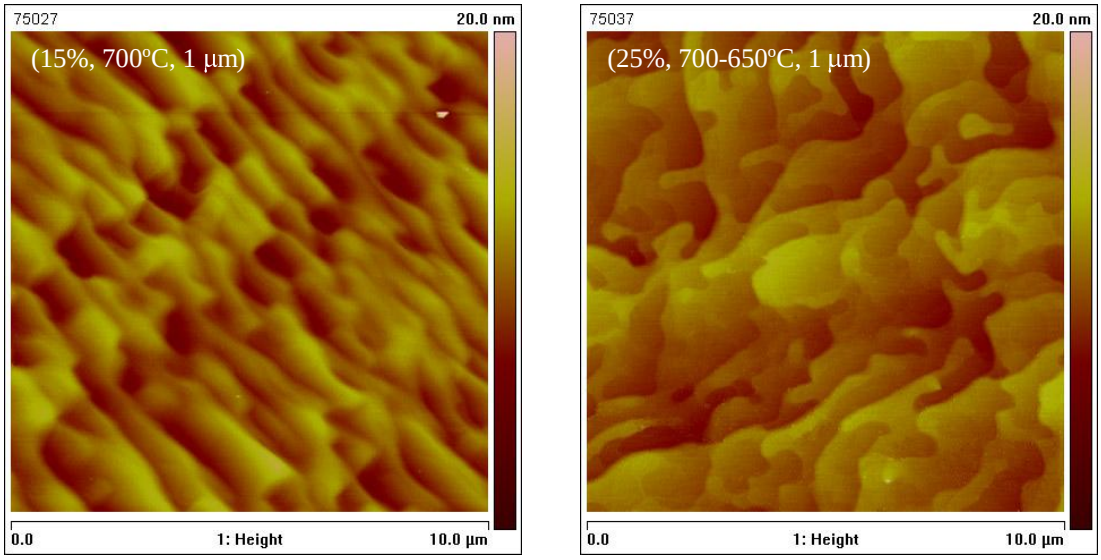

(a) (b)

Figure 4.13 – 10 μm x 10 μm area atomic force height profile scans for (a) 75027 (b) 75037.

The surface of 75027 (15%, 700ºC, 1 μm) shows only faint evidence of cross-hatch with spacing around 10 μm apart and many long thin terrace like features observed at higher magnification Figure 4.13(a). In comparison 75037 (25%, 700-650ºC, 1 μm), the equivalent 25% structure, shows an evolution toward far larger terrace structures at higher magnification, Figure 4.13(b), but shows more obvious cross-hatch at lower magnifications spaced around 5 μm apart (not shown).

Both 200 nm layer structured samples 75022 (15%, 700ºC) and 75030 (15%, 850ºC) show a more usual cross-hatched pattern, clearly having an increased trench to peak depth and an increased frequency of undulation at higher growth temperature,

Figure 4.14. The increased undulation depth and frequency are almost certainly the result of greater relaxation and X-ray results confirm a difference in relaxation of 10% between the pair.

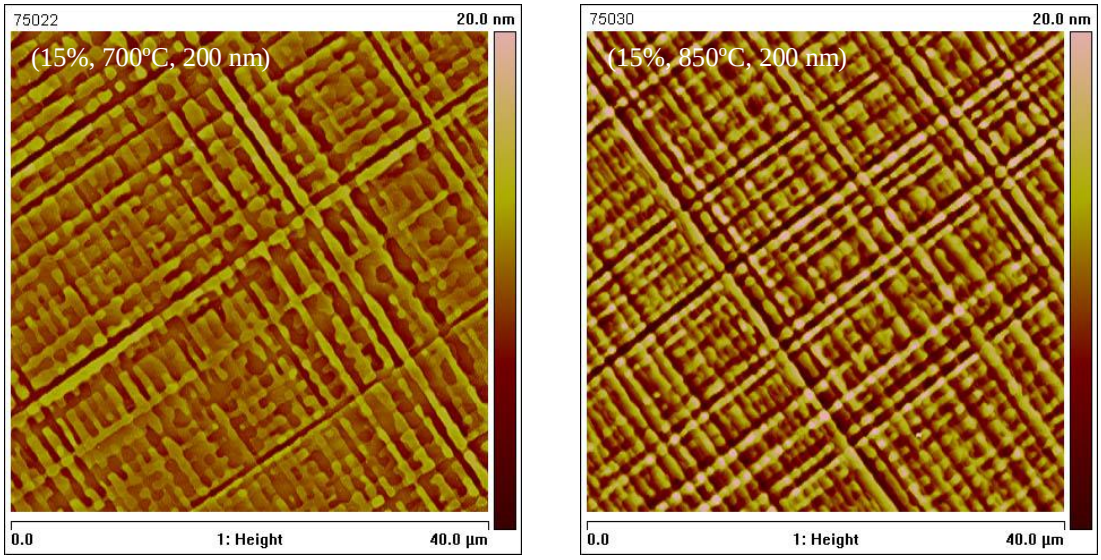

(a) (b)

Figure 4.14 – 40 µm x 40 µm area atomic force height profile scans for (a) 75022 (b) 75030

4.6 Schimmel Defect Etching

Comparison of the surface threading dislocation density is important to gauge the structural quality of layers in relation to one another. The detection of *threading dislocation pile-up is of particular importance* with regards to both surface morphology (Fitzgerald *et al.* 1997) and the detrimental influence on performance (Giovane *et al.* 2001). Standard Schimmel etching (section 3.4) was employed in defect revealing by etch pit formation (an example is given in Figure 4.15) for each of the 15% 1 µm layer structures (75027, 75034 and 75028) and a compilation of results is given in Table 4.9. A modified Schimmel etch was utilised when etching the 15% 200 nm layer structures, to provide an enhanced etch pit revealing rate (Table 4.9).

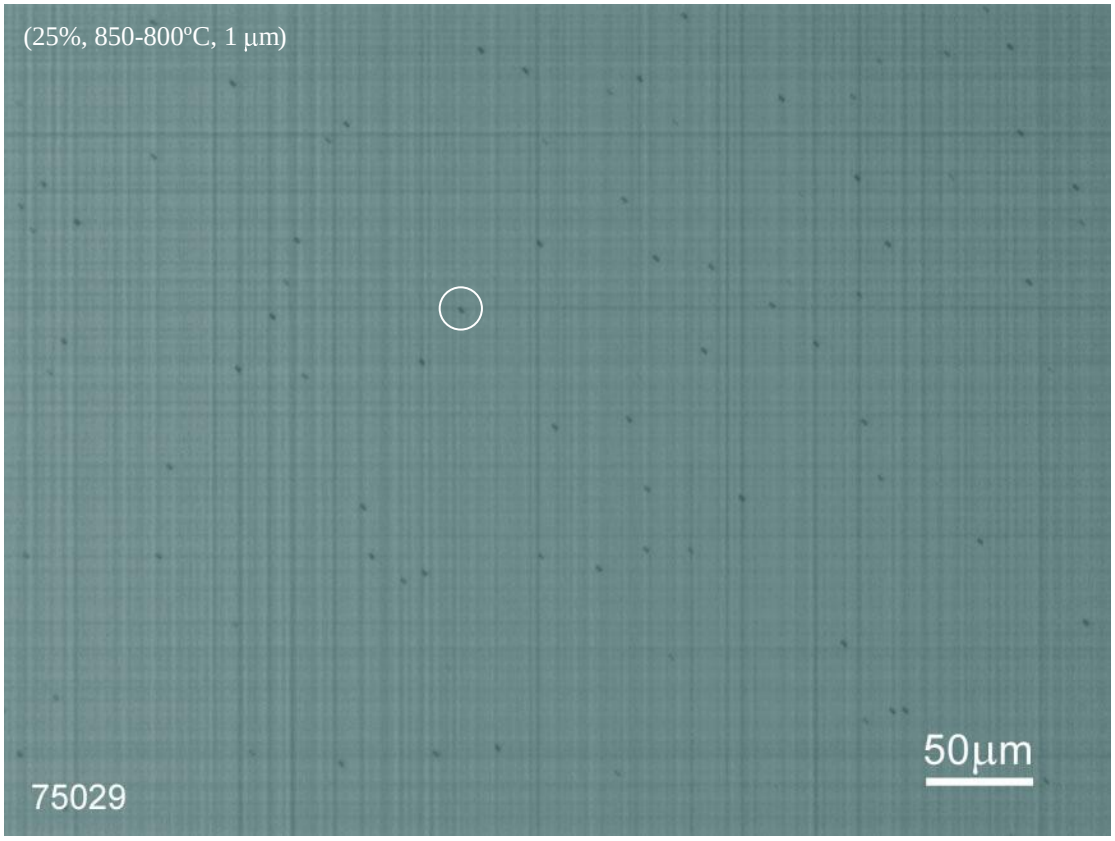

Figure 4.15 – Optical micrograph of defect etched sample 75029. The image was taken in the bright field without interference contrast at x10 magnification. A surface threading dislocation density of approximately $4x10^4/cm^2$ is revealed by etch pit counting. A circle highlights an etch pit for clarity.

A wide separation of threading dislocation densities is evident between the 15% 1 μm layer structured samples in Table 4.9. Interestingly the surface threading density does not increase sequentially with increasing growth temperature but peaks for the sample grown at an intermediate temperature. The expected trend would be for increasing threading dislocation density at lower growth temperatures (Fitzgerald *et al.* 1997) suggesting that perhaps a mechanism for surface threading dislocation annihilation is present at lower temperature. Alternatively an increased threading dislocation density at a particular composition could be an indication of a greater level of relaxation or an increase of dislocation pinning.

	75027 15% (700°C, 1 μm)	75034 15% (775°C, 1 μm)	75028 15% (850°C, 1 μm)	75030 15% (850°C, 200 nm)
Threading Density (/cm^2)	**5.3x10^2**	**7.3x10^4**	**6.5x10^3**	**1.7x10^3**
Standard Deviation (/cm^2)	**4.2x10^2**	**5.2x10^3**	**8.3x10^2**	**1.3x10^3**

Table 4.9 – Table containing threading dislocation densities for 15% 1 μm layer structured samples 75027, 75034 and 75028 and 200 nm layered structure 75030, calculated by counting surface etch pits, accompanied by standard deviations. Standard Schimmel etching was employed for the 1 μm thick samples whilst the modified Schimmel etch was utilised for the 200 nm sample.

A number of discrete threading dislocations were observed along a line in one of the <110> directions on the surface of 75028 (15%, 850ºC, 1 μm) (Figure 4.16), presumably halted by the presence of an underlying misfit pile-up due to dislocation multiplication as described in section 2.3.7.2. Such low levels of pinning will have little impact on the performance of devices processed on the surface and is debatable whether the label of threading dislocation *pile-up* is even appropriate, hence the new label *pseudo pile-up*.

It should be clearly noted again at this point that threading defect densities quoted below about 2x10^3/cm^2 should be treated with caution as this constitutes only *4 etch pits* within an image at x10 magnification. Confusion at this level with surface particulate contamination is possible and is difficult to preclude.

Table 4.9 shows that 75030 (15%) a 200 nm layer structured sample grown at 850ºC has a very low threading density when compared to 75028 (15%, 850ºC) the comparable 1 μm structure. A reasonable expectation would be to have found a higher threading dislocation density containing many clear instances of threading dislocation pile-up as a result of the tighter lateral confinement of the dislocation network. The low number of etch pits visible at the surface suggests that a lower level of relaxation has been achieved, with X-ray results confirming that the layer remains

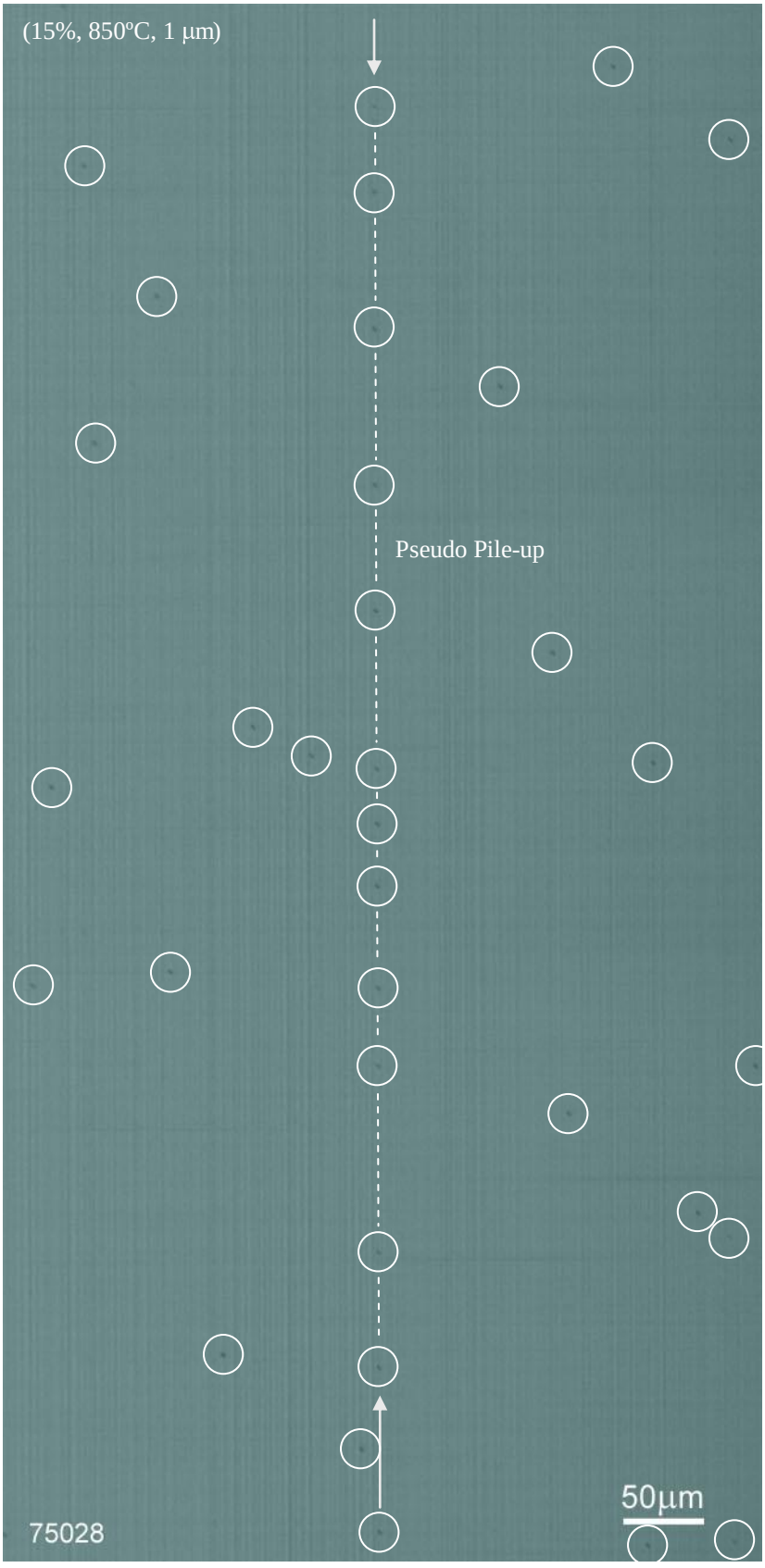

Figure 4.16 – Optical micrograph of the surface of sample 75028 (15%, 850ºC, 1 μm) after etching with a standard Schimmel etchant for 2 minutes. The arrows indicate the pseudo pile-up with low threading dislocation density and the circles highlight etch pits for clarity.

substantially strained with a relaxation of only 70%.

Standard Schimmel etching was again employed in defect revealing by etch pit formation for the 25% 1 μm layer structures 75037 (700-650ºC) and 75029 (850-800ºC) with the results given in Table 4.10.

	75037 20% (700°C, 1 μm)	75029 25% (850°C, 1 μm)
Threading Density (/cm^2)	1.5x10^3	4.1x10^4
Standard Deviation (/cm^2)	1.0x10^3	3.8x10^3

Table 4.10 – Table containing threading dislocation densities for 25% 1 μm layer structured samples 75037 (only 20% composition measured) and 75029. Densities calculated by counting surface etch pits, accompanied by standard deviations. The standard Schimmel etch was employed.

Comparison between Table 4.10 and Table 4.9 demonstrates that the dislocation density has increased with increasing germanium composition. The *increase in surface threading dislocation density by almost an order of magnitude* is very significant. The addition of a second terrace grade with the same or lower misfit difference than the first, with respect to the layer immediately below, should not result in an increase in threading dislocation density if the first layer had achieved a high degree of relaxation and the second layer is grown at an equivalent temperature. Clearly this is not the case suggesting either: increasing threading dislocation pinning which terrace grading aims to minimise; too large a reduction in growth temperature with composition; large amounts of dislocation annihilation has occurred; or insufficient relaxation of the lower layer (known to be around 94%). Interestingly the higher surface threading density generally displayed at higher growth temperatures is

the opposite of that found by Leitz *et al.* (2001) albeit for higher composition layers and Fitzgerald *et al.* (1997) mentioned previously in this section.

No instances of conventional pile-up have been observed at any point when etching the low composition samples.

4.7 Summary

The work in this chapter is distinguished not only for the low compositions investigated but also for not having full control of the germanium composition profile. Evidence from cross-sectional TEM and X-ray analysis appear to indicate that an initially sharp jump in composition was followed subsequently by a slow rise up to the desired composition rather than the intended linear grade. The unusual surface morphologies displayed by structures such as 75028 (15%, 850ºC, 1 μm) and 75029 (25%, 850-800ºC, 1 μm) in particular, is almost certainly the result of this initial grading. Improper calibration of either the silicon or germanium electron beam evaporators is responsible for this unintended profile and in future particular *care must be taken with regards to calibration of low flux rates (<0.05Å/s) as these have a large impact upon the initial grading profiles*.

High levels of relaxation have been achieved within the 1 μm layer structures starting growth at either 850ºC or 700ºC. Growth starting at 850ºC and descending to 800ºC at 25% is however clearly unsuitable for 200 nm layer structures were the build up of strain occurs too quickly to be relieved solely by introduction and extension of misfit dislocations resulting in 3-D growth. The surface roughness of the present samples is far greater than other leading published examples due again I believe to the unconventional grading and subsequent surface morphology. *A trend of increased*

surface roughness at higher temperature makes lower temperature growth preferable if it remains evident that there is no real gain in relaxation.

The dislocation density present within the higher temperature 15% 1 μm structure 75028 (15%, 850ºC, 1 μm) shows a threading dislocation density of only $6.5x10^3/cm^2$ that is lower than the best published linearly graded virtual substrate of Olsen *et al.* (2003) at $2x10^4/cm^2$ and compares favourably with other more exotic approaches. Significantly *defect etching suggests that threading dislocation density is reduced at a lower growth temperature of 700ºC* in contradiction to findings made using CVD growth systems (Fitzgerald *et al.* 1997; Leitz *et al.* 2001). A possible explanation could be that ion bombardment from the electron evaporators lead to an increased concentration of point defects within the grown material that upon annealing allowed a substantial annihilation of the threading dislocations to occur, though no work has yet been carried out to validate this claim.

The rise in threading dislocation density to $4.1x10^4/cm^2$ in the 25% terrace graded substrate 75029 (25%, 850-800ºC, 1 μm) is unexpected. Although a rise in surface threading dislocation density has been observed with increasing composition by Leitz *et al.* (2001) such a rise was due to excessive threading dislocation pile-up that is not event in this case. The pseudo pile-up highlighted in sample 75028 (15%, 850ºC, 1 μm) demonstrates that low levels of threading dislocations can become trapped within the space of one terrace grade and may indicate that a smaller compositional step would be beneficial. The possibility also remains that the reduction of growth temperature accompanying the compositional increase is too great and will be discussed in further detail in chapter 6.

Chapter 5

5 Medium Composition Regime (30-40%)

Virtual substrates in the medium composition regime (30-40%) are primarily of use in gaining a significant enhancement in the hole mobility in strained-silicon surface channel MOSFET devices. Oberhüber *et al*. (1998) theoretically predicted that little additional enhancement in the hole mobility is achieved in a strained silicon layer above a germanium concentration of 40% (Figure 4.1). Virtual substrates in this regime offer the potential of a future platform for advanced silicon based devices including strained-SOI. However for a relaxed virtual substrate composition of 40% the critical thickness for a strained-silicon channel is reduced to ~6 nm and may be too thin to form practical devices (Nicholas 2004). As was true in the previous chapter a key aim of producing high quality terrace graded virtual substrates in the medium composition regime is to provide a platform for further compositional increase towards pure germanium, discussed in chapter 6.

With traditional linear grading, threading dislocation densities as low as $3x10^4/cm^2$ have been achieved at 35% germanium with a surface RMS roughness of only 1.7 nm (Rosenblad *et al.* 2000), although no information on dislocation pile-up is given. Similarly, Leitz *et al.* (2001) have shown a 30% linearly graded buffer with a field threading density of $9.3x10^4/cm^2$ and a surface RMS roughness *around 10 nm* but, interestingly, a comparable density of dislocations were said to additionally be trapped in dislocation pile-ups. More exotic approaches such as step grading with high and low temperature steps followed by annealing after each layer have been published with threading densities in the $10^4/cm^2$ range at 30% (Gaiduk *et al.* 2000). Finally, of interest is the work of Kissinger *et al.* (1995) who have demonstrated that

high temperature annealing at 1050ºC for a period of 1 hour after step graded layers with 5% compositional steps can yield dramatic reductions in threading dislocation density, achieving between 10^2-10^3/cm^2 at ≤ 20%, although nothing was reported on surface roughness (appeared high in their cross-sectional TEM). The stepwise nature of this structure would likely not suffer the pile-up of traditional graded structures as intended for terrace grading and as such the effect of extended periods of high temperature *ex-situ* annealing shall be investigated in this current composition regime.

Presented in this chapter are a number of 30% and 40% terrace graded virtual substrates *all with graded and linear regions of 1 μm in thickness*. It seems certain that the grading profiles in the 15% and 25% layers were not as intended and recalibration of the germanium electron beam evaporator was conducted. This resulted in a straight rather than curved flux rate vs. power graph. A lower grading rate of 10%/μm is applied to all of the structures investigated in this medium composition range.

5.1 Growth Parameters

5.1.1 30% Terrace Graded Substrates with *In-Situ* Annealing

The initial 30% virtual substrates are similar in design to those layers previously investigated, utilising a constant growth temperature throughout each terrace grade followed by annealing and with a sequential 50ºC reduction for each terrace grade, designated 75046 (30%, 850-750ºC, *In-situ* Anneal) and 75048 (30%, 700-600ºC, *In-situ* Anneal), see Figure 5.1. An intermediate structure, 75049 (30%, 850-650ºC Ramping, *In-situ* Anneal), with growth beginning at 850ºC and an initial 100ºC temperature ramp down over the latter half of the constant compositional layer,

is introduced to evaluate the possible benefits of temperature grading. Growth of the next terrace begins at a temperature 50ºC above that at which the previous terrace had ended, see Figure 5.2.

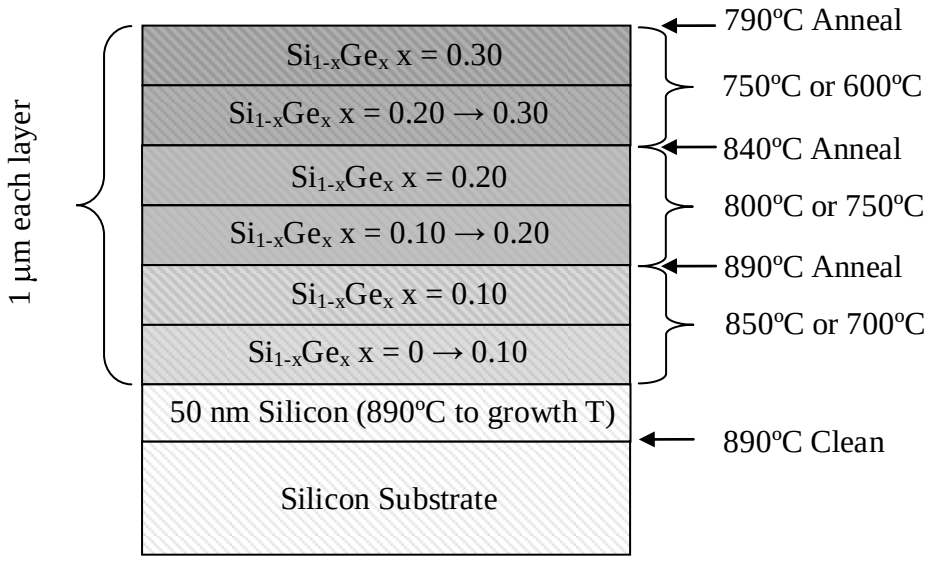

Figure 5.1 – Schematic representation of 30% virtual substrate specifications for 75046 (30%, 850-750ºC, *In-situ* Anneal) high temperature and 75048 (30%, 700-600ºC, *In-situ* Anneal) low temperature.

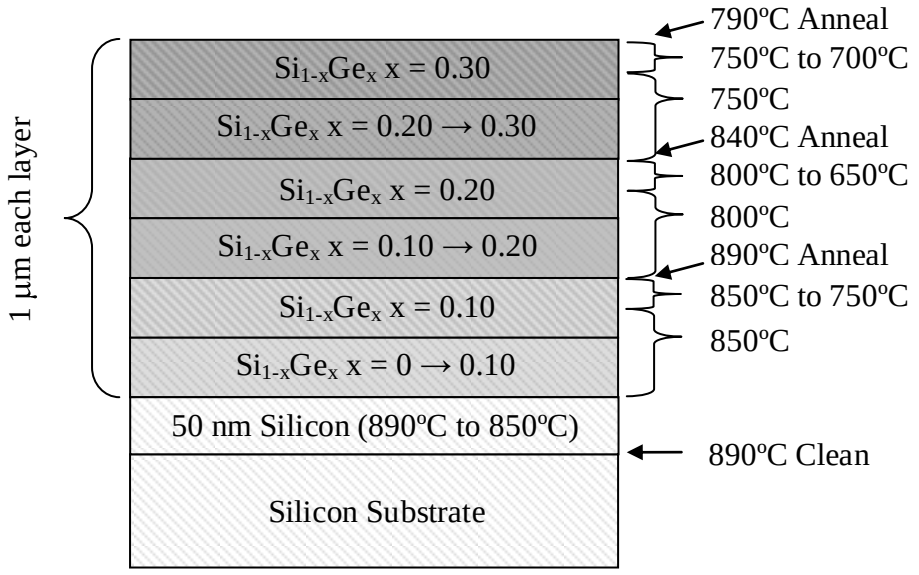

Figure 5.2 – Schematic representation of 30% virtual substrate specifications for 75049 (30%, 850-650ºC Ramping, *In-situ* Anneal) intermediate temperature.

5.1.2 30% Terrace Graded Substrates without *In-Situ* Annealing

A number of layers were grown without the inclusion of any growth interruptions or annealing to maintain the highest quality of material. Sample 75044 (30%, 800-725ºC Ramping, No Anneal) had the growth temperature held constant throughout each graded region. Initially grown at a temperature of 800ºC and then reduced by 25ºC during each constant composition layer, Figure 5.3.

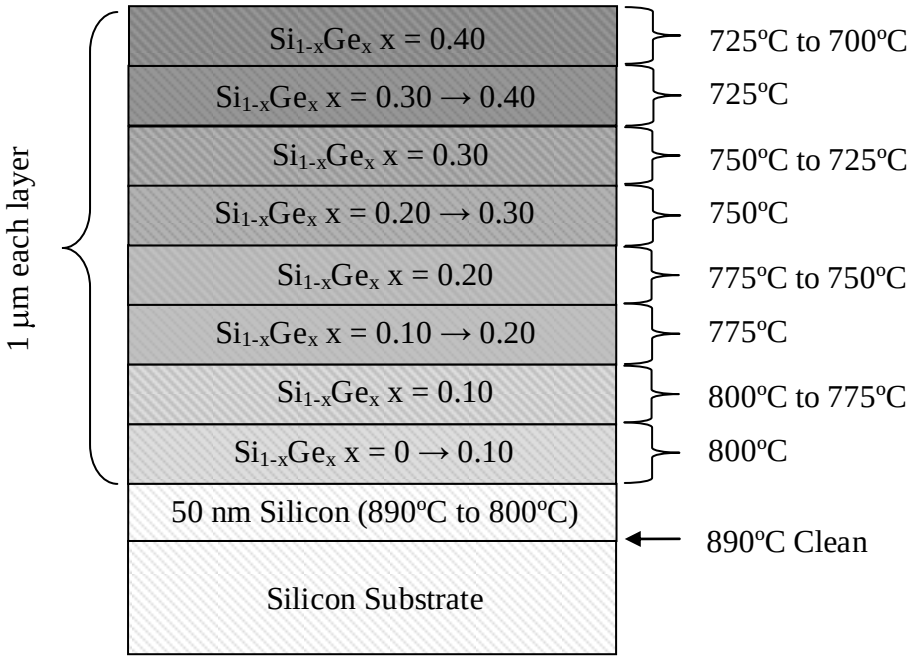

Figure 5.3 – Schematic representation of virtual substrate specifications for 75044 (30%, 800-725ºC Ramping, No Anneal) and 75043 (40%, 800-700ºC Ramping, No Anneal).

A further layer structure 75055 (30%, 825-725ºC Ramping, No Anneal) having an initial growth temperature of 825ºC is dropped 50ºC over the second half of the first constant composition layer; subsequently this drop is reduced to only 25ºC, see Figure 5.4. Additionally silicon marker layers have been included to gauge the impact on layer growth and additionally highlight any layer roughening that might occur.

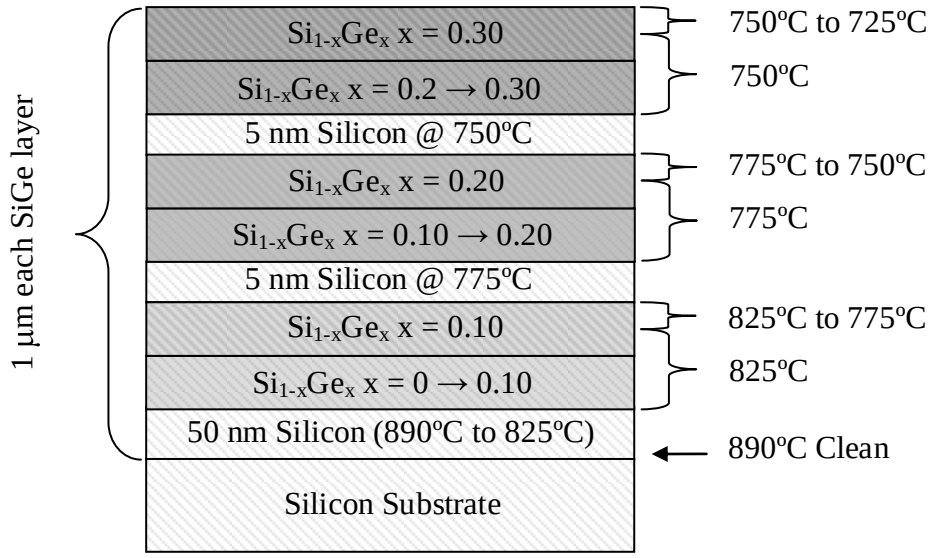

Figure 5.4 – Schematic representation of 30% virtual substrate specifications for 75055 (30%, 825-725ºC Ramping, No Anneal).

5.1.3 40% Terrace Graded Substrates without *In-Situ* Annealing

A single 40% virtual substrate 75043 (40%, 800-700ºC Ramping, No Anneal) was grown with an underlying structure identical to 75044 (30%, 800-725ºC Ramping, No Anneal) with the addition of a 40% terrace grade on top, see Figure 5.3.

5.1.4 30% Linear Graded Substrate with *In-Situ* Annealing

For fair comparison with a traditional linear graded structure a single 30% structure 76007 (30%, Linearly Graded, 850-750ºC, *In-situ* Anneal) was grown. The layer thickness, growth temperatures and anneals were chosen to be identical to those used for 75046 (30%, 850-750ºC, *In-situ* Anneal), differing only in the layer order, shown schematically in Figure 5.5.

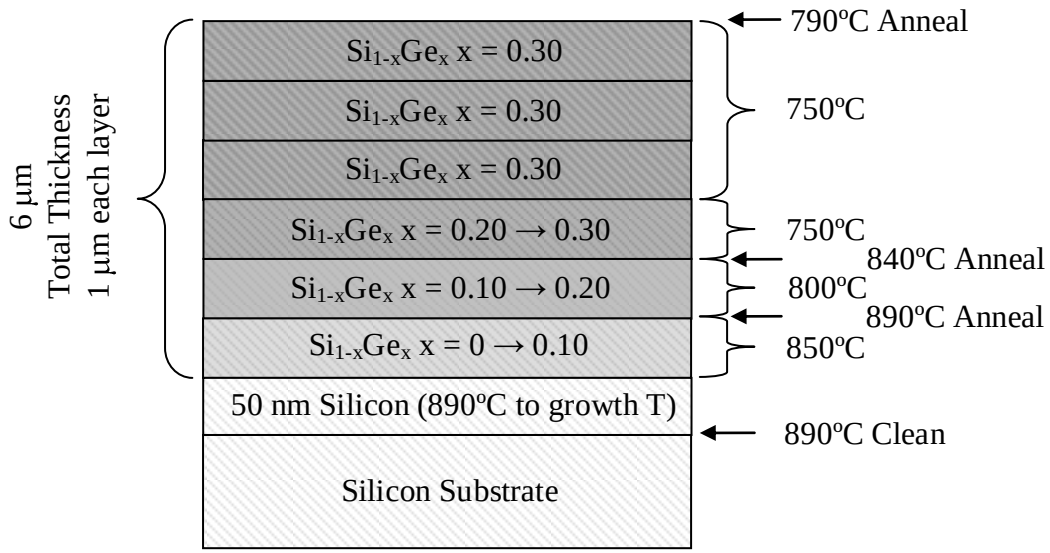

Figure 5.5 – Schematic representation of 30% virtual substrate specifications for a linear graded comparison 76007 (30%, Linearly Graded, 850-750ºC, *In-situ* Anneal).

5.2 Nomarski Interference Images

A selection of representative interference images are presented in Figure 5.6. All of the 30% samples appear to share surfaces of similar morphology, with only small differences in surface contrast and cross-hatch spacing. Most noticeably the sample grown at the lowest temperature 75048 (30%, 700-600ºC, *In-situ* Anneal), displays the least visible surface contrast, most likely indicating this to be the smoothest surface as was expected. Despite the sizable reduction of growth temperature over the later half of the constant composition layer, the surface of 75049 (30%, 850-650ºC Ramping, *In-situ* Anneal) remains very similar in appearance to 75046 (30%, 850-750ºC, *In-situ* Anneal). In examining these samples the quantitative limitations of this technique are apparent.

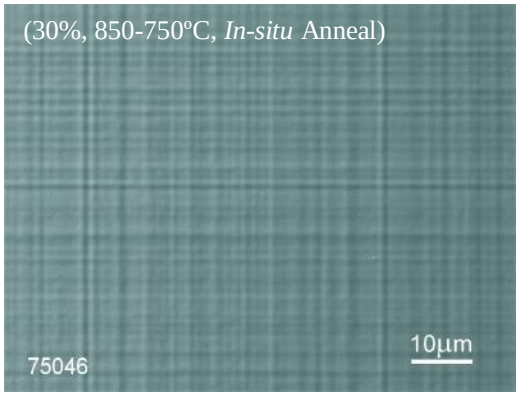

(a)

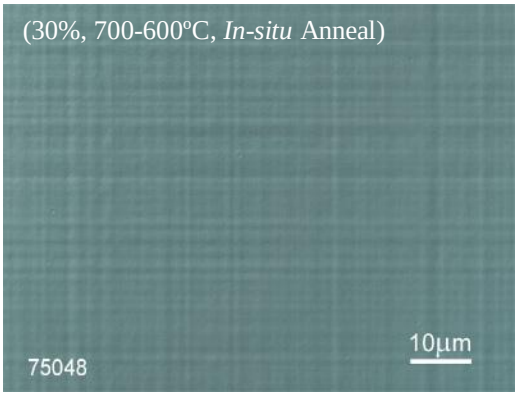

(b)

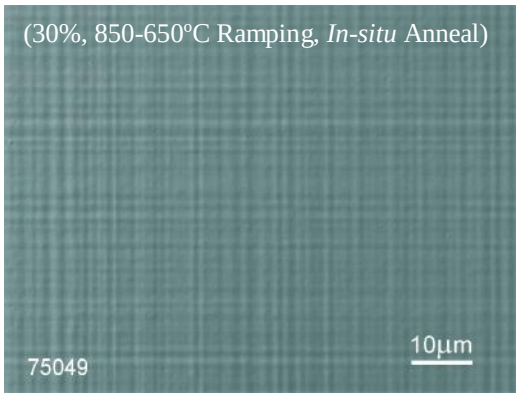

(c)

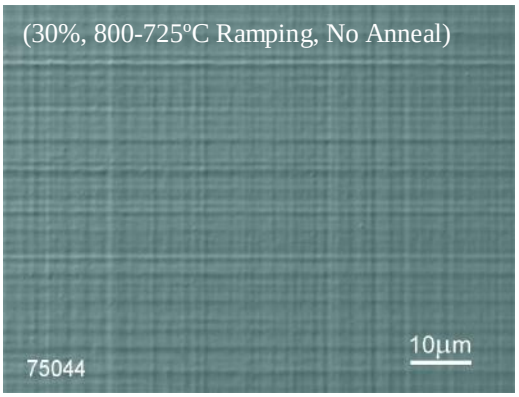

(d)

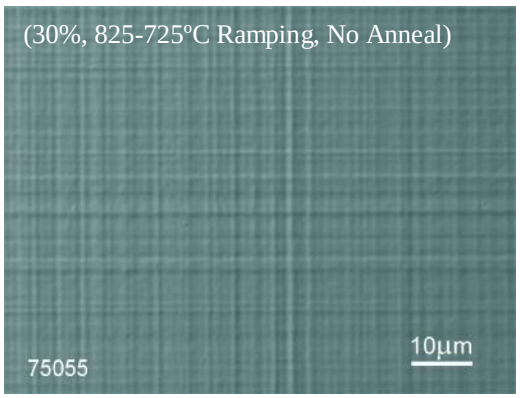

(e)

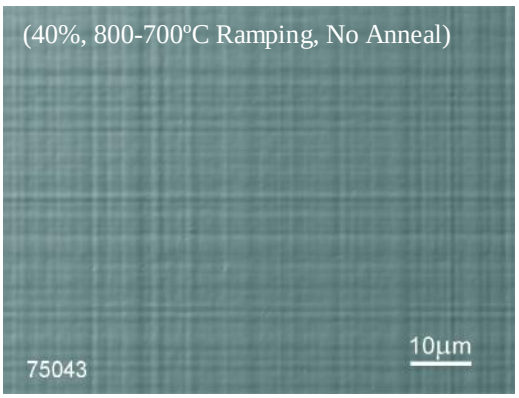

(f)

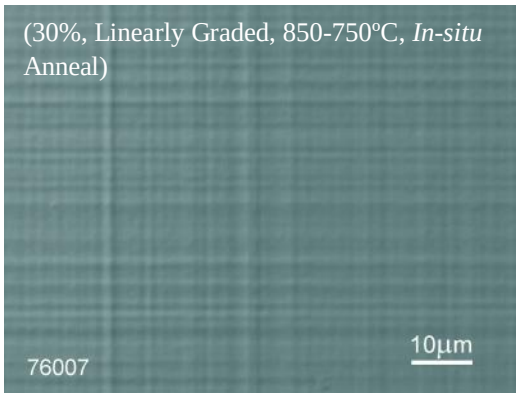

(g)

Figure 5.6 – Nomarski interference images taken at x50 magnification of samples (a) 75046, (b) 75048, (c) 75049, (d) 75044, (e) 75055, (f) 75043 and (g) 76007

The 30% linear graded comparison 76007 (850-750ºC, *In-situ* Anneal) shows a very similar contrast level to 75046 (30%, 850-750ºC, *In-situ* Anneal) its terrace graded counterpart. The smooth appearance of this sample surface is surprising; it could be expected that the continuous pile-up of multiplied misfit dislocations would produce a surface with greater undulation. Some smoothing of the surface may result from the 3 μm capping layer, authors such as Jesson *et al.* (1993) have commented on smoothing of undulating layers, though in such instances layers have undergone some degree of elastic deformation that is not expected here. Further, Fitzgerald *et al.* (1992) working with comparable virtual substrates have found that surfaces do not become significantly smoother with continued overgrowth. Another possibility, discussed further in section 5.6, is that the multiplication mechanism expected to be dominant in this situation is in competition with other heterogeneous nucleation mechanisms.

A striking difference becomes obvious if comparison is made between any of the 1 μm layer structures grown previously (chapter 4) and the current batch. The distinctive features that unmistakably covered their surfaces are not evident, surprising given that two previous samples had terminating compositions within 5% of these currently under investigation. *The only major differences between the samples occur in the grading region, highlighting the apparent importance of this region in determining surface morphology.*

The absence of *in-situ* annealing and differing thermal budgets utilised for samples 75043 (40%, 800-700ºC Ramping), 75044 (30%, 800-725ºC Ramping) and 75055 (30%, 825-725ºC Ramping) has had little noticeable impact on the surface morphology in comparison to 75046-49 (30%, 850-600ºC, *In-situ* Anneal). Comparison between layers with and without *in-situ* annealing *seems to show*

annealed samples to have a smoother surface, indicating that the act of *in-situ* annealing has a limited smoothing effect upon a well relaxed layer surface.

The presence of pile-up is indicated on the surface of 75055 (30%, 825-725ºC Ramping, No Anneal) near the centre of the wafer by discontinuous hatching, extending approximately 400 μm in Figure 5.7. Objectively this area is not representative of the surface in general, with no other instances of such large features discovered and few other instances at any size. Similarly much smaller isolated surface disturbances have been found on the surfaces the 30% samples 75044 (800-725ºC Ramping, No Anneal), 75049 (850-650ºC Ramping, *In-situ* Anneal) and 75048 (700-600ºC, *In-situ* Anneal). The inclusion of particulate contaminants during growth may be responsible although this is by no means certain.

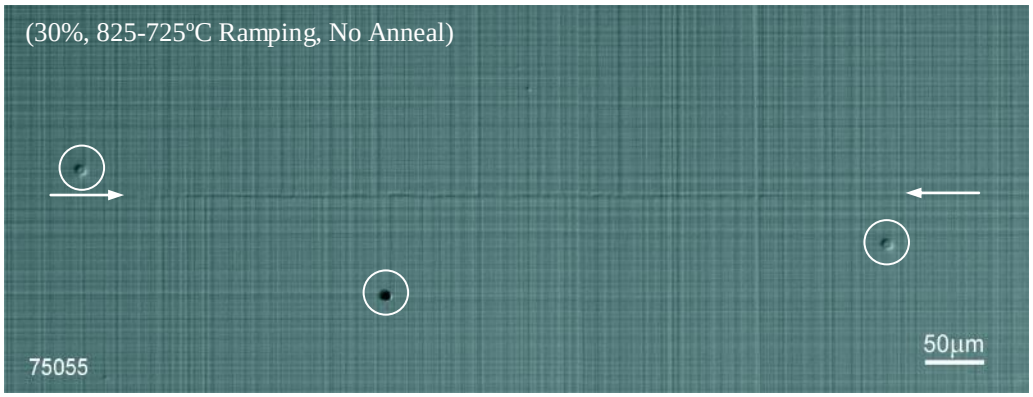

Figure 5.7 – Nomarski interference image taken of sample 75049 at x10 magnification. A disturbance (indicated by arrows) to the cross-hatch running vertically across the image is believed to be evidence of threading dislocation pile-up. Circles highlight localised surface disturbances due to particulate inclusion.

5.2.1 *Ex-Situ* Annealing

The effect of *ex-situ* furnace annealing on the 30% samples 75046 (850-750ºC, *In-situ* Anneal), 75048 (700-600ºC, *In-situ* Anneal) and 75049 (850-650ºC Ramping, *In-situ* Anneal) was explored with the samples given a 15 hour anneal in flowing nitrogen at 900ºC. Primarily the effect of the anneal was to be investigated by cross-sectional TEM, defect etching and X-ray analysis, but Nomarski imaging allowed for quick observation of any dramatic morphological changes. No obvious changes in the surface morphology or contrast could be observed for any of the samples, Figure 5.8.

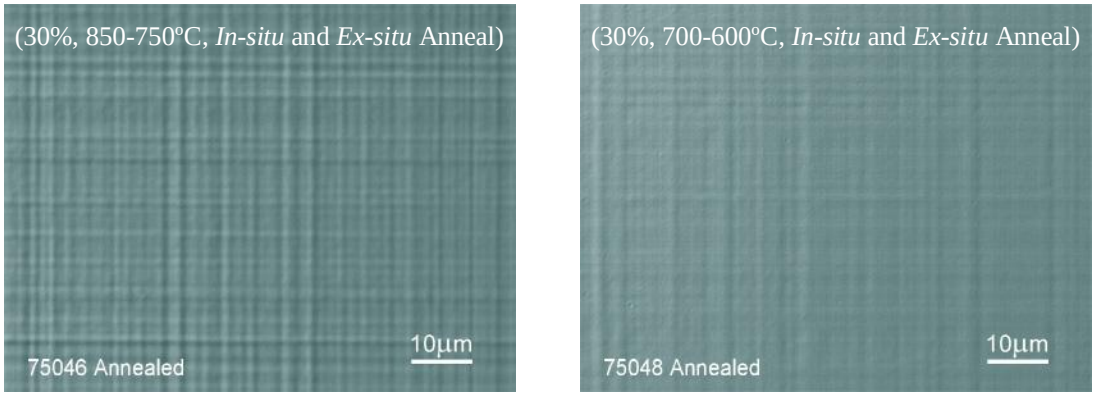

(a) (b)

Figure 5.8 – Nomarski interference image taken at x10 magnification after an *ex-situ anneal* has been performed at 900ºC for 15 hours on samples (a) 75046 and (b) 75048.

5.3 Cross-Sectional Transmission Electron Microscopy (XTEM)

Few dislocations are seen to propagate between the graded layers in any of the as-grown 30% or 40% terrace graded structures investigated. It appears that the 30% as-grown samples which received *in-situ* anneals share similar levels of relaxation, despite a maximum growth temperature difference of 150ºC between 75046 (850-750ºC) Figure 5.9 and 75048 (700-600ºC) Figure 5.10.

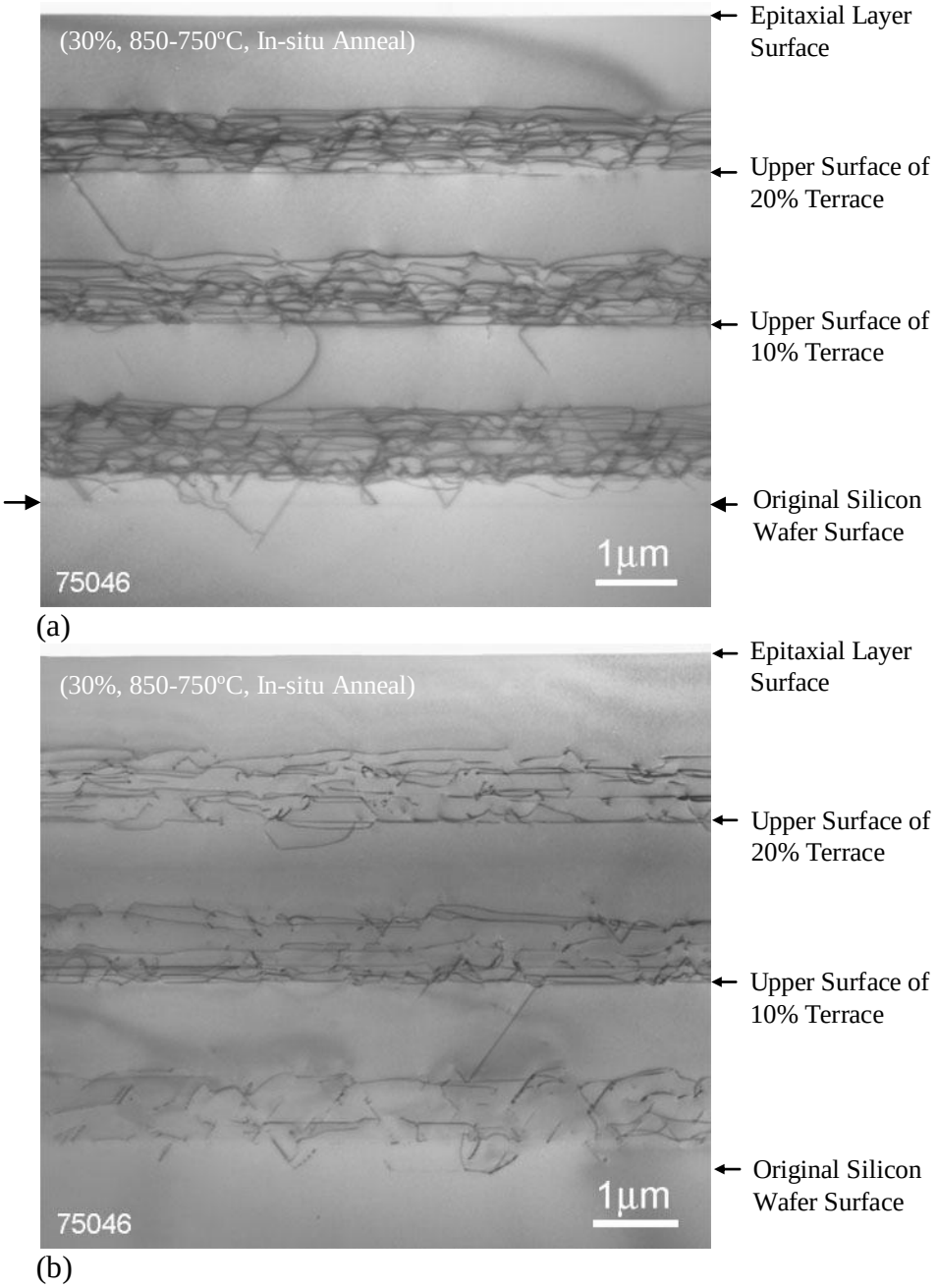

Figure 5.9 – Cross-sectional transmission electron micrographs (in the (220) two beam diffraction condition) of sample 75046 (a) relatively thick section (b) relatively thin section.

It is difficult to ascertain the relative thickness of the sample in the region that individual images are taken, making comparison of features between samples difficult. The aim of multiplication source decoupling between graded regions appears to have been achieved to a significant degree and with no evidence of any surface threading dislocations in the numerous regions viewed. It is clear in Figure

5.9 (b), unlike those images presented in Chapter 4 that *these layers do appear to be linearly graded* at low composition with no dense network of dislocations obvious at or near the initial growth interface and the dislocations appearing uniformly spread.

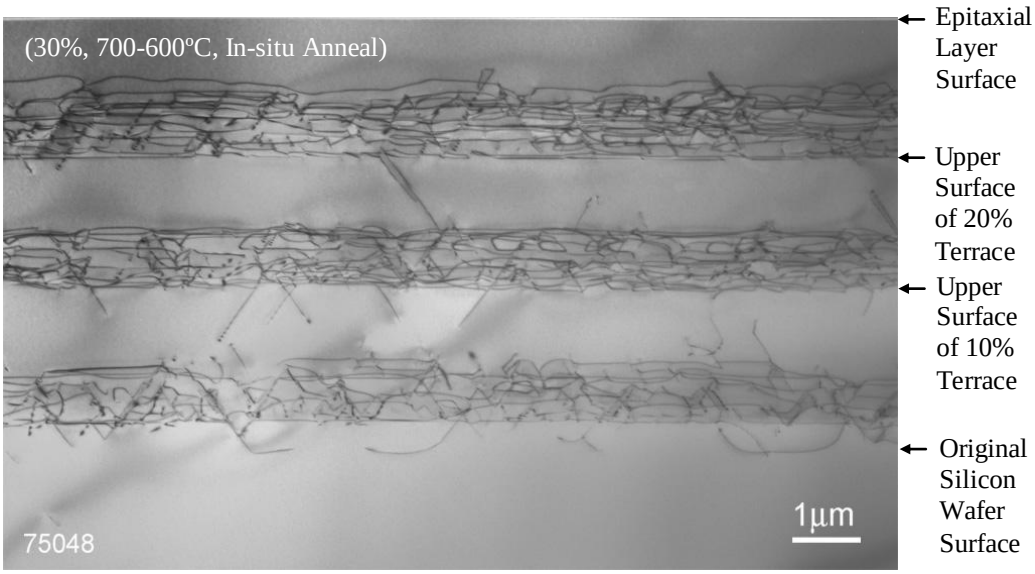

Figure 5.10 – Cross-sectional transmission electron micrograph (in the (220) two beam diffraction condition) of sample 75048.

The addition of a 40% terrace grade and the initially higher growth temperature (25ºC) of sample 75043 (800-700ºC Ramping, No Anneal) with respect to 75055 (30%, 825-725ºC Ramping, No Anneal) appears to have had little effect upon dislocation formation or confinement in upper terraces (Figure 5.11). Additionally the silicon marker layers placed at the top of each terrace in sample 75055 (30%) appear to have little effect.

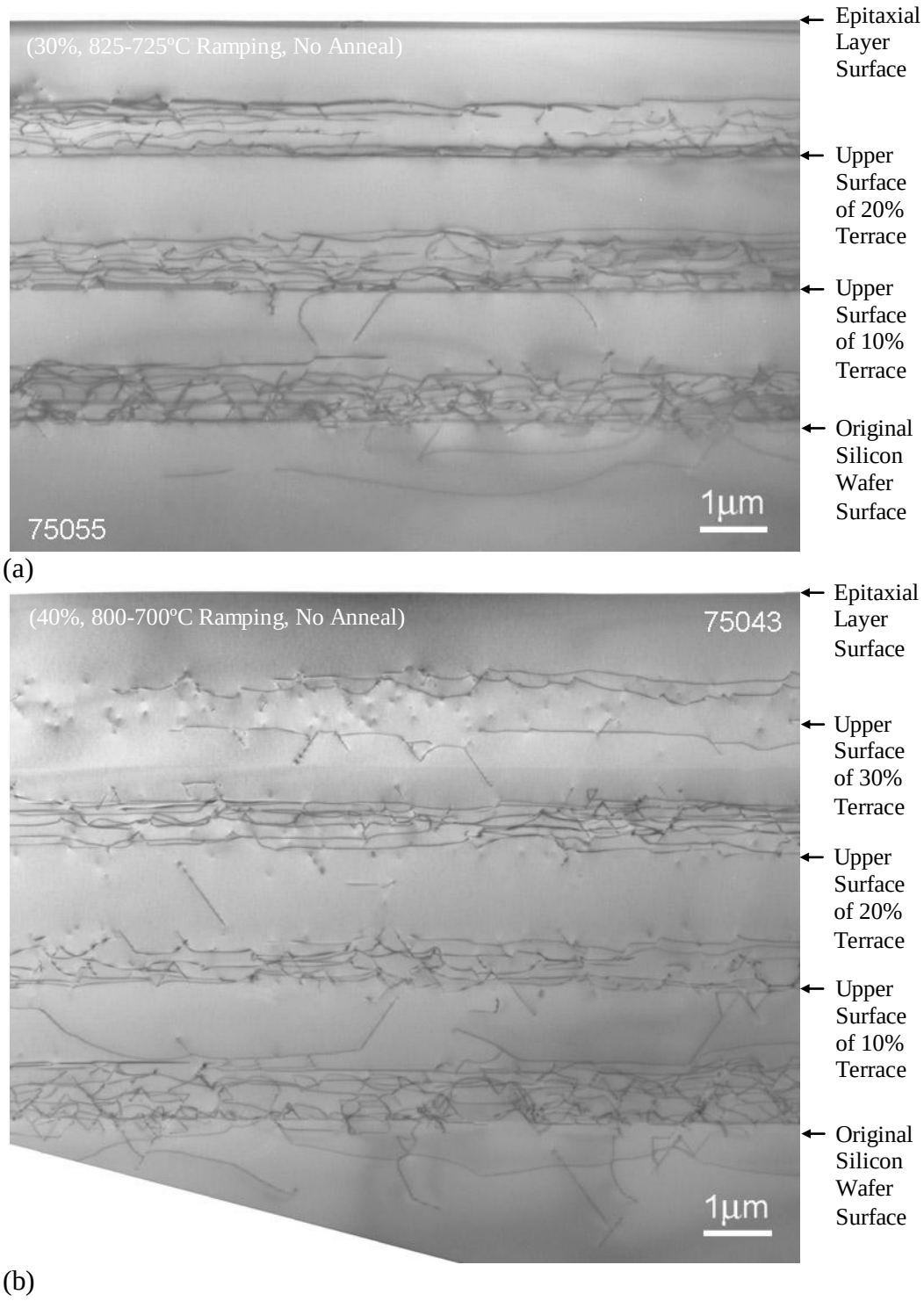

Figure 5.11 – Cross-sectional transmission electron micrographs (in the (220) two beam diffraction condition) of sample (a) 75055 (b) 75043.

Comparison between cross-sectional images of samples 75055 (30%, 825-725ºC Ramping, No Anneal) and 75043 (40%, 800-700ºC Ramping, No Anneal) shown in Figure 5.11, that did not receive *in-situ* anneals after each terrace, and samples 75046 (30%, 850-750ºC, *In-situ* Anneal) and 75048 (30%, 700-600ºC, *In-situ* Anneal) (Figure 5.9 and Figure 5.10) show no significant effect upon the dislocation network observed. *The low level of interaction between terrace graded layers in Figure 5.11 indicates that a high level of relaxation is achieved at the completion of each linear region, even without in-situ anneals*. Importantly, none of the surfaces appear to have macroscopically roughened, indicating as before, that the 1 μm thick layers are able to relieve the accumulating strain at a fast enough rate to avoid the need for elastic deformation of the growth surface. A clear example of the dislocation structure resulting from multiplication by the modified Frank-Read nucleation mechanism can be seen in the lower right hand corner of Figure 5.11 (b).

An interesting detail can be seen in images taken of 75046 (30%, 850-750ºC, *In-situ* Anneal) shown in Figure 5.9 (a), just below the bottom of the initial linear grade, at a depth of around 50 nm a fine dark band is perceivable (indicated by lower arrows). This corresponds to the original silicon wafer surface and although not definite, is highly likely to be due to the presence of carbon contamination. Such contamination is not removed by the *in-situ* high temperature oxide desorption utilised in these instances (Kasper *et al.* 1998), and would require an *ex-situ* chemical clean such as an RCA clean detailed in Appendix A.1. Trace amounts of carbon can form precipitates across the wafer surface when taken to higher temperatures (Dynna *et al.* 1992). The presence of such contamination is always a possibility without chemical cleaning but had been assumed to be of little consequence for thicker structures. Quite clearly in a number of instances, pairs of dislocations emerge from this level

into the layer, though this interaction may have occurred during the growth of the overlaying layers with multiplying dislocations pushed down. Leitz *et al.* (2001) noted that the presence of heterogeneous nucleation sources led to an increased field and pile-up threading dislocation density. The number of instances in which dislocations interact at this level in the present case could suggest that this contamination (whatever it may be) may have a noticeable effect upon the evolution of crystal relaxation. Indeed if dislocations were formed in this region in significant numbers earlier than would have otherwise been possible by multiplication, it may have greatly limited the level of dislocation multiplication that has actually occurred. Such an action could well explain the smaller than expected improvement of terrace grading over conventional linear grading in sections 5.2 and 5.6.

5.3.1 *Ex-Situ* Annealing

The effect of *ex-situ* annealing on epitaxially grown layers is of significant importance, as most such structures if used in real applications would almost certainly be subjected to high temperature processing steps, typically rapid thermal annealing (RTA) such as 950ºC for 30 seconds. The possibility of reducing the surface threading density has also been discussed in the introduction as a motivation for such experimentation.

The high temperature layer 75046 (30%, 850-750ºC, *In-situ* Anneal) shows no change in its dislocation structure after annealing, with almost all visible dislocations confined within the graded regions, Figure 5.12 (compare with Figure 5.9). This demonstrates that a *high level of relaxation was present throughout growth of this structure and very little residual strain remains to be relaxed*.

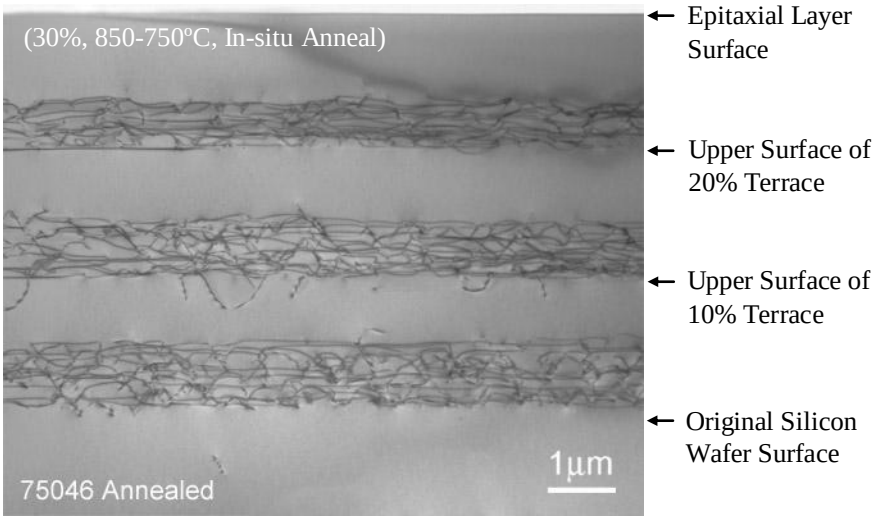

Figure 5.12 – Cross-sectional transmission electron micrograph (in the (220) two beam diffraction condition) of sample 75046 Annealed at 900ºC for 15 hours.

On the contrary the low temperature structure 75048 (30%, 700-600ºC, *In-situ* Anneal) appears to contain many more dislocations within its terraced regions after *ex-situ* annealing, particularly in the region between the upper two graded layers, Figure 5.13 (compare with Figure 5.10). This would suggest that the *upper layer had retained some degree of residual strain after growth*. Although the presence of dislocations in the terraced layers indicates multiplication sites have spawned numerous dislocations, it would appear that these multiplication sites have not persisted between graded layers, and although this is logical in this case, it is still important to note.

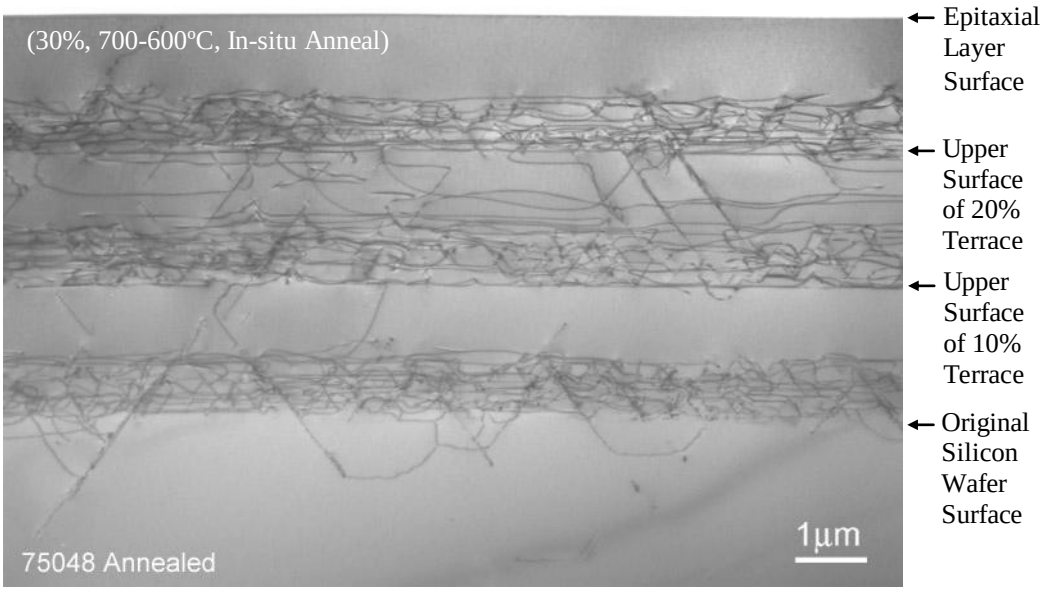

Figure 5.13 – Cross-sectional transmission electron micrograph (in the (220) two beam diffraction condition) of sample 75048 Annealed at 900ºC for 15 hours.

The intermediate structure of 75049 (30%, 850-650ºC Ramping, *In-situ* Anneal) straddles the prior two extremes, with a small amount of dislocation penetration into the intervening constant composition layers, displayed in Figure 5.14. Dislocations have also been visibly pushed deep into the silicon substrate in this instance.

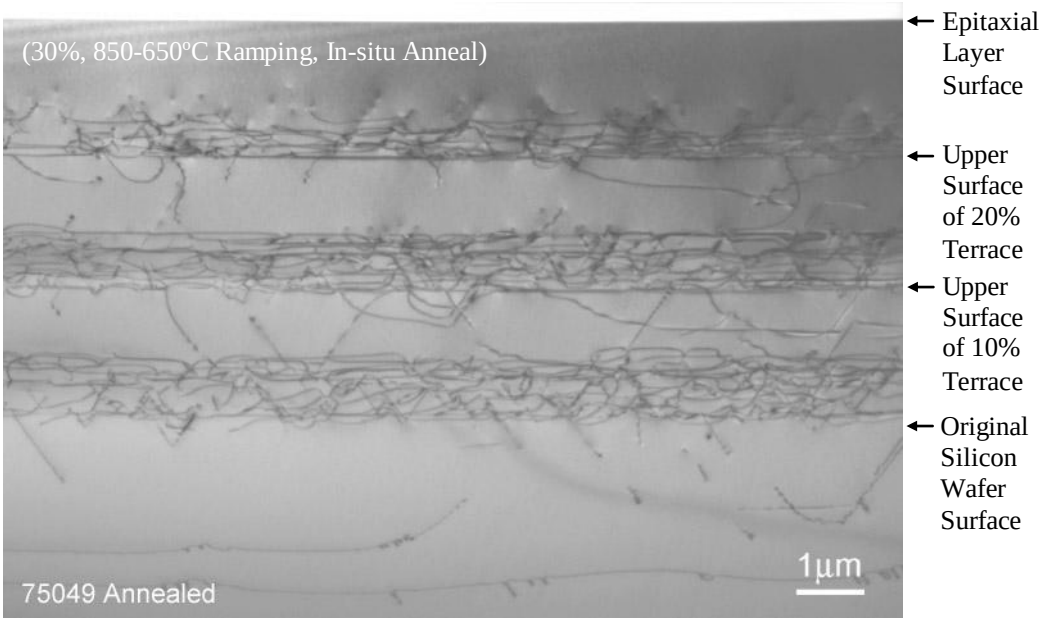

Figure 5.14 – Cross-sectional transmission electron micrograph (in the (220) two beam diffraction condition) of sample 75049 Annealed at 900ºC for 15 hours.

5.3.2 Energy Dispersive X-ray Spectroscopy (EDS)

A summary of the composition analysis performed on each terrace visible in the prepared cross-sectional TEM samples are presented below.

	10%	20%	30%	40%
75046 (30%)	9%	21%	32%	-
75048 (30%)	9%	19%	30%	-
75055 (30%)	9%	17%	25%	-
75043 (40%)	10%	20%	30%	38%

Table 5.1 – EDS composition data for samples 75046 (30%, 850-750ºC, *In-situ* Anneal), 75048 (30%, 700-600ºC, *In-situ* Anneal), 75055 (30%, 825-725ºC Ramping, No Anneal) and 75043 (40%, 800-700ºC Ramping, No Anneal). Composition error of ±5%.

The analysis shows that a close similarity between the intended and actual compositions has been achieved for most of the 30% and 40% samples. Examination of the cross-sectional TEM images would suggest that the compositional grading in each of these samples is close to that expected if it were linear and hence the differences in observed structure will be due largely to variations in growth temperature and perhaps surface contamination.

5.4 Atomic Force Microscopy (AFM)

A quantitative measurement of surface roughness is an important structural parameter providing insight into layer quality and serving as a useful comparison between similar structures for which data has been published. Contact mode atomic force measurements were conducted for the *in-situ* annealed 30% samples 75046 (850-750ºC) and 75048 (700-600ºC), representative plots are given in Figure 5.15 having undergone a 3rd order XY plane fit.

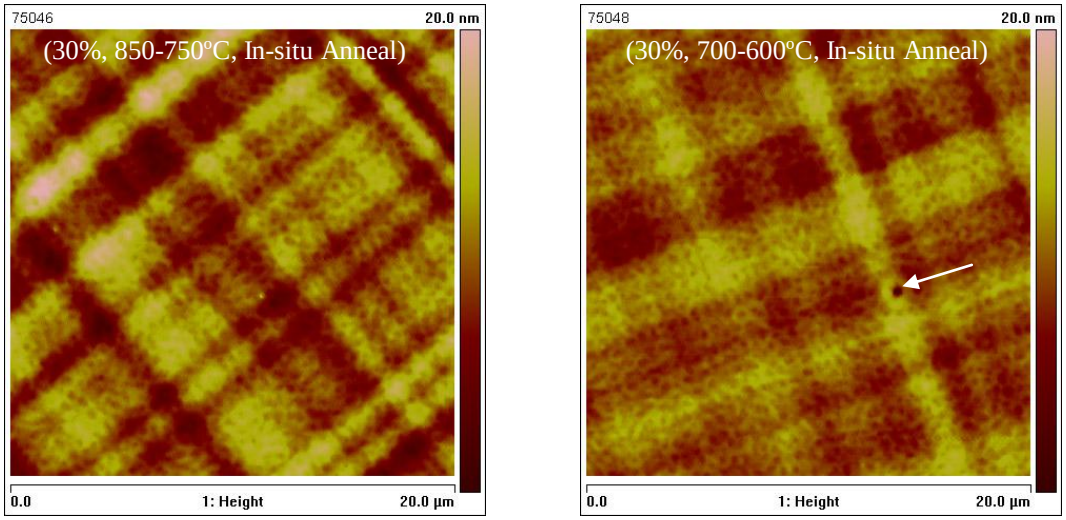

(a) (b)

Figure 5.15 – 20 µm x 20 µm area atomic force height profile scans for (a) 75046 (b) 75048. A possible threading dislocation is indicated by an arrow in image (b).

A cross-hatch pattern is clear on the surfaces of both samples indicative of substrates that have relaxed through the extension of glissile misfit dislocations. The *in-situ* anneal conducted at the end of each completed terrace grade layer may be responsible for the unusual mottled appearance of the surface. The dark hole visible near the centre of Figure 5.15 (b) is most likely a threading dislocation highlighted by reduced adatom incorporation due to locally higher strain (Fitzgerald *et al.* 1997).

The RMS surface roughness calculated for samples 75046 (30%, 850-750ºC, *In-situ* Anneal) and 75048 (30%, 700-600ºC, *In-situ* Anneal) is presented in Table 5.2. It is immediately obvious that higher growth temperatures have led to an increased surface roughness that is nearly double that of 75048 (700-600ºC), although both remain comparable to measurements published at similar compositions. This trend (limited in data points) is the opposite of that found by Leitz *et al.* (2001) were the surface roughness decreased slightly for the higher temperature growth of a linearly graded virtual substrate.

	75046 (30%) (850-750°C)	75048 (30%) (700-600°C)
As-Grown	**3.2 nm ± 0.2nm**	**1.9 nm ± 0.2 nm**
Annealed	**3.6 nm ± 0.3nm**	**2.0 nm ± 0.4 nm**

Table 5.2 – RMS surface roughness measurements determined from AFM images of samples 75046 (30%, 850-750°C, *In-situ* Anneal) and 75048 (30%, 700-600°C, *In-situ* Anneal) as-grown and annealed at 900°C for 15 hours.

5.4.1 *Ex-Situ* Annealing

Contact mode atomic force measurements were also conducted to examine the effect of a high temperature *ex-situ* anneal upon the surface morphology and roughness of 75046 (30%, 850-750°C, *In-situ* Anneal) and 75048 (30%, 700-600°C, *In-situ* Anneal). Representative plots are given in Figure 5.16 having undergone a 3rd order XY plane fit.

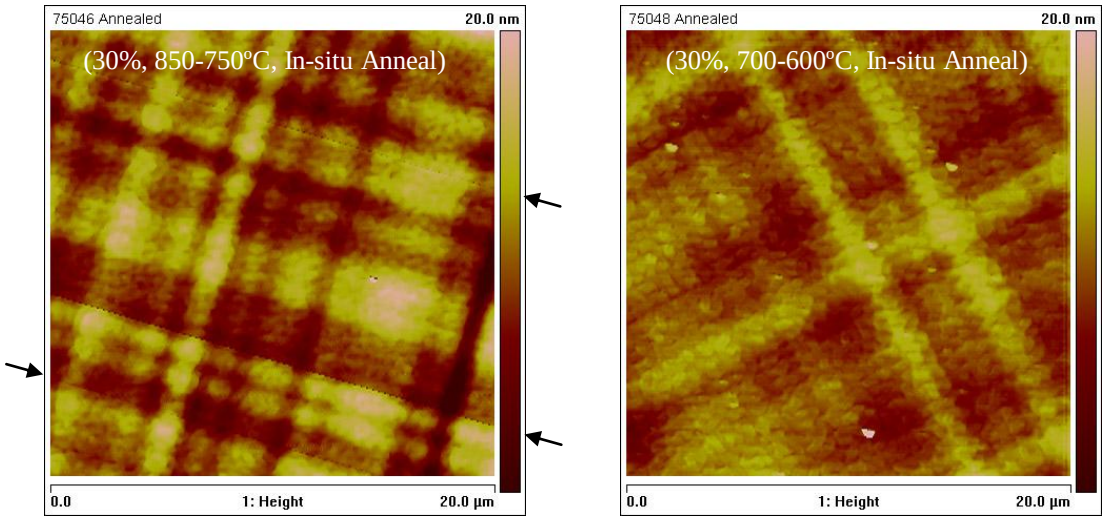

(a) (b)

Figure 5.16 – 20 µm x 20 µm area atomic force height profile scans for (a) 75046 Annealed (b) 75048 Annealed

The surface morphology of both *ex-situ* annealed samples has clearly been affected, with slightly higher values of RMS roughness (see Table 5.2) and lessening of the unusual mottled surface pattern. Sharp features are visible in Figure 5.16 (a)

traversing across the image in line with the cross-hatch, with two toward the bottom of the image and one near the top. These features appear to be surface displacements like those described by Lutz *et al.* (1995) arising from motion of 60º dislocations within the film. Single dislocations are calculated to produce a step height of only 2.8 Å, although this figure increases linearly with the accumulation of additional dislocations, consistent with the steps observed here ranging from around 1 nm to 3 nm. This indicates the propagation of numerous threading dislocations along the same or very closely spaced planes, typical of multiplication sources within the layer, as a result of annealing. The frequency of such features is uncertain as they are only visible in one of three scans obtained from 75046 (30%, 850-750ºC, *In-situ* Anneal) and further work would be required to ascertain the abundance of such steps and whether similar features exist on the annealed surface of 75048 (30%, 700-600ºC, *In-situ* Anneal).

5.5 High Resolution X-ray Diffraction

The importance of a highly relaxed structure has been highlighted previously. The results of X-ray measurements are therefore of significant importance toward a fuller understanding of these structures. Two sets of reciprocal lattice maps along the [004] and [224] directions have been obtained with 90º rotations in phi (Φ). The terrace layer concentration and relaxation determined for the 30% samples 75046 (850-750ºC, *In-situ* Anneal) and 75048 (700-600ºC, *In-situ* Anneal) are presented in Table 5.3.

	75046 (30%)			75048 (30%)		
	Comp. %	Relaxation %		Comp. %	Relaxation %	
Terrace		Φ=0°	Φ=90°		Φ=0°	Φ=90°
10%	10	100	97	10	96	99
20%	20	99	98	21	96	100
30%	30	97	95	30	95	97

Table 5.3 – X-ray composition and relaxation data for samples 75046 (30%, 850-750°C, *In-situ* Anneal) and 75048 (30%, 700-600°C, *In-situ* Anneal). Compositional error no more than ±0.5%, relaxation error up to ±5%.

This compositional analysis corroborates the EDS data obtained previously. Both 30% terrace graded structures with *in-situ* anneals are confirmed have achieved high levels of relaxation throughout the structure. A general trend in relaxation is evident throughout the structures, with upper layers being in general less relaxed than lower layers. A systematic difference in relaxation levels exist between the two phi (Φ) orientations (though these differences fall within the experimentally determined error in their value). Such a difference in strain relaxation may be attributable to a misorientated wafer surface (discussed later).

The [004] lattice maps appear to show that the (004) planes in successive terraces are not parallel with one another or the underlying silicon substrate, see Table 5.4. In one phi (Φ) orientation the peak intensities corresponding to the terrace layers do not deviate significantly from one another in omega, as would be expected for parallel layers. However for a displacement of 90° in phi (Φ) the peak intensities now appear to shift from a central omega (ω) value to a maximum of around 0.05°, indicating a rotation of successive terraces in this direction. Interestingly it appears that layers in [004] directions that show the largest deviation from the silicon peak in omega (ω) correspond to the direction showing the greatest relaxation.

	75046 (30%)		75048 (30%)	
	Angle between Substrate and layer		Angle between Substrate and layer	
Terrace	**[004] Φ=0º**	**[004] Φ=90º**	**[004] Φ=0º**	**[004] Φ=90º**
10%	**-0.01**	**-0.01**	**-0.01**	**0.00**
20%	**-0.02**	**-0.01**	**-0.01**	**0.01**
30%	**-0.05**	**-0.01**	**-0.01**	**0.02**

Table 5.4 – Data collected of angular separation in omega between (004) planes in the silicon substrate and constant composition layers for samples 75046 (30%, 850-750ºC, *In-situ* Anneal) and 75048 (30%, 700-600ºC).

In an attempt to ascertain whether any significant surface offcut existed for these nominally (001) silicon wafers, four additional omega (ω) – psi (φ) scans each separated by 90º in phi (Φ) were conducted according to Halliwell *et al.* (1998) for sample 75046 (30%, 850-750ºC, *In-situ* Anneal). From these measurements the surface was calculated to have an offcut of ~0.1º, in a phi (Φ) direction in which the [004] lattice maps had shown deviation (deviating by only 2º). From the previous observation of dissimilar strain relief in the two phi (Φ) orientations, the direction of highest relaxation corresponds to the direction of surface reorientation. Caution must be taken when putting emphasis on this result given that the experimental error in the initial psi (φ) zero setup is of the order of 0.1º. This result does however verify that no significant offcut exists (<0.5º).

Studies of virtual substrate growth on offcut wafer surfaces (Mooney *et al.* 1994) have observed a tilting of the top surface with respect to the underlying silicon substrate that has the effect of reducing the angle between the (001) planes and the surface (in (001) silicon wafers). Mooney *et al.* (1994) highlight that a 60º dislocation is composed of a screw component, tilt component and misfit component and that an

offcut surface has the effect of altering the magnitude of the misfit relieving component of a dislocation, the projection of its Burgers vector onto the growth surface, for dislocations on different (111) glide planes. Since the driving force for dislocation introduction is strain relief, those dislocations which relieve most strain will be favoured, and it is this unequal introduction of dislocations on different glide planes that results in a net tilt of the surface. A literature search has failed to produce any publications that specifically identify dissimilar relaxation in orthogonal directions.

Mooney *et al.* (1994) specifically treats the case of tilt for offcut toward the [101] direction and its effect on the modified Frank-Read relaxation mechanism. Four slip systems are considered and denoted by MFR1-4 (shown schematically in Figure 5.17). The nucleation barrier and glide velocity of MFR3 and 4 are not affected by the misorientation, whilst it is increased for MFR2 and reduced for MFR1.

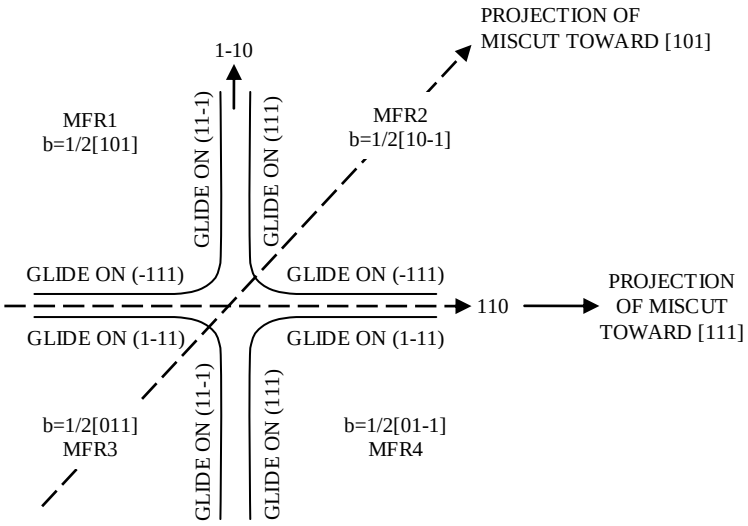

Figure 5.17 – Schematic representation of the dislocation configurations for the four slip systems of the MFR mechanism. A dislocation loop has two branches, one gliding on each of the two slip planes comprising the slip system. The two branches have the same Burgers vector but different line directions. Reproduced from a paper by Mooney *et al.* (1994).

It is also importantly noted that *the two branches in each slip system are in all cases affected equally*, and both branches of each slip system have glide velocities equal to one another. In this case the imbalance between nucleation from MFR1 and MFR2 allows the net tilt for reorientation of the surface.

In the case of an offcut toward the (111) for each of the four slips systems each branch is affected differently as detailed by Mooney *et al.* (1994). The nucleation barrier for the glide planes contributing to MFR1 are increased for (11-1) and unchanged for (-111); MFR2 are reduced for (111) and unchanged for (1-11); MFR3 are increased for (11-1) and unchanged for (1-11); MFR4 are reduced for (111) and unchanged for (-111).

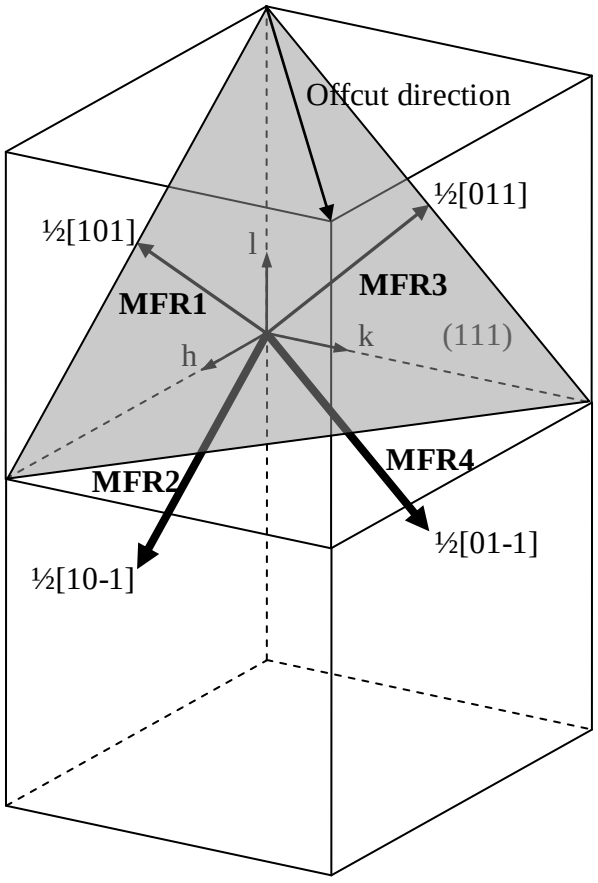

Figure 5.18 – Schematic diagram representing the Burgers vectors corresponding to four modified Frank-Read slips systems (MFR1-4), highlighting their relationships to one another and the (111) glide plane.

Overall MFR2 and 4 have a reduced nucleation barrier whilst MFR1 and 3 have an increased nucleation barrier, hence a net imbalance of tilt exists that allows the surface to be rotated away from the (111) plane back toward the (001).

Along the [1-10] direction the nucleation barrier will be made lower and glide velocity higher on the (111) and opposite on the (11-1). Whilst along the [110] direction the nucleation barrier and glide velocity remain unchanged and equal for (-111) and (1-11). *Strain relief is only provided by the misfit component of the dislocation projected on to the growth plane, supplying relaxation perpendicular to its line direction*. If MFR2 and 4 are favoured due to an average reduction in their nucleation barriers then the dislocation arm created along the [1-10] direction will glide more quickly reducing greater amounts of strain than the other perpendicular arm. The opposite will of course be true for MFR1 and 3 but if these sources nucleate fewer dislocations then a balance may not be maintained resulting in a greater net relaxation along one orthogonal direction.

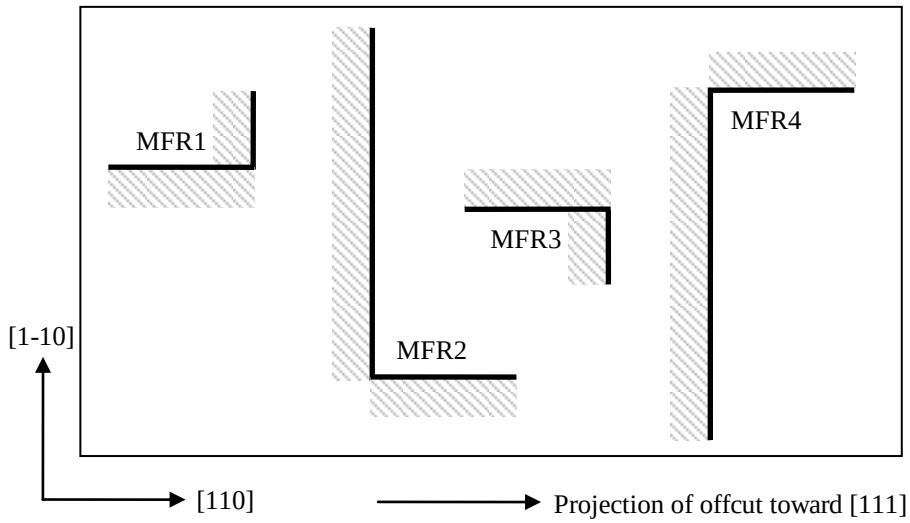

Figure 5.19 – Schematic diagram illustrating the greater misfit lengths along orthogonal directions, with strain relief in a direction orthogonal to the misfit line direction represented by the hatched area.

This demonstrates that *the greatest relaxation*, assuming an imbalance in nucleation exists between MFR2 and 4 and MFR1 and 3, *occurs in the direction of layer tilt* as found in the X-ray analysis. Nucleation by means other than multiplication would also preferably occur on the glide plane with lowest nucleation barrier.

5.5.1 *Ex-Situ* Annealing

The data obtained on the composition and relaxation of samples 75046 (850-750ºC), 75048 (700-600ºC) and 75049 (850-650ºC Ramping) after *ex-situ* annealing is presented in Table 5.5 with orientation data presented in Table 5.6.

	75046 (30%) (850-750ºC) Annealed			75048 (30%) (700-600ºC) Annealed			75049 (30%) (850-650ºC Ramping) Annealed		
Terrace	Comp. %	Relaxation %		Comp. %	Relaxation %		Comp. %	Relaxation %	
		Φ=0º	Φ=90º		Φ=0º	Φ=90º		Φ=0º	Φ=90º
10%	10	99	97	10	94	96	10	102	100
20%	20	99	98	20	98	96	21	102	98
30%	30	96	96	30	96	95	31	103	97

Table 5.5 – X-ray composition and relaxation data for samples 75046 (30%, 850-750ºC, *In-situ* Anneal), 75048 (30%, 700-600ºC, *In-situ* Anneal) and 75049 (30%, 850-650ºC Ramping, *In-situ* Anneal) after annealing *ex-situ* at 900ºC for 15 hours. Compositional error no more than ±0.5%, relaxation error up to ±5%.

High temperature *ex-situ* anneal has made no significant difference to the overall relaxation of the previously measured structures and still appears to show greater relaxation in the direction of greatest omega (ω) separation (see Table 5.6). The greater than 100% relaxation displayed even in the uppermost layer by 75049 (850-650ºC Ramping) highlights the experimental error in this measurement, though the data seems to suggest that it is more relaxed than either the higher or lower

temperature samples. *Temperature grading during the constant composition layer may have a positive impact upon layer relaxation*. The general direction in which relaxation is found to be greatest continues to relate to the direction with the greatest peak deviation in omega (ω).

	75046 (30%) (850-750ºC) Annealed		75048 (30%) (700-600ºC) Annealed		75049 (30%) (850-650ºC Ramping) Annealed	
	Angle between Substrate and layer		Angle between Substrate and layer		Angle between Substrate and layer	
Terrace	**[004] Φ=0º**	**[004] Φ=90º**	**[004] Φ=0º**	**[004] Φ=90º**	**[004] Φ=0º**	**[004] Φ=90º**
10%	**-0.02**	**-0.02**	**0.03**	**0.01**	**-0.01**	**-0.01**
20%	**-0.03**	**-0.02**	**0.04**	**0.02**	**-0.03**	**-0.01**
30%	**-0.06**	**-0.03**	**0.04**	**0.01**	**-0.06**	**-0.02**

Table 5.6 – Data collected of angular separation in omega between (004) planes in the silicon substrate and constant composition layers for samples 75046 (30%, 850-750ºC, *In-situ* Anneal), 75048 (30%, 700-600ºC, *In-situ* Anneal) and 75049 (30%, 850-650ºC Ramping, *In-situ* Anneal) after annealing *ex-situ* at 900ºC for 15 hours.

In an attempt to obtain more accurate values for relaxation and layer tilts a series of 12 individual omega (ω) omega-2theta (ω–2θ) scans were performed on sample 75046 (30%, 850-750ºC, *In-situ* Anneal) that had been *ex-situ* annealed. Each scan was performed around a previously identified layer peak, allowing the elimination of scanning areas that offer no useful data and scanning at a higher angular resolution than previously utilised. Scanning around individual peaks is only possible once lower resolution maps have been completed and requires the sample to have not been disturbed. The results are summarised in Table 5.7.

	75046 (30%) (850-750ºC) Annealed				
	Comp. %	Relaxation %		Angle between Substrate and layer	
Terrace		Φ=0º	Φ=90º	[004] Φ=0º	[004] Φ=90º
10%	10	98	97	-0.01	-0.02
20%	20	98	98	-0.03	-0.02
30%	30	98	96	-0.07	-0.04

Table 5.7 – X-ray composition, relaxation and angular (omega) separation data for sample 75046 (30%, 850-750ºC, *In-situ* Anneal) obtained at higher angular resolution than previous scans. Compositional error no more than ±0.5%, relaxation error up to ±5%.

Only marginal improvement in the accurate location of peak centres has been obtained resulting from poor peak definition. A reduction in signal noise would be beneficial but require far greater scan times. The calculated values of relaxation and tilt compare closely to those in Table 5.5, still displaying a small difference between layer relaxations in orthogonal directions.

The high resolution scans have revealed that the 30% layer peak is in fact composed of two peaks, closely spaced in omega (ω), being most clearly identifiable in the phi (Φ) = 0º scan and far less distinct for phi (Φ) = 90º. A representative scan is presented in Figure 5.20. This phenomenon indicates the presence of a *mosaic structure* within this layer (Fewster 1996). A mosaic block is a discrete diffracting body that is connected to the underlying matrix by small angle grain boundaries, with the misorientation accommodated by a series of dislocations leaving no voids between the block and matrix (Fewster 2000). Clearly a surface consisting of differently orientated domains will have implications on its suitability for device processing.

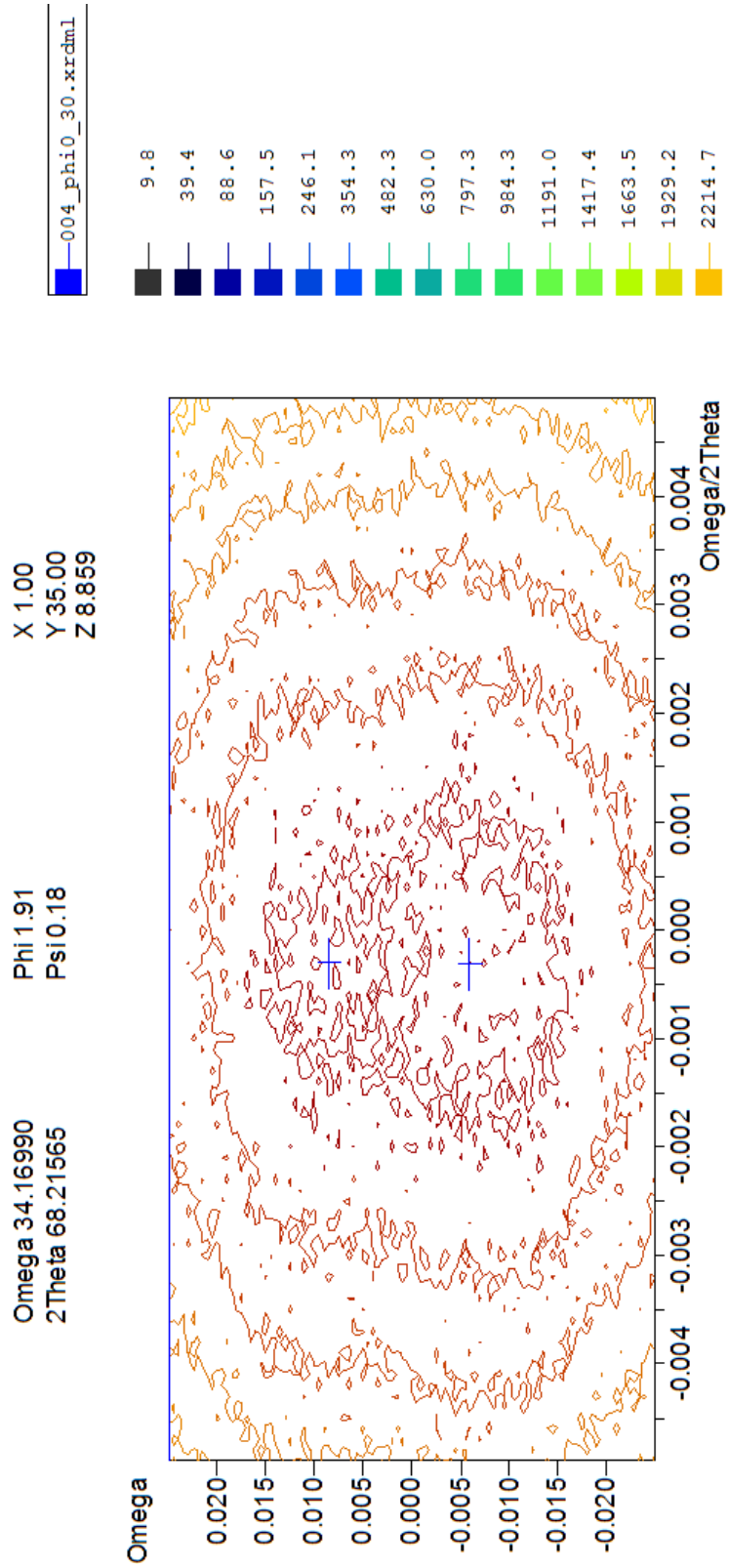

Figure 5.20 – High resolution omega (ω) omega-2theta (ω–2θ) scan in the [004] direction from sample 75046 (30%, 850-750°C, *In-situ* Anneal) *ex-situ* annealed with phi (Φ)=0°. Crosses mark the central regions of the two distinct peak maxima.

5.6 Schimmel Defect Etching

The surface threading density of a virtual substrate structure is an extremely important quantity. The line threading density of threading dislocation pile-up is particularly important as this is far more likely to result in complete device failures. Defect etching was performed on all of the 30% and 40% virtual substrate samples using a standard Schimmel etchant.

Samples 75046 (30%, 850-750ºC, *In-situ* Anneal), 75044 (30%, 800-725ºC Ramping, No Anneal), 75055 (30%, 825-725ºC Ramping, No Anneal) and 75043 (40%, 800-700ºC Ramping, No Anneal) readily revealed a large number of easily identifiable and countable etch pits at an optical magnification of x10 after etching in the region of 1-5 minutes. A compilation of the calculated threading densities along with the standard deviation derived from variation in threading counts is presented in Table 5.8.

	75046 (30%)	75055 (30%)	75044 (30%)	75043 (40%)
Threading Density (/cm^2)	**2.0×10^5**	**2.3×10^5**	**1.9×10^5**	**4.1×10^5**
Standard Deviation (/cm^2)	**6×10^3**	**1×10^4**	**8×10^3**	**6×10^3**

Table 5.8 – Table summarising threading dislocation densities for samples 75046 (30%, 850-750ºC, *In-situ* Anneal), 75055 (30%, 825-725ºC Ramping, No Anneal), 75044 (30%, 800-725ºC Ramping, No Anneal) and 75043 (40%, 800-700ºC Ramping, No Anneal) calculated by counting surface etch pits, accompanied by standard deviations.

The variation in thermal treatments applied between the 30% terrace graded virtual substrates shown in Table 5.8 has had little effect on the surface threading dislocation density *but the addition of a further terrace grade, raising the terminating composition to 40%, has had the effect of doubling the threading density*. This large and undesirable rise points toward too few mobile threading dislocations, even though

the same amount of strain is relieved between the 20%-30% layers as between the 30%-40% layers.

Such an increase in threading density with terminating composition has also been found by Leitz *et al.* (2001) even though theoretically such a rise was not expected. It is concluded that the increase with increasing composition is due to the presence of impediments to dislocation glide, specifically increasing misfit pile-up, and is thus related to threading dislocation pile-up. For the case of a terrace graded structure however any strain fields due to misfit pile-up should be reset after each new terrace. If the source of escalating surface threading density is indeed due to the presence of impediments, then perhaps some other source is responsible in this instance. It is possible that the reduction in growth temperature, in line with silicon and germanium melting points, is too great and this is resulting in the need for additional dislocation nucleation to maintain adequate strain relief. Alternatively perhaps the continual inclusion of particulate contaminants during MBE growth, discussed later, is having an effect.

Comparison with the threading densities found in the low compositional regime is limited with regards to the fundamentally different underlying grading structure, although a general increasing trend with percentage is apparent, being almost exponential, Figure 5.22.

The most important revelation defect etching has provided is the noticeable absence of any observed threading dislocation pile-up in the terrace graded layer structures. After extensive etching only a few isolated instances of pile-up have been found, occurring either at the very edge of a wafer or as a result of *in-situ* particulate contamination. Comparison between two terrace graded samples, an externally

sourced virtual substrate (grown by LEPECVD), as well as a linearly graded layer is show in Figure 5.21 serving to highlight this difference.

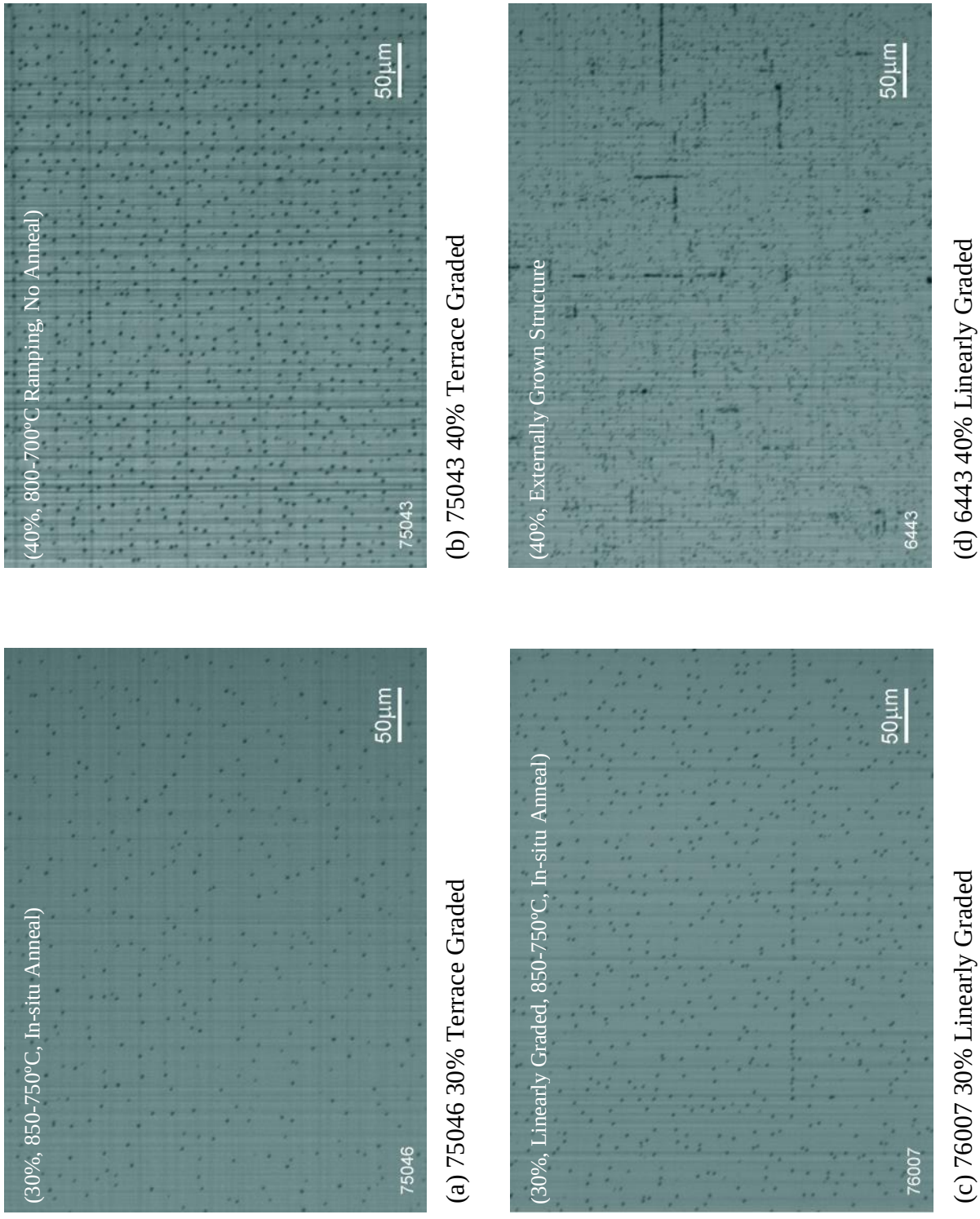

Figure 5.21 – Optical micrographs of defect etched samples (a) 75046 30% terrace graded, (b) 75043 40% terrace graded, (c) 76007 30% linearly graded and (d) 6443 40% linearly graded (externally grown by LEPECVD).

	6443 (40%)	76007 (30%)
Threading Density (/cm^2)	**1.7x10^6**	**3.5x10^5**
Standard Deviation (/cm^2)	**1x10^5**	**8.6x10^3**

Table 5.9 – Table containing threading dislocation densities for samples 6443 (externally grown LEPECVD) and 76007 (30%, Linearly Graded, 850-750ºC, *In-situ* Anneal) calculated by counting surface etch pits, accompanied by standard deviations.

It seems evident that the Schimmel etch reveals the presence of pile-up more quickly than individual threading dislocations, demonstrated in Figure 5.21 (d). The reduction and ultimately elimination of threading dislocation pile-up is a key aim of the terrace graded approach and these results provide a positive proof of principle at 1 μm layer thickness at least up to a composition of 40%.

It is clear comparing the etch pit densities of the terrace graded 75046 (30%, 850-750ºC, *In-situ* Anneal) and linearly graded 76007 (30%, Linearly Graded, 850-750ºC, *In-situ* Anneal) *that terrace grading results in a reduction of threading dislocation density by almost one half*. The surface of sample 76007 (30%, Linearly Graded, 850-750ºC, *In-situ* Anneal) in Figure 5.21 (c), shows instances of both pile-up and pseudo pile-up at a level far less than the externally grown 40% virtual substrate shown in Figure 5.21 (d). This is broadly consistent with a structure of lower composition although a higher density of pile-up had been anticipated. A possible explanation for the low pile-up density observed may result from the heterogeneous nucleation of dislocations. There is limited evidence to suggest the presence of numerous nucleation sources at the initial growth interface of 75046 in the cross-sectional TEM image of Figure 5.9 (a) which is likely to be common for structures grown during this work. Operation of modified Frank-Read multiplication sources are known to require clean growth conditions to efficiently operate so that

dislocation pinning does not occur too closely together, as discussed by LeGoues *et al.* (1992). In this instance initial defect source separations of around 1600 nm are observed (Figure 5.9 (a)) but could be far closer owing to the limited sample thickness observed (probably less than 300 nm in depth), and are close to the minimum distances between pinning locations calculated by LeGoues (1992). *If these assumptions are correct then intentional* seeding *of a wafer surface may provide a reduction in pile-up density for both linear and terrace graded structures.*

5.6.1 Exceptionally Low Threading Dislocation Densities

The 30% samples grown at lower temperature, 75048 (700-600ºC, *In-situ* Anneal) and 75049 (850-650ºC Ramping, *In-situ* Anneal) did not reveal a countable number of etch pits at x10 magnification, with or without interference contrast. This was most unusual implying a defect density $\leq 10^3/cm^2$. The increasing density of threading dislocations between high and low temperature samples is presented graphically in Figure 5.22.

A trend seems to exist between the high growth temperature samples and if a similar trend is assumed to exist between the low temperature samples then a threading density of $\sim 3x10^3$ cm^{-2} would be expected for sample 75048 (30%, 700-600ºC, *In-situ* Anneal). This translates to the appearance of on average 6 threading dislocations per micrograph image at x10 magnification, a level that would be clearly identifiable. Repeated etching confirmed dissolution of the samples surface by consistently revealing what is believed to be the first underlying dislocation network after 10-12 minutes in solution (see Figure 5.24 for example). Further more, etching of a wafer edge piece revealed evidence of isolated pile-up, shown in Figure 5.23, but

did seem to indicate a slower rate of reveal in comparison to structures grown at higher temperature.

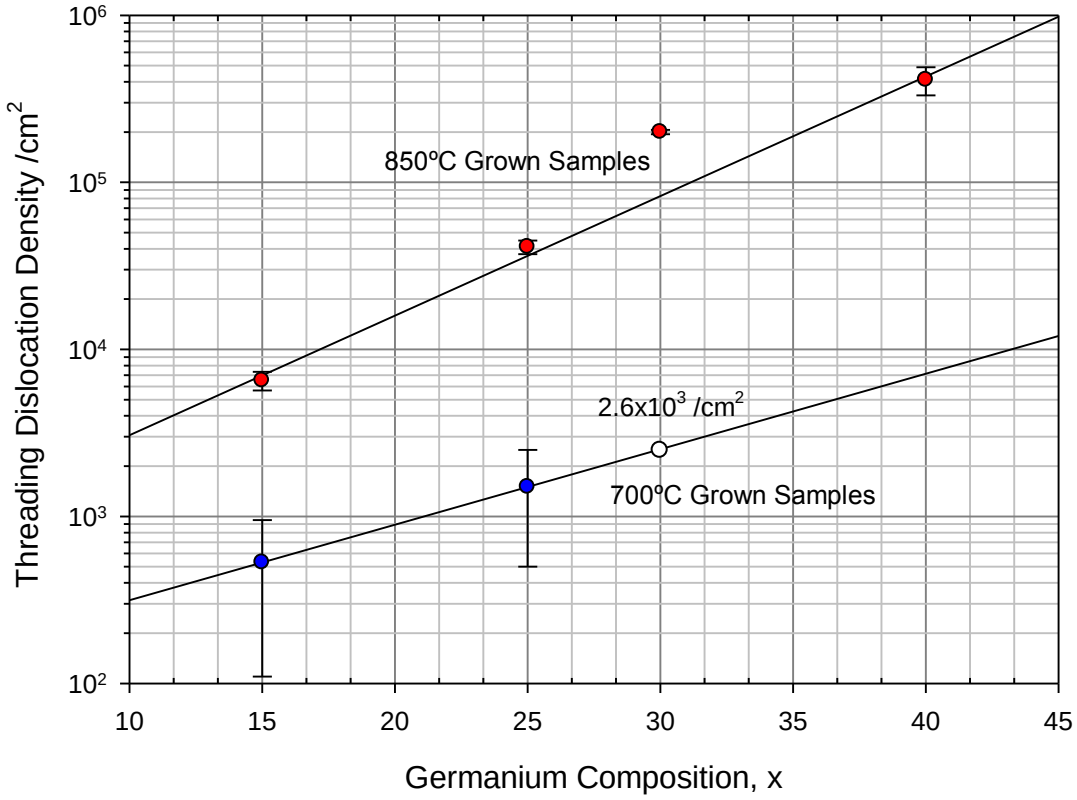

Figure 5.22 – Graph comparing the surface threading dislocation densities of terrace graded virtual substrates grown from high temperature (850ºC) and low temperature (700ºC).

Etching was also repeated with a *modified* Schimmel etch (Werner *et al.* 2004), that allows a more rapid defect reveal. As a control, the modified Schimmel etch was tested on sample 75046 (30%, 850-750ºC, *In-situ* Anneal) revealing the same number of etch pits as the conventional etch. This modified etch made no difference to the number of countable etch pits on either 75048 (30%, 700-600ºC, *In-situ* Anneal) or 75049 (30%, 850-650ºC Ramping, *In-situ* Anneal). *All of the available evidence suggests that the surface threading densities of the lower growth temperature samples are* $\leq 10^3/cm^2$ *and is a significant result.*

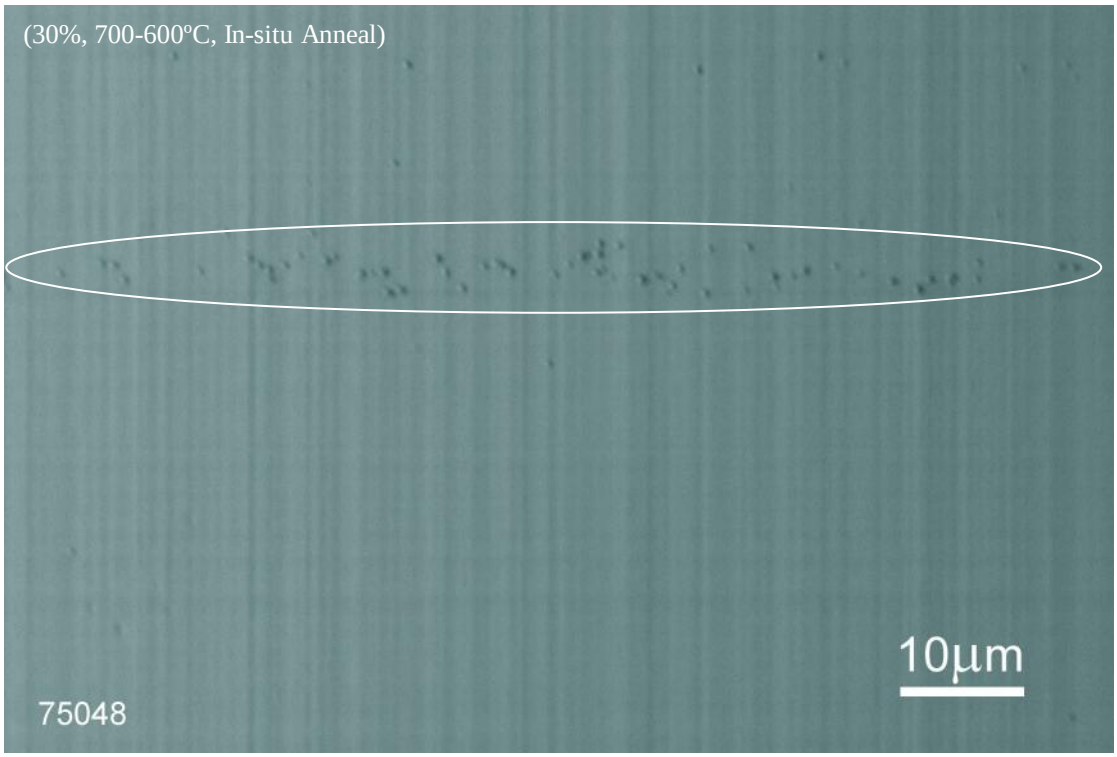

Figure 5.23 – Optical micrograph of defect etched sample 75048. The image was taken in the bright field without interference contrast at x50 magnification. The oval indicates the threading dislocation pile-up.

5.6.2 *Ex-Situ* Annealing

Schimmel etching is now utilised to explore the effect of a high temperature *ex-situ* anneal on the surface threading dislocation density of 75046 (850-750ºC), 75048 (700-600ºC) and 75049 (850-650ºC Ramping) (annealed pieces ~10 mm x 10 mm in size). It is reasonable to anticipate two possible outcomes of annealing at a temperature in excess of that deployed during growth, resulting in either an increased or unchanged surface threading density. A highly relaxed layer may achieve additional relaxation by extension of existing mobile threading dislocations whilst layers with greater residual strain are unlikely to contain sufficient numbers of mobile threading dislocations to accommodate further relaxation without additional dislocation nucleation. In each case, just as prior to *ex-situ* annealing a large number of closely spaced etch pits were revealed after approximately 12 minutes of etching,

believed to indicate intersection of the top most misfit dislocation network, indicating that the overall etch rate had not been significantly altered. Just as prior to *ex-situ* annealing the 30% samples 75048 (700-600ºC) and 75049 (850-650ºC Ramping) displayed an unchanged threading density $\leq 1x10^3/cm^2$. A surprising difference was found between annealed and as-grown pieces of 75046 (30%, 850-750ºC), with *annealed pieces showing a significant reduction in threading dislocation density*. Time lapse images showing the progression of etch pit formation, highlighting the difference between as-grown and annealed pieces of 75046 (30%, 850-750ºC) are given in Figure 5.24.

Careful examination of sequential images in Figure 5.24 (b) appears to indicate the persistence of only a small number of objects. If these objects are taken to be threading dislocations then a massive reduction in density to approximately $5x10^3/cm^2$ (from $2x10^5/cm^2$) is indicated (around 10 objects in field of view at x10 magnification), still with absolutely no observed threading dislocation pile-up. Contamination of the sample surface during annealing could be proposed as responsible for the absence of etch pit formation, however given that etch pits are quickly formed after 12 minutes of etching (repeatedly), this explanation would appear flawed.

Kissinger *et al.* (1995) demonstrated that high temperature annealing at 1050ºC under a hydrogen ambient can yield a dramatic reduction in threading dislocation density for a step graded layer structure although their proposal that the dramatic reduction is due simply to the glide of dislocations across the entire wafer to the edge seems unlikely due to the dependence of dislocation glide velocity on remaining mismatch strain (equation (2.3)).

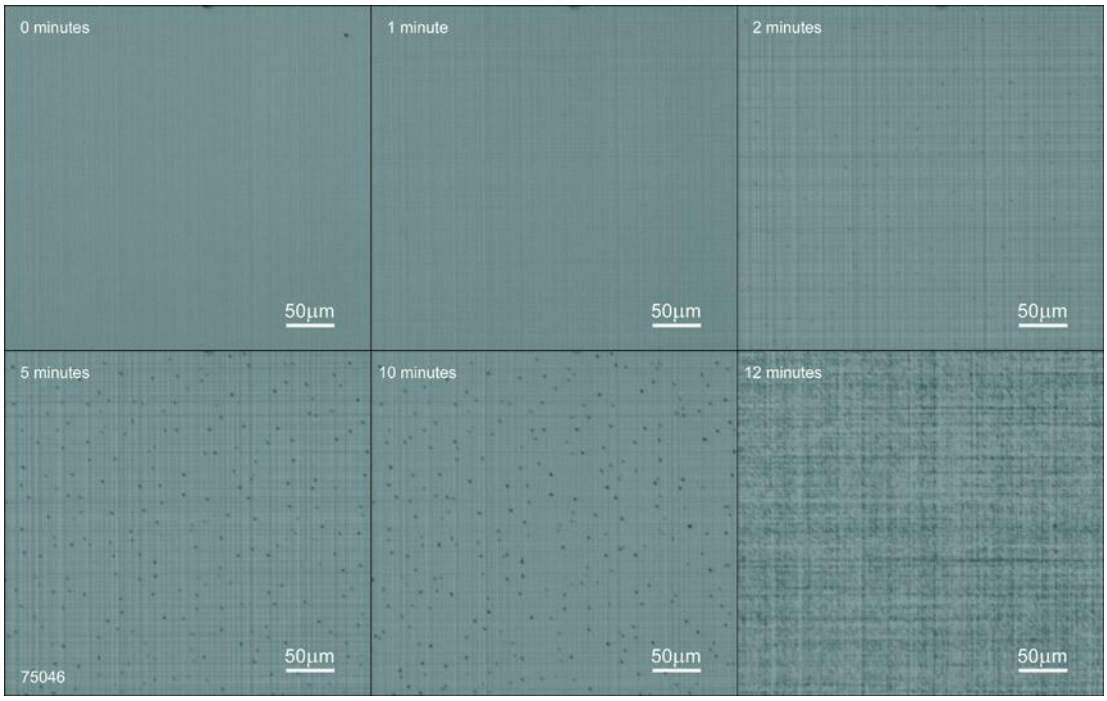

(a) 75046 (30%, 850-750ºC, *In-situ* Anneal, Terrace Graded)

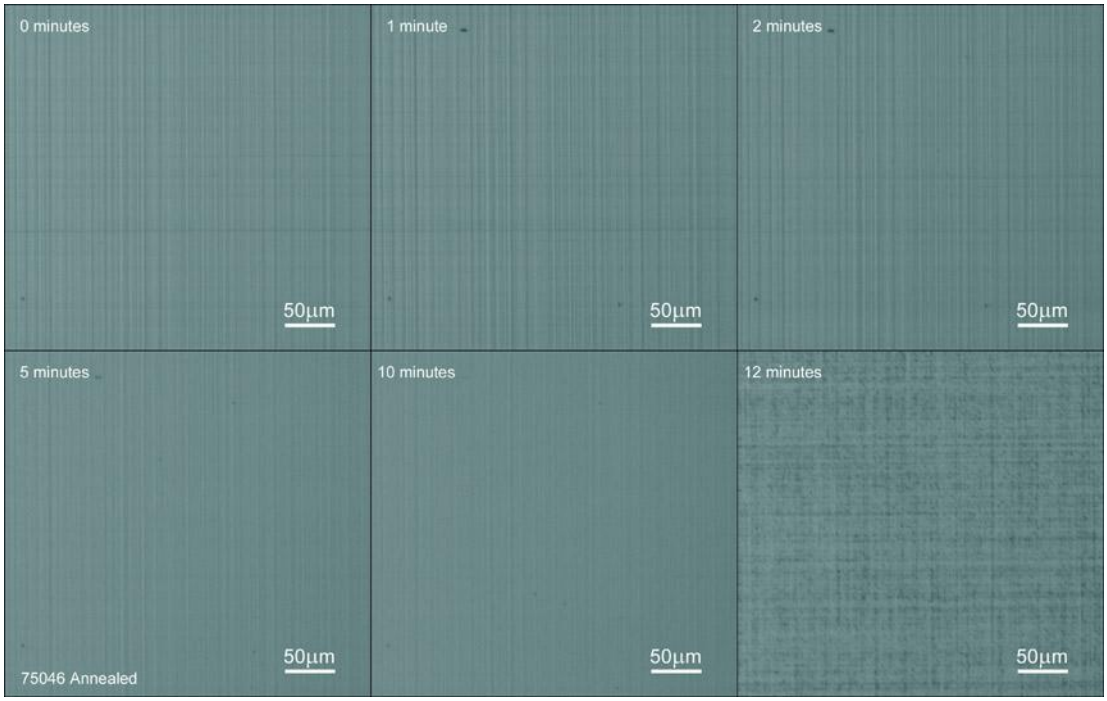

(b) 75046 (30%, 850-750ºC, *In-situ* Anneal, Terrace Graded) with *ex-situ* anneal

Figure 5.24 – Time lapse images showing etch pit formation after continued Schimmel etching (a) 75046 as-grown (b) 75046 *ex-situ* anneal at 900ºC for 15 hours.

Alternatively and intriguingly some form of enhanced dislocation movement and annihilation may have occurred. Such an occurrence has been postulated in other material systems and is proposed to occur through the climb of dislocations, facilitated by an increased vacancy (or possibly interstitial) concentration (Arias *et al.* 1991). Ahn *et al.* (1989) have observed vacancy injection due simply to the presence of an Si/SiO_2 interface when annealed under Argon (inert environment) at 1100ºC. It is believed that the loss of SiO from the oxide surface leads to the movement of Si or SiO toward the top of the oxide layer resulting in vacancy injection (Dunham 1992). This mechanism is most prolific for thinner oxide layers such as the native oxide formed on the surface of the samples studied in this instance. Unfortunately the dependency of this vacancy injection mechanism upon anneal temperature has not been studied and so the operation of such a mechanism in the current work is uncertain. Stach *et al.* (1998) have additionally found that the presence of an oxide surface led to a dislocation glide velocity that was 3 times greater than the same bare reconstructed silicon surface.

An *ex-situ* anneal was provided to the externally grown linearly graded sample 6443 (40%, Linearly Graded) and the results are again presented as a series of time lapse images in Figure 5.25. The as-grown 6443 (40%, Linearly Graded) clearly reveals a high threading dislocation density as well as substantial dislocation pile-up. In contrast to Figure 5.24 (b) the images in Figure 5.25 (b) clearly show the continued presence of threading dislocations in the main field. The presence of pile-up is less clear although still perceivable, apparently disguised by a rapidly roughening surface. This sequence of etching would again appear to support the notion that the role of the Schimmel etch has not been dramatically affected, even if the morphological evolution of the surface of 6443 (40%, Linearly Graded) has been altered.

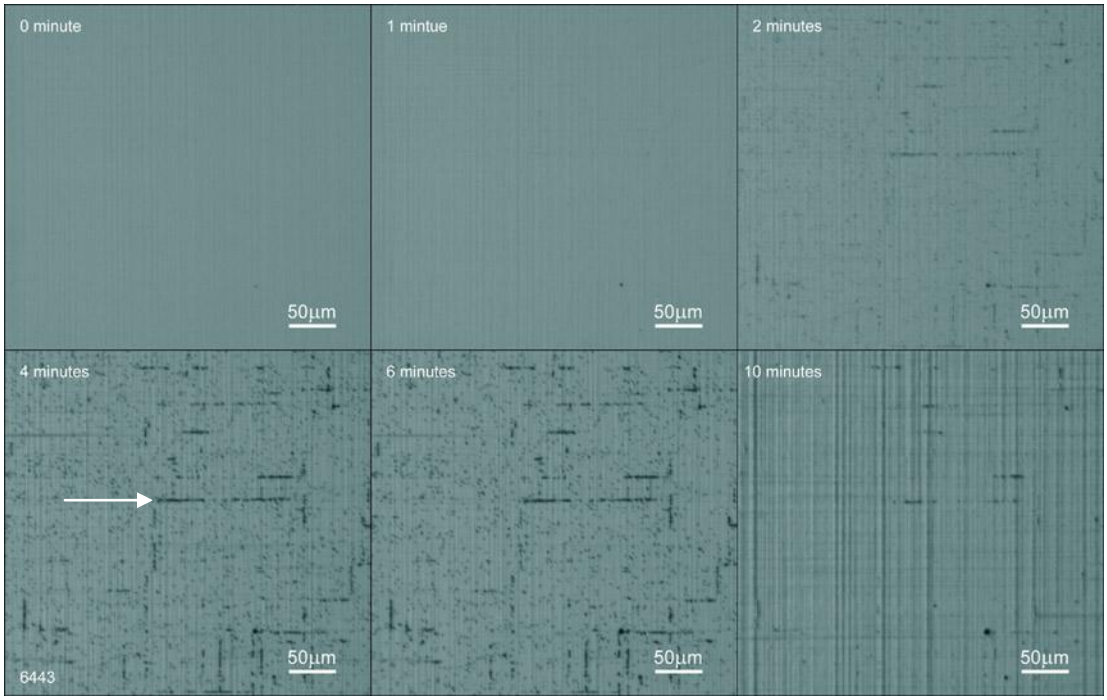

(a) 6443 (40%, Linearly Graded) Grown Externally

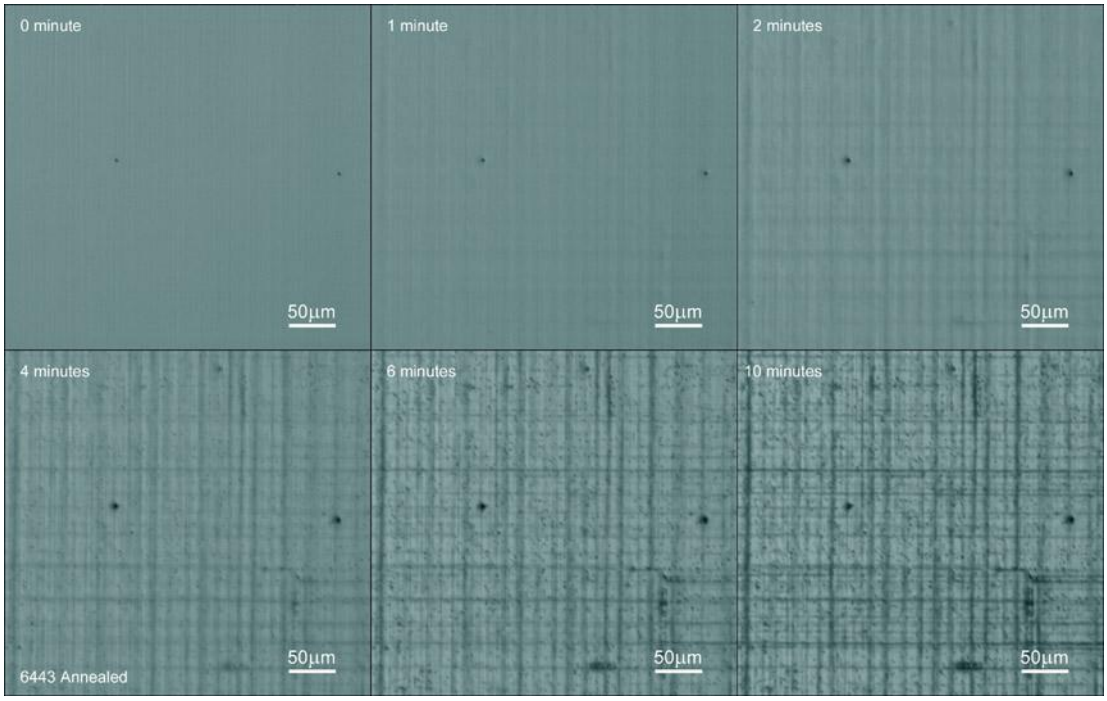

(b) 6443 (40%, Linearly Graded) Grown Externally with *ex-situ* anneal

Figure 5.25 – Time lapse images showing etch pit formation after continued Schimmel etching (a) 6443 as-grown (b) 6443 *ex-situ* anneal at 900ºC for 15 hours. An arrow indicates a region of threading dislocation pile-up.

5.7 Summary

The production of virtual substrates at compositions of 30% and 40% with no measurable pile-up is a most significant breakthrough for terrace grading as is the production of *30% virtual substrates with threading dislocation densities* $\leq 10^3/cm^2$. The significant reduction in threading dislocation density subsequent to high temperature annealing for an extended period is also important. It is clear from X-ray analysis that all of the 1 μm layer structures undergoing *in-situ* annealing have achieved a significant level of relaxation throughout, and is likely the same for those that were not *in-situ* annealed judging from cross-sectional TEM and etch pit analysis.

Surface threading dislocation densities for the best as grown 30% structures are $\leq 10^3/cm^2$ which compared to one of the best conventional linearly graded comparisons at 35% of $3x10^4/cm^2$ (Rosenblad *et al.* 2000) is an order of magnitude lower. Although not mentioned, pile-up in that instance would also most certainly have been present as it was grown using the same LEPECVD (low energy plasma enhanced chemical vapour deposition) technique as the 40% structure 6443 (40%, Linearly Graded) and is considered here to be a greater detriment than individual threading dislocations. It is also worth reiterating that *ex-situ annealing has been found to result in a measurable drop in threading density of almost two orders of magnitude* in the case of 75046 (30%, 850-750ºC).

The surface roughness measured for the high and low temperature 30% *in-situ* annealed samples (~2-3 nm RMS) were comparable with previously published works. *Ex-situ* annealing had little effect on the RMS surface roughness of either 75046 (30%, 850-750ºC) or 75048 (30%, 700-600ºC). The surface-cross hatching in this compositional regime has a more usual appearance, almost certainly as a result of achieving the intended grading.

The unexpectedly low threading dislocation pile-up density present on the surface of the linearly graded 30% structure (Figure 5.21 (c)) together with the cross-sectional TEM observations of dislocation formation at the initial growth interface (Figure 5.9 (a)) may suggest that surface contamination, believed to be carbon, could have a significant effect upon dislocation formation. Houghton *et al.* (1995) found a linear dependence between surface particulate density and misfit dislocation nucleation rate, but did not study the effect of an initially high nucleation source on the threading dislocation pile-up density resulting from virtual substrate growth and further work appears warranted in this area. To this end a series of linear or terrace graded layers should be grown upon chemically cleaned substrates and comparison made between the same structures grown upon substrates where controlled amounts of carbon have been purposely deposited (seeded). I speculate that *a seeded layer may be beneficial in reducing threading dislocation pile-up* in linearly graded samples and could even be of benefit in terrace grading and may explain why in this instance the terrace graded structure showed only a two fold improvement over the linearly graded comparison structure.

A trend of increasing field threading density with final layer composition is apparent from Figure 5.22 but is not expected to occur for terrace graded structures. A similar trend of increasing field threading dislocation density has been observed by Leitz *et al.* (2001) between 30% and 40% virtual substrates although it was accompanied by an increasing pile-up density to which it was attributed. In the present work the absence of observable surface threading dislocation pile-up indicates that few instances of large misfit pile-ups exist, as intended for terrace graded growth. The rising field threading dislocation density is thus likely to be a consequence of

either too great a reduction in growth temperature, reduced with increasing composition to maintain a planar growth surface or contamination.

A higher threading density at lower temperatures has been observed by the authors Leitz *et al.* (2001) and Bogumilowicz *et al.* (2005) due to the necessity for a greater misfit density to compensate for the reduced threading dislocation glide velocity. However, the current work contradicts these findings showing far lower threading dislocation densities at lower growth temperatures. As discussed in chapter 4 the presence of point defects formed from ion bombardment, not removed during growth, may be responsible for dislocation annihilation upon annealing. A further possible source of point defects highlighted by Fitzgerald *et al.* (1997) is the formation of jogs by the interaction between moving glissile dislocations; once formed jogs can only move though (climb) the generation of point defects. Repeated growth of lower temperature structures without the final *in-situ* anneal step may shed light upon this situation and is left as further work.

Chapter 6

6 High Composition Regime (60-100%)

The virtual substrate structures fabricated and analysed in this high composition regime are ultimately to provide (i) a pure germanium platform upon a silicon substrate that could then be utilised for integration of III-V optical devices and (ii) to provide a platform for the fabrication of strained or relaxed bulk germanium epitaxial layers (e.g. for transistor manufacture). According to Fitzgerald *et al.* (1997) the production of usable III-V light emitting structures requires a surface threading dislocation density between 10^4 and $10^6/cm^2$ depending on application and is more stringent than that for majority carrier devices such as MOSFET's. With the need for high-k dielectrics approaching in standard silicon MOSFET devices, it may be advantageous to move directly toward germanium channel devices with an exotic high-k dielectric.

Current state of the art virtual substrates with germanium termination have been manufactured by Currie *et al.* (1998) through conventional linear grading at a rate of 10%/μm and at descending temperature (750-500ºC). A CMP (chemical mechanical polishing) stage is incorporated midway to reduce surface roughening and threading pile-up density. This yields a 100% germanium virtual substrate with a surface threading density of $2.1x10^6/cm^2$ and a surface roughness of 24 nm. This compares to a more traditional linearly graded structure grown at 900-800ºC without interruption having a surface dislocation density ~$1x10^7/cm^2$ and surface roughness of 210 nm (Fitzgerald *et al.* 1997).

Kwon *et al.* (2005) have already demonstrated the fabrication of a working AlGaInP light emitting diode structure upon a germanium virtual substrate (Currie *et*

al. 1998) and even found improvements over structures grown on existing III-V based substrates. GaAs epitaxy has additionally been demonstrated by Andre *et al.* (2003) upon a virtual substrate structure (Currie *et al.* 1998).

More exotic structures and methods have been attempted by various authors in the production of virtual substrates with a pure germanium termination that also achieve threading density of ~$10^6/cm^2$. A reduction of surface RMS roughness to only 3.2 nm ($3x10^6/cm^2$) has been demonstrated by Luo *et al.* (2003) by combining low temperature growth, annealing and large step changes in composition. An intriguing approach has been taken by Li *et al.* (2004) in the formation of a germanium layer upon an ultra thin SiO_2 layer through which it can "touch down" acting as a nanoscale seed for germanium over-layer growth. This resulted in a defect density of $2x10^6/cm^2$, though unfortunately no roughness data was included. Promising results have been obtained by Nayfeh *et al.* (2004) through high temperature annealing under a hydrogen atmosphere of CVD germanium material, grown directly onto a silicon wafer surface. A surface roughness of only 3 nm has been demonstrated for a 200 nm thick germanium layer; no information on surface threading density has been published.

Having established that terrace grading does have a positive impact on the structural quality of a virtual substrate, this investigation is extended toward a pure germanium terminating composition. The increasing length of time required in growing comparable virtual substrate structures with high compositions, combined with a greater likelihood of MBE growth system error at some point during growth, result in a limited number of sample structures. Presented here are three virtual substrate structures, two with terminating compositions of 60% and one reaching pure germanium.

6.1 Growth Parameters

The initial 60% terrace graded virtual substrate is similar in structure to layers grown in the preceding composition regimes, consisting of a 1 μm graded layer followed by a 1 μm layer of constant composition that is repeated every 10%, 75056 (60%, 1 μm/1 μm, 825-650ºC), Figure 6.1.

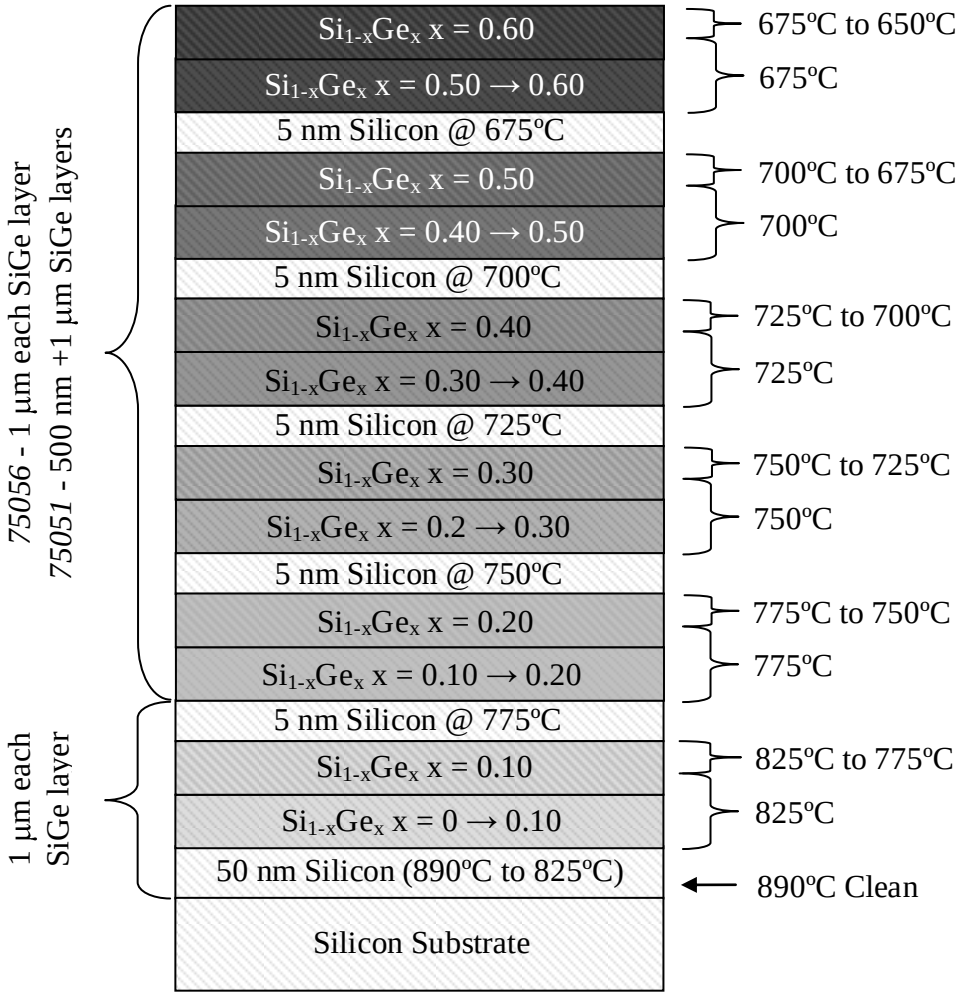

Figure 6.1 – Schematic representation of 60% virtual substrate specifications for 75051 (60%, 500 nm/1 μm, 825-650ºC) and 75056 (60%, 1 μm/1 μm, 825-650ºC).

The growth temperature was held constant throughout the graded region and through half of the constant composition region before being linearly ramped down over the later half. The initial temperature drop was chosen to be 50ºC compared to only 25ºC

in all subsequent ramps, aiming to achieve a high degree of relaxation in the bottom most layers. Silicon markers layers were included at the top of each buried constant composition layer to show any roughening of the surface should this occur.

An additional 60% virtual substrate was grown, 75051 (60%, 500 nm/1 μm, 825-650ºC), identical in all respects to the previous 60% except that after the initial graded layer (0-10%) all subsequent graded layers were reduced in thickness to only 500 nm, see Figure 6.1. This was done to investigate both the smoothing effect of the overlying layers and to determine whether the graded layer thickness could be reduced without too great an impact on structural quality.

A first attempt was made at a terrace graded virtual substrate with a 100% germanium terminating composition using thick 1 μm layers, 76009 (100%, 1 μm/1 μm, 825-550ºC). The underlying structure is identical to that of 75056 (60%, 1 μm/1 μm, 825-650ºC) with an additional four terrace graded layers, culminating at a final terminating composition of 100% germanium at a growth temperature of 550ºC. Due to the extremely long growth time (approximately 70 hour's) the silicon charge became heavily depleted at its centre and required melting back, described in chapter 3 (section 3.2.1.4). Growth was interrupted during the silicon capping layer at a composition of 50%, the electron evaporators ramped down and the wafer transferred under UHV conditions to the preparation chamber where it was isolated. A melt-back was performed and the wafer subsequently returned to the growth chamber. Growth restarted after the temperature had been raised to 675ºC and the structure completed. The structure is shown schematically in Figure 6.2.

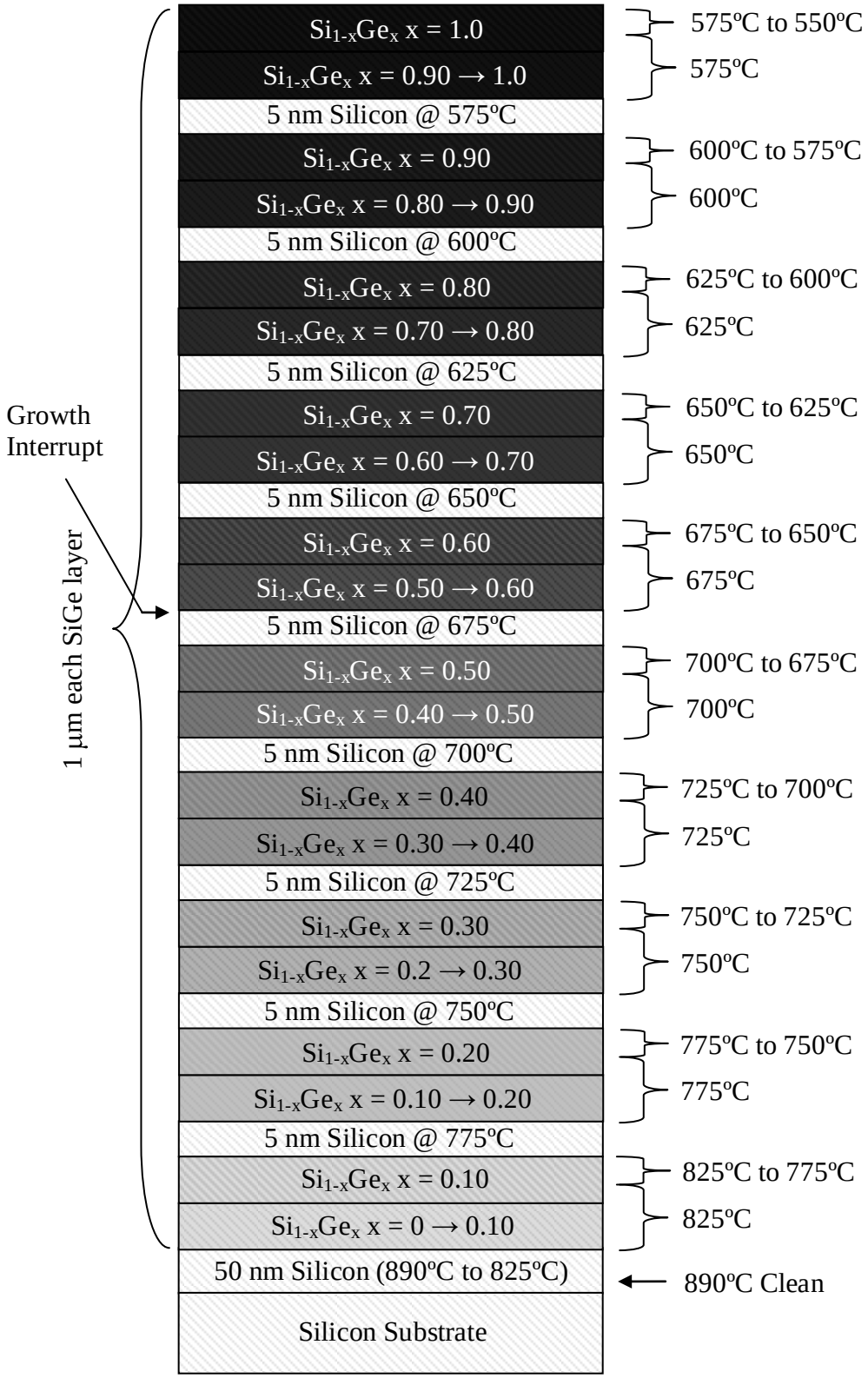

Figure 6.2 – Schematic representation of 60% virtual substrate specifications for 76009 (100%, 1 μm/1 μm, 825-550ºC).

6.2 Nomarski Interference Imaging

A representative selection of images obtained optically using Nomarski interference imaging of samples 75056 (60%, 1 μm/1 μm, 825-650ºC), 75051 (60%, 500 nm/1 μm, 825-650ºC) and 76009 (100%, 1 μm/1 μm, 825-550ºC) are given in Figure 6.3.

A striking difference in image contrast and cross-hatch density is obvious between the two 60% structures. The reduction in graded layer thickness of sample 75051 (60%, 500 nm/1 μm, 825-650ºC) has clearly resulted in cross-hatch with a reduced period of undulation and can be attributed to the greatly reduced spatial separation of misfit dislocations within the graded region. The increased contrast additionally indicates the onset of surface roughening, confirmed by cross-sectional TEM analysis (section 6.3) and demonstrates that a grading rate of 20%/μm is too great at this growth temperature.

At lower magnification the cross-hatch displayed by 75056 (60%, 1 μm/1 μm, 825-650ºC) appears similar to the 30% and 40% surfaces examined in chapter 5, Figure 6.3 (a). At higher magnifications flat topped features are visible in Figure 6.3 (b) and appear similar in appearance to features seen in the low composition regime attributed to non-linear grading. Here X-ray analysis indicates that the change in composition between subsequent terraces is less than intended, deviating most greatly for higher compositions, though the grading appears to be linear. It would appear that adatom incorporation has begun to occur preferentially outward from raised surface features, primarily at the intersection between prominent hatches. It is unclear why such structures have not been reported in published literature in this area, though it is possible that these features may be unique to terrace grading.

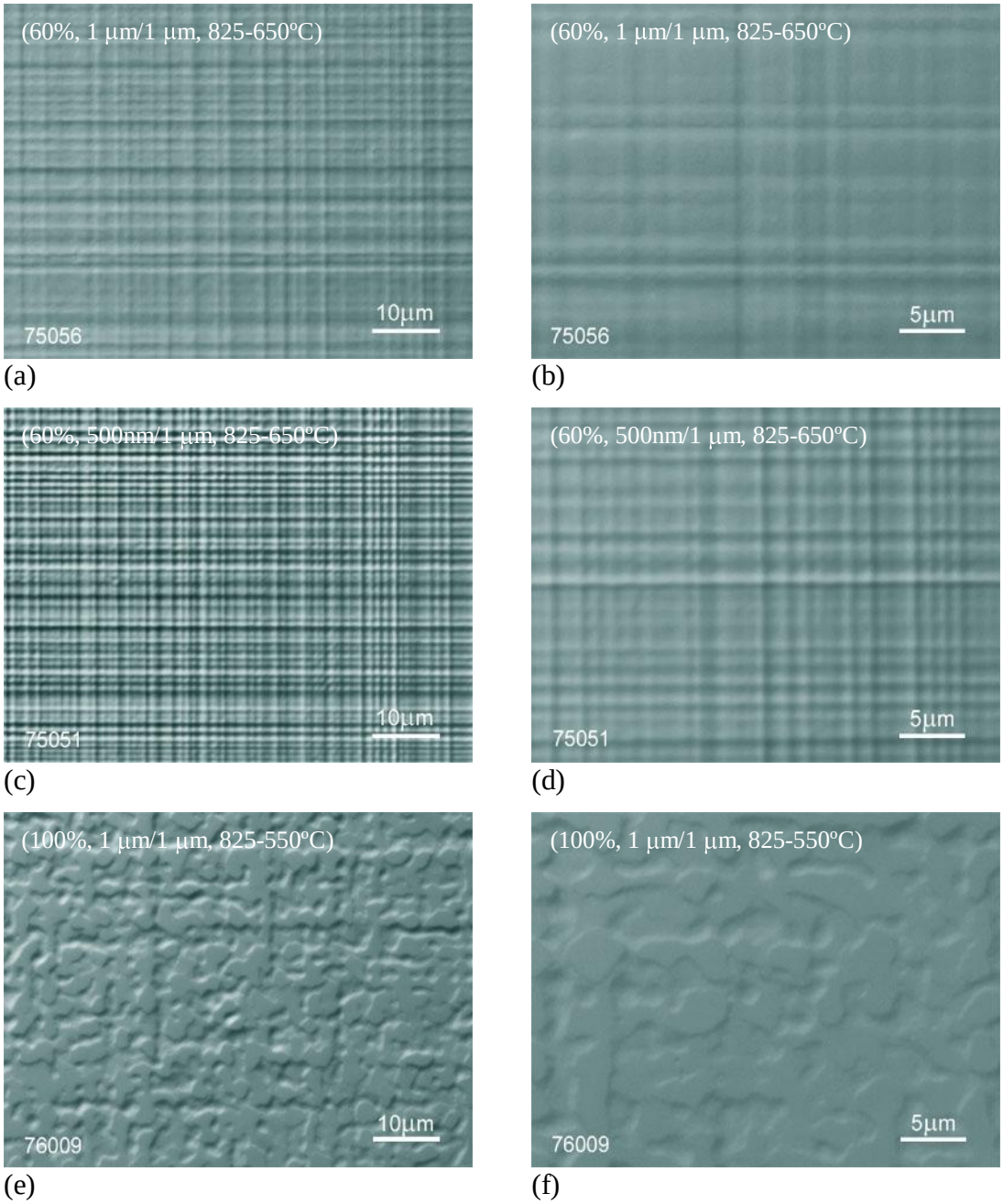

Figure 6.3 – Nomarski interference images taken at x50 and x100 magnification. (a) and (b) sample 75056, (b) and (c) sample 75051, (e) and (f) sample 76009.

An important observation evident on the surface of both 60% virtual substrates at low magnification is the high level of particulate debris, especially on sample 75056 (60%, 1 μm/1 μm, 825-650ºC) and may have an appreciable affect on the means and level of layer relaxation. The source of this particulate debris is clearly within the SS-MBE growth chamber. Material not epitaxially deposited upon a

wafers surface coats the inside of the growth chamber, in some cases forming fine whiskers of material that may be electrostatically attracted to the wafer surface. At over 9-12 μm of growth, particulate contamination is almost inevitable, especially toward the end of a growth series after deposition of many hundreds of microns of material, see Figure 6.4.

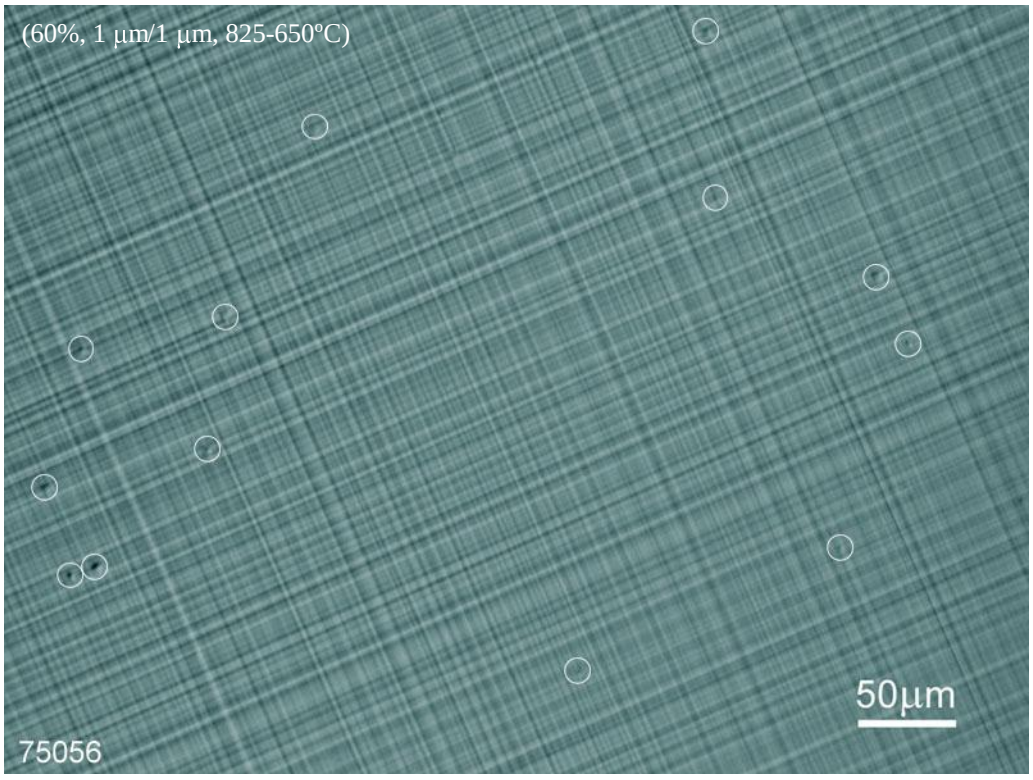

Figure 6.4 – Nomarski interference image of sample 75056 taken at x10 magnification. Particulate contamination is highlighted with white rings.

The surface of 76009 (100%, 1 μm/1 μm, 825-550ºC), Figure 6.3 (e and f), is very unusual in comparison to the cross-hatched surface on virtual substrates of lower terminating surface concentrations, showing a weak cross-hatch pattern consisting of many large flat interconnected island regions. The greater contrast of these surface features indicate that the surface may have roughened to form islands which is supported by cross-sectional TEM and AFM. The origin of this surface morphology

may be the result of a large jump in composition experienced by the capping germanium layer as revealed by X-ray analysis (section 6.5). The apparent coalescence of islands to form a continuous film surface has been reported by Sheldon *et al.* (1985) and may explain the merging appearance. The density of particulate contamination on the surface of 76009 (100%, 1 μm/1 μm, 825-550ºC) appears lower than for 75056 (60%, 1 μm/1 μm, 825-650ºC) and is likely the result of growth in a system in a cleaner state.

6.3 Cross-Sectional Transmission Electron Microscopy (XTEM)

The dislocation network within 75051 (60%, 500 nm/1 μm, 825-650ºC) is highlighted using the (220) diffraction condition and presented in Figure 6.5 (a). Whilst the initially thick graded region contains a well separated dislocation network, dislocations within subsequent regions are more closely spaced as intended. The lack of visible dislocations spanning between graded regions demonstrates that a high degree of relaxation has been maintained throughout growth. It is clear from the upper surface that macroscopic surface roughening has taken place, reinforcing the optical surface observations made previously.

Examination of 75051 (60%, 500 nm/1 μm, 825-650ºC) in the (004) two beam diffraction condition proves enlightening, with the 5 nm silicon spacer layers serving there purpose in this instance, Figure 6.5 (b). The silicon layer placed at the top of each buried constant composition layer reveals the morphology of the surface at the instance it was buried, here roughening of the surface layers commences around the 30% region becoming progressively roughened. As suspected a graded layer thickness of only 500 nm results in elastic deformation of the surface and a reduction in growth temperature would be required in order to suppress this surface roughening.

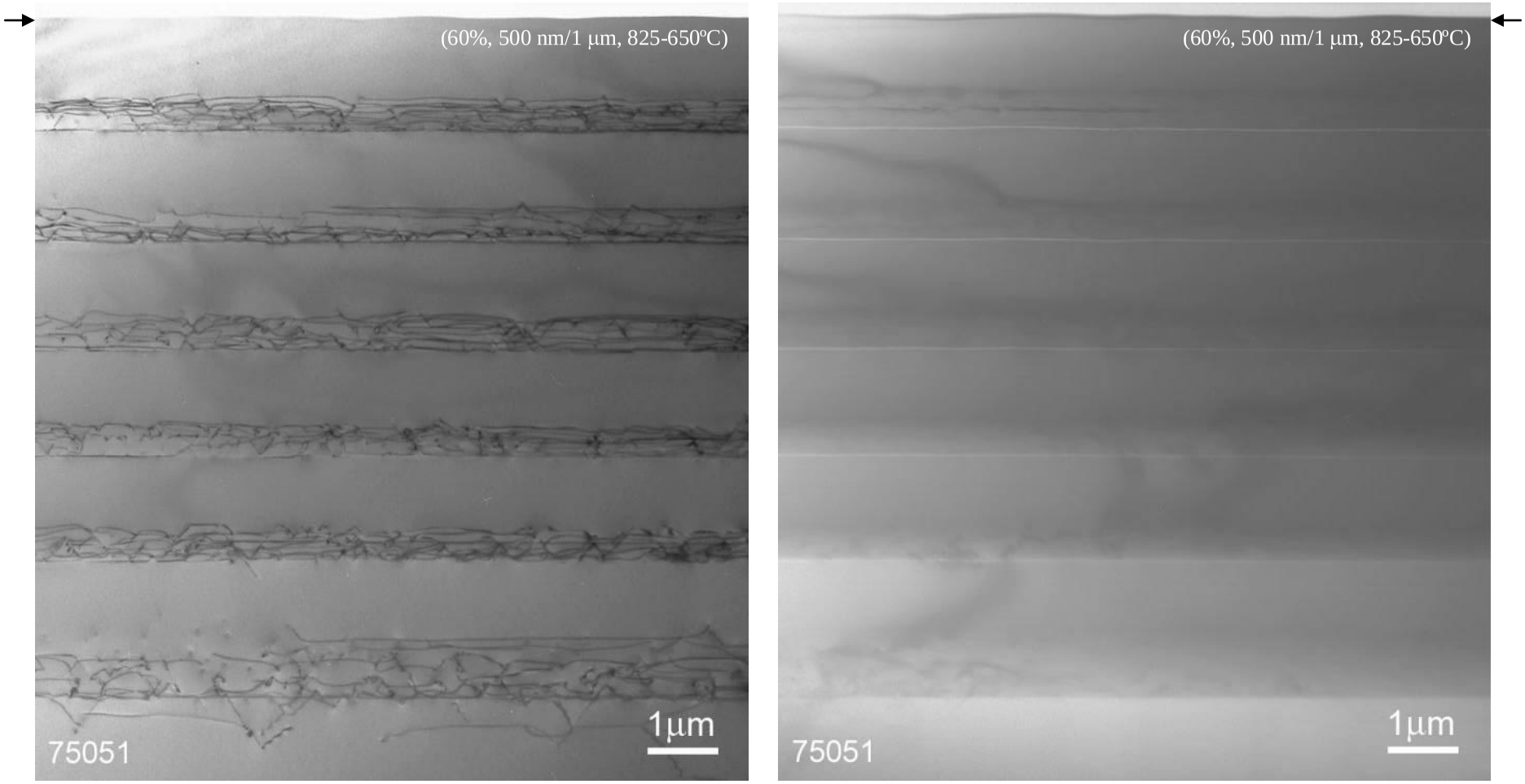

(a) (b)

Figure 6.5 – Cross-sectional TEM images of sample 75051 (a) (220) two beam 6.5 – Cross-sectional TEM images of sample 75051 (a) (220) two beam diffraction Cross-sectional TEM images of sample 75051 (a) (220) two beam diffraction condition

EDS measurements of layer composition along with thickness measurements of each terrace graded layer are presented in Table 6.1. The layer compositions are close to that intended as are the layer thicknesses.

	10%	20%	30%	40%	50%	60%
Composition	9%	20%	32%	42%	50%	56%
Thickness	1.9 μm	1.5 μm	1.5 μm	1.5 μm	1.6 μm	1.6 μm

Table 6.1 – EDS composition data for 75051 (60%, 500 nm/1 μm, 825-650ºC) as well as thickness measurements made from cross-sectional TEM images. Compositional error of ±10% due to thickness of sample. Combined layer thickness ± 5%.

In contrast to the above, cross-sectional TEM images of sample 75056 (60%, 1 μm/1 μm, 825-650ºC) show no signs of macroscopic surface roughening as evident in Figure 6.6 and Figure 6.7. The lack of obvious roughening is a good indication that grading at 10%/μm at the chosen growth temperature allows a high degree of relaxation at a rate great enough to prevent strain build-up. It should be noted that signs of large scale dislocation multiplication are much less evident than in comparable published structures (LeGoues *et al.* 1993; Hartmann *et al.* 2000; Rosenblad *et al.* 2000). The upper two graded regions (40-50% and 50-60%) appear to contain fewer dislocations than preceding layers (Figure 6.6), indicating either a lower level of relaxation or a reduced compositional difference between the bounding constant composition layers. EDS analysis of this sample proves enlightening, supporting the latter case, Table 6.2.

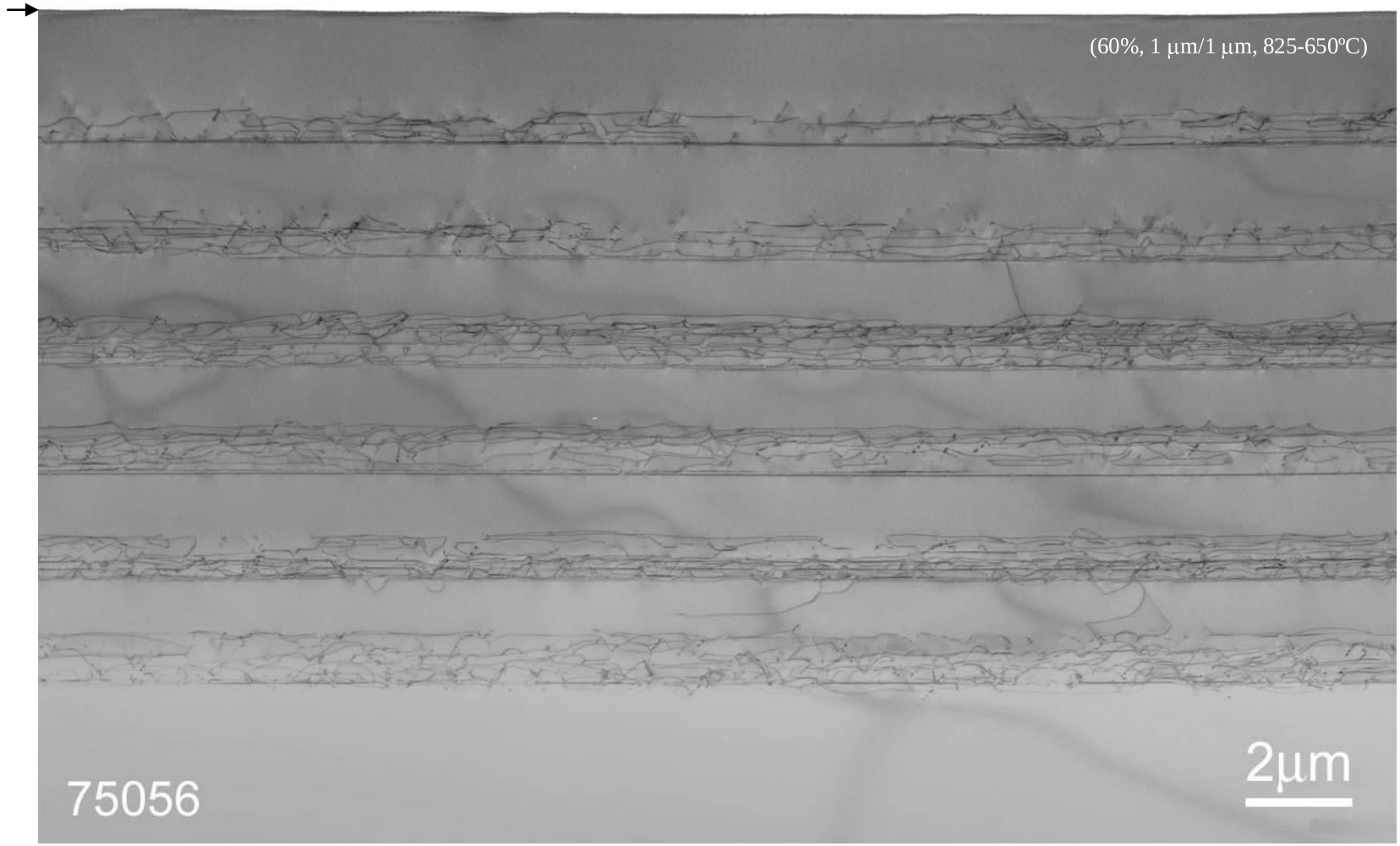

Figure 6.6 – Cross-sectional TEM image of sample 75056 in the (220) two beam 6.6 – Cross-sectional TEM image of sample 75056 in the (220) two beam diffraction Cross-sectional TEM image of sample 75056 in the (220) two beam diffraction

Figure 6.7 – Cross-sectional TEM image of sample 75056 in the (004) two beam – Cross-sectional TEM image of sample 75056 in the (004) two beam diffraction sectional TEM image of sample 75056 in the (004) two beam diffraction condition TEM image of sample 75056 in the (004) two beam diffraction condition highlighting

	10%	20%	30%	40%	50%	60%
Composition	9%	18%	27%	37%	44%	48%
Thickness	2.0 μm	2.0 μm	2.0 μm	2.1 μm	2.2 μm	2.4 μm
Calculated Composition	10%	20%	30%	40%	45%	50%

Table 6.2 – EDS composition data for 75056 (60%, 1 μm/1 μm, 825-650ºC) as well as thickness measurement made from cross-sectional TEM images. A calculated composition based upon additional layer thickness being solely attributed to excess silicon deposition is also presented. Compositional error of ±10% due to thickness of sample. Combined layer thickness ± 5%.

There is an increasing discrepancy between the intended composition and that achieved throughout the structure. This discrepancy can almost certainly be attributed to the flux monitoring system utilised in the V90S growth system. Growth of 75056 (60%, 1 μm/1 μm, 825-650ºC) required a total deposition of more than 12 μm of material, far in excess of the limit envisioned for such a system. The thickness of each terrace graded layer has been determined through measurement of the distance between silicon spacer layers (Figure 6.7) and for lower layers by measurement between the bottoms of dislocation networks (Figure 6.6) with the results presented in Table 6.2.

Calculations of layer composition assuming the observed increase in layer thickness is solely attributable to excess silicon deposition are also presented in Table 6.2 and the trend observed closely matches these calculated values. The sharp deviation visible in the top two layers illustrates how the flux monitoring system is increasingly vulnerable to over compensation as the charge is depleted. Separate work has been undertaken by the author to correct the geometric problems that appear to be the route cause of such situations by resituating the internal flux monitoring heads directly above the electron evaporators. An overview of this work was given in chapter 3 (section 3.2).

The cross-sectional TEM image of 76009 (100%, 1 μm/1 μm, 825-550ºC), presented in Figure 6.8 shows a variety of unique and interesting features. Quite clearly a dramatic event has occurred after completion of the 50% constant composition layer and corresponds to the interruption in growth necessary to perform a melt-back of the silicon electron beam evaporator charge. The re-growth surface has produced a cascading increase in threading dislocation density that is clearly visible in the cross-sectional TEM image (Figure 6.9). It is not clear why the location of the dislocation cascade remains fixed through successive layers (Figure 6.9) or why the dislocation density continues to rise with continued growth. The source of contamination on the re-growth surface was accrued presumably during transfer between chambers. An oxide layer may have formed, had this been anticipated a high temperature clean could have been performed before growth recommenced at 50%. EDS analysis of 76009 (100%, 1 μm/1 μm, 825-550ºC) is presented in Table 6.3.

	10%	20%	30%	40%	50%	60%	70%	80%	90%	100%
76009 (100%)	10%	20%	30%	41%	49%	62%	68%	76%	81%	97%

Table 6.3 – EDS compositional data for 76009 (100%, 1 μm/1 μm, 825 550ºC). Compositional error of ±10% due to thickness of the sample.

The presence of a large number of threading dislocations highlights an interesting event occurring across the final constant composition layer. The number of threading dislocations penetrating through the final layer to the surface has been dramatically reduced in comparison to the underlying layers, Figure 6.8, Figure 6.9 and Figure 6.10.

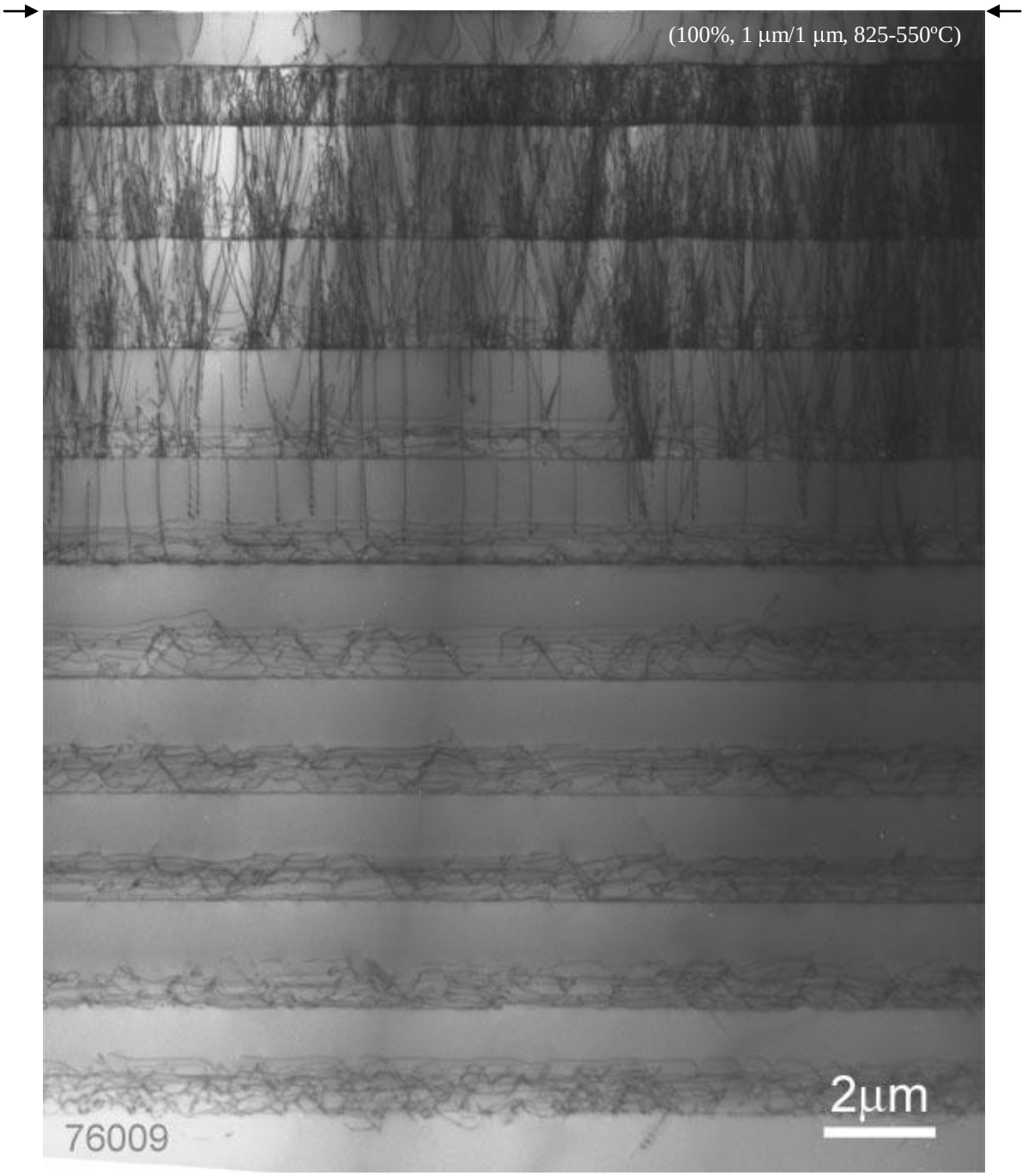

Figure 6.8 – Cross-sectional TEM image of sample 76009 in the (220) two beam diffraction condition highlighting dislocations within the structure. Arrows indicate the structures surface.

No structural difference had been intended for this later layer but EDS composition measurements (Table 6.3) show that a large change in composition did occur between the final two constant composition layers. More informative is the X-ray analysis that indicates a large compositional *jump* between the final graded and constant

composition layer. A detailed explanation of the compositional deviation is given in section 6.5.

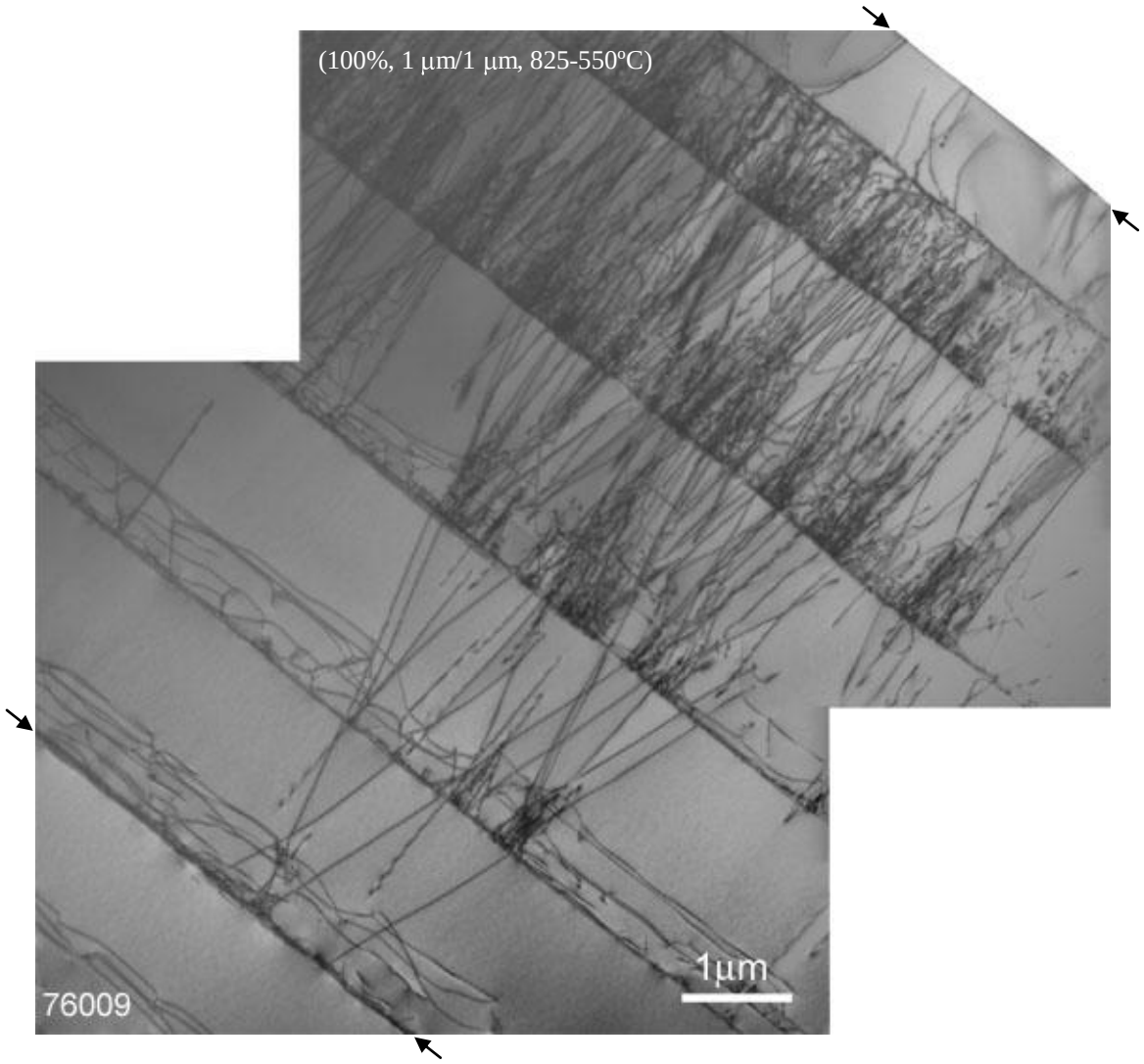

Figure 6.9 – Cross-sectional TEM image of upper structure of sample 76009 in the (220) two beam diffraction condition, highlighting dislocations within the layers. A cascade of dislocations is initiated at the upper interface of the 50% constant composition layer. The upper arrows indicate the structures surface and the lower arrows the re-growth interface (50%).

Yang *et al.* (2004) have found an almost identical filtering effect when incorporating a step change in a virtual substrate structure. It was found that a critical compositional change was required for this effect to occur. The reduction *or blocking* of dislocations was considered to be the result of dislocation bending due to the stress field at the interface. Dislocation blocking could be of enormous benefit if such an

effect were to exist at a lower threading density; it is possible that such a reduction may only occur for the confinement of a very large number of dislocations at a single interface. The case of lower threading dislocation densities, not observable in cross-sectional TEM, is not considered by Yang *et al*. (2004) with further investigation warranted for this regime.

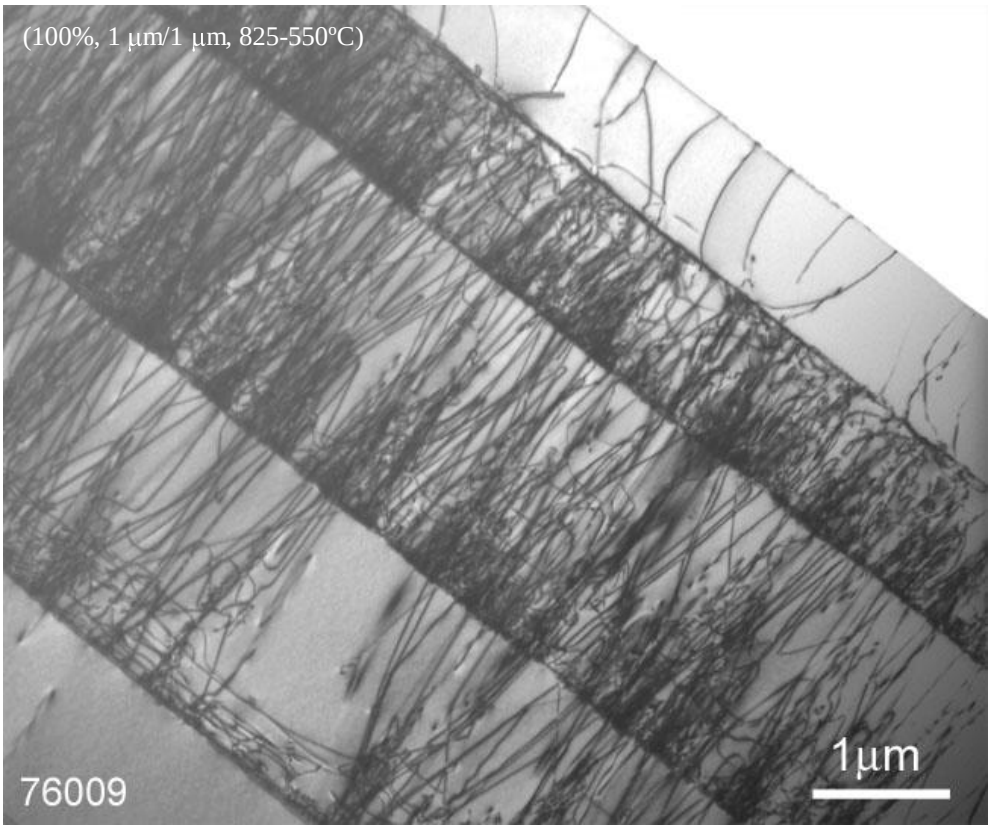

Figure 6.10 – Cross-sectional TEM image of upper structure of sample 76009 in the (220) two beam diffraction condition highlighting dislocations within the layers. A substantial reduction in dislocation density is evident between the upper interface of the final graded region and the overlaying germanium cap.

6.4 Atomic Force Microscopy (AFM)

Contact mode atomic force measurements were conducted on all of the high composition samples. All of the height profiles presented in this section have undergone 3rd order XY plane fit post processing.

The soft rounded appearance of the hatches on the surface of 75051, revealed by AFM in Figure 6.11, suggest that the grading rate of 20%/μm at the growth temperatures utilised has resulted in a 3-dimensional roughening of the surface and that the presence of 1 μm constant composition layers has had little or no planarising effect.

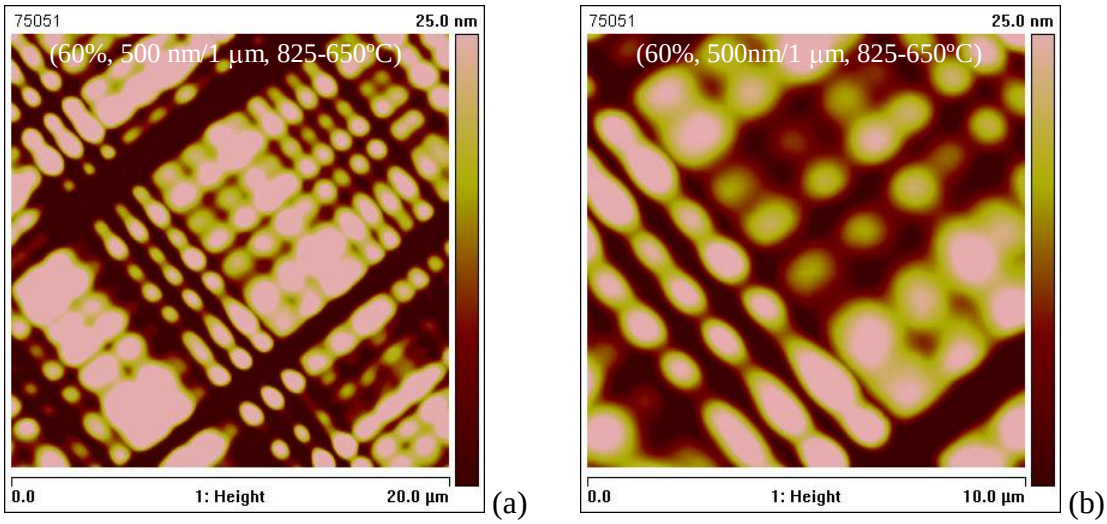

Figure 6.11 – Atomic force height profile scans of 75051 over an area of (a) 20 μm x 20 μm (b) 10 μm x 10 μm.

Optical imaging of 75056 (60%, 1 μm/1 μm, 825-650ºC) suggested that an unusual surface morphology had developed and is corroborated by the AFM images presented in Figure 6.12 that reveal a highly detailed and unusual cross-hatch structure. Flat topped islands are arranged following a cross-hatch pattern each bounded by multiple steps, larger than that of a single atomic step, ranging from

around 2-5 nm and diminishing in size away from the upper surface. X-ray and EDS analysis reveal that above the 40% region the grading rate effectively drops reaching a final terminating composition of only 50% with no other significant anomalies evident. There are no reports of comparable surface topology in the literature.

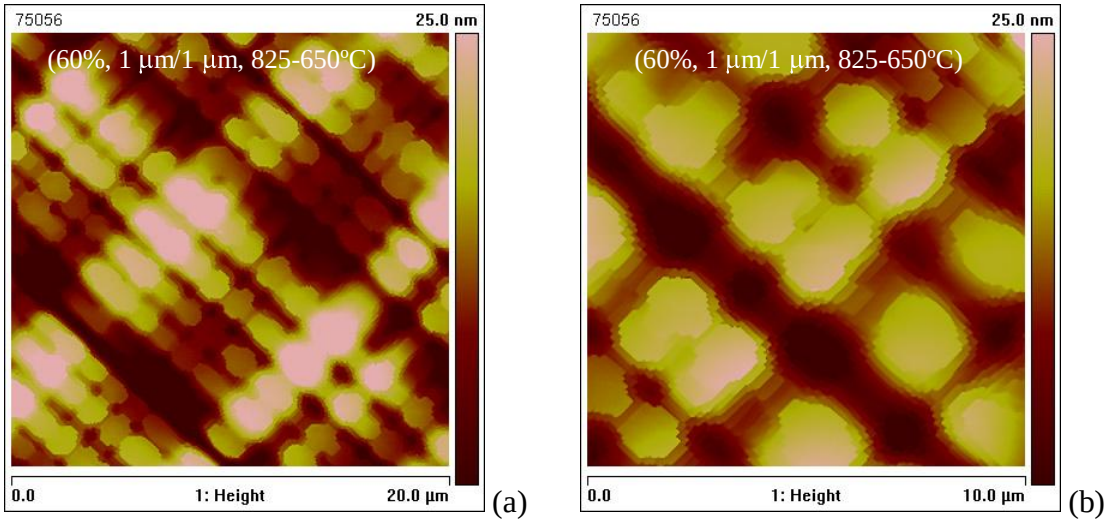

Figure 6.12 – Atomic force height profile scans of 75056 over an area of (a) 20 µm x 20 µm (b) 10 µm x 10 µm.

The surface of the 100% sample appears to consist of numerous multi-level islands loosely arranged in a cross-hatch pattern, see Figure 6.13. The large height variation between surface features could indicate that the structure has undergone a transition from layer-by-layer growth toward 3-D islanding or it may simply represent an evolution of the 60% surface structure. Interestingly each of the apparent islands remains flat topped. X-ray analysis (section 6.5) shows that the final constant composition layer experienced a large jump in composition (~18%) a result of incomplete compositional grading in the final graded region and could have had a significant effect upon the surface morphology. The high defect density seen in cross-sectional TEM could also have played a role.

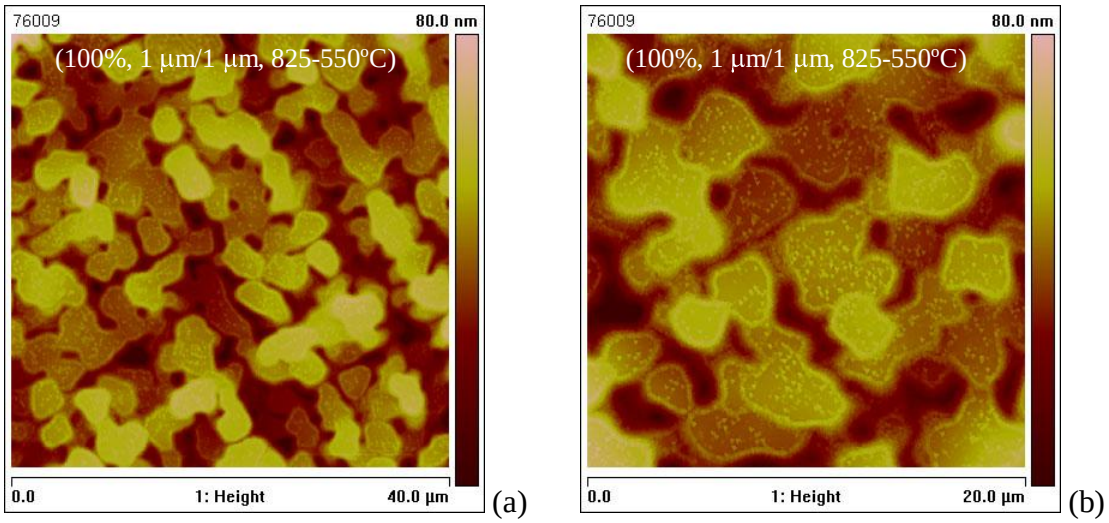

Figure 6.13 – Atomic force height profile scans of sample 76009 over an area of (a) 40 µm x 40 µm and (b) 20 µm x 20 µm.

Tiny features are visible on the surface of each plateau in Figure 6.13 (b), are perhaps silicon clusters sourced from the germanium flux that has been identified as containing around 1% silicon. The formation of silicon clusters on a bulk germanium surface is theoretically explicable because of the lower free energy of the germanium surface; silicon growth upon bulk germanium would be expected to follow the Volmer-Weber growth mode (chapter 2). Wang *et al.* (2004) have observed the formation of pyramidal 3D silicon clusters upon bare Ge (001) surfaces after deposition of several monolayers of silicon. More unusual is evidence of a raised perimeter around the edge of each of the plateaus, perhaps formed from silicon that has migrated out toward the edge becoming trapped at this location. Far greater study of this sample will be required to obtain a clearer understanding of these surface features, though such features would likely not be present if the layer had grown as intended.

Surface roughness measurements obtained from the AFM images are presented in Table 6.4. Caution should taken when making comparisons with the

RMS roughness measurements obtained for these samples as the AFM tip may have been unable to follow these abrupt changes precisely. These surfaces all share comparatively high levels of roughness and would require CMP before they could be used as suitable platforms for device processing.

	75051 (60%) 500 nm/1 μm, 825-650ºC	**75056 (60%)** 1 μm/1 μm, 825-650ºC	**76009 (100%)** 1 μm/1 μm, 825-550ºC
RMS Roughness	**14 nm ± 2 nm**	**8 nm ± 2 nm**	**13 nm ± 2 nm**
Height Range	**90 nm ± 15 nm**	**50 nm ± 15 nm**	**105 nm ± 15 nm**

Table 6.4 – RMS surface roughness and height range measurements determined from AFM images of samples 75051 (60%, 500 nm/1 μm, 825-650ºC), 75056 (60%, 1 μm/1 μm, 825-650ºC) and 76009 (100%, 1 μm/1 μm, 825-550ºC).

6.5 High Resolution X-ray Diffraction

Two sets of reciprocal lattice maps along the [004] and [224] directions have been taken with 90º rotations in phi (Φ). The determinations of terrace layer concentration and relaxation for samples 75056 (60%, 1 μm/1 μm, 825-650ºC) and 76009 (100%, 1 μm/1 μm, 825-550ºC) made from these measurements are presented in Table 6.5. The determination of layer composition for the 60% sample 75056 (1 μm/1 μm) agrees well with EDS measurements presented previously, showing that at 40% close agreement with the intended structure has been achieved. It is clear that the uppermost constant composition layer is less relaxed than the layer beneath which corroborates cross-sectional TEM observations of fewer dislocations in the top graded layer. An increase of only 5% in composition from the previously well relaxed layer results in a greater critical thickness and ultimately in less relaxation, this can be seen in Figure 6.14 (b).

The apparent trend of gradual increase in relaxation seen in Table 6.5 is unexpected, with the addition of overlying layers unrelaxed strain should preferentially be relieved in lower layers leaving them more relaxed.

	75056 (60%), 1 μm/1 μm, 825-650°C			76009 (100%) 1 μm/1 μm, 825-550°C		
	Comp. %	Relaxation %		Comp. %	Relaxation %	
Terrace		Φ=0°	Φ=90°		Φ=0°	Φ=90°
10%	10	94	95	10	99	94
20%	20	95	96	20	96	95
30%	28	96	97	30	98	96
40%	37	97	98	39	100	97
50%	44	99	99	46	102	98
60%	49	96	96	60	100	97
70%	-	-	-	66	100	98
80%	-	-	-	76	101	99
90%	-	-	-	83	102	100
100%	-	-	-	99	103	101

Table 6.5 – X-ray composition and relaxation data for samples 75056 (60%, 1 μm/1 μm, 825-650°C) and 76009 (100%, 1 μm/1 μm, 825-550°C). Compositional error no more than ±0.5%, relaxation error ±5%.

The angles between substrate and subsequent epitaxial layers in 75056 (60%, 1 μm/1 μm, 825-650°C) are found to be equal in magnitude but opposite in sign following a 90° rotation in phi (Φ) and reach a maximum deviation of 0.04° in omega (ω). This differs from previous results in the medium composition regime in which one direction generally exhibited a greater deviation. A possible explanation could be

that the wafer on which 75056 was grown had been offcut in a different direction to those previously investigated, perhaps toward [101] (at a surface angle of 45º to offcut in the [111] direction). This would help reinforce the idea that layer relaxation can differ in orthogonal directions due to offcut in a specific direction as the layers in this case share almost identical relaxation in both directions.

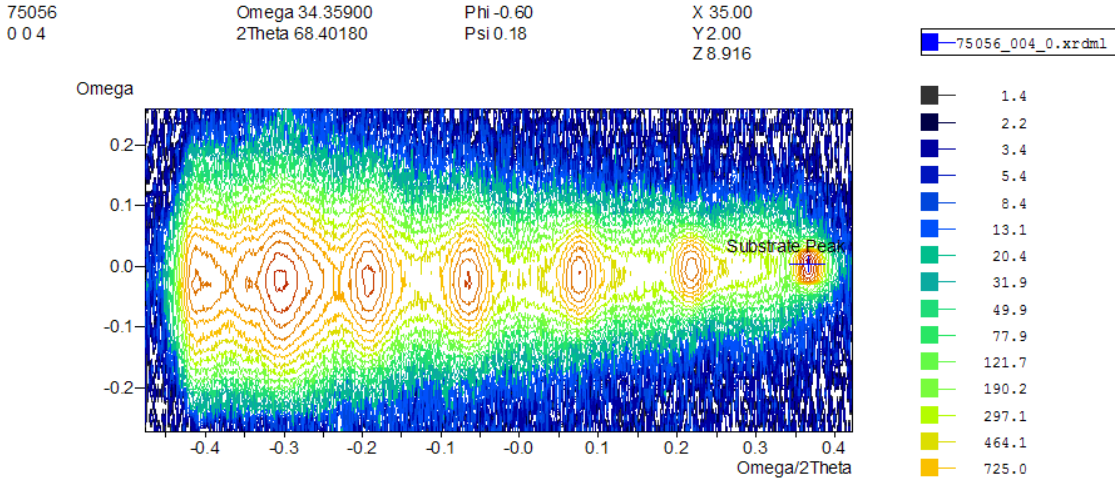

(a)

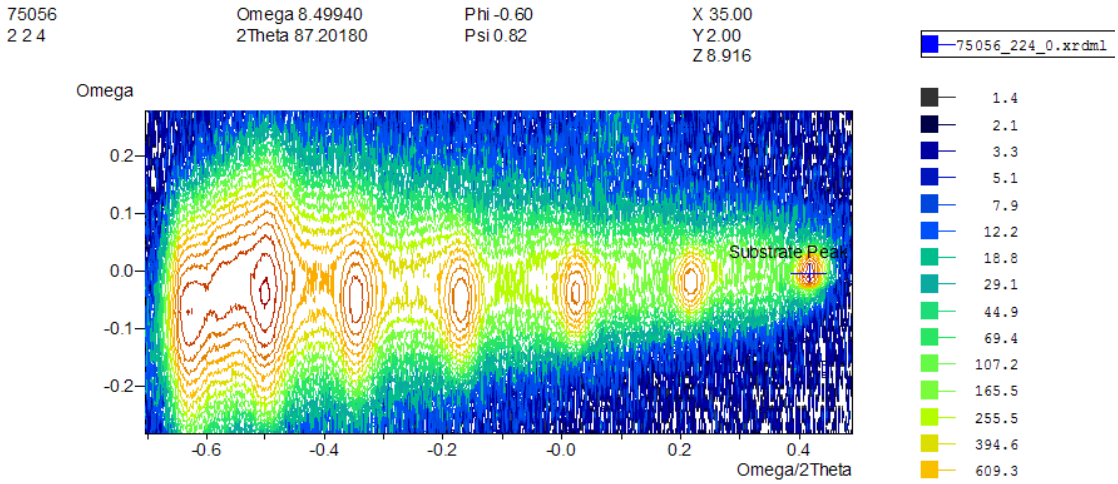

(b)

Figure 6.14 – Omega (ω) omega-2theta (ω–2θ) scans of sample 75056 (60%, 1 μm/1 μm, 825-650ºC) with phi (Φ) =0º along the (a) [004] direction (b) [224] direction. Peaks moving right to left correspond to increasing layer composition, with each peak resulting from a layer of constant composition.

The X-ray data obtained from the 100% sample 76009 had a number of interesting and noteworthy features. Taking the compositional variation throughout the structure in sections (Table 6.5), deviation from the intended profile can be better explained. The gradual deviation in composition of the constant composition layers up to 50% is attributable to the depletion of the silicon charge, as highlighted in section 6.3 and chapter 3 (section 3.2). The deviation in this instance is less than seen before, as expected for a newer charge the initially higher melt results in a smaller over compensation in power. It is clear the melt-back was successful, as the subsequent constant composition layer is almost exactly 60% as intended. The increasing compositional deviation moving to 90% terrace graded layers is unlikely to be the result of further silicon depletion, due to an ever decreasing silicon flux rate, nor does it seem likely to be the result of a depleting germanium charge as this would most certainly result in compositions greater than intended. This deviation is doubtless the result of a miss-calibration of the silicon power lookup curve, with the data suggesting that the power programmed for low silicon flux rates is too great. Elimination of such issues is entirely possible but will require greater diligence in the initial calibration of the systems electron evaporators.

It is clear from Figure 6.15 that the angle between the underlying silicon substrate and subsequent epitaxially grown constant composition layers varies differently in orthogonal phi (Φ) orientations in a manner similar that that previously seen in chapters 4 and 5. The departure in omega (ω) from that of the substrate suggests a reorientation of the layers in question, clearly the direction in which phi (Φ) = 0^{o} shows a steady departure in omega up to a maximum value of -0.11^{o} at 50% with the following layers all sharing this same deviation, see Table 6.6. This behaviour can be explained (described in chapter 5) by the unequal the projection of

equivalent Burgers vector onto the growth surface that cause a net tilt of the layer toward in this instance the (001), and once reached the imbalance between equivalent dislocations cesses to exist and the layer stops rotating, as witnessed past 50% in the present structure.

The distinct visible separation between the layer peak corresponding to the top surface and preceding linear layer in Figure 6.15 would suggest, that the final graded layer did not grade up to the intended terminating composition. This evidence is consistent with the observation of dislocation blocking observed between these layers in the cross-sectional TEM analysis, Figure 6.10.

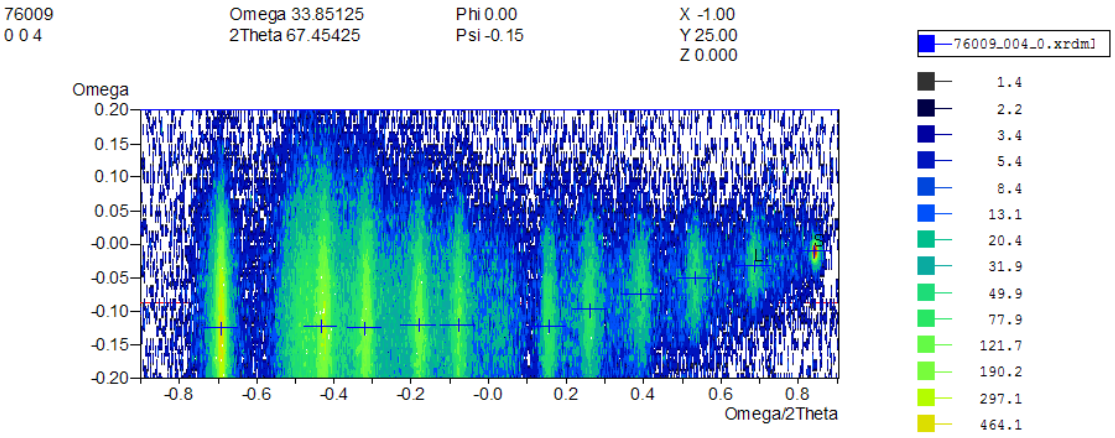

(a)

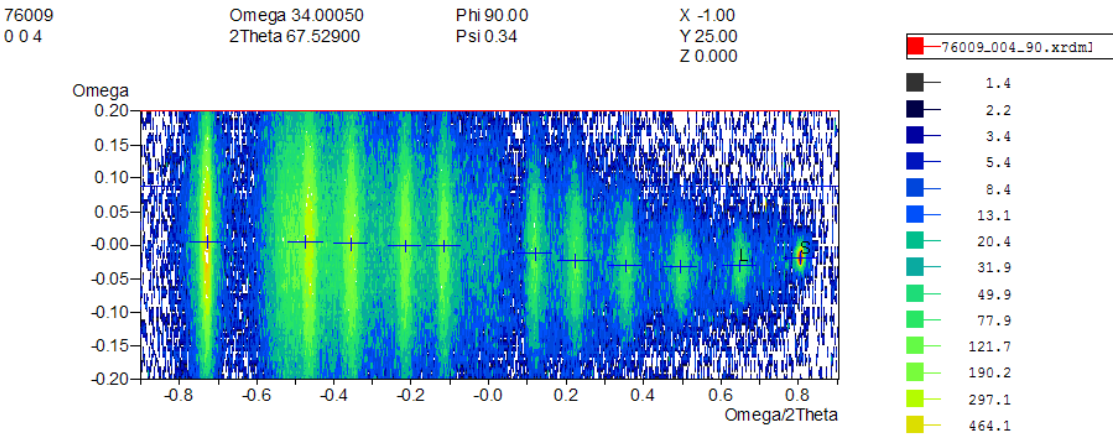

(b)

Figure 6.15 – Omega (ω) omega-2theta (ω−2θ) scans of sample 76009 (100%, 1 μm/1 μm, 825-550°C) along the [004] direction with (a) Phi (Φ) = 0° (b) Phi (Φ) = 90°. Peaks moving right to left correspond to increasing layer composition.

		76009 (100%, 1 μm/1 μm, 825-550°C)									
		10%	20%	30%	40%	50%	60%	70%	80%	90%	100%
α	Φ = 0°	-0.02	-0.04	-0.06	-0.09	-0.11	-0.11	-0.11	-0.11	-0.11	-0.11
	Φ = 90°	-0.01	-0.01	-0.01	0.00	0.01	0.02	0.02	0.02	0.02	0.02

Table 6.6 – Data collected for angular separation in omega between (004) planes in the silicon substrate and constant compositional layer, α, along orthogonal phi (Φ) directions. The error in determination of the angular separation ± 0.01°.

6.6 Schimmel Defect Etching

Surface threading dislocation density and pile-up have been highlighted as an important indicator of structural quality throughout the different compositional ranges investigated and this is no less true in the high composition range. Defect etching was performed using a standard Schimmel etchant only on the 60% samples. Schimmel etching was not performed on the 100% sample as it had become clear the surface threading dislocation density was extremely high, being visible in cross-section TEM. In addition to this Schimmel etching is not appropriate for defect revealing on a relaxed germanium surface, rather an Iodine etch should be utilised (Malta *et al.* 1992). A compilation of the calculated threading densities along with the standard deviation derived from variation in threading counts between images is presented in Table 6.7.

	75051 (60%) 500 nm/1 μm	75056 (60%) 1 μm/1 μm
Threading Density (/cm^2)	1.8×10^6	2.4×10^6
Standard Deviation (/cm^2)	1.6×10^5	1.1×10^5

Table 6.7 – Table containing threading dislocation densities for samples 75051 (60%, 500 nm/1 μm, 825-650°C) and 75056 (60%, 1 μm/1 μm, 825-650°C) calculated by counting surface etch pits optically at x50 magnification, accompanied by standard deviations. Standard Schimmel etchant employed.

The surface threading density of sample 75056 (60%, 1 μm/1 μm, 825-650ºC), a structure comparable with those grown previously at higher temperature, continues to increase in an exponential fashion as demonstrated in Figure 6.16.

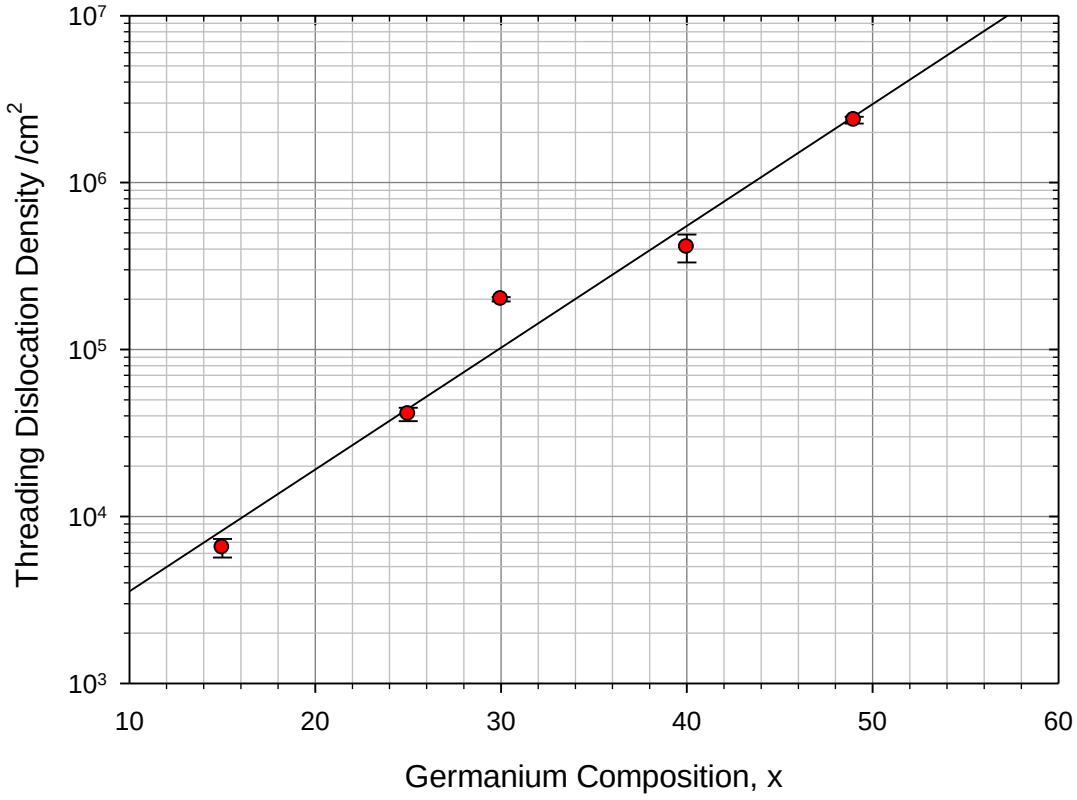

Figure 6.16 – Graph comparing the surface threading dislocation density between terrace graded virtual substrates grown at high starting temperature (850ºC). A distinct exponential trend is evident.

The continuing rise in threading dislocation density indicates that the introduction of additional misfit dislocations is necessary to maintain strain relaxation. In earlier structures the presence of large threading dislocation pile-ups was either uncommon or none existent. However a number can be seen dotted across the surface of all the current samples. The origin of pile-up in 75056 (60%, 1 μm/1 μm, 825-650ºC) does not appear to be intrinsically related to the structure but rather to the inclusion of many extrinsic particulates that litter the surface. An example of such

inclusions and the resulting pile-up revealed by Schimmel etching are shown in Figure 6.17. The line density of pile-up on the surface of 75056 (60%, 1 μm/1 μm, 825-650ºC) is far lower than observed previously in a 40% linear graded structure grown externally and examined in Chapter 5, 6443 (40%, Linearly Graded). That the presence of particulates at this high density play some role in the structural evolution of the layer cannot be excluded.

In contrast the surface of 75051 (60%, 500 nm/1 μm, 825-650ºC) contains a far greater instance of dislocation pile-up (Figure 6.18), expected because of the tighter lateral confinement of dislocations within the 500 nm graded region. The majority of the observed misfit pile-ups do not appear to originate at surface particulates although such instances are still present. The entire length of a dislocation pile-up is shown in Figure 6.18 (a) and at no point along its length (or even scanning some distance away) can any aligned particulates be seen, though the particulate at the lower left side of the image shows signs of less developed pile-ups forming outward. Interestingly there does not appear to be a large surface depression accompanying the pile-up, even in the higher magnification shown in Figure 6.18 (b), where individual threading dislocations within the pile-up can be distinguished.

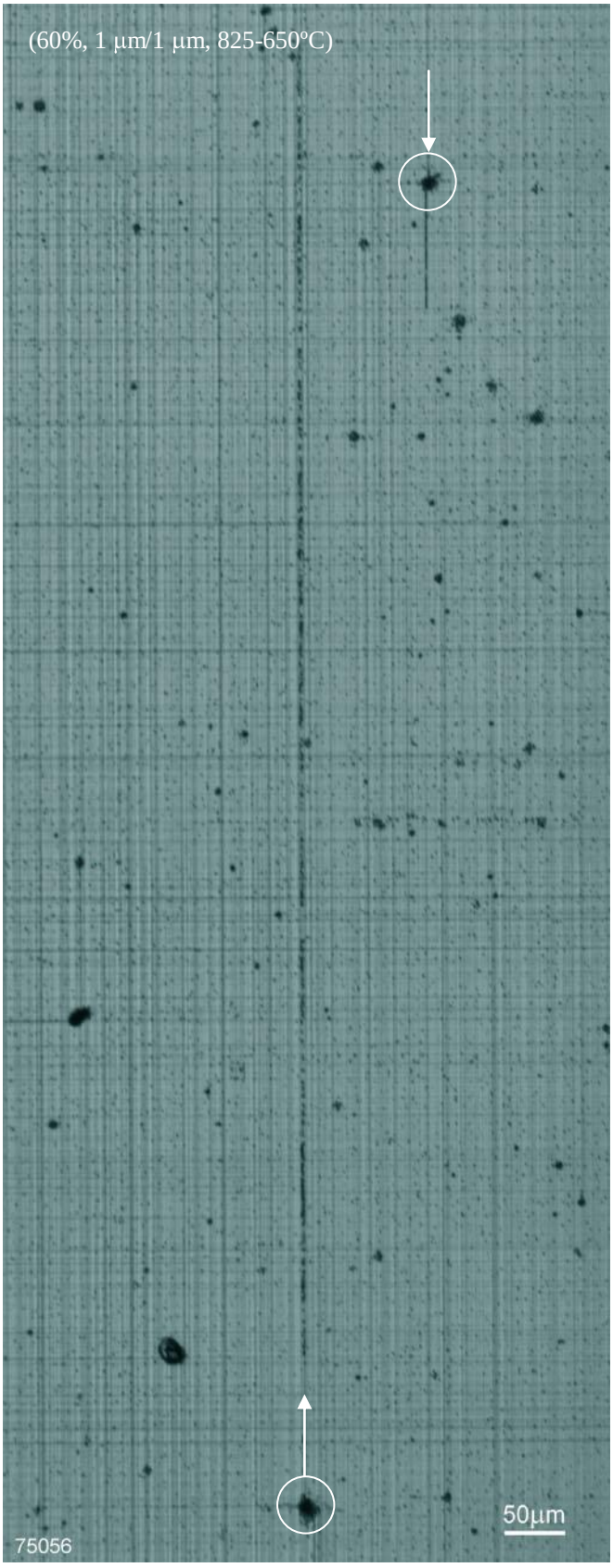

Figure 6.17 – Optical micrograph of the surface of sample 75056 after etching in a standard Schimmel etch for 3 minutes. Circles highlight particulate contamination that has resulted in threading dislocation pile-up, the arrows indicate the direction.

It should be realised that these images do not make use of optical interference that would more clearly highlight smaller surface features. The presence of a surface disturbance is evident in other images in the vicinity of pile-up, even without interference contrast (as etching tends to exaggerate such surface features). In a number of instances, pile-up can be seen to occur in the vicinity of far larger surface undulations (Figure 6.19) probably stopped short by an underlying strain field.

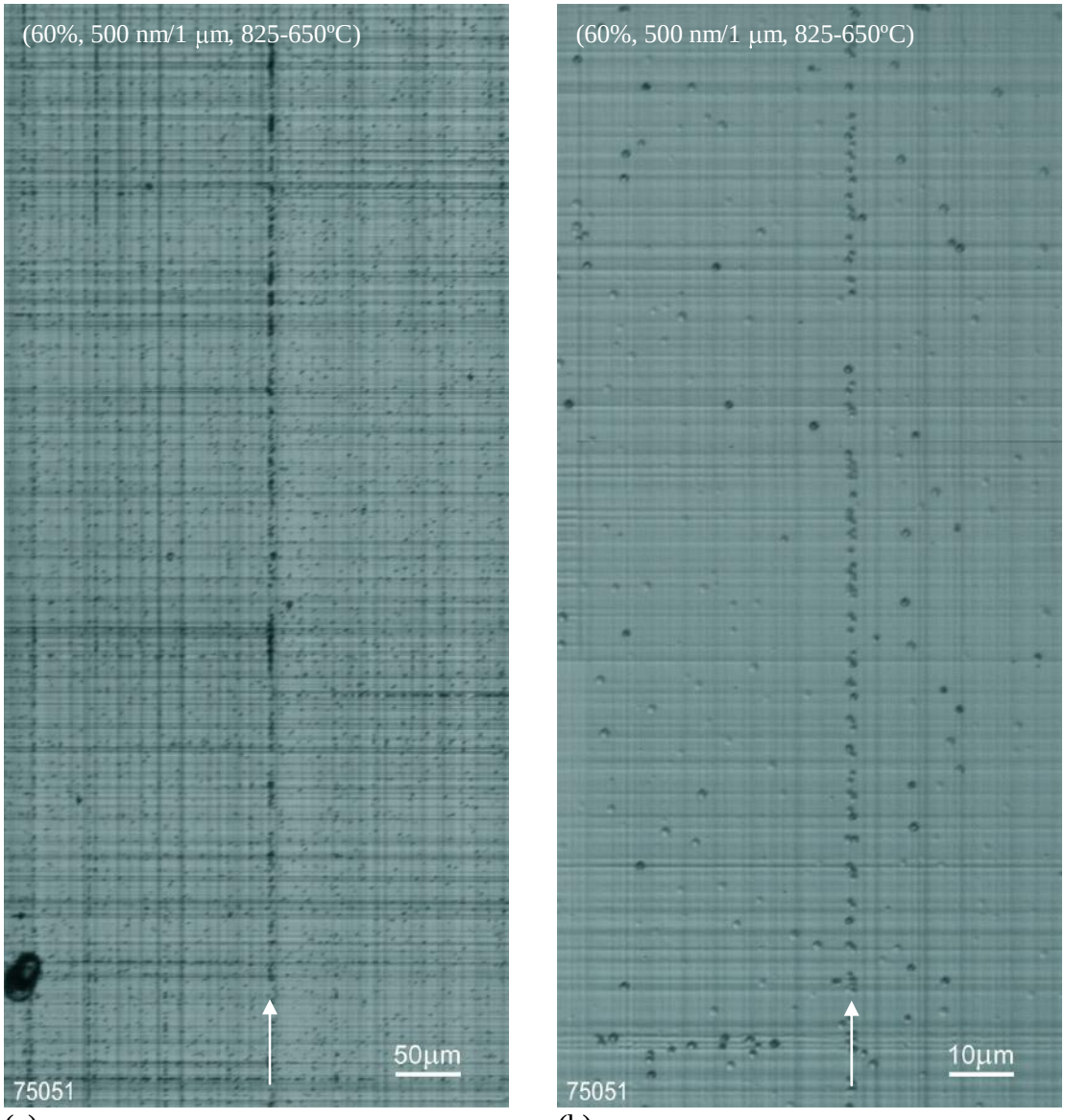

(a) (b)

Figure 6.18 – Optical micrographs of defect etched sample 75051 without optical interference at (a) x10 magnification (b) x50 magnification. The white arrows indicate the direction of threading dislocation pile-up. A surface particulate contaminant can be seen at the lower left of image (a).

Threading dislocations may still become trapped at deep surface undulations in the absence of a close accompaniment of misfit pile-up, but the depth must be sufficient to reduce the thickness of overlying layer to less than critical thickness required for dislocation motion, as stated by Freund (1990) and Fitzgerald *et al.* (1997). Such a reduction in layer thickness is clearly not present, and here all pinned threading dislocations will result from the reduction in excess stress by underlying arrays of misfit dislocations.

I believe that these observations demonstrate that terrace grading at 60% (1 μm/1 μm) has had the effect of releasing pinned threading dislocations between graded layers as intended and preventing the development of any deep surface trenches.

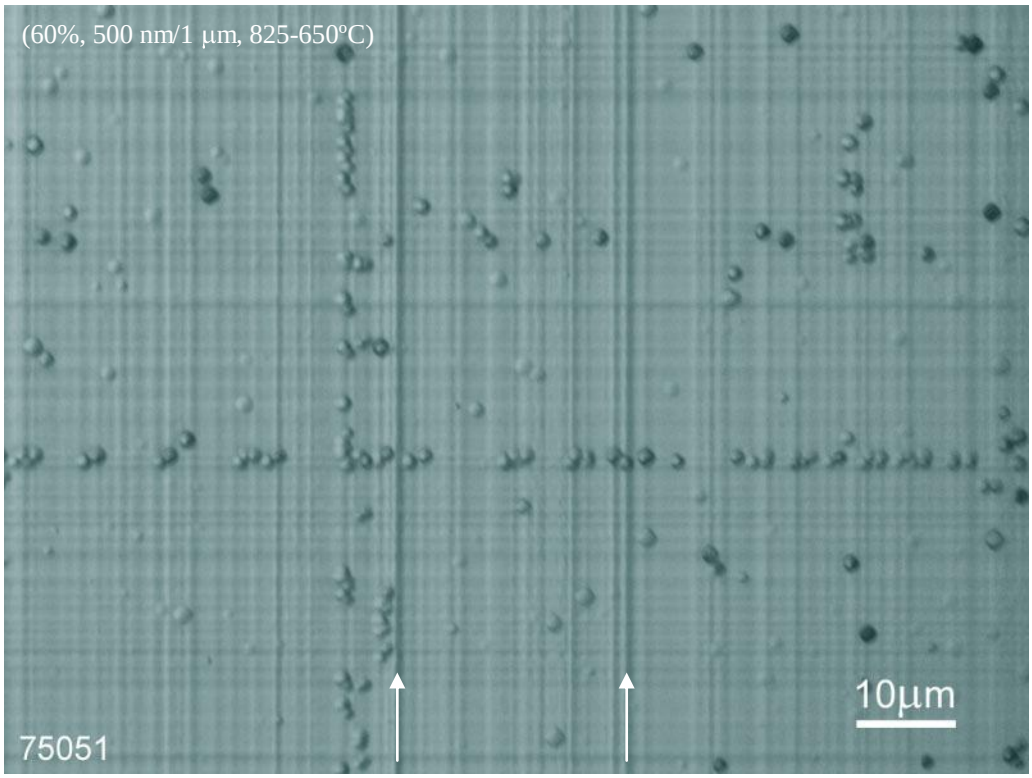

Figure 6.19 – Optical micrographs of defect etched sample 75051 without optical interference at x50 magnification. White arrows indicate large surface undulations that would appear favourable for dislocation pile-up yet have little.

6.7 Summary

In this high composition regime it has been found possible to eliminate threading dislocation pile-up, sample 75056 (60%, 1 μm/1 μm), originating intrinsically within the structure, although the inclusion of particulate contaminants had resulted in isolated instances of threading dislocation pile-up. The as-grown threading dislocation density of $2.4 \times 10^6/cm^2$ and RMS roughness of 8.4 nm at 50% compare unfavourably with values of $1 \times 10^6/cm^2$ and 3.1 nm respectively found by Capewell *et al.* (2002) for terrace graded structures with 200 nm thick graded and constant composition regions. However in the current study dislocation pile-up is largely absent and a high level of relaxation was achieved.

The continued exponential rise in threading dislocation density with composition, shown in Figure 6.16, should not occur for a terrace graded structure. In principle, the strain relieved by each terrace graded layer will be identical as long as layer relaxation remains high (which it appears to do). Deviation from this ideal situation could occur if (i) the mobile threading dislocations became pinned (or annihilated) or (ii) the glide velocity of the threading dislocations reduced with the growth of new layers. Table 6.8 shows the ratio of glide velocity for threading dislocations, under an identical level of strain, within different compositions at various temperatures utilised in the growth of 75056 (60%, 1 μm/1 μm, 825-650ºC), calculated using equation (2.3). The velocities have been normalised relative to that found for growth of the 10% layer at 850ºC. The glide velocity shows a similar variation for each terrace composition and temperature. The reductions would not appear significant enough to explain the exponential increase observed in threading dislocation density found from work in previous chapters. Since little dislocation

pinning is evident in the form of pile-up, a different mechanism would appear to be responsible.

	75056 (60%, 1 μm/1 μm, 825-650°C)					
	10%	**20%**	**28%**	**37%**	**44%**	**49%**
825	**1.0**					
775	**0.3**	**0.8**				
750		**0.4**	**0.8**			
725			**0.5**	**1.0**		
700				**0.6**	**1.0**	
675					**0.6**	**0.9**
650						**0.5**

Table 6.8 – Normalised ratio of dislocation glide velocity at various temperatures and compositions relative to that experienced at 10% composition at 825°C under identical levels of strain.

The inclusion of numerous particulates has been a continual problem for growth of structures and may provide an explanation for the rising dislocation density. *If the particulates were to provide a site for dislocation nucleation with a lower energy barrier than for continued glide of existing threading dislocations, then a rise in threading density could be expected*. Houghton *et al*. (1995) reported an activation energy of only 2.3 eV for thermally activated misfit nucleation close to that for dislocation glide (2 eV) and noted a linear relationship of nucleation with the initial contaminant level.

The unintended contamination of the 100% sample during the mid-growth interrupt resulted in a cascade of threading dislocations that served to highlight an important event at the final layer interface. The substantial reduction in threading

dislocation density, clearly visible in Figure 6.9, was an unexpected result. Dislocation filtering had been studied by Hull *et al.* (1989) by introducing strained superlattice structures into a silicon germanium epitaxial layer of uniform composition. Hull *et al.* (1989) reached the conclusion that the reduction of dislocation density occurred at a highly strained interface as a result of a deflection of threading dislocations into the interfacial plane, forming misfit dislocations at a common interface promoting dislocation annihilation. A simplistic model was proposed to determine the probability of dislocation annihilation that predicts a linear dependency on the threading dislocation density. This i*mplies that the effect upon lower threading densities would be negligible, as Hull et al. (1989) had found experimentally*.

Chapter 7

7 Conclusion

A detailed investigation into evaluating the full potential of the novel virtual substrate grading technique known as terrace grading has been conducted. Terrace grading describes a compositional profile composed of a series of linearly graded and uniform layers. The inclusion of uniform layers within the structure has been postulated to decouple multiplication mechanisms acting between successive terraced regions, such that large surface undulations and the pile-up of surface threading dislocations common to more conventional linear graded structures, are substantially reduced or eliminated. Whilst the previous work had clearly shown an improvement in this regard it had been limited to the investigation of structures with individual layer thicknesses of only 200 nm, involving grading rates far in excess of that commonly utilised. In this study the issue of layer thickness has been addressed along with the effect of growth temperature - pushing the technology of solid-source molecular beam epitaxy (SS-MBE) to its limit.

It was known at the outset that a high level of relaxation must be maintained throughout growth of a structure for the full advantage offered by terrace grading to be realised. *High resolution X-ray analysis confirmed that in the 1 μm layered structures a relaxation of > 95% was achieved for all compositions investigated*. It also revealed that in the 200 nm layered structures (with terminating compositions ≤ 25%), similar to those grown by Capewell (2002), that relaxation was ~70%. This result indicates that even with the application of *in-situ* annealing, layered structures of this dimension retain an unacceptably high level of strain, with further relaxation only achieved with additional growth. This apparent contradiction with earlier work

may be a result either from the inaccuracy of the simple X-ray scans employed previously to determine relaxation or as a result of the imprecise grading realised in the present study in the low composition regime. *It has become clear that precise control of the underlying grading is of paramount importance and has a pronounced impacted on surface morphology*.

For the various compositional regimes investigated it has been shown that *lower temperature growth results in smoother surfaces and in lower surface threading dislocation densities*, even though the latter is contrary to other published works. *A highly relaxed 30% silicon-germanium buffer grown at a temperature descending from 700ºC has been found to possess a surface threading dislocation density* $\leq 10^3/cm^2$ which is an order of magnitude lower than any other published works found by this author. This astounding result is believed to be the result of the formation and persistence of point defects within the structure allowing the annihilation of threading dislocations after each completed terrace during *in-situ* annealing. *A huge reduction in threading dislocation density has additionally been demonstrated through ex-situ annealing* of a 30% terrace graded structure, grown at a temperature descending from 850ºC and annealed under a nitrogen atmosphere at 900ºC for 15 hours. This extreme anneal also re-affirmed the high level of relaxation present within this structure, with little morphological change identifiable.

A complete absence of threading dislocation pile-up is demonstrated for terminating compositions up to 40% and is perhaps the most significant result of the current study. The complete elimination of threading dislocation pile-up is a major achievement for terrace grading and combined with a low threading dislocation density and high relaxation, undoubtedly places these structures among the very best achieved to date. *Comparison of a 30% terrace and linear graded structure grown at*

identical temperatures during this study revealed terrace grading to offer a 50 percent lower threading dislocation density. The low density of pile-up observed at the surface of the 30% linear graded comparison structure when compared to a 40% structure grown externally and along with evidence gained from cross-sectional TEM images of a 30% terrace graded sample, indicate that any possible contamination of the initial growth surface may play a role in the relaxation of a virtual substrate. The presence of heterogeneous nucleation sources at the start of growth could diminish the need for dislocation multiplication and could result in a reduced surface roughness for terrace graded layers.

As a consequence of the chosen grading rate (effectively 5%/μm) the overall thickness of virtual substrates with compositions > 30% was significantly greater than structures previously attempted within the VG V90S at the University of Warwick. *An initial attempt at producing a pure germanium virtual substrate resulted in a 20 μm thick structure requiring more than 70 hours of growth time*. The increasing density of particulate inclusion at compositions > 40% became a significant problem for SS-MBE growth and was found to allow the formation of localised pile-up as well as disrupting growth, complicating the analysis of such structures. *The presence of pile-up intrinsic to a terrace graded layer structure has only clearly been revealed at a composition of 60% in which the graded region had been reduced to 500 nm, clearly establishing a lower limit for realising the benefits of terrace grading*.

An undesirable increase in threading dislocation density with composition is evident between the terrace graded structures grown at higher temperature; such an increase was not expected to occur. The inclusion of particulate contaminants during growth has been suggested as a possible explanation, providing a nucleation source with an energy barrier similar to that for the continued glide of an existing dislocation.

7.1 Further Work

A number of intriguing avenues of further research have emerged as a result of the current study. A clear need exists to positively identify the source of increasing surface threading dislocation density with composition. Growth of multiple medium composition terrace graded structures at higher temperatures could allow thermally limited glide velocity to be eliminated as a cause. The effect of particulate contamination on threading dislocation density is however far more difficult to investigate as this is not a directly controllable parameter in SS-MBE. The surprisingly low threading dislocation density present for structures grown at lower temperature (700ºC and below) also clearly warrants further investigation and removal of *in-situ* annealing during growth may elucidate the mechanism for dislocation reduction. Further investigation into the effect of *ex-situ* annealing on terrace graded substrates at different temperatures and periods of time may help understanding of the dislocation reduction demonstrated in this instance.

The effect of chemical substrate cleaning and contamination at the initial growth interface on dislocation density, surface roughness and morphology deserves further investigation. Growth of a series of identical structures in which varying amounts of carbon are purposely deposited onto chemically cleaned substrates present a logical starting point. The presence of contamination below a certain level may prove beneficial in forming a smoother terrace graded surface, though possibly at the cost of an increased surface threading dislocation density.

Important lessons have been learned in growing a terrace graded virtual substrate with a pure germanium terminating composition and it is clear that regular growth interrupts are necessary to maintain accurate composition and thickness control by melting back the silicon charge. Ideally two melt-backs should be

performed in reaching pure germanium, at compositions of 30% and 60%; the wafer should be removed from the growth chamber during the procedure. Growth should be halted after deposition of a silicon marker layer and a high temperature desorb performed before growth is restarted to restore a clean surface. It is also important to ensure proper calibration of the silicon flux at low rates to avoid a large compositional jump to the final germanium layer.

Although solid-source MBE provides an excellent growth environment for research, the potential perturbing influences of particulate contamination on the strain relaxation process need to be fully understood and controlled before further systematic work is undertaken. In the pursuit of ultimate layer quality, the transfer of the terrace graded layer sequence to a chemical vapour deposition (CVD) growth tool would seem essential. Growth in a gas based system offers a number of key advantages such as; the elimination of particulate contaminants from flaking material within the growth chamber; a far higher growth rate than is typical in MBE, limited only by growth temperature; the continual presence of a surfactant (surface active agent) at lower temperature; and an almost inexhaustible supply of source material allowing growth of thick structures more easily with a far greater level of control. Early work conducted in this area at the University of Warwick confirms these benefits.

Appendix

A.1 Modified RCA Wet Chemical Clean

The aim of the RCA cleaning procedure (Radio Corporation of America) is to remove particulates both organic and inorganic as well as any chemically bonded contamination. The chemicals used in this clean were originally selected due to their availability at high purity and the clean empirically derived through experimentation. The solutions cause negligible etching of the silicon surface though this is critically dependant on temperatures and emersion times employed. The clean consists of two solutions known as SC-1 and SC-2 (SC stands for standard clean).

SC-1 is composed of deionised water (< 4 ppb), hydrogen peroxide (H_2O_2) and ammonium hydroxide (NH_3OH), in the ratio 5:1:1. The aim of this solution is to remove organic contaminants utilising the powerful oxidising properties of hydrogen peroxide, with the ammonium hydroxide acting as a complexing agent (keeping contaminants in solution). Ammonium hydroxide is additionally able to act as a complexing agent for light metal contaminants. The solution acts by dissolving the native oxide layer on the silicon surface before producing a new oxide layer. Each time this process is repeated any contaminants trapped within the new oxide layer are removed and larger particles dislodged.

SC-2 is composed of deionised water (<4 ppb), hydrogen peroxide and hydrogen chloride, in the ratio 6:1:1. The purpose of this solution is to remove heavy metal and ionic contaminants whilst preventing recontamination from solution. Unlike SC-1 this solution does not remove the oxide layer, it instead dissolves surface contaminants forming soluble complexes.

The modified RCA procedure adopted at the University of Warwick begins by immersing a carriage containing substrates in a 3 stage de-ionised water cascade rinse before transferring to SC-1 held at a temperature of 69ºC for 20 minutes. The carriage is then passed through the cascade rinse again before being given a brief 20 seconds 3% HF dip to remove the surface oxide. The procedure is then repeated with SC-2 but with the substrates individually spun dry after HF exposure, rather than immersing in the cascade, to retain hydrogen terminated surfaces. The passivated hydrogen surface can then be desorbed at relatively low temperature (550ºC) *in-situ* within the V90s growth system (Fuse *et al.* 1999).

A.2 Modified Piranha Wet Chemical Clean

Due to changing surface chemistry the RCA cleaning procedure is not appropriate for cleaning the surface of silicon-germanium virtual substrates (private communication T. J. Grasby). A Piranha clean consisting of sulphuric acid (H_2SO_4) and hydrogen peroxide (H_2O_2) in the ratio 3:1 is instead utilised on virtual substrates up to a composition of 60%. This clean is effective at removal of heavy organic particles by oxidation but does not desorb metallic contaminants. The mixture is self heating reaching about *130°C* and must be treated with extreme care; addition of H_2O initially aggravates the reaction. Substrates receive a 3 minute immersion in the piranha etch before being transferred to the cascade wash, followed shortly after by an HF dip for around 15 seconds (or long enough to make the surface hydrophobic). The HF dip strips the native oxide removing any impurities contained within leaving surfaces hydrogen terminated.

The reader is directed to the *Handbook of Semiconductor Wafer Cleaning Technology* (Kern 1993) for further details on the RCA cleaning procedure, as well as for a fuller investigation of the many other cleans available.

References

Agar, A. W. (1974). *Principles and Practice of Electron Microscope Operation*. Amsterdam, London, North-Holland.

Ahn, S. T., H. W. Kennel, *et al.* (1989). "*Vacancy Supersaturation in Si under SiO_2 caused by SiO Formation During Annealing in Ar.*" Journal Of Applied Physics **65**(8): 2957-2963.

AMD (2005). *AMD Athlon™ 64 X2 Dual-Core Processor Comparisons*, http://www.amd.com/us-en/Processors/ProductInformation/0,30_118_9485_13041%5E13076,00.htm.

Andre, C. L., J. J. Boeckl, *et al.* (2003). "*Low-temperature GaAs films grown on Ge and Ge/SiGe/Si substrates.*" Journal Of Applied Physics **94**(8): 4980-4985.

Archer, V. D. (1982). "*Methods For Defect Evaluation Of Thin (100) Oriented Silicon Epitaxial Layers Using A Wet Chemical Etch.*" Journal Of The Electrochemical Society **129**(9): 2074-2076.

Arias, J. M., M. Zandian, *et al.* (1991). "*Dislocation Density Reduction by Thermal Annealing of HgCdTe Epilayers Grown by Molecular-Beam Epitaxy on GaAs Substrates.*" Journal Of Vacuum Science & Technology B **9**(3): 1646-1650.

Bauer, G., J. H. Li, *et al.* (1995). "*X-ray Reciprocal Space Mapping of $Si/Si_{1-x}Ge_x$ Heterostructures.*" Journal Of Crystal Growth **157**(1-4): 61-67.

Bogumilowicz, Y., J. M. Hartmann, *et al.* (2005). "*Chemical Vapour Etching of Si, SiGe and Ge with HCl; Applications to the Formation of Thin Relaxed SiGe Buffers and to the Revelation of Threading Dislocations.*" Semiconductor Science And Technology **20**(2): 127-134.

Bolkhovityanov, Y. B., O. P. Pchelyakov, *et al.* (2001). "*Silicon-Germanium Epilayers: Physical Fundamentals of Growing Strained and Fully Relaxed Heterostructures.*" Physics-Uspekhi **44**(7): 655-680.

Bronikowski, M. J., Y. J. Wang, *et al.* (1993). "*Antiphase Boundaries as Nucleation Centers in Low-Temperature Silicon Epitaxial-Growth.*" Physical Review B **48**(16): 12361-12364.

Burton, W. K., N. Cabrera, *et al.* (1951). "*The Growth of Crystals and the Equilibrium Structure of their Surfaces.*" Philosophical Transactions of the Royal Society of London. Series A, Mathematical and Physical Sciences **243**(866): 299-358.

Capewell, A. D. (2002). *Novel Grading of Silicon Germanium for High Quality Virtual Substrates*. University of Warwick. Dept. of, Physics.

Capewell, A. D., T. J. Grasby, *et al.* (2002). "*Terrace Grading of SiGe for High-Quality Virtual Substrates.*" Applied Physics Letters **81**(25): 4775-4777.

Chadi, D. J. (1983). "*Semiconductor Surface Reconstruction.*" Vacuum **33**(10-1): 613-619.

Chadi, D. J. (1987). "*Stabilities of Single-Layer and Bilayer Steps on Si(001) Surfaces.*" Physical Review Letters **59**(15): 1691-1694.

Cottrell, A. H. (1964). *Theory of Crystal Dislocations*, Blackie and Son Ltd.

Cullis, A. G. (1996). "*Strain-Induced Modulations in the Surface Morphology of Heteroepitaxial Layers.*" Mrs Bulletin **21**(4): 21-26.

Currie, M. T., S. B. Samavedam, *et al.* (1998). "*Controlling Threading Dislocation Densities in Ge on Si using Graded SiGe Layers and Chemical-Mechanical Polishing.*" Applied Physics Letters **72**(14): 1718-1720.

Dodson, B. W. and J. Y. Tsao (1987). "*Relaxation of Strained-Layer Semiconductor Structures via Plastic-Flow.*" Applied Physics Letters **51**(17): 1325-1327.

Dunham, S. T. (1992). "*Interactions of Silicon Point-Defects with SiO_2 Films.*" Journal Of Applied Physics **71**(2): 685-696.

Dutartre, D., P. Warren, *et al.* (1994). "*Fabrication of Relaxed $Si_{1-X}Ge_x$ Layers on Si Substrates by Rapid Thermal Chemical-Vapor-Deposition.*" Journal Of Vacuum Science & Technology A-Vacuum Surfaces And Films **12**(4): 1009-1014.

Dynna, M., D. D. Perovic, *et al.* (1992). "*Localized Perturbations in Si-Ge Strained Layers Grown by MBE - The Pagoda Defect.*" Philosophical Magazine A-Physics Of Condensed Matter Structure Defects And Mechanical Properties **66**(3): 375-386.

Eifler, G., E. Kasper, *et al.* (2002). "*Investigation of the Silicon Ion Density During Molecular Beam Epitaxy Growth.*" Journal Of Vacuum Science & Technology A-Vacuum Surfaces And Films **20**(3): 945-949.

Farrow, R. F. C. (1995). *Molecular Beam Epitaxy - Applications to Key Materials*, William Andrew Publishing/Noyes.

Fewster, P. F. (1996). "*X-ray Analysis of Thin Films and Multilayers.*" Reports On Progress In Physics **59**(11): 1339-1407.

Fewster, P. F. (2000). *X-ray Scattering from Semiconductors*. London, Imperial College Press.

Fitzgerald, E. A., M. T. Currie, *et al.* (1999). "*Dislocations in Relaxed SiGe/Si Heterostructures.*" Physica Status Solidi A-Applied Research **171**(1): 227-238.

Fitzgerald, E. A. and S. B. Samavedam (1997). "*Line, Point and Surface Defect Morphology of Graded, Relaxed GeSi Alloys on Si Substrates.*" Thin Solid Films **294**(1-2): 3-10.

Fitzgerald, E. A., S. B. Samavedam, *et al.* (1997). "*Influence of Strain on Semiconductor Thin Film Epitaxy.*" Journal Of Vacuum Science & Technology A-Vacuum Surfaces And Films **15**(3): 1048-1056.

Fitzgerald, E. A., Y. H. Xie, *et al.* (1991). "*Totally Relaxed Ge_xSi_{1-X} Layers with Low Threading Dislocation Densities Grown on Si Substrates.*" Applied Physics Letters **59**(7): 811-813.

Fitzgerald, E. A., Y. H. Xie, *et al.* (1992). "*Relaxed Ge_xSi_{1-X} Structures for III-V Integration with Si and High Mobility 2-Dimensional Electron Gases in Si.*" Journal Of Vacuum Science & Technology B **10**(4): 1807-1819.

Föll, P. D. H. (2005). *Defects in Crystals*, http://www.tf.uni-kiel.de/matwis/amat/def_en/.

Frank, F. C. and J. H. van der Merwe (1949). "*One-Dimensional Dislocations. I. Static Theory.*" Proceedings of the Royal Society of London. Series A, Mathematical and Physical Sciences **198**(1053): 205-216.

Freund, L. B. (1990). "*A Criterion For Arrest Of A Threading Dislocation In A Strained Epitaxial Layer Due To An Interface Misfit Dislocation In Its Path.*" Journal Of Applied Physics **68**(5): 2073-2080.

Fuse, T., J. T. Ryu, *et al.* (1999). "*Adsorption of H on the Ge/Si(001) Surface as Studied by Time-Of-Flight Elastic Recoil Detection Analysis and Coaxial Impact Collision Ion Scattering Spectroscopy.*" Japanese Journal Of Applied Physics Part 1-Regular Papers Short Notes & Review Papers **38**(3A): 1359-1362.

Gaiduk, P. I., A. N. Larsen, *et al.* (2000). "*Strain-Relaxed SiGe/Si Heteroepitaxial Structures of Low Threading-Dislocation Density.*" Thin Solid Films **367**(1-2): 120-125.

Gawlinski, E. T. and J. D. Gunton (1987). "*Molecular-Dynamics Simulation Of Molecular-Beam Epitaxial- Growth Of The Silicon (100) Surface.*" Physical Review B **36**(9): 4774-4781.

Ghani, T., M. Armstrong, *et al.* (2003). *A 90nm High Volume Manufacturing Logic Technology Featuring Novel 45nm Gate Length Strained Silicon CMOS Transistors*.

Giovane, L. M., H. C. Luan, *et al.* (2001). "*Correlation Between Leakage Current Density and Threading Dislocation Density in SiGe P-I-N Diodes Grown on Relaxed Graded Buffer Layers.*" Applied Physics Letters **78**(4): 541-543.

Goodhew, P. J. (1972). *Specimen Preparation in Materials Science*. Amsterdam; London, North-Holland.

Goorsky, M. S. (2000). *Defect Studies in P/P^{+} Si*.

Grasby, T. (2002). *Private Communication "0.6 Angstroms is Optimal Growth Rate for SS-MBE"*.

Grasby, T. J. (2000). *Growth Techniques and Characterisation of $Si_{1-x}Ge_x$ Heterostructures for pMOS Applications*.

Halliwell, M. A. G. and S. J. Chua (1998). "*Determining Substrate Orientation using a High-Resolution Diffractometer.*" Journal Of Crystal Growth **192**(3-4): 456-461.

Hammond, C. (2001). *The Basics of Crystallography and Diffraction*. Oxford, Oxford University Press.

Hartmann, J. M., Y. Bogumilowicz, *et al.* (2004). "*Reduced Pressure Chemical Vapour Deposition of SiGe Virtual Substrates for High Mobility Devices.*" Semiconductor Science And Technology **19**(3): 311-318.

Hartmann, J. M., B. Gallas, *et al.* (2000). "*Gas-Source Molecular Beam Epitaxy of SiGe Virtual Substrates: II. Strain Relaxation and Surface Morphology.*" Semiconductor Science And Technology **15**(4): 370-377.

Hecht, E. (1997). *Optics*. Harlow, Addison-Wesley.

Houghton, D. C., J. M. Baribeau, *et al.* (1995). "*Misfit Dislocation Injection, Interfacial Stability and Photonic Properties of Si-Ge Strained Layers.*" Journal Of Materials Science-Materials In Electronics **6**(5): 280-291.

Hull, D. and D. J. Bacon (2002). *Introduction to Dislocations*, Butterworth Heinemann.

Hull, R. and J. C. Bean (1989). "*Nucleation Of Misfit Dislocations In Strained-Layer Epitaxy In The Ge_xSi_{1-X}/Si System.*" Journal Of Vacuum Science & Technology A-Vacuum Surfaces And Films **7**(4): 2580-2585.

Hull, R. and J. C. Bean (1993). "*New Insights Into The Microscopic Motion Of Dislocations In Covalently Bonded Semiconductors By In-Situ Transmission Electron-Microscope Observations Of Misfit Dislocations In Thin Strained Epitaxial Layers.*" Physica Status Solidi A-Applied Research **138**(2): 533-546.

Hull, R., J. C. Bean, *et al.* (1989). "*Role of Strained Layer Superlattices in Misfit Dislocation Reduction in Growth Of Epitaxial $Ge_{0.5}Si_{0.5}$ Alloys on Si(100) Substrates.*" Journal Of Applied Physics **65**(12): 4723-4729.

Intel (2005). *Moore's Law, The Future - Technology & Research at Intel*, http://www.intel.com/technology/silicon/mooreslaw/index.htm.

IQESiltronic (2005). *Ultra Smooth Specification for 17% and 20% Strained Silicon Substrates*, http://www.iqesilicon.com/capabilities/ssi17.pdf

http://www.iqesilicon.com/capabilities/ssi20.pdf.

Jernigan, G. G. and P. E. Thompson (2001). "*Temperature dependence of atomic scale morphology in Si homoepitaxy between 350 and 800 degrees C on Si (100) by molecular beam epitaxy.*" Journal Of Vacuum Science & Technology A-Vacuum Surfaces And Films **19**(5): 2307-2311.

Jesson, D. E., S. J. Pennycook, *et al.* (1993). "*Interplay Between Evolving Surface-Morphology, Atomic-Scale Growth Modes, And Ordering During Si_xGe_{1-X} Epitaxy.*" Physical Review Letters **70**(15): 2293-2296.

Kasper, E. (1995). *Properties of Strained and Relaxed Silicon Germanium*. London, INSPEC.

Kasper, E., M. Bauer, *et al.* (1998). "*Quantitative Secondary Ion Mass Spectrometry Analysis of SiO_2 Desorption during In-situ Heat Cleaning.*" Thin Solid Films **321**: 148-152.

Kasper, E. and K. Lyutovich (2004). "*Strain adjustment with thin virtual substrates.*" Solid-State Electronics **48**(8): 1257-1263.

Kern, W. (1993). *Handbook of Semiconductor Wafer Cleaning Technology - Science, Technology, and Applications*, William Andrew Publishing/Noyes.

Kim, E., C. W. Oh, *et al.* (1997). "*Diffusion Mechanism of Si Adatoms on a Double-Layer Stepped Si(001) Surface.*" Physical Review Letters **79**(23): 4621-4624.

Kissinger, G., T. Morgenstern, *et al.* (1995). "*Stepwise Equilibrated Graded Ge_xSi_{1-X} Buffer with Very-Low Threading Dislocation Density on Si(001).*" Applied Physics Letters **66**(16): 2083-2085.

Kubiak, R. A., S. M. Newstead, *et al.* (1991). "*Improved Flux Control from the Sentinel III Electron-Impact Emission-Spectroscopy System.*" Journal Of Vacuum Science & Technology A-Vacuum Surfaces And Films **9**(4): 2423-2425.

Kulkarni, M. S. (2003). "*A Review and Unifying Analysis of Defect Decoration and Surface Polishing by Chemical Etching in Silicon Processing.*" Industrial & Engineering Chemistry Research **42**(12): 2558-2588.

Kwon, O., J. Boeckl, *et al.* (2005). "*Growth and Properties of AlGaInP Resonant Cavity Light Emitting Diodes on Ge/SiGe/Si Substrates.*" Journal Of Applied Physics **97**(3).

Lambert, A. D. (2000). *Issues Concerning the use of H and Sb Surfactant in Si and $Si_{1-x}Ge_x$ MBE*.

Larsen, A. N. (2000). "*Defects in Epitaxial SiGe-Alloy Layers.*" Materials Science And Engineering B-Solid State Materials For Advanced Technology **71**: 6-13.

Lefebvre, A., C. Herbeaux, *et al.* (1991). "*Interactions Of Misfit Dislocations In $In_xGa_{1-X}As/GaAs$ Interfaces.*" Philosophical Magazine A-Physics Of Condensed Matter Structure Defects And Mechanical Properties **63**(3): 471-485.

LeGoues, F. K. (1994). "*Self-Aligned Sources For Dislocation Nucleation - The Key To Low Threading Dislocation Densities In Compositionally Graded Thin-Films Grown At Low-Temperature.*" Physical Review Letters **72**(6): 876-879.

LeGoues, F. K. (1996). "*The Effect of Strain on the Formation of Dislocations at the SiGe/Si Interface.*" MRS Bulletin: 38-44.

LeGoues, F. K., B. S. Meyerson, *et al.* (1992). "*Mechanism and Conditions for Anomalous Strain Relaxation in Graded Thin-Films and Superlattices.*" Journal Of Applied Physics **71**(9): 4230-4243.

LeGoues, F. K., P. M. Mooney, *et al.* (1993). "*Crystallographic Tilting Resulting From Nucleation Limited Relaxation.*" Applied Physics Letters **62**(2): 140-142.

Leitz, C. W., M. T. Currie, *et al.* (2001). "*Dislocation Glide and Blocking Kinetics in Compositionally Graded SiGe/Si.*" Journal Of Applied Physics **90**(6): 2730-2736.

Li, Q. M., Y. B. Jiang, *et al.* (2004). "*Heteroepitaxy of High-Quality Ge on Si by Nanoscale Ge Seeds Grown Through a Thin Layer of SiO_2.*" Applied Physics Letters **85**(11): 1928-1930.

Linder, K. K., F. C. Zhang, *et al.* (1997). "*Reduction of Dislocation Density in Mismatched SiGe/Si using a Low-Temperature Si Buffer Layer.*" Applied Physics Letters **70**(24): 3224-3226.

Luo, G. L., T. H. Yang, *et al.* (2003). "*Growth of High-Quality Ge Epitaxial Layers on Si(100).*" Japanese Journal Of Applied Physics Part 2-Letters **42**(5B): L517-L519.

Lutz, M. A., R. M. Feenstra, *et al.* (1995). "*Influence of Misfit Dislocations on the Surface-Morphology of $Si_{1-X}Ge_x$ Films.*" Applied Physics Letters **66**(6): 724-726.

Malta, D. P., J. B. Posthill, *et al.* (1992). "*Low-Defect-Density Germanium on Silicon Obtained by a Novel Growth Phenomenon.*" Applied Physics Letters **60**(7): 844-846.

Matthews, J. W. and A. E. Blakeslee (1974). "*Defects in Epitaxial Multilayers: I. Misfit Dislocations.*" Journal of Crystal Growth **27**: 118.

Mo, Y. W. and M. G. Lagally (1991). "*Anisotropy In Surface Migration Of Si And Ge On Si(001).*" Surface Science **248**(3): 313-320.

Mo, Y. W., D. E. Savage, *et al.* (1990). "*Kinetic Pathway In Stranski-Krastanov Growth Of Ge On Si(001).*" Physical Review Letters **65**(8): 1020-1023.

Mooney, P. M. (1996). "*Strain Relaxation and Dislocations in SiGe/Si Structures.*" Materials Science & Engineering R-Reports **17**(3): 105-146.

Mooney, P. M., J. L. Jordansweet, *et al.* (1995). "*Evolution of Strain Relaxation in Step-Graded SiGe/Si Structures.*" Applied Physics Letters **66**(26): 3642-3644.

Mooney, P. M., F. K. Legoues, *et al.* (1994). "*Nucleation of Dislocations in SiGe Layers Grown on (001)Si.*" Journal Of Applied Physics **75**(8): 3968-3977.

Moore, G. E. (1965). "*Cramming More Components onto Integrated Circuits.*" Electronics **38**(8).

Nayfeh, A., C. O. Chui, *et al.* (2004). "*Effects of Hydrogen Annealing on Heteroepitaxial-Ge Layers on Si: Surface Roughness and Electrical Quality.*" Applied Physics Letters **85**(14): 2815-2817.

Nicholas, G. (2004). *Investigation into the Electrical Properties of Tensile Strained Silicon MOSFETS*.

Oberhüber, R., G. Zandler, *et al.* (1998). "*Subband Structure and Mobility of Two-Dimensional Holes in Strained Si/SiGe MOSFET's.*" Physical Review B **58**(15): 9941-9948.

Olsen, S. H., A. G. O'Neill, *et al.* (2003). "*High-Performance nMOSFETs using a Novel Strained Si/SiGe CMOS Architecture.*" Ieee Transactions On Electron Devices **50**(9): 1961-1969.

Paul, D. J. (1999). "*Silicon-Germanium Strained Layer Materials in Microelectronics.*" Advanced Materials **11**(3): 191-204.

Paul, D. J. (2004). "*Si/SiGe Heterostructures: From Material and Physics to Devices and Circuits.*" Semiconductor Science And Technology **19**(10): R75-R108.

Peierls, R. (1940). "*The size of a dislocation.*" Proceedings of the Physical Society **52**(1): 34.

People, R. and J. C. Bean (1985). "*Calculation Of Critical Layer Thickness Versus Lattice Mismatch For Gexsi1-X/Si Strained-Layer Heterostructures.*" Applied Physics Letters **47**(3): 322-324.

Rim, K., R. Anderson, *et al.* (2003). "*Strained Si CMOS (SS-CMOS) Technology: Opportunities and Challenges.*" Solid-State Electronics **47**(7): 1133.

Roland, C. (1996). "*Effects of Stress on Step Energies and Surface Roughness.*" MRS Bulletin: 27.

Rosenblad, C., H. von Kanel, *et al.* (2000). "*A Plasma Process for Ultrafast Deposition of SiGe Graded Buffer Layers.*" Applied Physics Letters **76**(4): 427-429.

Roth, A. (1996). *Vacuum Technology*. Amsterdam, Elsevier Science B.V.

Schaffler, F. (1997). "*High-mobility Si and Ge structures.*" Semiconductor Science And Technology **12**(12): 1515-1549.

Schimmel, D. G. (1979). "*Defect Etch for (100) Silicon Evaluation.*" Journal Of The Electrochemical Society **126**(3): 479-483.

Sheldon, P., B. G. Yacobi, *et al.* (1985). "*Growth and Characterization of GaAs/Ge Epilayers Grown on Si Substrates by Molecular-Beam Epitaxy.*" Journal Of Applied Physics **58**(11): 4186-4193.

Shiryaev, S. Y., J. L. Hansen, *et al.* (1995). "*Strain Relaxation and Self-Organization Phenomena in Heteroepitaxial Systems.*" Physical Review B **52**(22): 15881-15888.

SIA-Online (2005). *SIA Issues - Economy*, http://www.sia-online.org/iss_economy.cfm.

Soitec (2003). *Soitec Receives World Class Supplier Award from Advanced Micro Devices, Inc.*, http://www.soitec.com/en/news/pr65.htm.

Stach, A., R. Hull, *et al.* (2000). "*In-situ Transmission Electron Microscopy Studies of the Interaction Between Dislocations in Strained SiGe/Si(001) Heterostructures.*" Philosophical Magazine A-Physics Of Condensed Matter Structure Defects And Mechanical Properties **80**(9): 2159-2200.

Stach, E. A., R. Hull, *et al.* (1998). "*Effect of the Surface upon Misfit Dislocation Velocities during the Growth and Annealing of SiGe/Si (001) Heterostructures.*" Journal Of Applied Physics **83**(4): 1931-1937.

Stranski, J. N. and L. Krastanov (1938). "*Theory of Orientation Separation of Ionic Crystals.*" Sitzungsberichte der mathematisch - naturwissenschaftlichen Classe der kaiserlichen Akademie der Wissenschaften. Wien. **146**: 797.

Takagi, S., T. Mizuno, *et al.* (2005). "*Sub-Band Structure Engineering for Aadvanced CMOS Channels.*" Solid-State Electronics **49**(5): 684-694.

Takagi, S. I., J. L. Hoyt, *et al.* (1996). "*Comparative Study of Phonon-Limited Mobility of Two-Dimensional Electrons in Strained and Unstrained Si Metal-Oxide-Semiconductor Field-Effect Transistors.*" Journal Of Applied Physics **80**(3): 1567-1577.

Taur, Y. (1998). *Fundamentals of Modern VLSI Devices*. Cambridge, Cambridge University Press.

Tezuka, T., N. Sugiyama, *et al.* (2002). "*Dislocation-Free Formation of Relaxed SiGe-on-Insulator Layers.*" Applied Physics Letters **80**(19): 3560-3562.

Tuppen, C. G. and C. J. Gibbings (1990). "*A Quantitative-Analysis Of Strain Relaxation By Misfit Dislocation Glide In Si1-Xgex/Si Heterostructures.*" Journal Of Applied Physics **68**(4): 1526-1534.

Veeco (2000). *Scanning Probe Microscopy Training Notebook v3.0*, Digital Instruments, Veeco Metrology Group.

Volmer, M. and A. Weber (1926). "*Nuclei Formation in Supersaturated States.*" Zeitschrift Fur Physikalische Chemie **119**: 277-301.

Wang, J., M. Li, *et al.* (2004). "*Sb-Mediated Si Heteroepitaxial Growth on Ge(001).*" Surface Science **560**(1-3): 12-26.

Werner, J., K. Lyutovich, *et al.* (2004). "*Defect Imaging in Ultra-Thin SiGe(100) Strain Relaxed Buffers.*" European Physical Journal-Applied Physics **27**(1-3): 367-370.

Xie, Y. H., G. H. Gilmer, *et al.* (1994). "*Semiconductor Surface-Roughness - Dependence on Sign and Magnitude of Bulk Strain.*" Physical Review Letters **73**(22): 3006-3009.

Yang, T. H., G. L. Luo, *et al.* (2004). "*Interface-Blocking Mechanism for Reduction of Threading Dislocations in SiGe and Ge Epitaxial Layers on Si(100) Substrates.*" Journal Of Vacuum Science & Technology B **22**(5): L17-L19.